Small scale disturbances in the lower dayside ionosphere of Mars as seen by the MaRS radio science experiment on Mars Express

Inaugural-Dissertation
zur
Erlangung des Doktorgrades
der Mathematisch-Naturwissenschaftlichen Fakultät
der Universität zu Köln
vorgelegt von
Kerstin Peter
aus Moers

Köln, 2018

Berichterstatter: Priv. Doz. Dr. Martin Pätzold
(Gutachter)

Prof. Dr. Andreas Eckart

Tag der mündlichen Prüfung: 26.02.2018

Abstract

The lower dayside ionosphere of Mars consists of two major features, the main ionospheric layer M2 and the lower and weaker M1 region. In 2005, *Pätzold et al.* (2005) discovered a local and sporadic third layer below the established two layered structure in the observations of the Mars Express MaRS radio science experiment. Radio science experiments can only sense the electron density distribution but not the ions, therefore the origin and composition of the newly discovered features remained unknown. Until today, no in-situ observations of the atmospheric and ionospheric composition have been conducted in the altitude region between 70 and 110 km. Models predict a possible meteoric origin of these layers due to the ablation and ionization of meteoric magnesium.
This work focuses on the origin of the small scale sporadic electron density structures merged with the main ionospheric body (Mm). Potential sources for the excess electron densities are i.) the interaction of short solar X-ray radiation with the planetary upper mesosphere and thermosphere, ii.) the influx and ionization of meteoric material, iii.) internal gravity waves in the neutral atmosphere at mesospheric / thermospheric heights and iv.) the influx of solar energetic particles. The focus of this work is on a potential correlation between the merged excess electron densities and the short solar X-ray interaction with the planetary neutral atmosphere.
More than 10 years of Mars Express MaRS radio science observations (2004 - 2014) provide a profound data base for this exploration. Statistical correlations between the occurrence rate/characteristics of the identified Mm and the observational and environmental parameters of the observation provide information about potential formation processes. Approximately 44% of the investigated observations contain pronounced merged excess electron densities. They are found for all solar zenith angles of the ionospheric dayside accessible with the MaRS data set (50 ° to 90 °) in approximately 70 to 110 km altitude. The bulk of Mm has been identified over regions with low crustal magnetic fields, which makes the wind-shear theory (sporadic E layer formation on Earth) an unlikely origin. The merged excess electron densities show a positive correlation with the Sun's activity and their base is on average found deeper in the atmosphere, than the base of the averaged undisturbed MaRS electron density profiles. This indicates a dependence of the formation process on energy sources which penetrate deep into the atmosphere.
IonA-2 is a 1-D time-marching photochemical transport model with an implemented di-

urnal cycle. It has been developed to investigate the potential Mm formation by solar X-ray and explore the effect of a changing neutral atmosphere on the Mm composition. The characteristics of the potential Mm derived from the IonA-2 model electron density depend directly on the solar radiation below 1.5 nm. They show good agreement with the general V-shape structure of the observed Mm, and with regard to altitude range, maximum electron density and total vertical electron content. An increase/decrease in solar flux $<$ 1.5 nm yields a prompt (in minutes) increase/decrease of the potential Mm, which might partially explain the sporadic appearances of the Mm structure in the MaRS observations. The higher the NO^+/O_2^+ ratio of a potential merged excess electron density, the longer is its lifetime during a decrease in short solar X-ray. IonA-2 shows, that short solar X-ray which ionizes the local neutral atmosphere provides a satisfying explanation for the identified V-shaped merged excess electron densities in the MaRS observations. This result is in contrast to previous model predictions who assumed a meteoric origin of the sporadic layers. However, other potential sources might provide an additional electron density contribution (meteoric Mg^+), additional sub-structures (gravity waves) or strong Mm enhancements with large disturbances in the ionosphere (SEPs). The sporadic occurrence of the merged excess electron densities in the MaRS observations is assumed to be a combination of observational (increased observation noise level, shift of the lower baseline by ionospheric deviations from radial symmetry) and environmental (solar flux variation, changes in the neutral atmospheric composition) factors.

Zusammenfassung

Die untere Ionosphäre auf der Tagseite des Mars besteht aus zwei Hauptmerkmalen, der ionosphärischen Hauptschicht M2 und der unteren und schwächeren M1-Region. Im Jahr 2005 entdeckten *Pätzold et al.* (2005) eine lokale und sporadische dritte Schicht unterhalb der etablierten Zweischicht-Struktur in den Beobachtungen des Mars Express MaRS radio science Experiments. Die radio science Methode erfasst nur die Elektronendichteverteilung, nicht aber die Verteilung der Ionen. Daher blieben Ursprung und Zusammensetzung der neu entdeckten Schicht unbekannt. Bis heute wurden keine in-situ Beobachtungen der atmosphärischen und ionosphärischen Zusammensetzung im Höhenbereich zwischen 70 und 110 km durchgeführt. Modelle sagen jedoch einen möglichen meteoroidischen Ursprung dieser Schichten voraus, aufgrund der Ablation und Ionisation von meteoroidischem Magnesium.
Diese Arbeit konzentriert sich auf den Ursprung der kleinräumigen sporadischen Elektronendichte-Strukturen (Mm), welche mit der Hauptionosphäre verbunden sind. Mögliche Quellen für die Elektronendichteüberschüsse sind i.) die Wechselwirkung von kurzwelliger solarer Strahlung mit der planetaren oberen Mesosphäre und Thermosphäre, ii.) der Fluss von meteoroidischem Material in die planetare Atmosphere und dessen Ionisation, iii.) Gravitationswellen in mesosphärischen/thermosphärischen Höhen und iv.) der Zustrom von solaren energetischen Partikeln (SEPs). Diese Arbeit untersucht eine möglichen Korrelation zwischen den Mm und der Wechselwirkung von kurzwelliger Röntgenstrahlung mit der Neutralatmosphäre des Mars.
MaRS Beobachtungen von mehr als 10 Jahren (2004 - 2014) bieten eine profunde Datenbasis für diese Untersuchung. Statistische Korrelationen zwischen der Häufigkeit des Auftretens / den charakteristischen Merkmalen der Mm und abgeleiteten MaRS Beobachtungs- und Umgebungsparametern liefern Informationen über mögliche Entstehungsprozesse. Ca. 44% der untersuchten MaRS Beobachtungen enthalten Mm. Diese Mm finden sich in ca. 70 - 110 km Höhe und verteilen sich auf alle Sonnenzenitwinkel der Tagesseite, welche mit dem MaRS-Datensatz zugänglich sind (50 ° bis 90 °). Der Großteil der Mm wurde über Regionen mit niedriger Krustenmagnetfelddichte beobachtet, was die wind-shear Theorie (Entstehung der sporadischen E Schichten auf der Erde) zu einem unwahrscheinlichen Ursprung für ihre Entstehung macht. Die Mm zeigen eine positive Korrelation mit der Sonnenaktivität. Zusätzlich befindet sich ihre untere Grenze im

Durchschnitt tiefer in der Atmosphäre als die Basis der gemittelten ungestörten MaRS Elektronendichteprofile. Dies deutet auf eine Abhängigkeit des Entstehungsprozesses der Mm von tief in die Atmosphäre eindringenden Energiequellen hin.
IonA-2 ist ein 1-D photochemisches Modell mit implementierten Transportprozessen und Tageszyklus. Es wurde entwickelt, um die mögliche Entstehung von Mm durch solar Röntgenstahlung und den Effekt einer sich verändernden Neutralatmosphäre auf die Zusammensetzung der Mm zu untersuchen. Die Eigenschaften der modellierten Mm hängen direkt von der solaren Strahlung unterhalb von 1.5 nm ab. Sie zeigen eine gute Übereinstimmung mit der allgemeinen V-Form der beobachteten Mm, dem Höhenbereich, der maximalen Elektronendichte und dem totalen vertikalen Elektroneninhalt (TEC). Ein Anstieg/Abfall des solaren Flusses $<$ 1,5 nm führt zu einer prompten (in Minuten) Zunahme/Abnahme der Mm, was ihr sporadische Auftreten in den MaRS Beobachtungen teilweise erklären könnte. Je größer das Verhältnis von NO^+/O_2^+ in den Mm, desto länger ist deren Lebensdauer während einer Abnahme der kurzwelligen Röntgenstrahlung. IonA-2 zeigt, dass die Ionisation der lokalen Neutralatmosphäre durch kurzwellige Röntgenstrahlung eine zufriedenstellende Erklärung für die V-förmigen Mm in den MaRS Beobachtungen bietet. Dieses Ergebnis steht im Gegensatz zu früheren Modellvorhersagen, die einen Ursprung der sporadischen Schichten im Zufluss von meteoroidischem Material annehmen. Andere Quellen könnten jedoch einen zusätzlichen Elektronendichtebeitrag liefern (meteoroidisches Mg^+), zusätzliche Unterstrukturen erzeugen (Gravitationswellen) oder ausgeprägte Mm mit starken Störungen in der Ionosphäre verursachen (SEPs). Das sporadische Auftreten der Mm in den MaRS Beobachtungen entsteht durch eine Kombination aus Beobachtungsfaktoren (erhöhter Rauschpegel, Verschiebung der unteren Basislinie durch ionosphärische Abweichungen von der Radialsymmetrie) und Umgebungsfaktoren (Variation des solaren Flusses, Veränderungen in der Zusammensetzung der Neutralatmosphäre).

To my family

Contents

Chapter 1

Introduction and motivation

The Earth ionosphere is regularly sounded by ground based radar (*Zolesi and Cander*, 2013), Global Positioning System (GPS) satellites (e.g. *Schaer* (1999); *Arras et al.* (2008)), and in-situ rocket sounding (e.g. *Istomin* (1963); *Kopp* (1997)). This wealth of observations leads to a good knowledge of the Earth ionosphere and its dependence on external and environmental parameters. For Mars, the number of ionospheric observations is much lower. Planetary ionospheres are accessible either by in-situ or remote sensing observations by spacecraft. In-situ measurements are constrained: the spacecraft needs to fly through the altitude region of interest which is in essence well below 200 km for Mars. In-situ observations of the ionospheric composition and density structure of the Mars ionosphere were made during the two Viking lander descents (*Hanson et al.* (1977)). Until the end of 2014 and before the arrival of the Mars Atmosphere and Volatile Evolution Mission (MAVEN) (*Jakosky et al.*, 2015b) at Mars, these were the only available in-situ data for the Martian ionosphere, providing only a coarse altitude and compositional resolution. Remote sensing experiments like radio soundings allow a more frequent and full scale observation at a significantly higher altitude resolution. Although the radio waves are only sensing the electron distribution, it is assumed that this is representative for the ionospheric plasma. The ionospheric composition, however, cannot be revealed.
The vast amount of radio science observations of the Mars ionosphere with more than 5000 publically available datasets has been made by Mars Global Surveyor (*Albee et al.*, 1998) from 1999 to 2006. But due to *i.)* the short calibration baseline of the observations, *ii.)* single-frequency instead of dual-frequency observations and *iii.)* the high noise level, no reliable analysis of the small scale and sporadic structures of the lower dayside ionosphere could have been made until the arrival of Mars Express (*Wilson*, 2004) at Mars in December 2003. In 2005, *Pätzold et al.* (2005) identified a local and sporadic third layer below the established two layered structure of the ionospheric dayside of Mars. The Mars Radio Science (MaRS) (*Pätzold et al.*, 2004) observations indicate that this sporadic layer can be found in the altitude region between 65 and 120 km with an average electron density of $0.8 \cdot 10^{10}\ m^{-3}$, for which models predict a possible meteoric origin (e.g. *Whalley*

and Plane (2010)) due to the ablation and ionization of meteoric magnesium. Since the beginning of the MaRS observations in 2004, more than 850 observations of the Mars ionosphere have been made, yielding an excellent possibility for the detailed investigation of these sporadic structures of the Mars dayside ionosphere. This work provides for the very first time a thorough investigation of this phenomenon using the entire (undisturbed) MaRS data set of the dayside ionosphere from 2004 - 2014.
The sporadic structures in the region of the ionospheric base are divided into two categories. One group is merged with the main ionospheric body and is therefore called merged excess electron density (Mm). The other group is called detached excess electron density (Md), because the observed excess electron density is detached from the main ionospheric body. The formation processes for this feature are yet unknown, because the whole lower ionosphere of Mars is regularly sounded only by remote radio science observations, which provide the electron density, but not the ion composition of the ionospheric structure. The data base for this work is provided by the "quiet" MaRS dayside ionospheric observations from 2004 - 12/2014. "Quiet" in this context means no large observational noise and no strong disturbances of the ionospheric topside above the main peak. Only dayside observations are investigated, because the nightside ionosphere is patchy and highly irregular. The quiet dayside electron density profiles yield an excellent data base for the determination of the characteristics and the occurrence rate of the excess electron densities under otherwise undisturbed ionospheric conditions. Potential sources for the excess electron densities are i.) the interaction of short solar X-ray radiation with the planetary upper mesosphere and thermosphere, ii.) the influx and ionization of meteoric material, iii.) internal waves in the neutral atmosphere at mesospheric/thermospheric heights and iv.) the influx of solar energetic particles. The focus of this work is on a potential correlation between the merged excess electron densities and the short solar X-ray interaction with the planetary neutral atmosphere. Chapter 2 contains a brief history of the Mars ionospheric exploration and a summary of the current state of research for the ionosphere and the neutral atmosphere at ionospheric altitudes. Chapter 3 describes the radio science method and its potential sources for uncertainties. Chapter 4 contains the derivation of the MaRS ionospheric data base for this work and associated observational parameters. Chapter 5 contains the derivation of the environmental and solar parameters for the time of the selected MaRS observations for comparison with the characteristics and occurrence rate of the merged excess electron densities. Chapter 6 provides a description of the developed ionospheric models and the underlying physics. Two ionospheric models have been developed for this work, IonA-1 and IonA-2. The 1-D photochemical steady state model IonA-1 is used for the determination of the ionospheric state from the MaRS observations. The 1-D time-marching photochemical and transport model IonA-2 is used to investigate short solar X-ray as potential source for the merged excess electron densities by using external data bases for the Martian neutral atmosphere and model solar flux at the Martian position for certain MaRS observations. Chapter 7 correlates the characteristics and occurrence rates of the identified merged excess electron densities with

the observational and environmental parameters of Chapter 4 and 5 to identify potential sources for the Mm formation. Chapter 8 applies the IonA-2 model to the atmospheric and solar flux conditions of two selected MaRS observations with merged excess electron densities to identify the effect of short solar X-ray on the planetary neutral atmosphere and ionosphere. In addition, the other potential sources for the merged excess electron densities are shortly discussed. Chapter 9 gives a summary of the work and provides future applications of this work and the IonA-2 model.

Chapter 2

The Mars ionosphere: exploration and current state of research

This Chapter recapitulates the history of the Mars upper atmosphere and ionosphere exploration. Important spacecraft payloads for this work are introduced, the characteristics of the Mars surface, atmospheric and plasma environment are summarized and categories of models for the Martian ionosphere are briefly described.

2.1 History of the Mars upper atmosphere/ionosphere exploration and important spacecraft payloads

2.1.1 Early exploration of the upper neutral atmosphere and ionosphere

In 1965, the Mars atmosphere and ionosphere were sounded with radio occultation for the first time during the flyby of Mariner 4 (*Kliore et al.*, 1965). The results were consistent with a CO_2 dominated atmosphere and a millibar surface pressure. Mariner 9, which was the first spacecraft orbiting another planet, arrived at Mars in 1971 and added few S-band occultation observations of the Martian atmosphere and ionosphere (*Kliore et al.*, 1972). The first in-situ observations of the Martian atmosphere below 90 km were conducted by the Mars-6 lander in 1974 (*Kerzhanovich*, 1977), which sent 244 s of partly unusable data, before it was lost during descent. The two Viking orbiters arrived at Mars in 1976 and provided dual-frequency radio occultation observations in the S-Band (2.3 GHz) and X-Band (8.4 GHz) frequency range (*Lindal et al.*, 1979). The Viking landers (*Seiff and Kirk*, 1977; *Soffen*, 1977) provided the first in-situ observations of the composition of the Mars upper atmosphere/ionosphere and ion/electron temperatures (*Nier and McElroy*, 1976, 1977; *Hanson et al.*, 1977). On July 20, 1976 the Viking lander 1 descended to Chryse Planitia (22.27 °N, 312.05 °E planetocentric coordinates, 4:13 p.m.

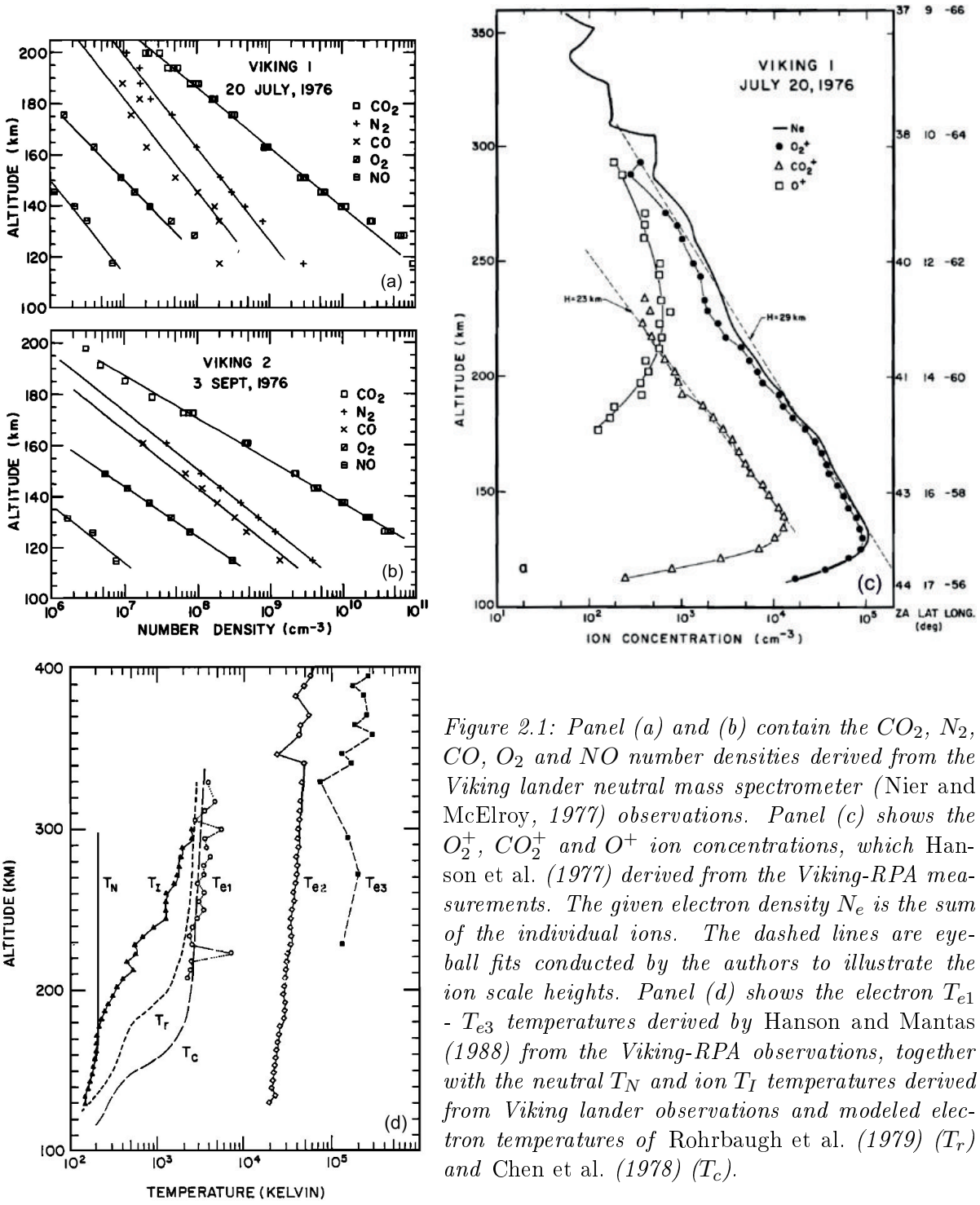

*Figure 2.1: Panel (a) and (b) contain the CO_2, N_2, CO, O_2 and NO number densities derived from the Viking lander neutral mass spectrometer (*Nier and McElroy*, 1977) observations. Panel (c) shows the O_2^+, CO_2^+ and O^+ ion concentrations, which* Hanson et al. *(1977) derived from the Viking-RPA measurements. The given electron density N_e is the sum of the individual ions. The dashed lines are eyeball fits conducted by the authors to illustrate the ion scale heights. Panel (d) shows the electron T_{e1} - T_{e3} temperatures derived by* Hanson and Mantas *(1988) from the Viking-RPA observations, together with the neutral T_N and ion T_I temperatures derived from Viking lander observations and modeled electron temperatures of* Rohrbaugh et al. *(1979) (T_r) and* Chen et al. *(1978) (T_c).*

local Mars time)[1] and 45 days later on September 9, 1976, the Viking lander 2 arrived at Utopia Planitia (47.64 °N, 134.29 °E planetocentric coordinates, 9:49 a.m. local Mars time)[2]. This corespondents to a solar longitude L_S of 97 ° and a solar zenith angle of χ = 57.3 ° for Viking lander 1 and L_S = 117.6 ° and χ = 36.5 ° for Viking lander 2. The solar zenith angle χ is the angle between the vertical and the direction of the incoming solar radiation. The solar longitudes are close to aphelion and northern summer (see Figure 2.5) and the observations took place during solar minimum conditions with an approximately solar flux at 10.7 cm (2800 MHz) F10.7 index at Earth of 70[3]. Mass spectrometers on the aeroshell of the landers provided information about the neutral densities of CO_2, N_2, Ar, O_2, NO and CO (Panel (a) and (b) of Figure 2.1) and about the ionospheric densities of CO_2^+, O_2^+ and O^+ (Panel (c) of Figure 2.1). The dominance of neutral oxygen in higher altitudes (which is used in all actual models of the Mars upper atmosphere and ionosphere) is inferred from the mass spectrometer ion measurements. While neutral NO was identified in the atmosphere, NO^+ could not be uniquely identified from the Viking lander observations (*Hanson et al.*, 1977). No observation of N was made. This will be important for the discussion of the N_2 cycle and the upper mesospheric and lower thermospheric composition in Chapter 8. Panel (d) of Fig. 2.1 is taken from *Hanson and Mantas* (1988). The authors derive electron temperatures for two thermal electron populations e_1 and e_2, and one suprathermal electron population e_3 from the Viking Retarding Potential Analyzer (Viking-RPA) observations during the lander descent. Electron temperatures for the main thermal electron population e_1 could only be derived down to an altitude of approximately 215 km. Panel (d) also contains the observed ion temperature and the neutral temperature derived by *Nier and McElroy* (1977) from the Viking lander observations. Due to the fact that measurements of the electron temperature are not available in the region of the ionospheric main peak, modelers usually rely on model electron temperatures, e.g. those of and two model electron temperature profiles of *Rohrbaugh et al.* (1979) and *Chen et al.* (1978) also shown in the Figure.

2.1.2 Modern exploration of the Mars upper atmospheric region

Subsequently, the Mars Global Surveyor (MGS) spacecraft went in orbit around Mars in September 1997 (*Albee et al.*, 1998) and remained in good health until the end of 2006, when it went into save mode and further contact attempts failed. The spacecraft carried five experiments and a relay receiver for communication with the Mars Rovers on the surface. Important for this work are the Mars Orbiter Laser Altimeter (MGS-MOLA), the MAGnetometer and Electron Reflectometer (MGS-MAG/ER) and the Radio Science

[1]NASA: https://nssdc.gsfc.nasa.gov/nmc/spacecraftDisplay.do?id=1975-075C

[2]NASA: https://nssdc.gsfc.nasa.gov/nmc/spacecraftDisplay.do?id=1975-083C

[3]ftp://ftp.ngdc.noaa.gov/STP/space-weather/solar-data/solar-features/solar-radio/noontime-flux/penticton/penticton_adjusted/listings/listing_drao_noontime-flux-adjusted_daily.txt

experiment (MGS-RS). MGS-MOLA transmitted infrared laser pulses to the Martian surface and received the reflected signals. The signal travel time provides a measure for the range between spacecraft and surface and resulted in the development of high resolution spherical harmonic models for the Mars topography and shape (*Smith et al.*, 2001). The MGS-MAG/ER experiment consists of two redundant triaxial fluxgate magnetometers and an electron reflectometer (*Acuña et al.*, 2001). The instrument measured the magnetic properties of the Mars environment and determined the interior and crustal magnetic field of the planet for the first time. MGS carried an UltraStable Oscillator (USO), which provides a stable signal for radio science MGS-RS observations. The radio science experiment provided more than 5,000 publicly available single X-Band observations of the Mars ionosphere (*Hinson et al.* (1999); *Bougher et al.* (2004)). The MGS ionospheric observations, however, were constrained geometrically by the sun-synchronized and low altitude orbit, optimized for the imaging experiments. Radio occultations were limited to high planetary northern and southern latitudes above 60 degree. The low circular orbit of 400 km limited the achievable sensing altitude to an area below 220 - 240 km.
The 2001 Mars Odyssey spacecraft (ODY) (*Saunders et al.*, 2004) arrived at Mars in 2001. It's main goals were the further investigation of the Mars surface mineralogy and morphology and determination of the Martian radiation environment for future human exploration. Atmospheric density observations of MGS and ODY during their individual aerobraking phases put further constraints on the upper atmosphere, including the influence of general and gravity waves (see e.g. *Fritts et al.* (2006)). In March 2006, the Mars Reconnaissance Orbiter (MRO) reached Mars (*Zurek and Smrekar*, 2007) and provided additional information about the upper atmosphere during its aerobraking phase (*Keating et al.*, 1998, 2009). Indirect observations of the ionosphere were conducted with the SHAllow subsurface RADar MRO-SHARAD (*Seu et al.*, 2007). The instrument transmits radar signals and collects surface and near-surface reflections to investigate the distribution of competent rock, soil, water, and ice in the Martian surface. For this subsurface sounding, the influence of the Mars ionosphere on the emitted and reflected radio signals need to be corrected. This correction contains a phase parameter, which has a linear correlation with the vertical electron content (TEC) and is used to determine the vertical ionospheric TEC on a regular basis (*Mendillo et al.*, 2017).

The Mars Express spacecraft

On June 2. 2003, the ESA spacecraft Mars Express (MEX) (*Wilson*, 2004; *Fletcher*, 2009) was launched from the Baikonur Cosmodrome in Kazakhstan on a Soyuz/Fregat launcher. The spacecraft arrived at Mars in December 2003 and went into a quasi-polar orbit with a pericenter of 250 km, apocenter of 10,142 km, an inclination of 86.35 ° and a 6.75h period. The lander Beagle 2 was deployed five days before the arrival of Mars Express at Mars. Its fate remained unknown until 2015, when it was identified only partly

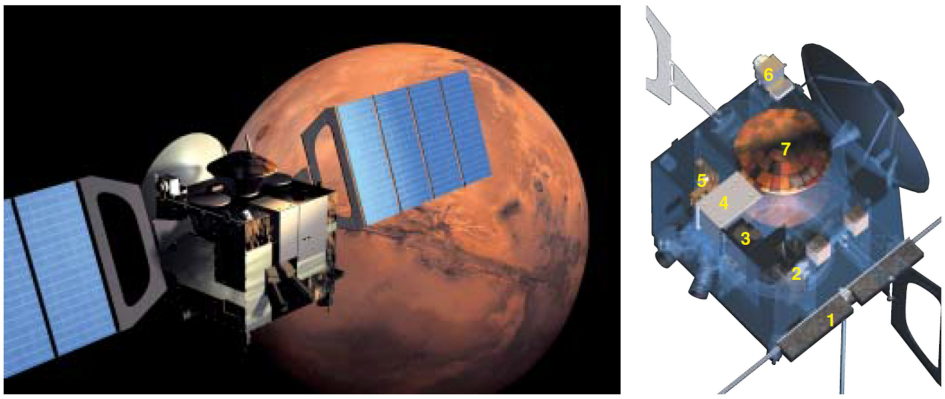

Figure 2.2: The left Panel shows the Mars Express spacecraft with the Beagle 2 capsule, while the right Panel shows the instruments of the Mars Express mission: 1: MARSIS, 2: HRSC, 3: OMEGA, 4: PFS, 5: SPICAM, 6: ASPERA, 7: Beagle 2. The fixed High Gain Antenna (HGA) 1.6m dish is clearly visible on the right side of the rightside Panel, the Low Gain Antennas (LGA)s are shown in front of the spacecraft. The radio science experiment MaRS makes use of the high gain antenna during its planetary occultation observations. The Figure is taken from Chicarro et al. *(2004).*

deployed in images of the high resolution camera of the MRO spacecraft[4]. Mars Express celebrated 10 years in orbit in at the End of 2013 and 5,000 days in orbit in 2017 during its ongoing mission. The scientific goals of Mars Express are the exploration of the Martian surface, subsurface structures, gravity field, planetary atmosphere and ionosphere. Figure 2.2 illustrates the payload of Mars Express, which consists of seven experiments. The High Resolution Stereo Camera MEX-HRSC (*McCord et al.* (2007) and references therein) consists of nine parallel mounted charge-coupled device (CCD) line sensors who provide along-track high-resolution multicolor stereo images of the Mars surface. The Mars Advanced Radar for Subsurface and Ionospheric Sounding MEX-MARSIS (*Picardi et al.*, 2004) experiment is a Martian ground penetrating / ionospheric sounder and altimeter. It investigates the altitude distribution of the ionospheric electron density, but only down to the ionospheric main peak. The Observatoire pour la Minéralogie, l'Eau les Glaces et l'Activité MEX-OMEGA (*Bellucci et al.*, 2004) is a visible and near-infrared mineralogical mapping spectrometer, while MEX-PFS is a double-pendulum infrared Planetary Fourier Spectrometer (*Formisano et al.*, 2004). The SPectroscopy for the Investigation of the Characteristics of the Atmosphere of Mars MEX-SPICAM (*Bertaux et al.*, 2004; *Montmessin et al.*, 2017) consists of an ultraviolet and an infrared atmospheric spectrometer. Among other observation modes, it determines the atmospheric nightglow caused by the recombination of N and O atoms to NO. N and O are produced in the thermosphere

[4] *www.esa.int/Our_Activities/Space_Science/Mars_Express*

by photochemistry and transported on the planetary nightside (see e.g. *Stiepen et al.* (2015)). Those observations can be used to determine the characteristics of the nitrogen cycle in the upper atmosphere and ionosphere of Mars. The Analyzer of Space Plasmas and Energetic Atoms-3 MEX-ASPERA3 (*Barabash et al.*, 2004) investigates the different plasma domains of Mars, especially the upper atmosphere/interplanetary medium/solar wind interaction and the atmospheric escape. The imaging of energetic neutral atoms (ENAs), which occur during the interaction of the neutral planetary atmosphere with the solar wind, is done with three sensors. Of those three, the 'top hat' electrostatic analyzer ELectron Spectrometer (ELS) sensor can be used for determining the potential origins of the excess electron densities, because it provides an indirect method for determining the presence of strong solar energetic particle events at Mars (see Chapter 8 for details).
The Mars Radio Science experiment MaRS (*Pätzold et al.* (2004, 2009, 2016b)) has been in operation since April 2004. Beside radio occultations the operational goals of MaRS are the (i) bistatic radar: Mars Express transmits radio signals at a certain location on the Mars surface where the signals are scattered and then received by a ground station on Earth. The received signal is used to determine the dielectric and scattering properties of the Mars local surface material. (ii) determination of anomalies in the gravity field of Mars: The internal mass distribution of the planet determines its external gravity field which is reflected in the orbit parameters of Mars Express. Unexpected velocity changes of the spacecraft along the line-of-sight between spacecraft and ground station reflect gravity anomalies not yet included in the orbit predictions. Evaluating these differences yields an insight into the internal mass structure of Mars and the evolution of its lithosphere and crust. (iii) determination of the mass and low-order gravity field harmonics of the Mars moon Phobos by close fly-bys and (iv) Solar Corona observations: The plasma corona of the Sun can be investigated by Mars Express when Mars is in conjunction to Earth. Within approximately 10° elongation with respect to the Sun the dispersive effects on the radio signals are dominated by the Sun's plasma, providing an unique way to determine the Sun's coronal properties. The radio occultation method uses radio signals to remotely investigate the neutral atmosphere and ionospheric electron density of Mars during Earth occultations. During an occultation, the spacecraft is moving behind the planet as seen from the Earth. In an occultation ingress, the continuous radio signal is sounding the ionosphere and neutral atmosphere of Mars from top to bottom and provides information about the state of the ionosphere and neutral atmosphere. Chapter 3 contains a detailed description of the radio occultation method, data acquisition and processing.

The MAVEN spacecraft

On November 18. 2013, the Mars Atmosphere and Volatile EvolutioN (MAVEN) orbiter (*Jakosky et al.*, 2015b,a) was launched and arrived at Mars in September 2014. The spacecraft (see Figure 2.3) was inserted into an elliptical orbit with a periapsis of approximately

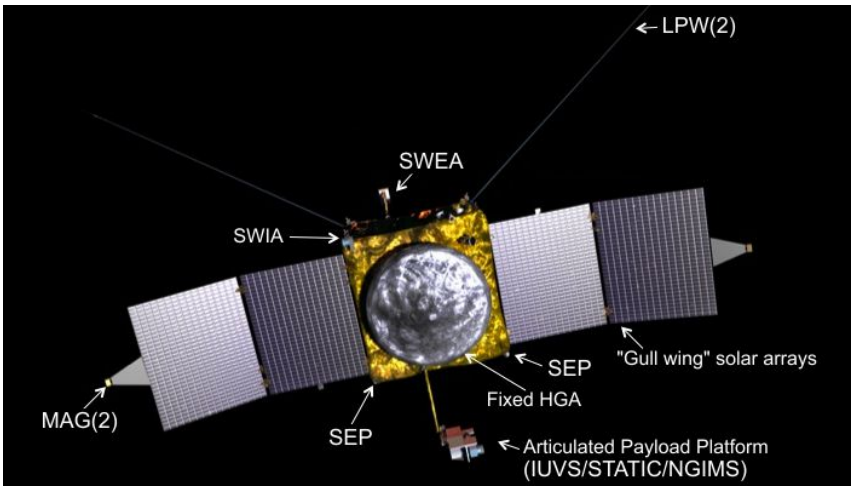

Figure 2.3: The MAVEN spacecraft. The Figure labeling is lightly altered, original Figure from http : //lasp.colorado.edu/home/maven/about/spacecraft/.

150 km and an apoapsis of approximately 6200 km. The inclination of 74° and period of 4.5h cause a precession of the periapsis in planetary latitude and local solar time to provide a good coverage of the Mars environment. During several 'deep-dip' campaigns the periapsis of MAVEN is lowered to approximately 125 km for few consecutive orbits (7 deep-dips until September 2017), allowing in-situ observations of the ionosphere and neutral atmosphere shortly below the ionospheric main peak. After completion of the commissioning phase and the one Earth-year primary mission, MAVEN is now in its extended mission phase. The spacecraft is designed to determine the atmospheric gas loss to space and its impact on the Mars climate and habitability. For that, i.) the interaction of the Sun and solar wind with the Mars upper atmosphere and magnetosphere, ii.) the present composition and structure of the upper atmosphere / ionosphere and iii.) the escape rates of the upper atmosphere to space are determined including the processes controlling them. These parameters will be extrapolated backwards in time to determine the atmospheric loss rate and with that the habitability and climate of the early Mars.
The payload of the MAVEN spacecraft consists of three packages with eight instruments. The MAVEN Particles and Fields Package consists of six instruments. The Solar Wind Electron Analyzer (MVN-SWEA) (*Mitchell et al.*, 2016) is an electrostatic analyzer for the investigation of the solar wind, magnetosheath and ionospheric photo-electrons. The Solar Wind Ion Analyzer (MVN-SWIA) (*Halekas et al.*, 2015) is a torodial energy analyzer, which in-situ determines the plasma density, velocity, pressure and heat flux. The Solar Energetic Particle instrument (MVN-SEP) (*Larson et al.*, 2015) in-situ measures the input of Solar Energetic Particles (SEPs) into the Mars environment. The Suprathermal and Thermal Ion Composition instrument (MVN-STATIC) (*McFadden et al.*, 2015) is a toroidal 'top hat' electrostatic analyzer combined with a time-of-flight velocity an-

alyzer. It observes in-situ the cold ions of the collisional Mars ionosphere, the heated suprathermal plasma tail of those ions in the upper ionosphere and the pickup ions which are accelerated by solar wind electric fields to escape velocities. The Langmuir Probe and Waves instrument (MVN-LPW) consists of two components, the MVN-LPW Langmuir probe (*Andersson et al.*, 2015) and the MVN-LPW-EUV photometers (*Eparvier et al.*, 2015). The MVN-LPW Langmuir probe is designed to measure the electron density, electron temperature and electric field wave power at low frequencies (ion heating) and wave spectra of natural/generated Langmuir waves (measurement calibration). The MVN-LPW-EUV consists of three broadband radiometers to measure the soft solar X-rays and EUV irradiance (0.1-3 nm and 17-22 nm, 0.1-7 nm, 121-122 nm) at Mars. The Magnetometer (MVN-MAG) instrument (*Connerney et al.*, 2015) consists of two independent tri-axial fluxgate magnetometers to measure the ambient vector magnetic field. The second instrument package (remote sensing) consists of the Imaging Ultraviolet Spectrometer MVN-IUVS (*McClintock et al.*, 2015) only. The instrument has four modes to measure the upper atmospheric structure and composition: (i) during near periapsis limb scanning, vertical profiles of H, C, N, O, CO, N_2, C^+ and CO_2^+ are measured from the homopause up to two scale heights above the exobase, (ii) in the disc mapping mode, column abundance maps of H, C, N, O, CO_2, O_3 and dust are derived from the illuminated and visible part of the upper atmosphere, (iii) in coronal scans, vertical profiles of the exospheric hot species H, D and O are derived, (iv) stellar occultations provide vertical profiles of CO_2 and O_3 of the mesosphere and thermosphere. Additionally to this primary goals, MVN-IUVS is capable of detecting the presence of Mg, Mg^+, Fe and Fe^+ in the Mars upper atmosphere (*Schneider et al.*, 2015; *Crismani et al.*, 2017). The third payload package of MAVEN consists of the Mass Spectrometry Package. It contains only one instrument, the Neutral Gas and Ion Mass Spectrometer (MVN-NGIMS) (*Mahaffy et al.*, 2015b). MVN-NGIMS is a quadrupole mass spectrometer which measures the atmospheric (He, N, O, CO, N_2, NO, O_2, Ar and CO_2) and thermal ionospheric composition (O_2^+, CO_2^+, NO^+, O^+, CO^+, C^+, N_2^+, OH^+ and N^+) along the spacecraft track between 500 km altitude and the MAVEN pericenter. Additionally, several isotope ratios and the density of metallic ions of meteoric origin are observed (*Benna et al.*, 2015b).

2.2 The Mars environment

Figure 2.4 shows a to-scale comparison of Earth and Mars. The length of the orbital semimajor axis of Mars is 1.52[5] Astronomical units (AU), which means that the planet is on average 1.52 times as far from the Sun as Earth, whose semimajor axis is ~ 1 AU ($149.6 \cdot 10^6 km$). The Mars orbit has a relatively large eccentricity of 0.094 compared to the eccentricity of the Earth orbit of 0.017. Mars pericenter distance to the Sun is 1.381 AU, while its apocenter lies at 1.666 AU. This difference between apocenter and pericenter causes a large variation in the available solar flux at the Mars position. The tropical orbit period of Mars, which is the time Mars needs for a full orbit from from Northern spring equinox to Northern spring equinox, is 686.973 days. The numbering of Martian years follows the widely used calendar of *Clancy et al.* (2000). Mars Year 1 began on April 11, 1955 with L_S= 0°. On May 5. 2017, Mars reached vernal equinox and passes into Mars Year MY 34[6]. A planets obliquity is the angle between its orbital plane and the equatorial plane. With 25.19° for Mars and 23.44° for Earth, the obliquity of both planets is quite similar. Figure 2.5 illustrates the Martian seasons in dependence of the solar longitude L_S, which is the angle between the Mars-Sun line at the northern hemisphere spring equinox where $L_S = 0°$ and the actual Mars-Sun line. The summer solstice of the northern hemisphere ($L_S = 90°$) occurs close to aphelion, the autumn equinox of the northern hemisphere relates to $L_S = 180°$. The northern winter solstice (or southern summer) occurs at $L_S = 270°$, close to perihelion. The seasons on Mars are dominated by its obliquity, which is similar to Earth. In addition, the orbit eccentricity of Mars reinforces the seasons on the southern hemisphere (see *Smith et al.* (2017) and references therein). An average solar day on Mars lasts 24.6597 hours, which is quite comparable to the 24 hours on Earth.

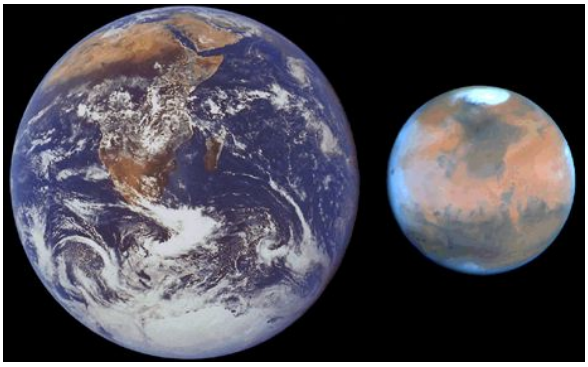

Figure 2.4: Earth and Mars on a similar scale. The Earth image was taken during the final mission of the Apollo program, Apollo 17. The Mars image was taken by the Viking spacecrafts. Cropped figure from esa.int.

With a volumetric mean radius of 3389.5 km, Mars has approximately half the diameter of Earth and with a value of 0.0059 only a slightly larger polar flattening ([equatorial radius - polar radius]/equatorial radius) than Earth. The mean density of Mars is with $3.9 \cdot 10^3\, kg/m^3$ much smaller than that of Earth with $5.5 \cdot 10^3\, kg/m^3$. This results in a

[5] *https://nssdc.gsfc.nasa.gov/planetary/factsheet/marsfact.html*
[6] *https://mars.nasa.gov/allaboutmars/extreme/martianyear/*

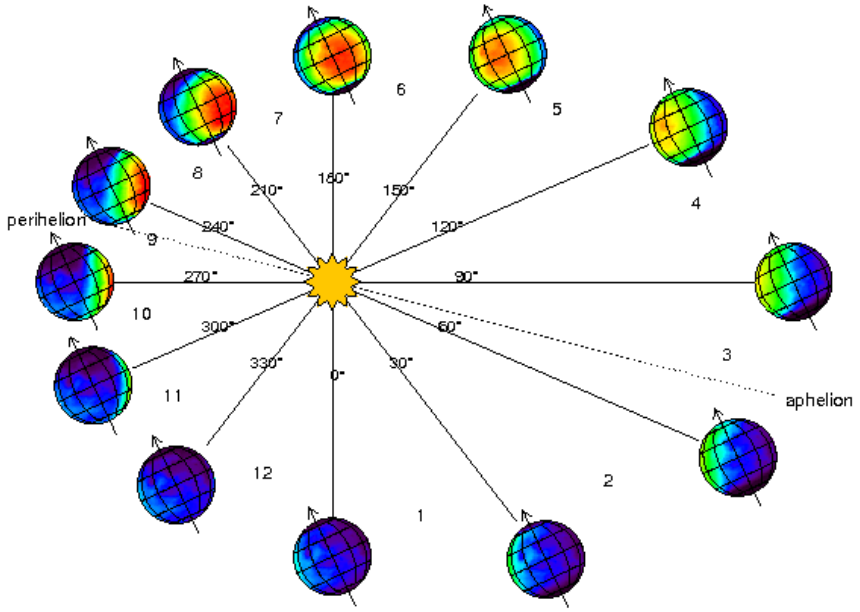

Figure 2.5: Illustration of the Mars-Sun interaction during a Martian year.[a]

a= Figure from $http://www-mars.lmd.jussieu.fr/mars/time/solar\_longitude.html$

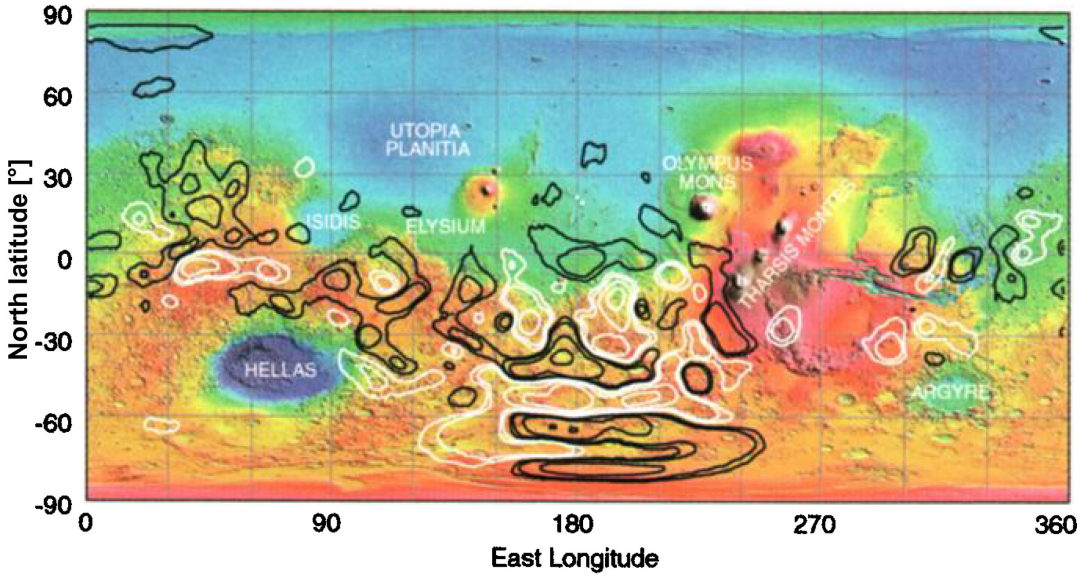

Figure 2.6: Overlay of the crustal magnetic field with the Mars topography. The black and white lines indicate isomagnetic contours of the radial field component at (400 ± 30) *km altitude for* $B = \pm 10, 20, 50, 100, 200\,nT$ *derived from the MGS-MAG/ER magnetic field observations and the MGS-MOLA topography measurements. The map is taken from* Connerney et al. *(2001).*

Martian planetary mass of $0.64 \cdot 10^{24}\,kg$, which is approximate only 11% of the Earth's mass, causing a surface gravity of approximately $3.71\,m/s^2$, which is small compared to the surface gravity of Earth with approx $9.81\,m/s^2$.
Figure 2.6 shows an overlay of the Mars topography with the crustal magnetic field. The most fundamental crustal feature of Mars is its dichotomy between the northern and the southern hemisphere. The relief between the northern lowlands and southern highlands of Mars is always larger than 2.5 km with maximum differences larger than 6 km. The occurrence rate (or frequency distribution) of terrain elevation shows a difference of approximately 5.5 km between the elevation distribution peaks for highlands and lowlands (see summary of *Watters et al.* (2007) and references therein). The topography on Mars has a much stronger variation in surface relief than Earth, differing approximately 29.4 km from the floor of the Hellas basin (-8.2 km) to the top of the shield vulcan Olympus Mons (+21.2 km) (*Carr*, 2006). The MGS-MAG/ER twin fluxgate magnetometer and electron reflection analyzer on the MGS spacecraft determined that Mars has no global magnetic field, but observed small-scale crustal magnetic fields in its mapping orbit of 400 km altitude. The magnetic fields are mainly associated with the ancient, strongly cratered highlands of the Mars southern hemisphere (*Acuña et al.*, 1999). A review of this topic is found in *Connerney et al.* (2015). *Connerney et al.* (2001) compiled the MGS-MAG/ER observations into a global map of the crustal magnetization. The remnant magnetization of the Mars crust is attributed to an early global magnetic field. It is assumed, that the planetary dynamo demised approximately 4 billion years ago due to the last large surface impacts, which left basins with unmagnetized material. The strongest magnetic features are found east-west aligned at Terra Cimmeria and Terra Sirenum (southern hemisphere) with its center on 180° east longitude. *Connerney et al.* (2005) propose, that the planetary crust was magnetized during crustal spreading/cooling in the presence of a reversing planetary dynamo and that thermal demagnetization of the surface occurred by covering the crust with flood basalts of few kilometer thickness.

2.3 The neutral atmosphere in ionospheric heights

A planetary atmosphere can be classified by several parameters, e.g. temperature, composition or grade/kind of ionization. Figure 2.7 shows a comparison between Earth and Mars temperature profiles for the time of the Viking landers together with the associated general temperature categorization/nomenclature for Earth and Mars. As discussed in *Prölss* (2004), the classification of the Earth neutral atmosphere by the vertical temperature profile has four atmospheric regions. The troposphere is the atmospheric region closest to the surface. The temperature decreases with increasing distance to the warm surface due to radiative cooling. The temperature gradient in this region is usually described by dry (low water content) and moist (high water content) adiabatic processes. The subsequent region is called stratosphere, where the temperature rises again due to the

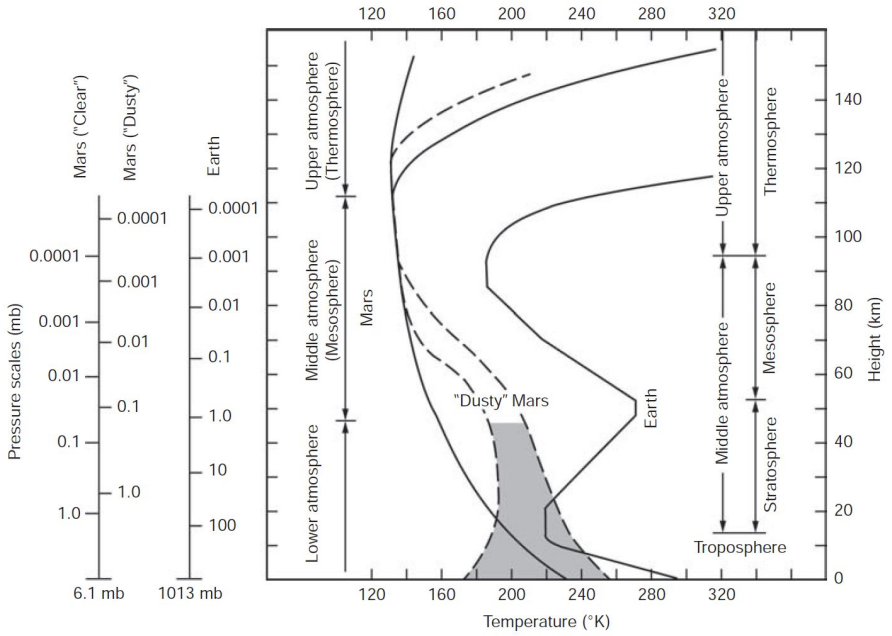

Figure 2.7: The black solid lines on the right and left sides represent the U.S. standard atmosphere for 1976 and the neutral temperature profile derived from Viking Lander 1 observations by Seiff and Kirk *(1977), respectively. The dashed temperature curves indicate effects of aerosols during large atmospheric dust events. The annotations contain the description of the associated atmospheric regimes, while the pressure scales show exemplary hydrostatic pressure profiles for Earth and Mars. The Figure is a reproduction from* Zurek *(1992) and taken from* Zurek *(2017).*

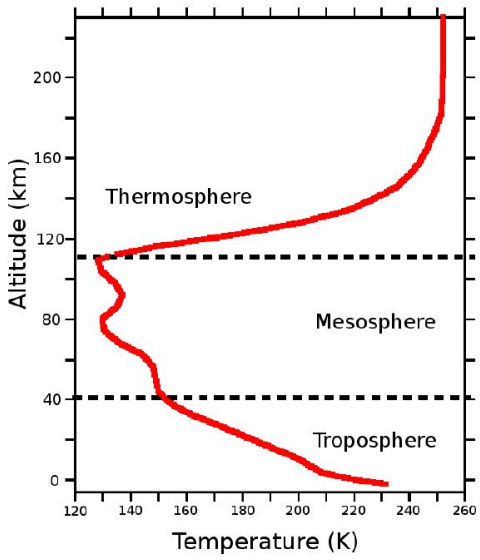

Figure 2.8: LMD-GCM model neutral temperature taken from González-Galindo et al. *(2008).*

absorption of solar radiation by O_3. Above the stratosphere, the temperature decreases to its absolute minimum in the mesosphere. This occurs due to radiative cooling, because solar radiation absorption is less important here. In the thermosphere, the temperature increases strongly due to the absorption of photons up to the ultraviolet wavelength range and due to the absence of efficient processes for heat loss. Figure 2.8 shows a more recent model neutral temperature profile of the Mars atmosphere derived with the Global Climate Model for the Martian atmosphere from the Laboratoire de Météorologie Dynamique (LMD-GCM). The average surface temperature of Mars is 210 K[7] and the subsequent Mars troposphere shows dry adiabatic behavior due to the low amount of available water. The Mars atmosphere has no stratosphere, because the O_3 density is too small to absorb enough solar photon energy for additional heating. However, if the atmospheric dust load is high enough, a temperature inversion similar to the Earth stratosphere is possible due to additional heating. The lower thermosphere shows a strong temperature increase similar to Earth due to heating by the absorption of solar ultraviolet radiation. The temperature in the upper thermosphere increases asymptotically. This is caused by the high conductivity of the upper Martian atmosphere which prevents large temperature gradients (*González-Galindo et al.*, 2008).
Another criterion for the atmospheric classification is its composition. In the homosphere, the planetary atmosphere is well mixed and the densities of all gases decrease with the same neutral scale height $H_n = k_B T_N/(< m > g)$, where k_B is the Boltzmann constant, T_N is the neutral temperature, $< m >$ is the average mass in the homosphere and g is the gravity acceleration. The region is connected to the heteorosphere by a transition region. In the heterosphere collisions between particles become less frequent and the density of each species decreases according to their individual scale heights. The boundary between the two regimes is called the homopause. The altitude of the homopause is individual for each atmospheric species. At Earth, the homopause is approximately found at 100 km altitude (*Prölss*, 2004). At Mars, the MVN-NGIMS instrument identified the homopause for ^{40}Ar and N_2 at 130 km altitude for $L_S = 326\,^\circ$ and Ω_{lat} between $-2\,^\circ$ to $-5\,^\circ$ (*Mahaffy et al.*, 2015a). In the LMD-GCM, the homopause altitude is predicted at approximately 120 km altitude with strong seasonal and spatial variability (*González-Galindo et al.*, 2009). Gravitational binding divides planetary atmospheres into two regimes. The region, where the atmosphere is fully bound to a planet is called barosphere, while the region, where light species can escape into space is called the exosphere. The lower border of the exosphere is the exobase, which is defined as that altitude above which a radially outward moving particle experiences on average less than one backscatter collision. Due to their individual masses, there is an individual exobase for each species. For Earth, the exobase is found approximately in 500 km altitude (*Schunk and Nagy*, 2009). On Mars, the average model exobase altitude for the planetary dayside during moderate solar activity is 220 km for Argon and CO_2 ((*Terada et al.*, 2017) and references therein).

[7] NASA: *https://nssdc.gsfc.nasa.gov/planetary/factsheet/marsfact.html*

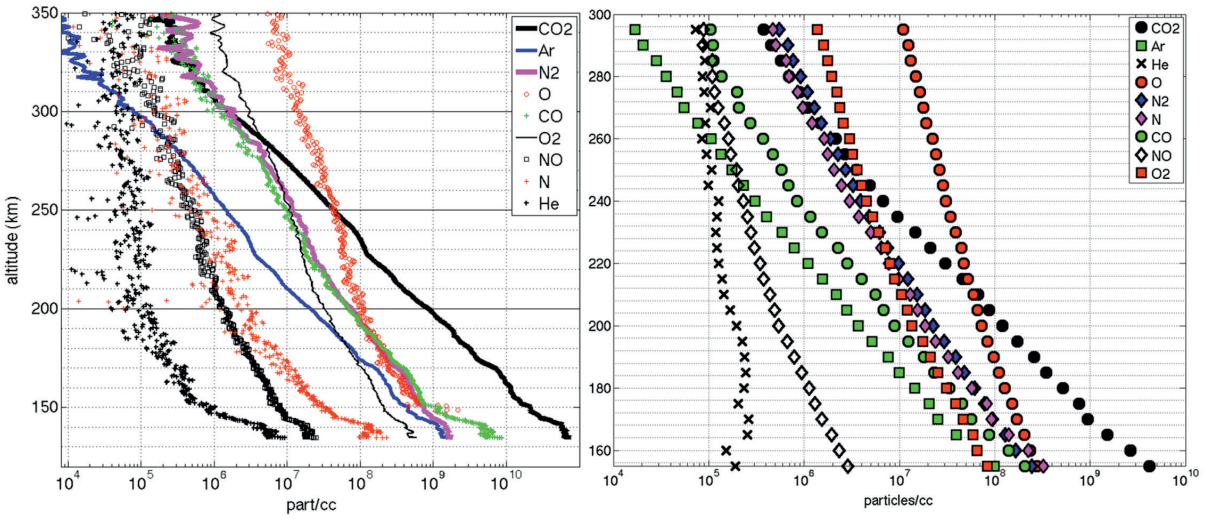

Figure 2.9: (left) MVN-NGIMS in-situ observation of atmospheric neutral species on the inbound leg of orbit 1064 with L_S = 256°, 11:50 a.m. local solar time and Ω_{lat} = -4.5° at orbit periapsis. (right) Averaged MVN-NGIMS profiles for L_S = 288-326°, Ω_{lat} = 46° to -4.3° and a solar zenith angle of 45°. Both observations do not show wave-like activity. While the left Panel observation simply does not contain waves, the right Panel is an average over many MVN-NGIMS observations and density waves are smoothed out. The Figures are taken from Mahaffy et al. *(2015a).*

It was already determined with the Mariner Spacecrafts and the Viking landers, that the dominant species in the lower atmosphere of Mars is CO_2 with a surface pressure of approximately 6.36 hPa at the mean radius and a variability of 4.0 - 8.7 hPa in dependence of the planetary season. The mixing ratios of major species are 95.3 % for CO_2, 2.7 % for N_2, 1.6 % for Ar, 0.13 % for O_2 and 0.08 % for CO, while available minor species are H_2O with 210 ‰ and NO with 100 ‰[8]. The composition of the Mars atmosphere changes significantly in the heterosphere. In Figure 2.9 the measured composition of the Martian neutral atmosphere is shown. The left panel contains one deep-dip observation of MVN-NGIMS, while the right Panel shows MVN-NGIMS neutral density profiles sampled and averaged over 202 MAVEN orbits (*Mahaffy et al.*, 2015a). The change of atmospheric parameters in dependence of the planetary longitude Ω_{lon} and latitude Ω_{lat} affects all continuous in-situ observations. This is especially true at the orbit pericenter, where the spacecraft is fast and the temporal change of Ω_{lon} and Ω_{lat} along the spacecraft track is large. Therefore the neutral density profiles in Panel (a) are not only a function of height, but also a function of the planetary position. Panel (b) shows MVN-NGIMS observations for a certain solar zenith angle, which are averaged over a long time-span. This smooths out wavelike structures and other short-term changes. It was found, as already deduced

[8]NASA: *https : //nssdc.gsfc.nasa.gov/planetary/factsheet/marsfact.html*

from the Viking lander observations, that O becomes the dominant species in the upper Mars atmosphere. At even higher altitudes, H_2 and H dominate the Mars corona. H_2 and H are not shown in Figure 2.9 due to the fact that they are not measured by MVN-NGIMS.

Internal or upward traveling atmospheric waves are a possible source for the lower ionospheric excess electron densities investigated in this work. Internal waves play a large role in the vertical coupling of the atmosphere/ionosphere system on Earth (see review of *Yiğit et al.* (2016); *Yiğit and Medvedev* (2015) and references therein). Primary source for internal waves are meteorological processes in the lower atmosphere (e.g. flow over topography, instabilities in weather systems or jets, atmospheric convection), who produce a wide spectrum from small scale (10 - 100 km) to planetary scale waves with temporal scales from few minutes to few days. Internal waves interact with the local atmosphere during upward propagation and therefore influence the mass, momentum and energy balance by acceleration/deceleration, heating/cooling and mixing. The activity of upward traveling waves increases with altitude due to the approximately exponential decrease of the atmospheric density. Gravity waves are the natural buoyancy waves of the atmosphere. When dissipation is neglected, the wave amplitudes increase with altitude due to the decreasing background density. Dissipation of gravity waves in the upper atmosphere causes transport of momentum from the lower atmosphere and connects the two atmospheric regimes. A summary of detected waves in the Martian atmosphere, their spatial and temporal characteristics and derived results is found in *England et al.* (2017). High upper atmospheric variability observed in the aerobraking data of the MGS, ODY and MRO spacecrafts were early indications for internal waves at Mars. Density disturbances with dominant horizontal scales of 100 - 300 km consistent with gravity waves have been identified in MGS accelerometer data (*Creasey et al.*, 2006). From MGS and ODY aerobraking data *Fritts et al.* (2006) determined significant spatial and temporal variability of gravity waves. Typical spatial scales are 20 - 200 km in the lower aerobraking altitudes (100 - 130 km). Density fluctuations vary from approximately 5 to 50 %. The amplitudes of gravity waves increase with altitudes, while their apparent horizontal scales remain constant. *Yiğit et al.* (2015) determined thermospheric CO_2 density perturbations from the observations of the MVN-NGIMS instrument and compared the results with a gravity wave model. The studied planetary region covers 60° - 75° latitude, 2 - 10 h local time and an altitude range from 180 - 220 km. Typical amplitudes of determined waves are 20 - 30 % of the atmospheric background density and wave signatures have been observed up to 250 km altitude. Comparisons between observations and the model for gravity wave propagation show a qualitative agreement. In addition, a high variability of the model gravity wave characteristics is found. At 100 km, density fluctuations larger than 150 % of the underlying atmosphere are predicted, while at 150 km the model predicts wave amplitudes of 50 - 100 % of the atmospheric density. *Terada et al.* (2017) used MVN-NGIMS Ar densities to determine the wave activity at the Mars exobase altitude. Small-scale perturbations were found with apparent wavelengths between 100 and 500 km and average

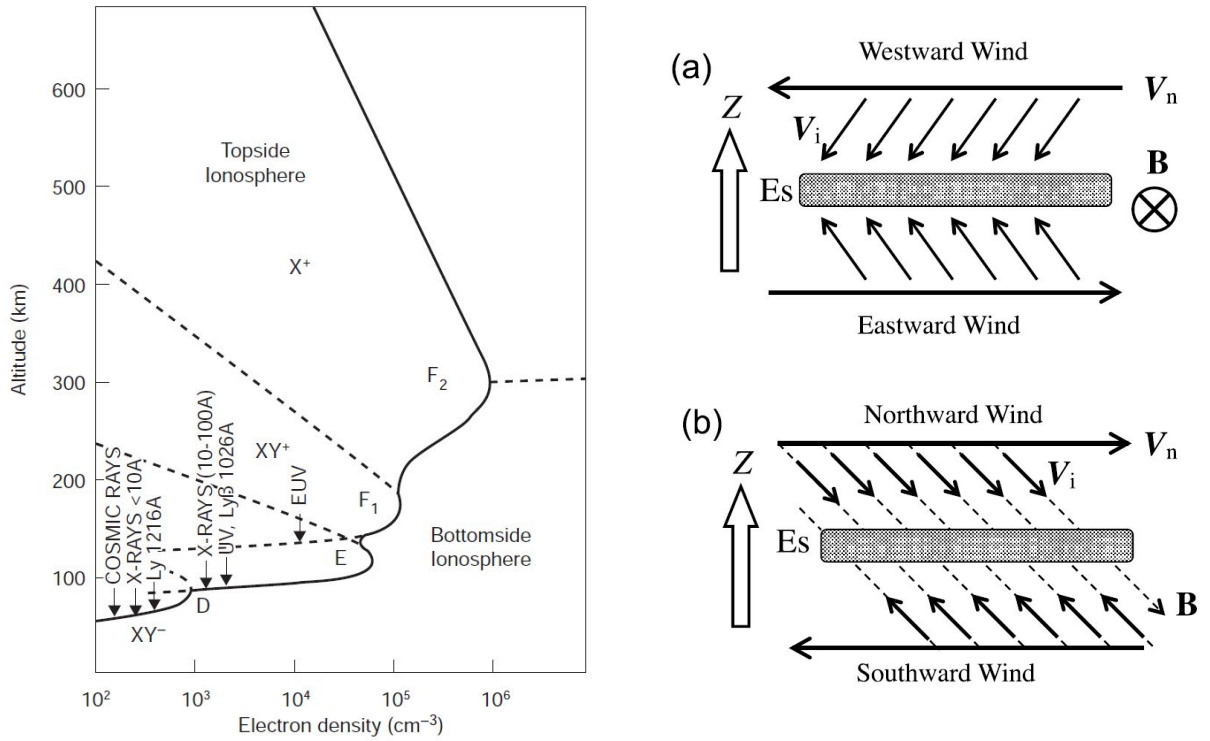

Figure 2.10: (left) Regions of the Earth dayside ionosphere and their sources. The Figure is taken from the reproduction in Bougher et al. *(2017), the original is from* Bauer and Lammer *(2004). (right) E_S formation in the Earth ionosphere by wind-shear induced ion convergence. (a) In zonal wind-shear with a neutral species velocity v_n, the ions are forced upwards/downwards to the node of the two wind regimes. (b) In meridional wind-shear the ions are dragged horizontally by the neutral wind and are forced to gyrate perpendicularly to the inclined magnetic field lines. The ions finally move along the magnetic field* **B** *with velocity v_i, causing an E_S layer at the node of the wind shear region. Figure from* Shinagawa et al. *(2017).*

amplitude of approximately 10 % on the planetary dayside and approximately 20 % on the night side. The authors suggest, that the small-scale wave amplitudes at the exobase are essentially set by the convective breaking and saturation of the waves in the upper Martian atmosphere.

2.4 The Mars plasma environment and the ionosphere

The left Panel of Figure 2.10 contains a sketch of the Earth's dayside ionosphere. The shown ionospheric features and their formation processes are briefly discussed here (see e.g. Chapter 2 of *Zolesi and Cander* (2013) and *Bougher et al.* (2017) for further information) as a starting point for the discussion of the current knowledge about the Mars

ionosphere. The focus is given to the formation of the sporadic E_S layers in the lower Earth ionosphere, because the wind-shear mechanism is a potential source for the excess electron densities on Mars. The regular regions of the Earth ionosphere are denoted D, E and F from the base to the topside ionosphere. The terrestrial ionosphere is topped by the plasmasphere, which consists mainly of H^+ ions. The ionospheric F region is found on the terrestrial dayside between approximately 140 and 600 km altitude. Its primary ion production source are solar photons in the EUV range between 10 and 100 nm. The F region is split up into two separate regions F1 and F2 during specific solar-terrestrial conditions. The F1 region is in photochemical equilibrium and found at approximately 140 - 210 km altitude. It consists mainly of NO^+ and O_2^+ with some additional N^+ and O^+. After sunset the F1 region vanishes, while the F2 region is persistent during the night. In the F2 region, transport processes become dominant. It consists mainly of O^+ with some additional H^+ and He^+. In the ionospheric E region between 90 to 140 km altitude molecular ions dominate (mostly NO^+, O_2^+ with additional O^+ and N_2^+). The major primary ion source on the dayside is the absorption of solar X-ray mainly in the 8 to 10.4 nm interval and between 80 - 102.6 nm (UV, Ly-β) range. During the night the ionization in the E region is reduced, but the region always stays weakly ionized.
Under certain conditions, a second E layer (E2) or a sporadic E_S layer is observed. The origin of the E2 layer is still under investigation. Actual results indicate that the major control mechanism is the variability of the solar UV. The sporadic E_S layers (see e.g. the review of *Haldoupis* (2012), *Gubenko et al.* (2017) and *Shinagawa et al.* (2017)) can have peak electron densities similar to those in the F region. Ionospheric radar soundings and rocket observations indicate that the sporadic E_S layers have a vertical thickness equal to or less than 1 km and occur in a similar altitude as does the ionospheric E layer. A statistical analysis of approximately 70 E_S observations over Japan provided a horizontally elongated structure ranging from 50 to 500 km with an average of 160 km (*Maeda and Heki*, 2015). The lifetimes of E_S layers range from few to several hours. Even if their formation is not yet fully understood, their origin is assumed to be independent of the general ionospheric mechanisms due to their widespread spatial (wide/small area), diurnal (sporadic day/night) and seasonal occurrence patterns for all latitudes. The most widely accepted theory for the origin of the sporadic E_S layers is the wind-shear theory (*Whitehead*, 1960; *Mathews*, 1998), whereby the wind-shear regions are assumed to be caused by several kinds of atmospheric waves. The right Panel of Figure 2.10 illustrates the zonal and meridional wind-shear mechanisms for the formation of E_S layers by ion convergence in a collision dominated altitude region. When charged particles are dragged along with neutral winds by neutral-ion collisions with a velocity v in a magnetic field $\mathbf{B}$, the ions experience a Lorentz-force in the direction of the cross product $\mathbf{v} \times \mathbf{B}$. When vertical shears in horizontal neutral winds cause ion drifts in opposite directions, charged particles can accumulate at the node of the two wind regimes. For an accumulation to occur, significant lifetimes of the ions against recombination are needed, which are provided by ions of meteoric origin like Fe^+ (*Kopp*, 1997). After formation, the layers drift

below 100 km altitude, where they are depleted of the meteoric ion content by three-body collisional recombination. The above described wind-shear formation processes for E_S, however, do neither efficiently work at the equator nor at the auroral zones near the magnetic pole due to the constellation of the strongly inclined magnetic field lines and the drift velocity of the ions. Therefore, the major E_S formation occurs at the mid-latitudes. E_S occurrences at higher latitudes are often attributed to the auroral electric field. E_S layers occur mostly during summer, which has been attributed to the change in metallic ion content of the terrestrial atmosphere (*Haldoupis et al.*, 2007) or the different vertical convergence patterns of metallic ions during the seasons (*Chu et al.*, 2014).
The D region of the terrestrial dayside ionosphere is found between 50 and 90 km altitude. NO^+ is the primary positive ion component in the D region, while the negative part consists of electrons and O_2^- in combination with other negative ions. Solar radiation at 121.6 nm (Ly-alpha) is actually assumed to be the most important source for the ionization of NO, while hard X-ray photons smaller than 0.8 nm ionize N_2, O_2 and Ar. Solar photons below 111.8 nm ionize unstable O_2 and galactic cosmic rays ionize all available atmospheric species. Solar electrons with energies larger than 10 keV, solar protons in the range of 1 to 100 MeV and solar cosmic rays can provide additional ionization to the terrestrial D region. The ionospheric C region between 50 and 70 km is generated by the atmospheric interaction with cosmic rays.

In contrast to Earth, Mars has no intrinsic global magnetic field. Therefore the interplanetary plasma interacts directly with the Mars atmosphere and ionosphere. Figure 2.11 illustrates the main features of the interaction of the supersonic solar wind plasma with the Martian plasma regions. The interaction of the solar wind with the planetary atmosphere and ionosphere slows down the supersonic plasma flow of the solar wind and creates a bow shock upstream of Mars. The bow shock is followed by the turbulent magnetosheath region, where the slowed-down plasma is flowing around Mars. Due to the missing intrinsic global magnetic field, the incoming solar wind interacts directly with the Martian ionosphere. This causes an induced magnetosphere, which is quite similar to that found at Venus. Its lower border is often called induced magnetosphere boundary (*Brain et al.*, 2017) or magnetic pile-up boundary (*Bertucci et al.*, 2003). Its shape is often approximated with a paraboloid with a revolution axis along the planet-Sun line. The magnetic field lines are frozen in the solar wind plasma flow and therefore are draped around the planet together with the plasma, forming a magnetotail. Multi-fluid magnetohydrodynamic simulations show, that the crustal magnetic field of Mars is strong enough to affect the ionospheric interaction with the solar wind (*Dong et al.*, 2014). This causes 'mini-magnetospheres' where the motion of the charged particles is guided by the crustal magnetic field lines.

The dayside ionosphere of Mars is mainly formed by photoionization by solar extreme ultraviolet (EUV) and X-ray radiation and, as a secondary effect, by photoelectron impact ionization. Figure 2.12 shows a selection of four electron density profiles of the Mars ionosphere observed by the Mars Express Radio Science Experiment MaRS (*Pätzold et al.*,

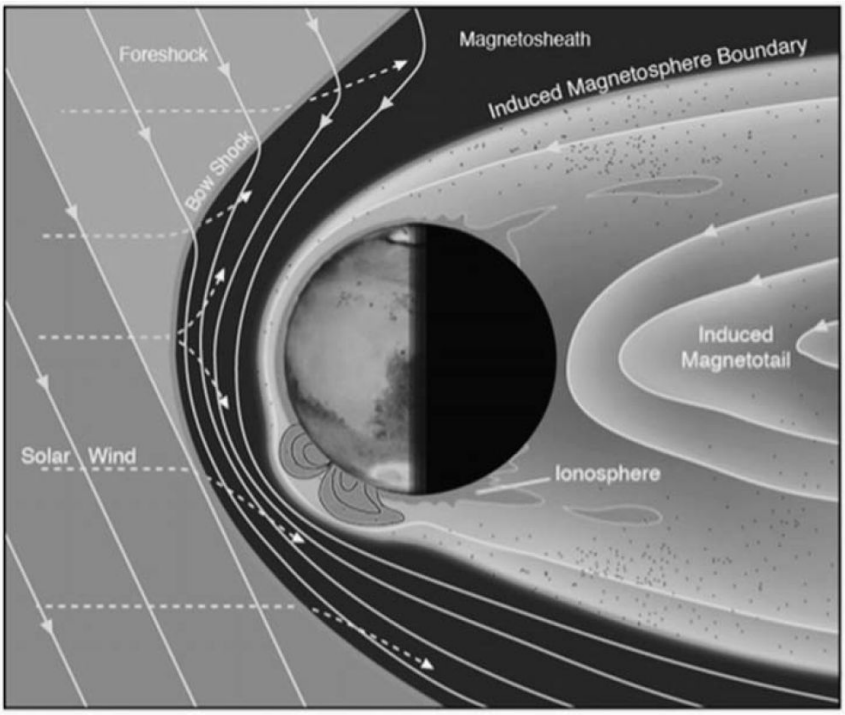

*Figure 2.11: Interaction of the solar wind with the plasma regions of Mars (*Brain et al.*, 2017).*

2004, 2009). The photochemical region of the ionosphere is dominated by two main layers: M2 at about 130 km and a second lower layer M1 at about 115 km. The dominant main layer M2 is mostly formed by solar EUV radiation. The M1 layer is formed in part by (a) solar X-rays and (b) by impact ionization of photoelectrons (*Fox et al.* (1996)). *Rishbeth and Mendillo* (2004) started to call the layers of the Mars ionosphere M1 and M2 for the lower and main layer, respectively. Some authors name the lower and upper Martian layers E and F1 similar to the ionospheric layers at Earth to indicate a comparable formation process (*Bauer and Hantsch* (1989); *Bougher et al.* (2001); *Fox and Yeager* (2006); *Haider et al.* (2009); *Mahajan et al.* (2009)). In this work, the system from *Rishbeth and Mendillo* (2004) is adopted. The M2 peak density and altitude are known to be highly variable, depending on solar zenith angle χ and driven by change in the solar flux. Day-to-day changes in the peak densities result from periodic changes of the solar EUV, which are particularly prominent during solar maximum (*Withers and Mendillo* (2005)). Eruptions of solar flares can cause an enhancement in the density of the M1 layer of up to 200 percent (*Mendillo et al.* (2006); *Haider et al.* (2009)). Moreover, additional variations, driven by atmospheric phenomena, have been inferred from the MGS database. These include:

- Upward propagating planetary scale waves originating from the lower atmosphere

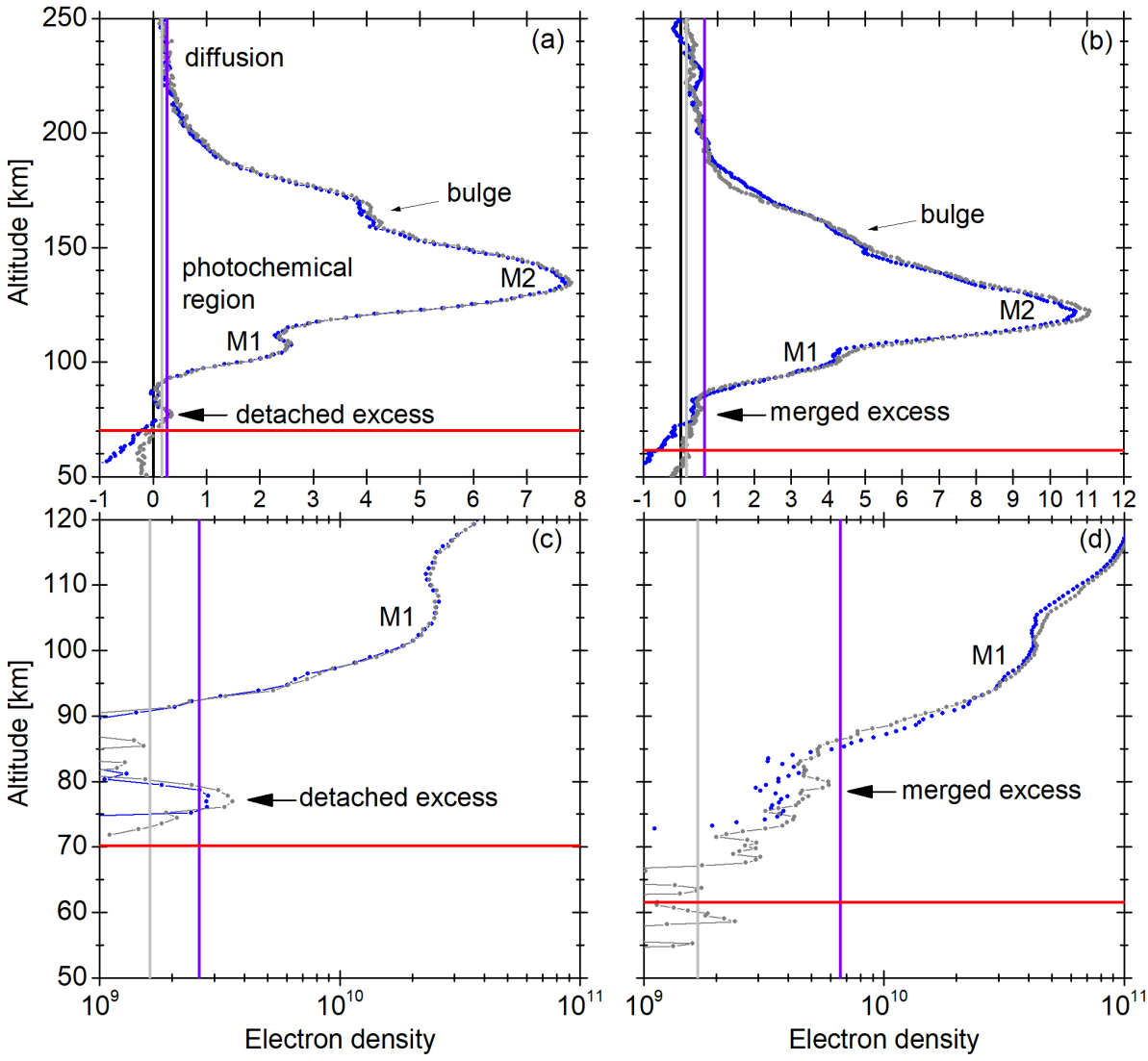

*Figure 2.12: Blue and gray dots show the electron density derived from X-band and diff. Doppler. Black, violet and light gray lines indicate the zero line, $3{\cdot}\sigma_{noise,UB}$ (X-band) and $3{\cdot}\sigma_{noise,UB}$ (diff. Doppler) , the red line is the lowest valid altitude $h_{L,val}$ - see Chapter 4 for details. Figure (a) and (b) contain linear electron density plots in $[10^{10}\,m^{-3}]$, Figure (c) and (d) logarithmic plots in $[m^{-3}]$. **(a)** MaRS: DoY 350 (2005), $L_S = 341.47°$, $\Omega_{lon} = 5.35°$, $\Omega_{lat} = 65.45°$, $\chi = 74.07°$. **(b)** MaRS: DoY 111 (2006), $L_S = 42.32°$, $\Omega_{lon} = 158.17°$, $\Omega_{lat} = 7.38°$, $\chi = 58.80°$. **(c)** contains an enlarged view (a), while **(d)** contains an enlarged view of (b). The explanation for the present negative electron densities is found in Chapter 3.*

drive oscillations in pressure, temperature and density of the neutral atmosphere at altitudes up to 150 km, thereby inducing variations of the M2 peak altitude (*Bougher et al.* (2004); *Keating et al.* (1998); *Withers et al.* (2003)).

- Transport of dust particles to high altitudes by dust storms heats the neutral gas, which expands and raises the base of the ionosphere (*Keating et al.* (1998); *Wang and Nielsen* (2003); *Liemohn et al.* (2012); *Witasse et al.* (2003)).

Nevertheless, the formation of quiet ionospheric layers at Mars during periods without major perturbations seems to be clearly under solar control. A summary of the observed variability of the dayside ionosphere is given in *Withers* (2009); *Withers et al.* (2012a,b) and *Peter et al.* (2014).
Some of the electron density profiles show an anomalous accumulation of electrons - referred to here as the "bulge" - in the region above the main peak (Panel (a) and (b) of Figure 2.12). The genesis of the "bulge" is yet unknown. One possibility in discussion is a change of electron temperature at about 150 - 170 km altitude (*Fox and Yeager*, 2006).
The often sharp outer boundary of the ionosphere, the ionopause, was first detected in the Venus ionosphere by the Pioneer Venus Orbiter spacecraft (see summarized results in *Brace and Kliore* (1991)). Many definitions are in use for this phenomenon, due to the large variety of instruments on board of the spacecraft. One definition of the ionopause is the altitude at which a pressure balance exists between the dynamical solar wind and the ionospheric plasma (*Schunk and Nagy*, 2009). A Martian ionopause is also observed under certain atmospheric and solar wind conditions (*Peter et al.* (2008); *Duru et al.* (2009)). At Mars and Venus, the ionopause is identified in electron density profiles as a strong negative electron density gradient that continues to the noise level within an increase in altitude of only a few tens of kilometers.
Whereas CO_2 is the primary photo-ionized species in the Mars atmosphere, rapid reactions with atomic oxygen create O_2^+, which is the dominant ion at the middle ionosphere. The Viking Retarding Potential Analyzers established, that the O^+ concentration becomes comparable to O_2^+ at altitudes above about 250 km. The ionospheric main peak consists mainly of O_2^+ with smaller amounts of CO_2^+ (*Hanson et al.*, 1977). Those observations have been in general confirmed after the arrival of MAVEN at the end of 2014. Panel (a) of Figure 2.13 shows altitude profiles of averaged ion densities observed by MVN-NGIMS. While O_2^+ is the dominant and CO_2^+ the second most common ion at approximately 150 km altitude, O^+ densities become comparable to O_2^+ densities above 300 km altitude. NO^+ shows a positive density trend towards lower altitudes. The converging scale heights of the ions above 270 km altitude are attributed to the large plasma temperature gradient in these altitudes. The Panels (b) to (e) show the spatial distribution of the ionospheric ion densities in dependence of solar zenith angle and altitude. For O_2^+ and NO^+, the densities on the planetary night-side are fairly large (not smaller than two orders of magnitudes than on the day-side) compared to the densities of CO_2^+ and O^+. For O^+, the night-side ionosphere is mostly depleted of ions above 200 km. For CO_2^+, the

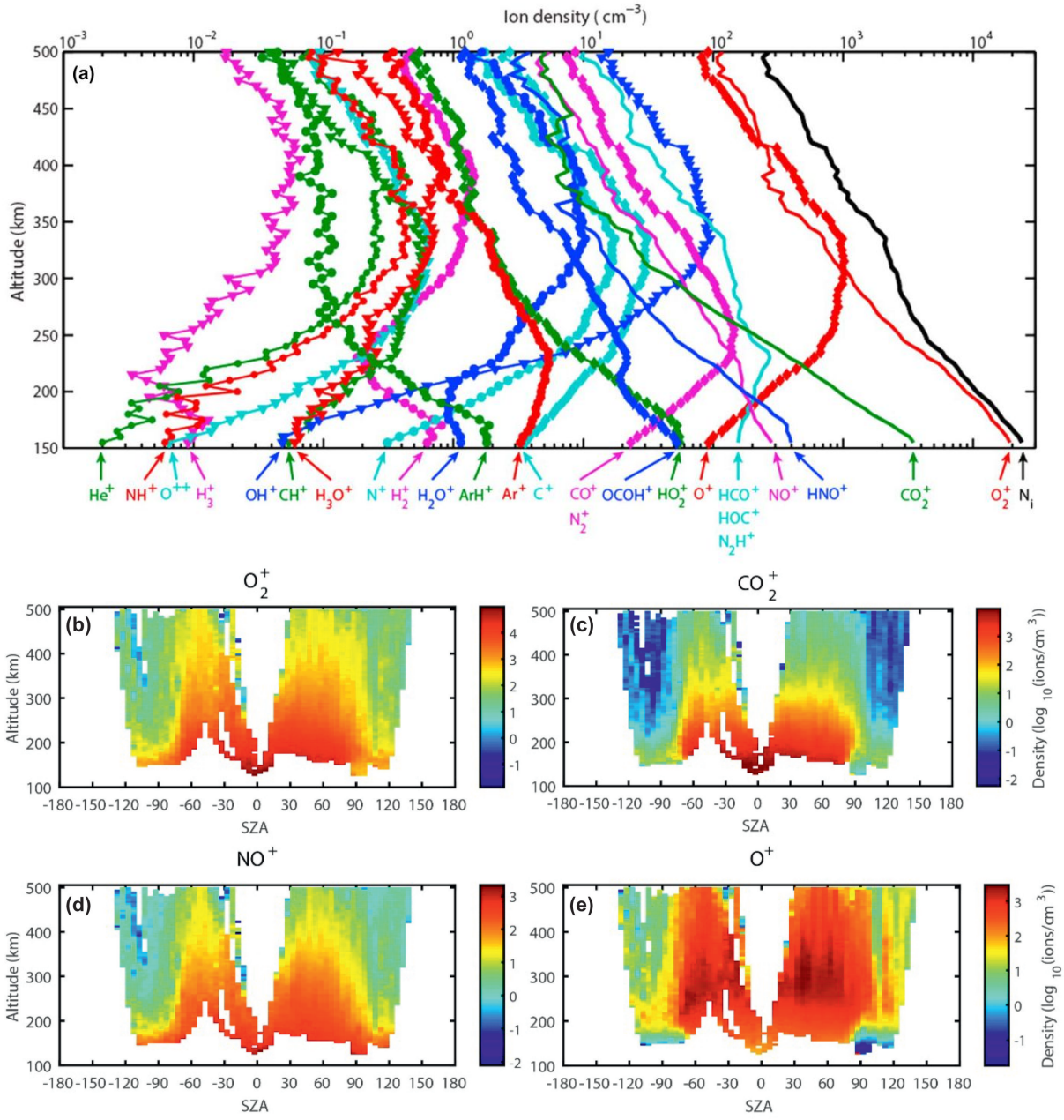

Figure 2.13: (a) Averaged altitude profiles (18. October 2014 to 18. May 2015) of the ionospheric densities observed by MVN-NGIMS for χ= 60°. The observation range covers an L_S of 216° to 348° and a F10.7 solar flux variance at Earth of 110 to 220. During that time span the MAVEN orbit precessed by approximately 95° in planetary latitude and approximately 25h in local time, so the data contain nearly 2/3 of the Mars northern hemisphere. The averaged profiles consist of 367 MVN-NGIMS orbits, averaged in 5 · 5km bins (from Benna et al. *(2015a)). The panels (b) - (e) show the spatial distribution of the O_2^+, CO_2^+, NO^+ and O^+ ions in the Mars ionosphere (from* Benna et al. *(2015a) - Supporting Information). The negative solar zenith angles indicate the dawn, the positive solar zenith angles the dusk hemisphere.*

ion densities on the night side are many orders of magnitude lower than on the day-side. All species show an obvious dawn/dusk asymmetry. A possible bias is introduced into the data due to the fact that all dawn observations were conducted at planetary latitudes of +30 ° and higher, while all dusk observation were conducted near the equator / on the southern hemisphere (*Benna et al.*, 2015a).
Sporadic formations of layers below M1 have been observed in the dayside ionosphere of Mars by *Pätzold et al.* (2005). Those first results presumed the transient layers the result of infalling meteoroids. The surface of these objects ablates during their flight through the atmosphere, depositing metal atoms below about 80 km, that eventually become ionized by photoionization, charge exchange with the background ionosphere, and/or meteoric impact ionization (e.g. *Pesnell and Grebowsky* (2000); *Molina-Cuberos et al.* (2003, 2008); *Withers et al.* (2008); *Whalley and Plane* (2010); *Pandya and Haider* (2014)). This work investigates the occurrence of the sporadic layers in greater detail. The observed layers are discriminated into merged transient layers, where the excess electron density is merged with the main ionosphere (example in Panel (b) and (d) of Figure 2.12) and detached layers, where the observed electron density is separated from the main ionosphere (example in Panel (a) and (c) of Figure 2.12).

Since the in-situ observations of the Viking Landers provided a first impression of the Martian upper atmosphere and ionosphere, models have been used to gain further insight into the local and global atmospheric composition and thermal structure. Input conditions for the classic 1-D convergence models of the Mars ionosphere are set by using single vertical profiles of the neutral atmospheric composition and selected environmental parameters. The ionospheric behavior for the selected environmental conditions is then determined by running the model until convergence is reached. While 1-D models which cover the full Martian atmosphere/ionosphere from the surface to the exobase are rare (e.g. *Nair et al.* (1994)), the typical 1-D models for the investigation of the Martian ionosphere have lower boundaries at 80 km altitude. Some of those models assume photochemical equilibrium without transport processes (e.g. *Martinis et al.* (2003); *Peter et al.* (2014)), where the electron density is computed independently for each altitude. Other 1-D models additionally consider the coupling the the neutral atmosphere and ionsphere by including vertical transport (e.g. *Krasnopolsky* (2002); *Fox* (2004); *Fox and Yeager* (2006); *Mendillo et al.* (2011); *Matta et al.* (2013); *Fox* (2015)). 1-D models applied to the determination of the influence of meteoric material on the Martian ionosphere are usually equipped with a lower altitude boundary (e.g. *Molina-Cuberos et al.* (2003); *Whalley and Plane* (2010)). The next class of 1-D models (e.g. (*Matta et al.*, 2014; *Crismani et al.*, 2017)) uses the diurnal output of another sophisticated model (e.g. the neutral atmosphere of a GCM) to determine the behavior of the Mars ionosphere for one Sol (one Mars day) in greater detail by including physical and chemical processes not implemented in the original model. More complex transport phenomena are considered in multidimensional models which cover the Martian atmosphere and ionosphere from the surface to the exosphere. The consideration of internal drivers as e.g. the interaction between the

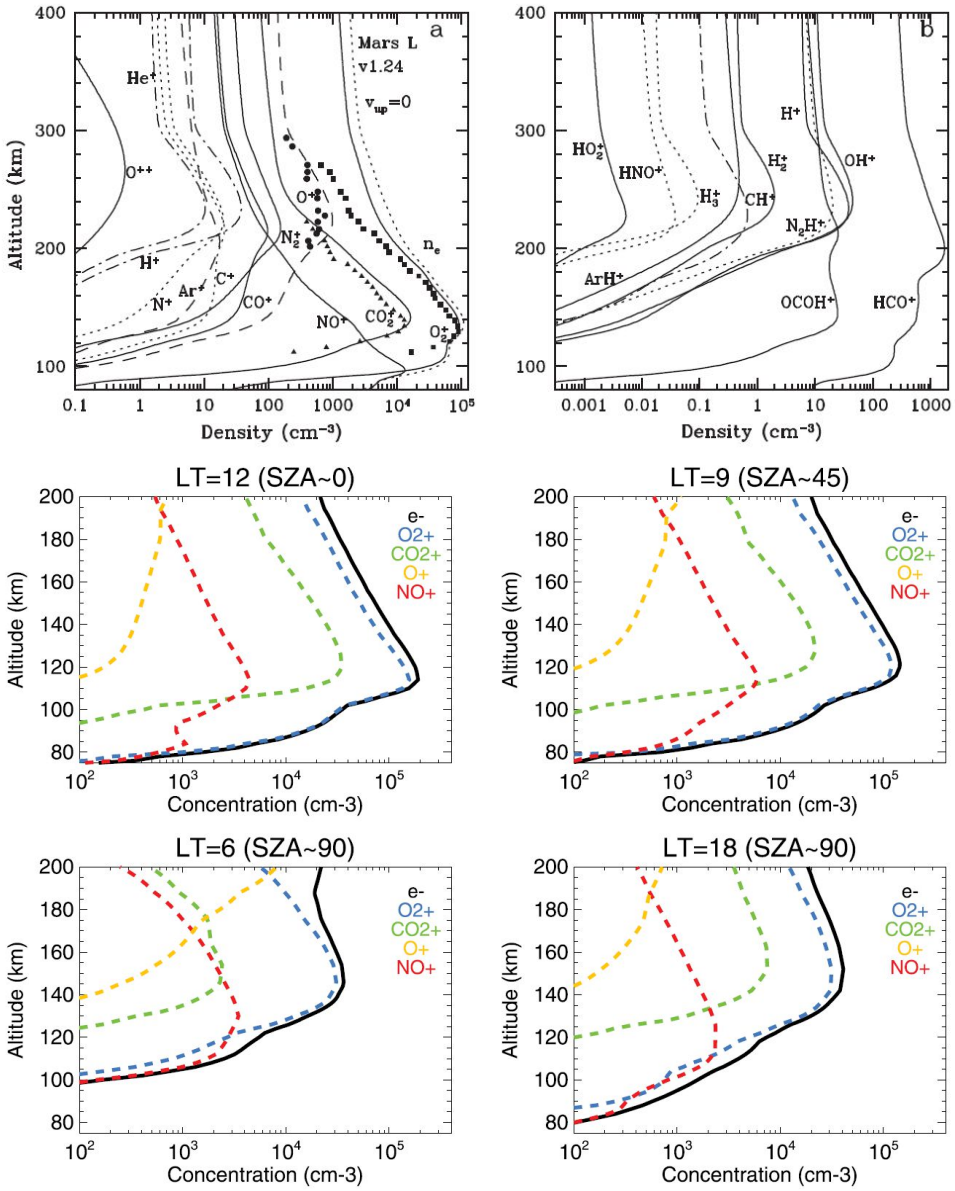

Figure 2.14: Both upper Panels contain the model ionosphere calculated by Fox *(2015) for* $\chi = 60\,^\circ$ *with a zero ion flux upper boundary condition. The* O_2^+, O^+ *and* CO_2^+ *of the Viking Lander 1 observations (*Hanson et al., *1977) are illustrated with filled squares, circles and triangles respectively. The four lower Panels show the results of the LMD-GCM for* $\Omega_{lon}= 0\,^\circ$, $\Omega_{lat}= 0\,^\circ$ *for local times of 12, 9, 6 and 18 hours. This correspondents to approximate solar zenith angles of* $0\,^\circ$, $45\,^\circ$, $90\,^\circ$ *and* $180\,^\circ$. *The Figure is taken from* González-Galindo et al. *(2013). Figure A.1 in the Appendix shows the associated LMD-GCM neutral atmosphere, provided by G. González-Galindo.*

lower and upper atmosphere/ionosphere by gravity waves and tides provide an estimate of the local and global transport processes. Two examples for those coupled 3-D models are the Mars Global Ionosphere-Thermosphere Model M-GITM (*Bougher et al.*, 2015b) and the general circulation model for the Martian ionosphere developed at the Laboratoire de Météorologie Dynamique LMD-GCM (*Forget et al.*, 1999; *Angelats i Coll et al.*, 2005; *González-Galindo et al.*, 2005, 2009, 2013; *Chaufray et al.*, 2015). The results of the LMD-GCM for certain conditions are freely available in form of the Mars Climate Database (MCD)[9]. Figure 2.14 shows model results for the Martian ionosphere from the 1-D model of *Fox* (2015) and the 3-D LMD-GCM (*González-Galindo et al.*, 2013). The highly sophisticated 1-D model of *Fox* (2015) shows a dominance of NO^+ over O_2^+ below a certain altitude. In the 3-D model results of *González-Galindo et al.* (2013) the available amount of NO^+ in the lower ionosphere varies with local time. These results imply, that the local ionospheric ions important in the merged excess electron density structures might be either O_2^+ or NO^+.
The 1-D time-marching IonA-2 model developed for this work and described in Chapter 6 covers an altitude range from 65 to 300 km altitude. This is necessary, because the boundaries of the identified excess electron densities in the MaRS observations are regularly found below 80 km altitude. The photochemical reaction scheme in combination with minor molecular diffusion of the minor neutral species and ambipolar diffusion of the ions in combination with the atmospheric day-night cycle allows a thorough analysis of short solar X-ray as a potential source for the merged excess electron densities.

[9] $http://www-mars.lmd.jussieu.fr/$

Chapter 3

The radio science method and the MaRS experiment

This Chapter contains a general description of the radio science method, the characteristics of the MaRS radio science experiment and an analysis of the potential sources for uncertainties in the derived electron density profiles.

3.1 The radio occultation method

When the light of a star is blocked by a celestial body so that it cannot reach a potential observer, a stellar occultation occurred. If the planet has an extended atmosphere, the emitted light of the star is affected by the gaseous region shortly before the occultation. The idea of using this effect for the investigation of planetary atmospheres was first published by *Pannekoek* (1903). The theory for the one-way radio science method was then developed by *Fjeldbo and Eshleman* (1965). In the one-way radio science method, a continuous signal is transmitted by a spacecraft in orbit around a planet and received by a ground station on Earth. When an occultation of the spacecraft occurs as seen from the Earth, the radio signal passes through the planetary ionosphere/neutral atmosphere. The interaction between the signal and the planetary atmosphere provides information about the state of the planetary atmosphere. In the Mariner 4 flyby at Mars a two-way radio occultation method was applied (*Kliore et al.*, 1965). A stable signal is transmitted from the ground station, received and re-emitted by the spacecraft and finally received by the ground station on Earth.
During the one-way downlink occultation ingress illustrated in Panel (a) of Figure 3.1, the spacecraft (SC) is transmitting a continuous radio signal while moving behind the planet as seen from the receiving ground station (GS) on Earth. The planetary atmosphere refracts the SC radio emission, which leads to a change in the signal path and therefore adds a Doppler shift to the signal frequency received at the ground station. While the

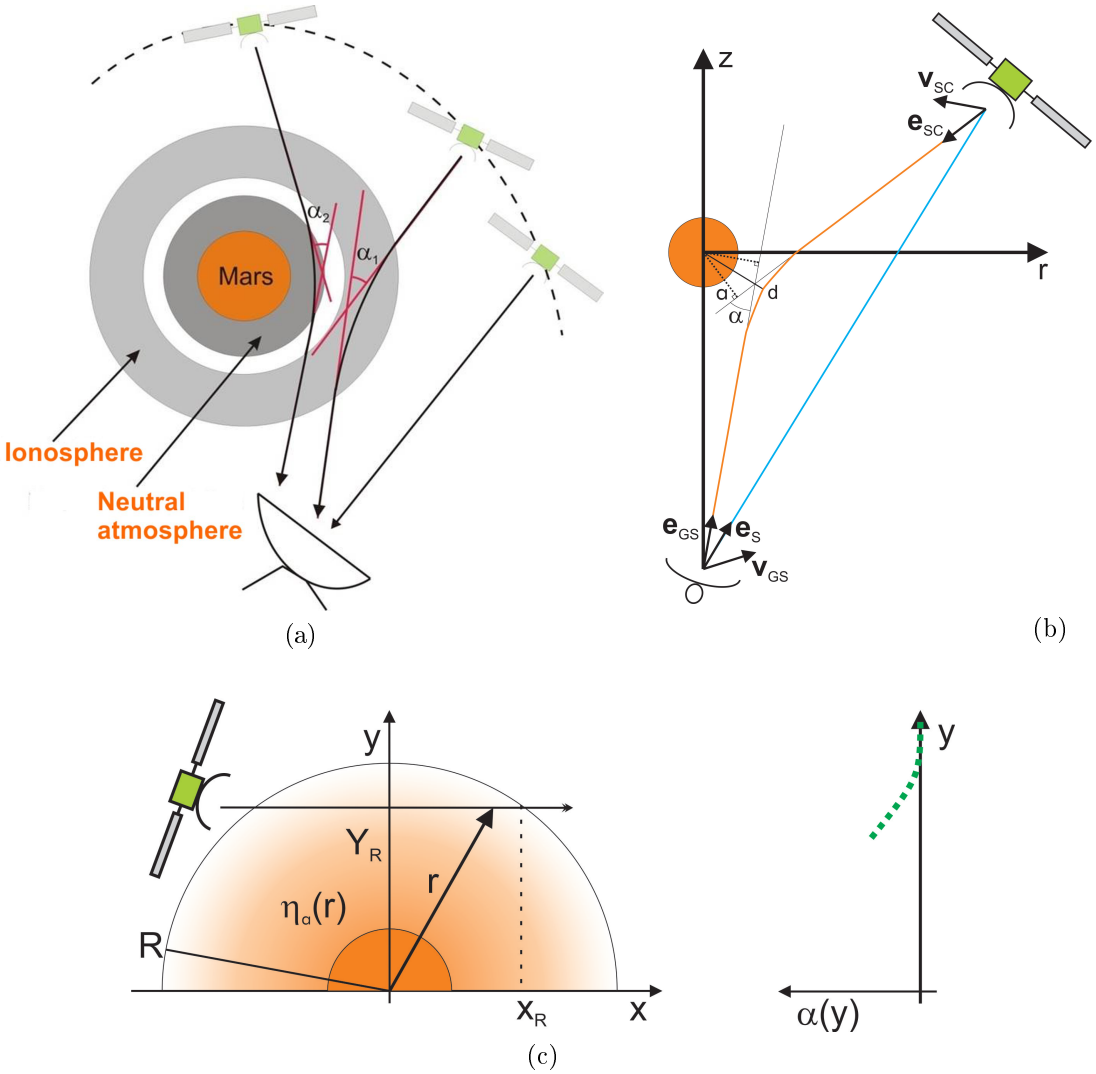

Figure 3.1: Geometric parameters of an one-way downlink occultation ingress. (a) α_1 and α_2 indicate the different bending angle signs in the ionosphere and neutral atmosphere. The Figure is taken from Peter *(2008). (b) The coordinate system for an one-way downlink radio occultation is spanned by the actual SC position at signal emission time, the position of the planet when it is sounded by the radio signal and the position of the ground station at ground-receive-time.* $\mathbf{v}_{SC}$ *and* $\mathbf{v}_{GS}$ *are the velocity vectors of the spacecraft and ground station respectively,* $\mathbf{e}_S$ *is the unit vector along the line-of-sight (blue), while* $\mathbf{e}_{SC}$ *and* $\mathbf{e}_{GS}$ *are the unit vectors along the asymptotes (black) of the refracted radio beam (orange). a is the ray parameter, while d is the radius of the ray periapsis. This illustration is based on Figures of* Schaa *(2005), originally provided by* Fjeldbo et al. *(1971). (c) Simplified relationship between the radially symmetric atmospheric refractive index* $\eta_a(r)$ *and the bending angle* $\alpha(y)$ *in a radio occultation observation. The radio ray is drawn as straight line to illustrate the geometrical approach to the Abel transform. The given parameters are described in the text.*

signal emission of the spacecraft is continuous, the signal is recorded with a distinct time resolution at the ground station.
The received Doppler shift can be converted into ionospheric electron densities for the upper atmosphere and neutral densities and temperatures for the lower atmosphere by a procedure developed by *Fjeldbo et al.* (1971). In the first step, the observed Doppler shift is converted into ray bending angles by a geometrical approach. In a second step, the bending angles are converted into atmospheric refractivity. The derived atmospheric refractivity depends on the local state of the planetary atmosphere (neutral pressure, density, temperature and ionospheric electron density) and can therefore be converted into atmospheric parameters. In the subsequent Sections, the basics of the radio science method of *Fjeldbo et al.* (1971) are summarized. For a detailed description see *Schaa* (2005).

3.1.1 From the received Doppler shift $\Delta f_{GS}(t)$ at the ground station to the bending angle $\alpha(a)$

Figure 3.1 illustrates the basic geometric principles of a radio occultation. For clarity, only the situation of an one-way downlink radio occultation is discussed. A 2-D coordinate system is created for each occultation time step, spanned by the SC position at signal emission time, the position of the planet when the signal traverses the atmosphere and the position of the ground station at the ground-receive-time. Without a disturbing planetary atmosphere, the signal path would be equal to the line-of-sight (LOS) between spacecraft and ground station (blue line in Fig. 3.1 (b)). The planetary atmosphere refracts the radio signal and the refractive index of the planetary atmosphere η_a along the curved signal path s_{sig} causes an extension of the phase path ΔL of the signal

$$\Delta L = \int_{SC}^{GS} \eta_a \left(s_{sig}\right) ds_{sig} - S_0 = \Delta\varphi\lambda \tag{3.1}$$

where $\Delta\varphi$ is the phase shift at signal wavelength λ and S_0 is the vacuum phase path along the line-of-sight. The time-derivative of $\Delta\varphi$ is equal to the frequency shift caused by the planetary atmosphere Δf_{atm}

$$\Delta f_{atm} = \frac{d}{dt}\Delta\varphi = \frac{f_{SC}}{c}\frac{d}{dt}\Delta L \tag{3.2}$$

with $c = f_{SC}\lambda$, where f_{SC} is the SC downlink frequency and c is the speed of light in vacuum.
A geometrical approach is used to link the observed Doppler shift at the ground station Δf_{GS} with the refractive structure of the planetary atmosphere. When other effects are neglected Δf_{GS} consists of two contributions: the kinetic component Δf_{kin} from the

relative movement of spacecraft and ground station and the atmospheric component Δf_{atm}

$$\Delta f_{GS} = \Delta f_{kin} + \Delta f_{atm} = \frac{f_{SC}}{c} \left(\mathbf{v}_{SC} \cdot \mathbf{e}_{SC} + \mathbf{v}_{GS} \cdot \mathbf{e}_{GS} \right). \tag{3.3}$$

$\mathbf{v}_{SC}$ and $\mathbf{v}_{GS}$ are the velocities of spacecraft and ground station, while $\mathbf{e}_{SC}$ and $\mathbf{e}_{GS}$ are the unit vectors along the asymptotes of the refracted radio signal. The equation for the kinetic Doppler component along the line-of-sight Δf_{kin} can be written as

$$\Delta f_{kin} = \frac{f_{SC}}{c} \left(\mathbf{v}_{SC} \cdot \mathbf{e}_{S} - \mathbf{v}_{GS} \cdot \mathbf{e}_{S} \right) \tag{3.4}$$

with $\mathbf{e}_S$ as the unit vector along the line-of-sight. Combining Equation 3.3 and 3.4 results in the equation for the Doppler shift caused by the planetary atmosphere Δf_{atm}

$$\begin{aligned} \Delta f_{atm} &= \Delta f_{GS} - \Delta f_{kin} \\ &= \frac{f_{SC}}{c} \left[(\mathbf{v}_{SC} \cdot \mathbf{e}_{SC} + \mathbf{v}_{GS} \cdot \mathbf{e}_{GS}) - (\mathbf{v}_{SC} \cdot \mathbf{e}_{S} - \mathbf{v}_{GS} \cdot \mathbf{e}_{S}) \right]. \end{aligned} \tag{3.5}$$

Δf_{GS} of Equation 3.5 can be derived from the ground station observation as a function of time. Subtracting a prediction of the line-of-sight kinetic Doppler shift $\Delta f_{kin}(t)$ from $\Delta f_{GS}(t)$ yields the time dependent atmospheric Doppler shift $\Delta f_{atm}(t)$.
$\Delta f_{atm}(t)$ is converted into a ray bending angle profile $\alpha(a(t))$ in dependence of the ray parameter $a(t)$ by an iterative procedure. The bending angle $\alpha(a(t))$ is the integrated direction change of the SC signal along its path through the atmosphere. The ray parameter $a(t)$ is given by the line connecting the planetary center and the ray asymptote in that way that it is perpendicular to the ray asymptote (see Figure 3.1). Each $\alpha(a(t))$ belongs to one Doppler shift sample $\Delta f_{atm}(t)$ and uniquely describes the associated refracted ray path. For this condition to be valid, a spherically symmetric atmosphere needs to be assumed. The procedure for deriving $\alpha(a)$ from $\Delta f_{atm}(t)$ starts at the top of the atmosphere where the bending angle α is still zero and is iterated downwards until the lowest data sample is reached. A detailed description of the iterative procedure implementation is found in *Schaa* (2005).

3.1.2 From the bending angle $\alpha(a)$ to the atmospheric refractive index $\eta_a(d)$

The problem of deriving N+1 dimensional distributions from observed N dimensional projections is a common physics problem. An example is computer tomography, where 2-D X-ray images from different angles of an object are combined to a 3-D image of the object. *Fjeldbo et al.* (1971) found, that the ray bending angle α is the Abel transform of the radially symmetric refractive index η_a of the atmosphere along the ray path s_{sig}. Today, the Abel-transform and -inversion are commonly used methods for solving the projection

problem for radially symmetrical objects (*Bracewell*, 2000). A detailed derivation of the equations is found in (*Schaa*, 2005), a geometrical approach to the Abel transform is given below.
The relationship

$$\alpha(y) = 2\int_0^{x_R} \eta_a\left(r\left(x\right)\right) dx. \tag{3.6}$$

between the assumed radially symmetric atmospheric refractive index distribution $\eta_a(r(x))$ and the bending angle profile $\alpha(y)$ is illustrated in Panel (c) of Figure 3.1 under the assumption that the radio ray is traversing the planetary atmosphere as a straight line. With the conversion into polar coordinates

$$x^2 + y^2 = r^2 \Rightarrow dx = \frac{rdr}{\sqrt{r^2 - y^2}} \tag{3.7}$$

Equation 3.6 yields for a straight radio ray

$$\alpha\left(y\right) = 2\int_{Y_R}^{R} \frac{\eta_a\left(r\right) r}{\sqrt{r^2 - y^2}} dr. \tag{3.8}$$

This kind of equation is called an Abel integral equation, named after the Norwegian mathematician Niels Henrik Abel (1802 - 1829) (*Simmons*, 2007). An integral equation contains the unknown function (here the atmospheric refractive index distribution $\eta_a(r)$) as integrand in a definite integral.
Fjeldbo et al. (1971) provides Equation 3.8 for the case when the radio signal is refracted in an atmosphere consisting of centric spherical shells with a constant atmospheric refractive index

$$\alpha\left(a\right) = 2a\int_{a'=a}^{a'=\infty} \frac{d\eta_a}{\eta_a da'} \cdot \frac{da'}{\sqrt{(a')^2 - a^2}} \tag{3.9}$$

with $a' = \eta_a r$.
The iterative inverse form of the Abel transform

$$\eta_a(d_i) = \exp\left[-\frac{1}{\pi}\int_{a_i}^{\infty} \frac{\alpha\left(a\right) da}{\sqrt{a^2 - a_i^2}}\right]. \tag{3.10}$$

yields then the refractive index $\eta_{a,i}(d_i)$ of an atmospheric shell i as a function of the radius of the ray periapsis $d_i = \alpha_i/\eta_{a,i}$. d_i is the smallest distance between the refracted ray and the center of the planet for layer i (see Panel (b) of Figure 3.1).

3.1.3 From the atmospheric refractive index $\eta_a(d_i)$ to atmospheric densities

The atmospheric refractivity N_a

$$N_a = (\eta_a - 1) \cdot 10^6 \tag{3.11}$$

is introduced to simplify the handling of the extremely small atmospheric refractive index η_a. The atmospheric refractivity N_a is the sum of the refractivity of the neutral atmosphere N_N and the refractivity of the ionospheric electron density N_e (see *Pätzold et al.* (2009, 2016a))

$$N_a = N_N + N_e$$
$$N_a(d_i) = \xi_1 k_B n_N(d_i) - \xi_2 \frac{n_e(d_i)}{f_{SC}^2}. \tag{3.12}$$

The first term on the right side of Equation 3.12 describes the non-dispersive approximation of the relation between the neutral number density n_N and the refractivity of the neutral atmosphere N_N. ξ_1 depends on the atmospheric composition. For Mars, ξ_1 is a constant ($1.307 \cdot 10^{-6}\, m\, K\, s^2\, kg^{-1}$) up to approximately 100 km altitude (*Pätzold et al.*, 2016a; *Essen and Froome*, 1951). k_B is the Boltzmann constant and $n_N(d_i)$ is the neutral number density at altitude d_i. The second term describes the dispersive relation between the ionospheric electron density $n_e(d_i)$ at altitude d_i and the ionospheric refractivity N_e. The constant ξ_2 is defined in Equation 3.19. The electron density n_e and density of the neutral atmosphere n_N are derived from Equation 3.12 by assuming, that only either the ionospheric term or the neutral atmospheric term is dominant.
The first part of Equation 3.12 is derived for the neutral atmosphere by assuming that the molecules of the neutral atmosphere of Mars behave like small dipoles in a dielectric medium. The electromagnetic wave traverses through the neutral gas and excites oscillations of the atoms/molecules in the medium. These oscillations produce secondary waves. The superposition of the original wave and the secondary waves leads to the effect of refraction. The refractivity for the neutral atmosphere of Mars N_N is approximated by

$$N_N \simeq \frac{q_i^2}{2\epsilon_0 m_i} \frac{1}{\omega_0^2 - \omega^2} \cdot 10^6 \cdot n_N = \xi_1 k_B n_N \tag{3.13}$$

(*Schaa*, 2005; *Feynman et al.*, 2010, volume 2, chapters 31/32). q_i is the ion charge of the atmospheric particles and m_i the ion mass. ϵ_0 is the vacuum permittivity, ω_0 is the natural angular frequency of the gas (the frequency at which the system oscillates, when there is no external force present) and ω is the exciting angular frequency.
The interaction of an electromagnetic wave with the planetary ionosphere resembles the interaction with a conductor, due to the available 'free' electrons. As described in volume 2, chapter 32 of *Feynman et al.* (2010), the refractive index η_a is described as the difference between the phase velocity v_{ph} of a wave in the medium and the speed of light c

$$\eta_a = \frac{c}{v_{ph}} = \frac{kc}{\omega}, \tag{3.14}$$

where k is the wave number and ω is the angular frequency.
With no restoring force on the free electrons, but some resistance to motion, the equation

for the complex refractive index η_a of an ionospheric conductor is

$$\eta_a^2 = 1 + \frac{n_e q_e^2}{m_e \epsilon_0} \cdot \frac{1}{-\omega^2 + i\beta\omega} = 1 + \frac{n_e q_e^2}{m_e \epsilon_0} \cdot \frac{\tau_{col}}{i\omega\,(1 + i\omega\tau_{col})} \tag{3.15}$$

with the electron charge q_e, the electron mass m_e, the imaginary unit i and a phenomenological damping constant β with $\beta = 1/\tau_{col}$. τ_{col} is the average time between collisions of a free electron. For small wavelengths with $\omega >> 1/\tau_{col}$, Equation 3.15 reduces to

$$\eta_a^2 = 1 - \frac{n_e q_e^2}{m_e \epsilon_0} \frac{1}{\omega^2}. \tag{3.16}$$

The plasma frequency ω_p of the ionosphere is a critical parameter. For frequencies $\omega < \omega_p$ a imaginary part of the refractive index η_a is available and the waves are attenuated. For frequencies $\omega >> \omega_p$, η_a is real and the medium becomes transparent for the waves. The plasma frequency of the ionosphere is defined as

$$\omega_p^2 = \frac{n_e q_e^2}{m_e \epsilon_0} \simeq 80.616 \cdot n_e. \tag{3.17}$$

Inserting Equation 3.17 into Equation 3.16 yields the frequency dependent relation between η_a and the ionospheric electron density n_e

$$\eta_a^2 = 1 - \left(\frac{\omega_p}{\omega}\right)^2 \Rightarrow \eta_a \simeq 1 - \frac{1}{2}\frac{80.616 \cdot n_e}{f_{SC}^2} = 1 - \frac{40.31 \cdot n_e}{f_{SC}^2}. \tag{3.18}$$

Equation 3.18 can be simplified by introducing the ionospheric refractivity N_e with $N_e = (\eta_a - 1) \cdot 10^6$

$$N_e = -\frac{40.31 \cdot 10^6}{f_{SC}^2} n_e. \tag{3.19}$$

3.2 Radio occultations with Mars Express

Mars Express possesses two antenna systems for radio signals: i.) two low gain antennas (LGA) which are equipped for receiving and transmitting S-band signals at 2.1 GHz and ii.) the high gain antenna (HGA) which is a fixed parabolic dish with 1.60 m width, 40 dBi gain in X-band and 28 dBi in S-band. The HGA can receive either X-band at 7.1 GHz or S-band while it can simultaneously transmit X-band (8.4 GHz) and S-band (2.3 GHz) signals. The HGA is the prime antenna for radio occultations. Mars Express radio occultations are conducted with coherent radio signals in two-way mode. The ground station transmits the uplink X-band carrier frequency, which is stabilized by a hydrogen maser oscillator, to establish the coherent downlink in X- and S-band from the spacecraft. The X-band uplink received by the spacecraft is multiplied by 880/749 and 240/749 respectively to convert the signal into downlink frequencies in a fixed ratio of 11/3. The

coherent two-way mode limits the observations to occultation ingress. The occultation egress observation, where the spacecraft emerges from behind the planet, is not possible due to the fact that the coherent radio link between ground station and spacecraft cannot be established fast enough. The downlink signal is received either by a tracking complex of ESA (35 m station New Norcia - Australia, 35 m station Cebreros - Spain, 35 m station Malargüe - Argentina) or by the Deep Space Network (DSN) of NASA.
The times for radio occultations are confined by geometrical constraints due to the position of Earth, Mars and the Sun, spacecraft power and by ground station availability. The geometrical requirements restrict the radio occultations to the so called occultation seasons, while spacecraft power and ground station availability further constrains the number of observations in the occultation seasons. Until the end of 2014, fourteen occultation seasons were successfully conducted. The occultation seasons are indicated as gray squares in Figure 5.2 of Chapter 5.
From a dual-frequency radio occultation observation three kinds of ionospheric electron density profiles can be derived: n_e^X from single X-band, n_e^S from single S-band and n_e^D from the differential frequency residuals called differential Doppler (DD). For ionospheric observations, n_e^X and n_e^D profiles bear the most advantages (explanation in Section 3.3). Therefore no ionospheric electron density from single S-band n_e^S is used in this work. The differential frequency residual Δf_{DP} is calculated from the received Doppler shift at the ground station for X-band $\Delta f_{GS,X}$ and S-band $\Delta f_{GS,S}$

$$\Delta f_{DP} = \Delta f_{GS,S} - \frac{3}{11}\Delta f_{GS,X}. \tag{3.20}$$

Introducing Equation 3.3 into Equation 3.20 and using the linear frequency dependence of the kinetic Doppler shift (see Equation 3.4) and the constant relation $f_{SC,S} = 3/11 \cdot f_{SC,X}$ for the SC downlink yields

$$\begin{aligned}\Delta f_{DP} &= \Delta f_{kin,S} + \Delta f_{atm,S} - \frac{3}{11}\left(\Delta f_{kin,X} + \Delta f_{atm,X}\right) \\ &= \Delta f_{kin,S} + \Delta f_{atm,S} - \Delta f_{kin,S} - \frac{3}{11}\Delta f_{atm,X} \\ &= \Delta f_{atm,S} - \frac{3}{11}\Delta f_{atm,X},\end{aligned} \tag{3.21}$$

showing that due to the downscaling of $\Delta f_{atm,X}$, Δf_{DP} is in general a S-band downlink without the influence of the kinetic Doppler shift. While the dispersive relation between electron density n_e and refractivity N_e (see Equation 3.12) yields results for the ionosphere, the terms $\Delta f_{atm,S}$ and $3/11\Delta f_{atm,X}$ cancel mostly out for the neutral atmosphere due to the fact that the relation between n_N and N_N is non-dispersive.

3.3 Uncertainties in the radio occultation method

The radio occultation method of *Fjeldbo et al.* (1971) is based on geometrical optics and the assumption of a radially symmetric atmosphere and ionosphere. In combination with a non-ideal environment, these requirements lead to specific uncertainties in the resulting electron densities. The strongest sources for uncertainties and liminations of the radio science method are discussed in detail in the subsequent paragraphs.

Unpredicted GS / SC movement and interplanetary plasma Neglecting ground station oscillator drifts and other instabilities, two sources may contribute largely to the errors in the observed frequency shift Δf_{GS}: (i) the unpredicted GS/SC movement along the line-of-sight and (ii) interplanetary plasma in the path of the radio ray.
Unpredicted movement of the spacecraft or the ground station along LOS adds additional kinetic Doppler shift $\Delta f_{kin,U}$ to the received Doppler shift Δf_{GS} of Equation 3.3

$$\Delta f_{GS} = \Delta f_{kin} + \Delta f_{kin,U} + \Delta f_{atm}. \tag{3.22}$$

Removing the known kinetic component Δf_{kin} from Δf_{GS} still leaves Δf_{atm} with the unknown component of the kinetic Doppler shift. $\Delta f_{kin,U}$ causes an additional and incorrect electron density component in n_e^X in the processing procedure. As shown in Equation 3.21, the electron density derived from differential Doppler n_e^D is not influenced by additonal motion along LOS, because the kinetic component cancels out.
The second prominent error source is the changing interplanetary plasma in the radio ray path. The frequency shift Δf for a one-way downlink due to plasma electron density n_e in the radio path s_{sig} is (*Pätzold et al.*, 2004)

$$\Delta f = \frac{40.31}{c} \cdot \frac{1}{f_{SC}} \cdot \frac{d}{dt} \int_{SC}^{GS} n_e ds_{sig}. \tag{3.23}$$

For a similar amount of traversed interplanetary plasma n_e, the frequency shift Δf is higher for the lower frequency S-band than it is for the higher frequency X-band downlink. Therefore there is a stronger influence of the additional plasma along the radio ray path on S-band than there is on X-band, yielding a stronger disturbance on n_e^D and n_e^S than on n_e^X.
The conclusion of the previous analysis is, that n_e^X has the advantage of a lesser sensitivity to interplanetary plasma, while n_e^D is not affected by additional motion in the radio ray path. n_e^S combines both negative effect, therefore no n_e^S profiles are used in this work.
The effect of interplanetary plasma and additional motion along LOS is illustrated in Figure 3.2. The upper baseline, illustrated in Panel (b), is that part of the MaRS observation, where the measurement is not yet affected by planetary plasma. Without any disturbances in the observations, a zero upper baseline would occur down to that altitude where the uppermost ionospheric electron density becomes available. External error

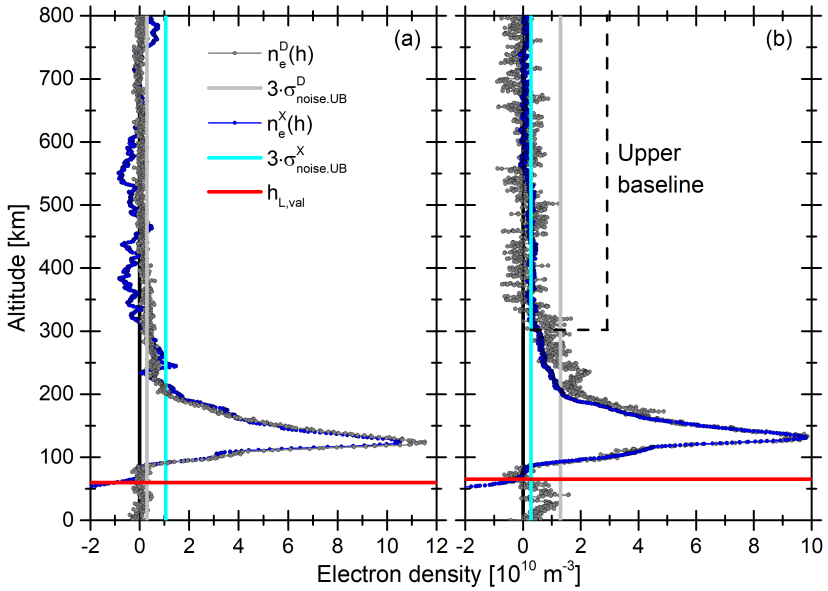

Figure 3.2: MaRS observation of (a) DoY 089 (2006) with $L_S = 32.20°$, $\Omega_{lon} = 86.73°$, $\Omega_{lat} = 19.28°$, $\chi = 54.58°$ and (b) DoY 145 (2004) with $L_S = 37.85°$, $\Omega_{lon} = 272.30°$, $\Omega_{lat} = 45.85°$, $\chi = 69.82°$. $\sigma^D_{noise,UB}$ is the noise level of the n_e^D profile, $\sigma^X_{noise,UB}$ the noise level of the n_e^X profile and $h_{L,val}$ is the lowest valid altitude of the observation (Parameter details are provided in Chapter 4). The dashed black line in Panel (b) illustrates the upper baseline range for n_e^X.

sources introduce disturbances in the observations, which cause fluctuations around the zero line. The negative electron densities in the topside of both Panels of Figure 3.2 have therefore no real physical meaning, but are introduced by deviations of the observation conditions from ideal experimental and environmental conditions. While on Panel (a), n_e^D is smooth, there is unpredicted movement of SC or GS causing disturbances in n_e^X. On Panel (b), n_e^X is quite smooth, while n_e^D is largely disturbed by interplanetary plasma effects or disturbances in the terrestrial ionosphere. Comparing the electron density profiles derived from differential Doppler and X-band, it is possible to separate the effects of plasma along the radio ray path from those due to motion.

Short upper observation baseline The baseline fit is a method to remove first order effects of spacecraft orbit uncertainties or plasma effects on the frequency residuals. In the upper baseline procedure a polynomial usually up to the first order is fitted on that part of the frequency residuals, where the spacecraft is not yet sounding the ionosphere of Mars. This part of the profile is expected to be zero in an ideal observation where no uncertainties in the spacecraft orbit/position of the ground station determination or plasma effects of the Earth ionosphere or interplanetary plasma are present. Fitting a polynomial to the upper part of the profile removes the drift in frequency caused by the described and other effects. If the observational baseline is very short, the reliability of

the resulting electron densities decreases due to a possibility of i.) removing real electron density features instead of observational noise from the observation by a badly suited fit and ii.) underestimating the real noise of the observation if not enough undisturbed data points for a reliable noise estimate are present.

Assumption of radial symmetry Converting the received Doppler shifts into atmospheric parameters by the method of *Fjeldbo et al.* (1971) requires the assumption of a locally radial symmetric atmosphere. This is problematic for the Martian night-side, where the ionosphere is patchy and irregular and at the terminator, where atmospheric conditions change fast over short distances. At other observation constellations it might become important, that the derived electron density profiles are not completely vertical. During an occultation observation, the geometry between the spacecraft, planet and Earth changes, which causes slight longitudinal and latitudinal changes in the intersection point of the ray periapsis d in Panel (b) of Figure 3.1 with the surface. Therefore small scale horizontal variations of the neutral atmosphere/ionosphere, e.g. caused by gravity waves, might affect the appearance of the resulting electron densities in certain altitudes by causing wavelike structures in the inversion algorithm.

Vertical resolution The refractivity at 2.1 km above the areoid for DoY 089, 2006 is approximately 0.00177. Equation 3.14 yields for that N_N a velocity in the atmosphere of 0.999999998 percent of c. A radio ray with this velocity would cross a distance of 9000 km in 0.03 seconds. Therefore the planetary atmosphere can be assumed as "frozen" during the passing of one radio ray. The vertical resolution of the radio ray however, is limited by the fact that the cross section of a radio ray is not infinitely small. The geometrical method for deriving mostly vertical profiles of the atmosphere described earlier in this Chapter neglects diffraction. Therefore the results are limited by diffraction effects, which are determined on the basis of geometrical optics.
The Huygens-Fresnel principle provides a calculation method for the vertical resolution by a combination of Huygens wave theory and Fresnel's principle of interference. As shown in *Born and Wolf* (1999) and *Freeman* (2007), Huygens describes the proceeding of electromagnetic waves with the superposition of secondary spherical elementary waves. Figure 3.3 illustrates this effect: after a certain time the electromagnetic wave transmitted by T reaches the position marked by t_1. Huygens considered this wavefront as the position of secondary sources, which emit spherical waves in the forward direction. The wave front at t_2 can therefore be constructed from the envelope of the emitted secondary waves. This principle makes it possible to construct the arriving wavefront at the receiver position R. Connecting positions where the phase of the traveling wavefront differs by $\lambda/2$ along a vertical plane at t_3

$$l_1 + l_2 = w_1 + w_2 + b\frac{\lambda}{2}. \tag{3.24}$$

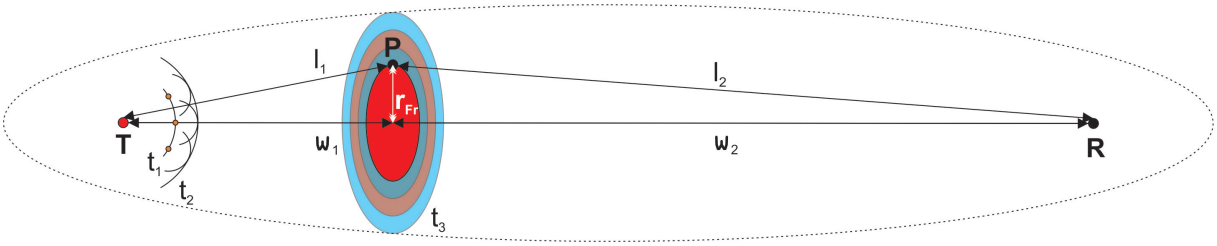

Figure 3.3: Illustration of the Huygens-Fresnel principle. The monochromatic wave is transmitted into a homogeneous medium by transmitter T and received by receiver R. The wavefront at t_1 illustrates the Huygens principle: secondary sources on the wave envelope emit spherical waves in the forward direction and their envelope yields the wavefront at t_2. A cut through the traversing wavefront is given in reddish and bluish colors. Highlighted are the borders, where the $l_1 + l_2 = w_1 + w_2 + b \cdot \lambda/2$. This yields the radially symmetric Fresnel-zones. Due to the construction pattern of the Fresnel-zone borders, the envelope of each Fresnel-zone is an ellipse, illustrated here for the fourth Fresnel-zone with radius r_{Fr}. Figure after Freeman *(2007)*

.

yields the colored circular intensity zones of the wave (not to scale in Figure 3.3). The variables of Equation 3.24 are illustrated in Figure 3.3 and b is a natural number. w_1 and w_2 can be assumed to be much larger than the radius of the Fresnel zone r_{Fr}. This yields for the triangles in Figure 3.3

$$l_1 = \left(w_1^2 + r_{Fr}^2\right)^{1/2} \simeq w_1 + \frac{r_{Fr}^2}{2w_1} \tag{3.25}$$

$$l_2 = \left(w_2^2 + r_{Fr}^2\right)^{1/2} \simeq w_2 + \frac{r_{Fr}^2}{2w_2} \tag{3.26}$$

and for Equation 3.24

$$r_{Fr} = \left(\frac{w_1 w_2 b\lambda}{w_1 + w_2}\right)^{1/2}. \tag{3.27}$$

Even though the varying refractivity field of a planetary atmosphere changes the Fresnel-zones to complexer shapes, Equation 3.24 is often used in the determination of the atmospheric vertical resolution. *Hinson et al.* (1999) provide Equations for radio occultations with the approximation, that the distance between the ground station and the limb of the planet is much larger than the distance between the spacecraft and the limb of the planet $w_2 >> w_1$. This yields for the first Fresnel-zone with $b = 1$

$$r_{Fr} = (w_1\lambda)^{1/2}. \tag{3.28}$$

The intensity contained in each Fresnel-zone decreases outward with increasing number. Zones with uneven numbers increase the intensity at the observers position, while the even zones lead to an decrease in intensity. Most of the signal intensity is contained in the first

center Fresnel-zone, therefore most information contained in the radio ray comes from this area of the ray. This limits the classical vertical resolution of the radio occultation observation to the height of the first Fresnel-zone, which will from now on only be called Fresnel-zone.
The range of the Fesnel zone at Mars depends on the observing geometry and is in the range of few hundred meters. Ionospheric features with an extent smaller than that are not detectable in the radio science observations.

Chapter 4

The MaRS ionospheric database and derived observational parameters

This Chapter contains a description of the MaRS ionospheric data set used in this work and information about the observational parameters derived from each observation.

4.1 The MaRS database of ionospheric electron density observations

To date, MaRS has obtained more than 850 radio occultation profiles of temperature, pressure, neutral density and electron density of the planetary day- and nightside (partly published in *Pätzold et al.* (2005); *Hinson et al.* (2008a,b); *Withers et al.* (2012a,b); *Tellmann et al.* (2013); *Peter et al.* (2014); *Pätzold et al.* (2016b)). Certain selection criteria are applied to reduce the large-scale noise level in the underlying data set for this work. The large-scale noise level of an electron density profile is a measure for strong external disturbances during the time of the observation and defined in the text below. Using only the reduced data set yields an increase in the reliability of the small-scale merged excess electron density detection in the the observations.
The first step for increasing the reliability of the merged excess electron density detection is to select only those MaRS ionospheric observations (2004 - 12/2014) which meet the following conditions:

- Complete ionopause to ionospheric base dual-frequency recording
  The dual-frequency recording provides the possibility to distinguish between disturbances in the ionospheric profiles caused either by unexpected movement of the spacecraft/ground station or by additional plasma in the radio ray path.

- The upper baseline exceeds 400 km altitude above the areoid.
  As discussed earlier, electron density profiles derived from radio science observations

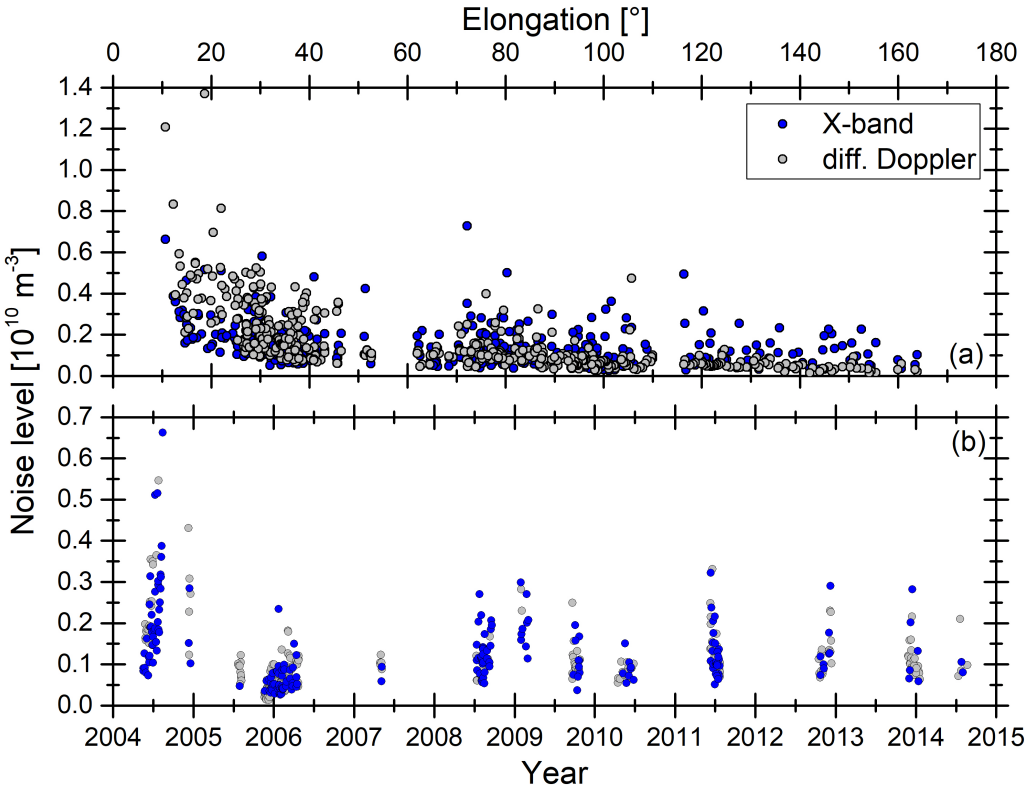

Figure 4.1: (a) Noise level of the MaRS observations derived from X-band and differential Doppler as a function of the elongation angle. (b) Noise level of the mixed source MaRS observations as a function of observation time.

with a long upper baseline are more reliable than profiles derived from observations with a short upper baseline.

- The observation has been conducted for a solar zenith angle lower than 90 °.
  The probability that the assumption of a radially symmetric ionosphere is locally fulfilled is higher on the ionospheric dayside. Therefore only dayside observations have been selected for this work to avoid the introduction of additional errors by large deviations from a radially symmetric ionosphere.

451 MaRS observations fulfill these criteria.

Due to the dual-frequency recording, electron density profiles derived from X-Band (n_e^X) and from differential Doppler (n_e^D) are available for each selected MaRS observation. Figure 4.1 proves, that the noise level of the data set is further reduced, when either the n_e^X or the n_e^D electron density profile of a certain MaRS observation is selected. Panel (a) of Figure 4.1 contains the X-band $\sigma^X_{noise,UB}$ and differential Doppler $\sigma^D_{noise,UB}$ noise level (Equation 4.2 in the next Section) for each of the chosen electron density profiles

in dependence of the Mars-Sun elongation at the time of the associated observations. The planetary elongation is the angle between the Earth-Sun and the Earth-Mars vectors as seen from the Earth. As expected from the discussion in Chapter 3, the noise level $\sigma^X_{noise,UB}$ of the X-band observations does not show any clear dependence on the planetary elongation. This is due to the fact, that the largest noise contribution for X-Band is usually introduced by the unexpected movement of spacecraft and ground station. The dependence of $\sigma^D_{noise,UB}$ on the elongation is explained by the fact, that the largest source for noise in the n^D_e profiles usually is the additional solar plasma in the radio ray path. The additional plasma content along the radio ray path is maximal when the elongation angle is small and minimal, when the elongation angle is large. For a small elongation angle, the distance between Mars and Earth is large and the radio ray is close to the Sun's corona and vice versa. Exceptions are possible, when the radio ray penetrates solar plasma of a traveling Coronal Mass Ejection (CME). This means, that the decision for either n^X_e or n^D_e of a measurement depends on the observation conditions. Selecting always the electron profile with the lower noise level yields a strong reduction in observational noise in the mixed source data set in Panel (b).
However, not short scale variations are problematic in the detection of the merged excess electron densities but large-scale plasma disturbances and unusual spacecraft or ground station motion. Therefore the second step for the noise reduction in the MaRS data set consists of combining electron density profiles derived from differential Doppler and X-band data in dependence of the large-scale noise level. The large-scale noise level $\sigma_{noise,L}$ of the ionospheric profiles was tested by the following procedure:

(1) For each MaRS observation, the electron density profiles derived from X-band n^X_e and differential Doppler n^D_e are smoothed by ten consecutive iterations of a short window moving average (for the test only) in order to reduce the small scale noise by applying

$$n_{e,av}(h_i) = \frac{2n_e(h_i) + \Sigma^2_{j\neq 0, j=-2} \frac{0.5\cdot|h_{i-1}-h_{i+1}|}{|h_{i+j}-h_i|} n_e(h_{i+j})}{2 + \Sigma^2_{j\neq 0, j=-2} \frac{0.5\cdot|h_{i-1}-h_{i+1}|}{|h_{i+j}-h_i|}} \tag{4.1}$$

where $n_{e,av}(h_i)$ is the smoothed electron density at altitude h_i. The described procedure suppresses most of the small scale noise and leaves the long scale disturbances caused by unusual S/C or GS motion and interstellar plasma.

(2) The smoothed electron density above the ionopause is mostly undisturbed by planetary plasma and therefore yields a good estimate for the intensity level of external disturbances. The large scale noise level $\sigma_{noise,L}$ of the profiles is therefore determined by calculating the standard deviations $\sigma_{noise,L,X}(n_{e,X})$ and $\sigma_{noise,L,D}(n_{e,D})$ of the averaged electron density above the planetary ionopause and selecting the profile with the lower noise level of each observation for further analysis.

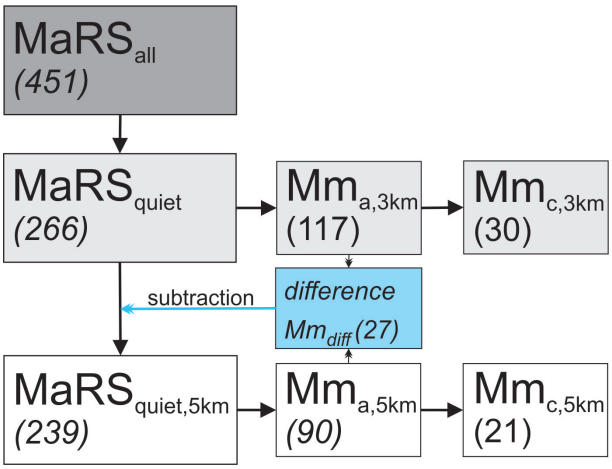

Figure 4.2: Structure of data sets ($MaRS_{all}$, $MaRS_{quiet}$, $MaRS_{quiet,5km}$) in combination with the two categories Mm_a and Mm_c for the identified merged excess electron densities.

This procedure results in a database of 451 electron density profiles consisting of either the $n_{e,D}$ or the $n_{e,X}$ profile for an individual MaRS observation. It will be referenced as MaRS_{all}.

Figure 4.2 illustrates the data structure of the three MaRS data sets and two categories for the merged excess electron densities used in this work. As discussed above, the 451 MaRS observations in the MaRS_{all} data set yield the basic data for further investigations. The 316 observations of MaRS_{all} with a $\sigma_{noise,L}$ below $1.0 \cdot 10^9$ provide the basis for the "quiet" data set. 31 additional observations are removed from the set after visual inspection and comparison of the n_e^D and n_e^X observations due to low data rates (5), incomplete lower part of the profile (2), large areas of negative electron densities above the main ionosphere (10), profiles with inconsistencies between n_e^D and n_e^X (7) and high scatter in the data (7). For three MaRS observations, the electron density profiles with the higher $\sigma_{noise,L}$ needed to be selected, because the data with the lower noise level contain flawed data. In addition, 19 further MaRS observations are removed, because their ionospheric topside is largely disturbed. This is done, because this work investigates the origin of the merged excess electron densities in the undisturbed ionosphere. This leaves the MaRS_{quiet} data set with 266 MaRS observations.

The investigations in Chapter 7 will show, that another set of MaRS observations is feasible. The $\text{MaRS}_{quiet,5km}$ data set is a subset of the MaRS_{quiet} observations, which consists of 239 MaRS observations. Removed are those observations for which merged excess electron densities (Mm) are identified in the $\text{Mm}_{a,3km}$ category, but not in the $\text{Mm}_{a,5km}$ category. $\text{Mm}_{a,3km}$ and $\text{Mm}_{a,5km}$ are defined later in this Chapter.

4.2 Derived observational parameters

The observational parameters contain general information about the MaRS observation, which include e.g. the altitude calibration, planetary position and observational noise level. In addition, information about the state of the lower ionosphere are derived from each observation of the MaRS_{quiet} data set. Those information are used in Chapter 7 to identify potential formation mechanisms of the merged excess electron densities in correlation with the environmental parameters derived in Chapter 5.

4.2.1 General parameters

Altitude calibration of the observation

The final MaRS electron density profiles are derived in dependence of the distance to the planet center. Due to the Martian dichotomy and a polar flattening of 0.0059 it is expected, that the altitude calibration by simply subtracting the average planetary radius will introduce a bias in the altitude distribution of the electron density profiles. Two concepts are available for altitude calibration: the areoid and the approximated surface of Mars.
The Earth reference equipotential surface of the combined gravitational and rotational forces at sea level is called the geoid (*Fowler*, 2011). The Mars geoid is called the areoid, its reference areoid is the equipotential surface for which the mean equatorial radius is 3396 km. Observations of the Mars Orbiter Laser Altimeter MGS-MOLA on board of the MGS spacecraft provide high resolution observations of the areoid and the surface topography of Mars (*Smith et al.*, 1999a,b, 2001). The routine heights.F (detailed description in (*Forget et al.*, 2015)), which is distributed as separate tool with the Mars Climate Database (detailed description of the content of the Mars Climate Database in Chapter 5.2), provides high resolution areoid and MGS-MOLA surface altitude values. The heights.F areoid data are based on the MGM1025 spherical harmonics solution for the Mars gravity field, which in turn is based on the X-Band tracking data of the MGS-MOLA experiment. As described in *Forget et al.* (2015), the MGM1025 model (or GMM 3) for the Mars areoid is an updated version of the Goddard Mars Model 2B (GMM 2B) (*Lemoine et al.*, 2001) and provides areoid values for the spherical harmonics of degree and order 80. The topographic surface altitudes provided by heights.F are based on the 32 pixels per degree file of the MGS-MOLA Precision Experiment Data Record[1], which give a resolution of 1850 m at the equator.
The MGS-RS ionospheric dayside observations[2] of the M2 maximum electron densities are used to evaluate the feasibility of both calibration methods. The radius of the M2 max-

[1] http://pds.jpl.nasa.gov

[2] The electron density data set was downloaded from http://nova.stanford.edu/projects/mgs/eds-public.html.

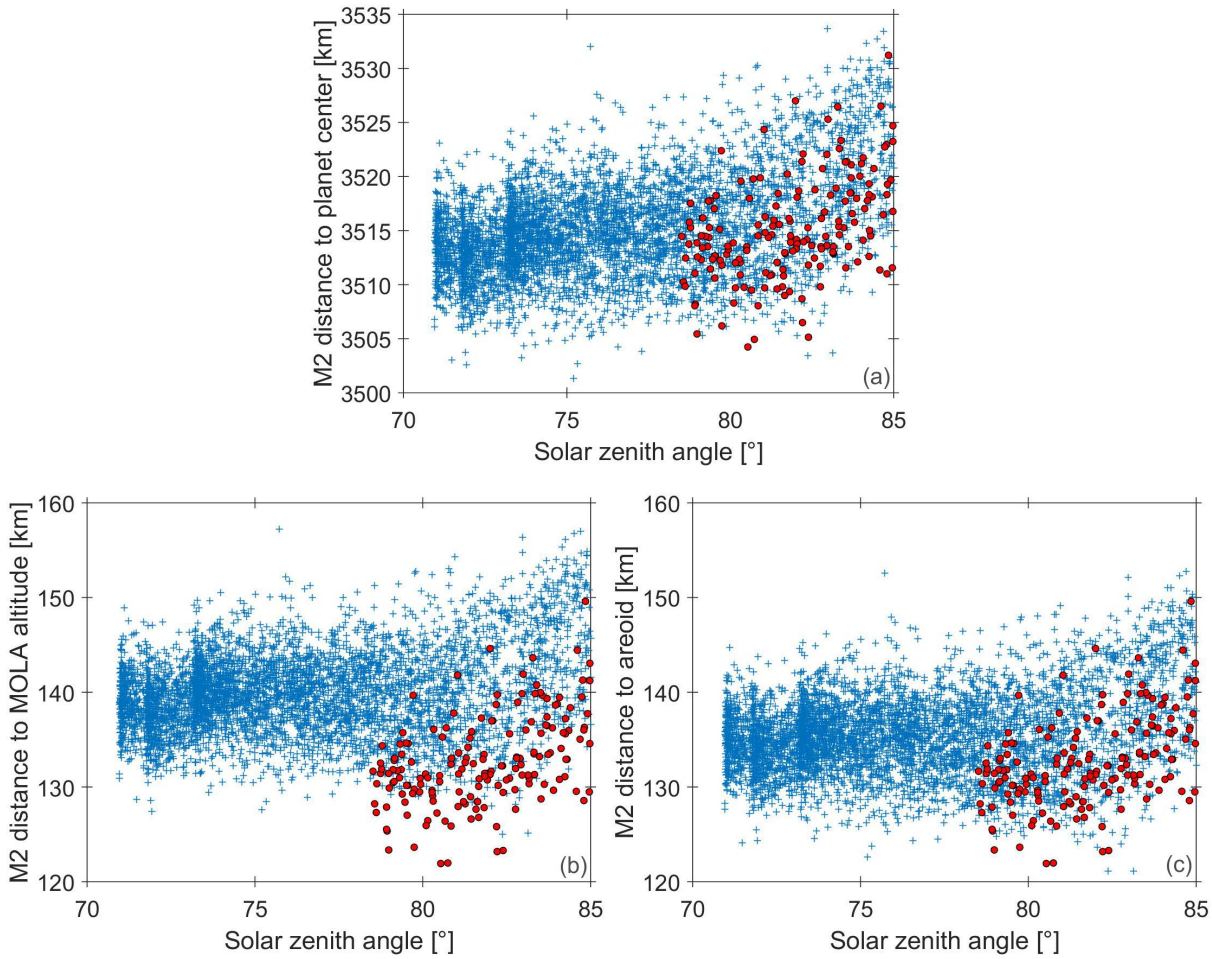

Figure 4.3: (a) Distance of the MGS-RS M2 maximum electron density to the planet center. (b) Distance of the MGS-RS M2 maximum electron density to the MGS-MOLA surface. (c) Distance of the MGS-RS M2 maximum electron density to the areoid. Data from the northern hemisphere are blue crosses, while data from the southern hemisphere are shown as red dots.

imum electron density, its planetary longitude and latitude are extracted for all publicly available MGS-RS observations of the Martian ionospheric dayside with a solar zenith angle below 85 ° (5231 observations, 5052 data sets for the northern hemisphere, 172 data sets for the southern hemisphere). The areoid and surface distance to the planet center are calculated with heights.F for each observation and the corrected M2 altitudes are shown in Figure 4.3 as function of solar zenith angle for both hemispheres. Subtracting the MGS-MOLA surface altitude (Panel b) from the M2 distance to the planet center (Panel a) introduces a bias into the M2 altitudes. The altitude difference between the observations on the northern and southern hemispheres increases. The M2 altitudes of the southern hemisphere are on average found lower in the atmosphere than the M2 observations on the northern hemisphere. This is caused by the calibration with the higher elevation of the southern highlands. For the M2 altitude calibration with the areoid data (Panel c), no such behavior is found. Therefore the altitude calibration of the MaRS electron density profiles is conducted with the individual areoid altitude determined for each observation.

Position of the observation

Even if the observed electron density is shown in dependence of altitude, the observed profile is not completely vertical. During an occultation entry, the footpoint of the observation, which is the surface intersection point of the straight line connecting the center of Mars and the lowest point of the radio ray in the ionosphere (d in Panel (b) of Figure 3.1), moves slightly over the surface of Mars. This leads to a slight longitudinal and latitudinal variation and with that to a small variation in solar zenith angle. For each observation, the values of Ω_{lon}, Ω_{lat} and χ at 130 km altitude above the areoid are used for comparison purposes in this work, because this altitude is always close to the position of the ionospheric maximum electron density. The change of the solar longitude L_S (see Figure 2.5) is negligible during the few minutes of an occultation.

Noise level and offset of the upper baseline

The upper baseline noise level of an electron density profile $\sigma_{noise,UB}$

$$\sigma_{noise,UB} = \sqrt{\frac{1}{N-1}\sum_{i=1}^{N}\left[\left(n_e^{obs}\right)_i - \mu_{UB}\right]^2} \tag{4.2}$$

is calculated as the standard deviation of the electron density samples $\left(n_e^{obs}\right)_i$ above the local areoid altitude + 800 km. If the number of data points N above this border is lower than 50, $\sigma_{noise,UB}$ is calculated from the electron density above the altitude, where the electron density falls below zero for the first time. If this procedure yields less than 50 data points, the highest 50 data points of the profile are used, detrended with a linear fit.

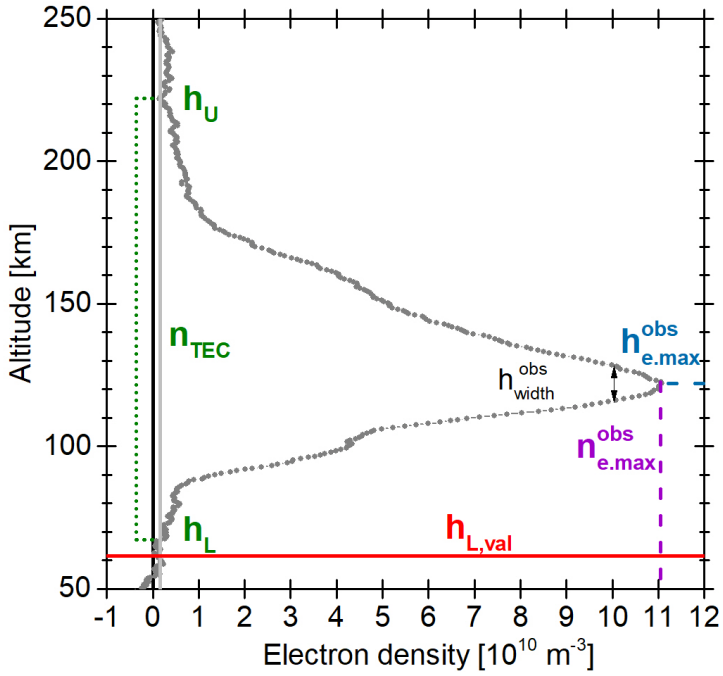

Figure 4.4: Selected observational parameters of the n_e^D MaRS observation of DoY 111 (2006), $L_S = 42.32°$, $\Omega_{lon} = 158.17°$, $\Omega_{lat} = 7.38°$, $\chi = 58.80°$. The definition of the parameters is found in the text.

The offset of the upper baseline of the MaRS profile μ_{UB} is calculated in the same altitude range as $\sigma_{noise,UB}$

$$\mu_{UB} = \frac{1}{N} \sum_{i=1}^{N} \left(n_e^{obs}\right)_i . \tag{4.3}$$

A perfect baseline fit in a radial-symmetric ionosphere that removes all external disturbances would provide $\mu_{UB} = 0.0$ in a region with neutral and ionospheric densities below the detection limit. Due to the fact, that the baseline fit is conducted with a low-degree polynomial (higher-degree polynomials are not feasible, because they are not supported by the dominant physical effects), there are always residual disturbances in the electron density. To avoid a bias of the extracted observational parameters (e.g. an increase in total vertical electron content by a shift of the profile to higher electron densities), all electron density profiles are calibrated by subtracting μ_{UB}.

Upper and lower altitude border of the electron density profile

The upper h_U and lower h_L altitude border of a MaRS electron density profile are illustrated in Figure 4.4. They are determined by the noise level $\sigma_{noise,UB}$ of the observation. h_U is that altitude, where the electron density appears from the background noise

($> 3{\cdot}\sigma_{noise,UB}$) for the first time, calculated with a linear interpolation. h_L is determined as that altitude, where the electron density falls below the background noise ($< 3{\cdot}\sigma_{noise,UB}$) for the first time below the main layer.
In addition, the smoothed lower altitude border $h_{L,smooth}$ is calculated from the smoothed electron density profile calculated by using the M1 smoothing algorithm described later in this Chapter. $h_{L,smooth}$ is used to investigate the influence of the presence of Mm excess densities on the extent of the ionospheric layers.

Lowest valid altitude

The n_e^D and n_e^X profiles in Figure 3.2 of Chapter 3 show, that the derived electron density profiles from differential Doppler and X-Band start to behave differently below approximately 100 km altitude. While n_e^D stays close to the zero line, n_e^X shows increasingly negative electron densities with decreasing altitude. This different behavior of n_e^D and n_e^X is caused by dispersion. Equation 3.12 in Chapter 3 shows, that the ionospheric refractivity N_e is frequency dependent, while the neutral atmospheric refractivity N_N is approximately frequency independent. The increasing neutral atmospheric density with decreasing altitude therefore has a different effect on n_e^D and n_e^X. The differential Doppler is calculated by subtracting $3/11{\cdot}\Delta f_{atm,X}$ of the X-band atmospheric Doppler shift from the atmospheric S-band Doppler shift $\Delta f_{atm,S}$ (see Equation 3.21). This procedure results in ionospheric electron densities n_e^D due to the dispersive relation between n_e and N_e. For the neutral atmosphere however, the relation between n_N and N_N is approximately frequency-independent. When N_N dominates, $\Delta f_{atm,S}$ and $\Delta f_{atm,X}$ should be equal and the Equation for the differential Doppler causes a slightly negative drift. It is only expected, that n_e^D is zero below the ionosphere, when i.) no deviations from a radially symmetric ionosphere occur, ii.) the neutral atmosphere is not yet strong enough to influence the radio ray, iii.) no other errors (e.g. additional plasma in the radio ray) are present and iv.) the atmospheric path differences between the X- and S-Band radio rays are not large yet, so that similar regions of the atmosphere are sounded.
The negative electron densities of n_e^X can be explained by the different sign of the ionospheric and neutral atmosphere term in Equation 3.12. As long as the ionospheric refractivity N_e dominates, the electron density is given as a positive value. As soon, as the refractivity of the neutral atmosphere N_N dominates, the sign of the resulting densities changes and becomes negative. These negative electron densities are therefore not valid, but an indicator for the dominance of N_N.
This discussion shows, that the n_e^X and n_e^D ionospheric electron density profiles are useful above a certain altitude only. Below that altitude, n_e^X becomes increasingly negative, while n_e^D is valid only until N_N dominates the refraction process or other sources bias the observation. The lowest valid altitude for n_e^X and n_e^D is determined from n_e^X. It is chosen to be that altitude at which the negative electron density reaches $-3{\cdot}\sigma^X_{noise,UB}$ for the last time (see Figure 3.2). It is assumed that below this altitude the neutral atmosphere is

strong enough to bias the n_e^D profile.

Vertical Electron Content (TEC)

The vertical Total Electron Content (TEC) n_{TEC}^{obs} is obtained by integrating the electron density profile over the significant altitude range from h_L to h_U

$$n_{TEC} = \int_{h_L}^{h_U} n_e(h)dh. \tag{4.4}$$

The altitude range for the vertical TEC integration is illustrated in Figure 4.4.

4.2.2 M2 parameters with error bars

The M2 main peak is the dominant feature of the Martian dayside ionosphere. Its parameters can be directly derived from the MaRS electron density profiles without any further data manipulation. Therefore, the derivation of the M2 parameters is only shortly discussed.

- M2 peak electron density $n_{e,max}^{obs}(M2)$
  $n_{e,max}^{obs}(M2)$ is derived as a simple maximum search in the electron density profile. An uncertainty of $3{\cdot}\sigma_{noise,UB}$ noise standard deviation is applied. All given $n_{e,max}^{obs}(M2)$ are larger than $3{\cdot}\sigma_{noise,UB}$.

- M2 peak altitude $h_{max}^{obs}(M2)$
  $h_{max}^{obs}(M2)$ is defined as the altitude of $n_{e,max}^{obs}(M2)$. The uncertainties $\sigma_{h,max,lw}(M2)$ and $\sigma_{h,max,up}(M2)$ are defined as the difference between $h_{max}^{obs}(M2)$ and the upper and lower altitudes where the electron density falls below $n_{e,max}^{obs}(M2)$ - $3{\cdot}\sigma_{noise,UB}$.

- M2 layer width $h_{width}^{obs}(M2) = h_{width,up}(M2)$ - $h_{width,lw}(M2)$
  The M2 layer width is defined by the difference in altitude at 90% of $n_{e,max}^{obs}(M2)$. The upper and lower bounds on $h_{width}^{obs}(M2)$, $\sigma_{h,width,up}(M2)$ and $\sigma_{h,width,lw}(M2)$ are defined by

$$\sigma_{h,width,up}(M2) = h\left(n_e\left(h_{width,up}(M2)\right) - 3\cdot\sigma_{noise}\right) - h\left(n_e\left(h_{width,lw}(M2)\right) - 3\cdot\sigma_{noise}\right) \tag{4.5}$$

$$\sigma_{h,width,lw}(M2) = h\left(n_e\left(h_{width,up}(M2)\right) + 3\cdot\sigma_{noise}\right) - h\left(n_e\left(h_{width,lw}(M2)\right) + 3\cdot\sigma_{noise}\right). \tag{4.6}$$

Figure 4.4 illustrates the M2 parameters. They are extracted for all observations in MaRS_{quiet}.

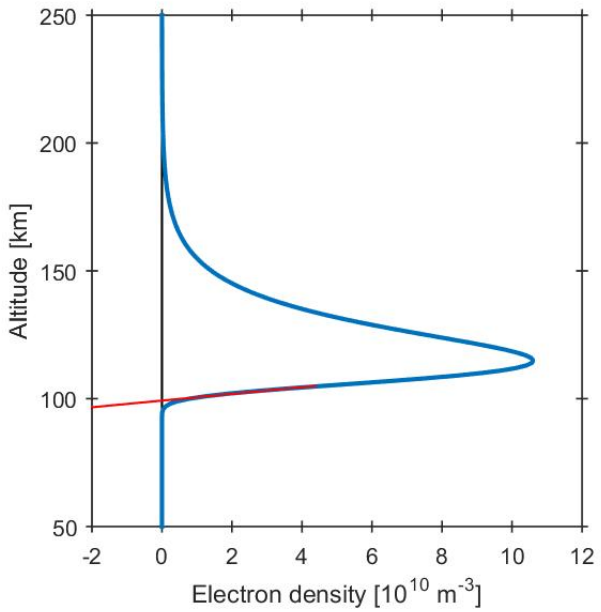

Figure 4.5: Chapman function (Eq. 4.7) calculated for H_n = 7 km, $h_{max,0}$ = 110 km, $n_{e,max,0}(M2) = 15.0 \cdot 10^{10}\, m^{-3}$ and $\chi = 0\,^\circ$ (blue) and straight line fit (red) between 100 and 105 km altitude.

4.2.3 M1 parameters with error bars

The two MaRS observations of the Mars ionospheric electron density in Figure 2.12 of Chapter 2 already show, that the appearance of the lower day-side ionosphere is very variable. M1 shapes can consist of pronounced layers, but also appear as nearly vanishing M1 shoulders. An indirect method for the determination of the M1 parameters has therefore been chosen to derive not only the parameters of the pronounced layers, but additionally those of the fainter M1 features.
Fitting a Chapman-function to the ionospheric main peak and interpreting the residuals as M1 layer is a classical way for the M1 parameter derivation (e.g. *Peter* (2008); *Fallows et al.* (2015) for Mars and *Girazian et al.* (2015) for Venus). The Chapman function (*Chapman*, 1931a; *Schunk and Nagy*, 2009) provides an analytical expression for an idealized ionospheric layer

$$n_e\,(h,\chi) = n_{e,max,0}\,(M2) \cdot \exp\left[\frac{1}{2}\left(1 - \frac{h - h_{max,0}}{H_n} - \frac{1}{\cos\,(\chi)} \exp\left(\frac{h_{max,0} - h}{H_n}\right)\right)\right] \quad (4.7)$$

with the altitude above the Mars areoid h, the altitude $h_{max,0}$ of the maximum electron density $n_{e,max,0}(M2)$ at solar zenith angle χ= 0 ° and the neutral scale height H_n. The equation represents the equilibrium between ion production by solar radiation and loss

by dissociative recombination of electrons and ions. The Equation applies for a horizontally stratified, isothermal, exponentially decreasing and single species neutral atmosphere combined with monochromatic solar radiation and is illustrated in Figure 4.5. The requirements for applying the Chapman-function are

horizontally stratified atmosphere The assumption of a horizontally stratified planetary atmosphere is only valid for $\chi = 0°$. For increasing solar zenith angle, the error introduced by the assumption of a horizontally layered atmosphere increases as shown in (*Smith and Smith*, 1972, Fig. 7). The error between $1/cos(\chi)$ and the Chapman-function for grazing incidence angle χ^* (details in Chapter 6) reaches 20 % at a solar zenith angle of approximately 85° (for a distance to the planetary center of 3389.5 + 140.0 km and atmospheric scale height of 7 km).

single species The MVN-NGIMS observations in Figure 2.9 of Chapter 2 show, that the neutral atmosphere at the ionospheric main peak consists mainly of CO_2. Panel (a) of Figure 2.13 (Chapter 2) shows however, that the main ionospheric species at 150 km altitude is O_2^+, followed by 14% of CO_2^+ (*Benna et al.*, 2015a). The resulting ionospheric density in the main peak region is therefore no single species derived from direct photo-ionization (see Chapter 6 for a detailed discussion of important ionospheric reactions), but a complex combination of photo-ionization, chemical reactions and electron impact ionization.

exponential decay of the atmosphere and constant temperature The two main diffusion processes in the Mars atmosphere are the eddy diffusion and the molecular diffusion. As discussed in Chapter 2, the homopause is the border between the well mixed lower atmosphere and the segregated upper atmosphere. The homopause altitude slightly varies for different species due to small variations in the molecular diffusion coefficients. During the second deep-dip campaign, MAVEN observations place the N_2 homopause at ∼130 km altitude for the subsolar region near the equator (LST=12-13 h, L_S approx. 327° to 330°) (*Bougher et al.*, 2015a). The main ionospheric region can therefore be found in an altitude where the atmospheric species do not simply show the exponential decay needed for the derivation of the Chapman-function.
The derivation of Equation 4.7 requires a constant temperature. *Bougher et al.* (2015a) derived averaged neutral temperatures for N_2 and Ar over several MAVEN orbits of the second deep dip campaign from 250 km down to ∼135 km and found a strong temperature gradient between 140 and 170 km due to peak EUV heating. In addition, Figure 2.8 shows the strong variation of the modeled LMD-GCM neutral temperature in ionospheric altitudes. This neutral temperature behavior is not conform with the requirements for the derivation of the Chapman-function.

neutral temperature The strongest loss process for the most abundant ionospheric ion O_2^+ at the main peak is its dissociative recombination with electrons (see Chapter 6). This reaction does not depend on the neutral, but on the electron temperature. Some authors suggest (e.g. *Rohrbaugh et al.* (1979); *Matta et al.* (2014)), that the electron temperature begins to deviate from the neutral temperature in the region of the ionospheric main peak.

monochromatic solar flux The input solar radiation into the Mars atmosphere does consist not only of one single wavelengths, but of a wide spectrum of solar radiation. Solar EUV and X-ray is absorbed in ionospheric altitudes, while photochemical and secondary processes form the lower ionosphere (see Chapter 6). This contradicts the assumption of a single solar wavelength as source for the main ionospheric peak.

Even if the requirements for an ionospheric Chapman-layer are not fully satisfied, the shape of the M2 peak region often resembles that described in Eq. 4.7. The main problem of deriving M1 parameters with the Chapman-fit method is however, that conducting a reasonable fit of a Chapman function to the main ionospheric peak is difficult: i.) The resulting fit of Eq. 4.7 depends strongly on the selected data range around the main peak. Increasing or decreasing the fit range by only one data point sometimes completely changes the appearance of the fit and with that the shape of the residual M1 layer. ii.) When both lobes of the ionospheric main peak are used to constrain the Chapman fit, the additional electron density of a present bulge (Panels a and b of Figure 2.12 in Chapter 2) adds an avoidable bias, because the physical mechanisms for the bulge are most probably different from those producing the M1 layer. iii.) Some MaRS observations of the dayside ionosphere do appear not Chapman-like (see e.g. *Withers et al.* (2012a)). Fitting a Chapman-function to those data sets would introduce errors into the derived M1 parameters.

Therefore instead of fitting Equation 4.7 on both lobes of the main ionospheric peak, a combination of three straight lines is fit to the lower M2 lobe. The three lines are used to estimate the ranges for the M1 parameters, because providing realistic absolute shapes is not possible in this complex ionospheric region. The M1 parameter ranges are estimated by fitting one center straight line for the parameter determination and using two additional straight lines for the determination of the M1 range. Figure 4.6 illustrates the M1 detection method for two MaRS observations. In a first step, the center straight line (green) is fitted to the lower M2 region where it is not yet strongly influenced by the primary sources of M1. The remaining residual electron density of M1 is then used to extract the altitude $h^{obs}_{max}(M1)$, electron density $n^{obs}_{e,max}(M1)$, width $h^{obs}_{width}(M1)$ and total vertical electron content of M1 $n^{obs}_{TEC}(M1)$. The lower and upper ranges of the M1 parameters are then determined from two additional lines (gray and orange).

Several procedures were tested for determining the M1 parameters and the method pre-

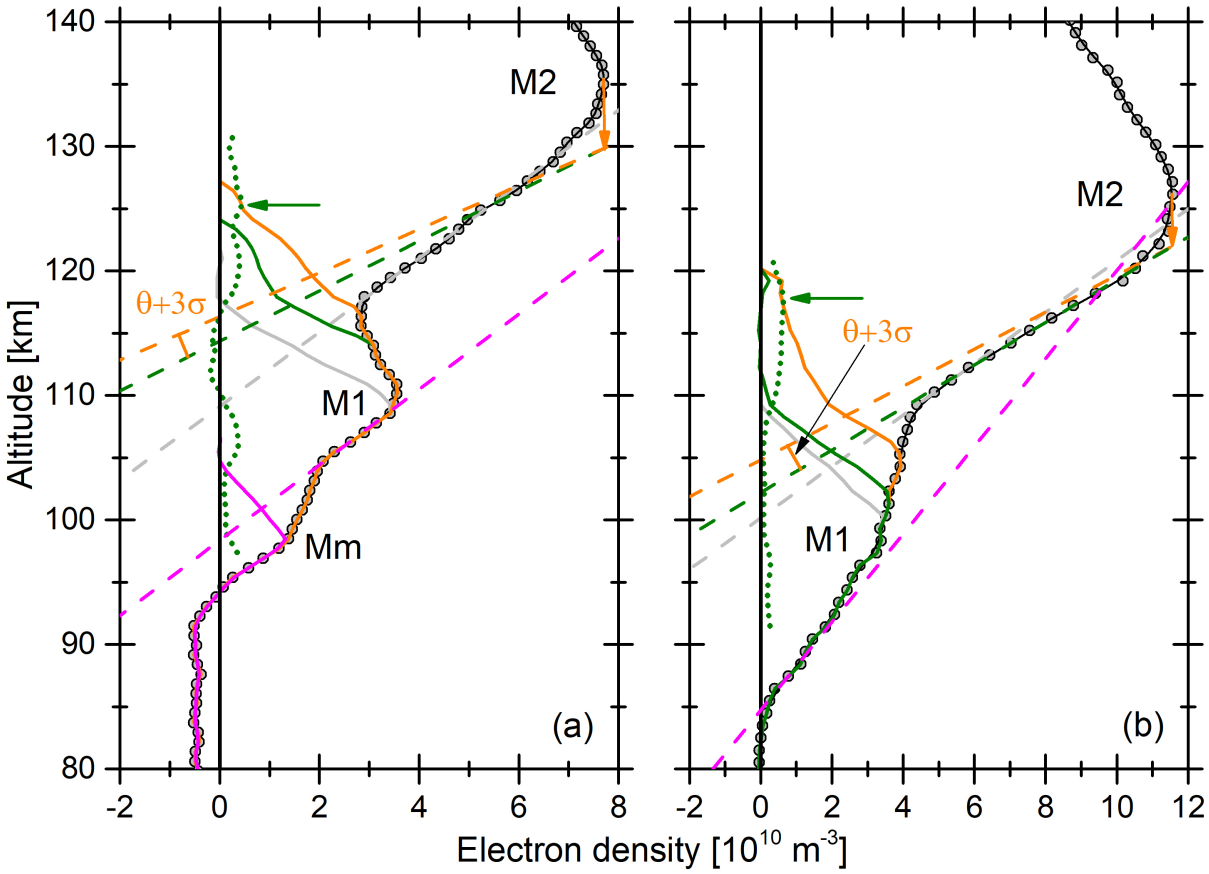

Figure 4.6: M1 and Mm parameter determination and range approximation. ***(a)*** *MEX MaRS n_e^D observation of DoY 337 (2005), $L_S = 334.41°$, $\Omega_{lon} = 300.88°$, $\Omega_{lat} = 66.82°$, $\chi = 78.52°$, $h_{L,val} = 59.6$ km.* ***(b)*** *MEX MaRS n_e^D observation of DoY 049 (2006), $L_S = 13.62°$, $\Omega_{lon} = 336.42°$, $\Omega_{lat} = 38.48°$, $\chi = 53.12°$, $h_{L,val} = 69.66$ km. The original n_e^D is shown as gray dots, while the smoothed electron density is indicated by the black line. The dotted green line illustrates the first derivation of the smoothed electron density $\left(n_{e,S}^{obs}\right)'$ and the green arrow the identified maximum $\left(n_{e,S}^{obs}\right)'_{max}$. The dashed green line is the fit on n_e^D in the range from $\left(n_{e,S}^{obs}\right)'_{max}$ to $0.7 \cdot \left(n_{e,S}^{obs}\right)'_{max}$, while the solid green line gives the associated residuals. The lower range of the M1 parameters is given by the dashed and the solid gray lines, which are derived from a fit on $0.85 \cdot \left(n_{e,S}^{obs}\right)'_{max}$ to $0.40 \cdot \left(n_{e,S}^{obs}\right)'_{max}$. The upper range of the M1 parameters is given by the orange lines, which are derived from the rotation of the dashed green line fit around the rotation point (orange arrow) by the determined rotation angle $\theta+3\cdot\sigma$ for the given $n_{e,max}^{obs}(M2)$ value. The magenta lines illustrate the availability of a Mm below M1 in (a) and the absence of it in (b).*

sented here yields the lowest number of automatic misdetections. For 26 observations of the MaRS_{quiet} dataset, the smoothing algorithm had to be manually corrected due to unusual M1 shapes and other problems. The automated procedure is described in detail below, followed by a discussion of the reliability of the derived M1 parameter ranges.

Data smoothing The M1 parameter detection algorithm depends on the first derivation of the electron density profiles in the lower ionosphere with respect to the altitude. It is therefore quite sensitive to data peaks/scatter. Smoothing the observed electron density data before calculating the first derivation reduces the risk for M1 misdetections. The smoothing of the observations is done in two steps. First, the large scale noise level $\sigma_{noise,L}$ of the electron density profile is determined by applying Equation 4.1 to the original data set in 10 consecutive steps with an averaging window of 1. Choosing a short window removes all small-scale noise and leaves only the large-scale disturbances $\sigma_{noise,L}$. In the second step, the original data set is repeatedly smoothed with an averaging window of 1 until its noise level $\sigma_{noise,UB}$ falls below $\sigma_{noise,L} + 1 \cdot 10^7\, m^{-3}$. This method reduces the available small scale noise level to a fixed border of $1.0 \cdot 10^7\, m^{-3}$, independent of the large scale noise.

Center M1 parameter determination The altitude range for the center straight line fit is determined from the first derivation of the smoothed electron density. The idea is to use that altitude range for the center line fit, where the M1 layer does not yet strongly affects the behavior of the lower lobe of the ionospheric peak. Panel (a) of Figure B.1 in Appendix B shows, that the first derivation of the IonA-1 model (1-D photo-chemical model without included transport processes - details in Chapter 6) electron density below the main peak is described by an idealized sinusoidal shape with the first maximum approximately at that altitude, where M1 is not yet strongly influencing M2. The real first derivation shapes in Figure 4.6 are less ideal, but using the maximum of the first derivation as a starting point for the line fit still yields a good estimate for the undisturbed part of M2.
The range for the center straight line fit is determined in three steps. First, the first derivation $\left(n_{e,S}^{obs}\right)'$ (dotted green line in Figure 4.6) of the smoothed electron density is calculated between the ionospheric main peak and that altitude where the electron density reaches 10 % of $n_{e,max}^{obs}(M2)$. Second, only the uppermost 2/3 of the $\left(n_{e,S}^{obs}\right)'$ data points are used to avoid problems of the detection algorithm with small or large scale oscillations below the M1 layer. Third, the altitude range for the straight line fit is set from the maximum first derivation $\left(n_{e,S}^{obs}\right)'_{max}$ of this reduced data range to $0.7 \cdot \left(n_{e,S}^{obs}\right)'_{max}$. While the range of the straight line fit is determined from the smoothed data, the fit itself is done on the original data set in the determined altitude range. A linear regression algorithm is applied with error bars of $3 \cdot \sigma_{noise,UB}$ assigned to each data point. The M1 maximum electron density $n_{e,max}^{obs}(M1)$, altitude $h_{max}^{obs}(M1)$ and TEC $n_{TEC}^{obs}(M1)$ are extracted from

the electron density residuals with a procedure similar to that for the M2 parameter determination. The M1 width is determined from that M1 altitudes, where the electron density residuals fall below 50 % of $n_{e,max}^{obs}(M1)$ instead of 90 % as for the M2 layer. $n_{e,max}^{obs}(M1)$ is much smaller than $n_{e,max}^{obs}(M2)$, which would result in only extremely small altitude differences, if a border of 90 % would be applied.

M1 lower and upper range approximation The lower and upper ranges of the M1 parameters are determined with two additional line fits. The lower range for the M1 parameters is calculated from the residuals of a straight line fit on the altitude range of $0.85 \cdot \left(n_{e,S}^{obs}\right)'_{max}$ to $0.4 \cdot \left(n_{e,S}^{obs}\right)'_{max}$ with detection algorithms similar to those used for the center M1 parameters determination. Those boundaries for the fit result in a smaller residual M1 layer and therefore provide the lower range of the M1 parameters. The presented boundaries for the first derivation are those with the fewest M1 mis-detections in the automated routine.
Panel (a) of Figure B.1 in Appendix B shows IonA-1 electron densities derived with a solar flux of 0.5 - 95 nm and 10 - 95 nm. While the full solar flux input results in typical dayside ionospheric electron density with a pronounced M2 and M1 layer, the reduced solar flux causes a complete vanishing of the M1 layer in the model. In addition, the ionospheric base moves slightly upwards for the reduced solar flux profile due to the missing contribution of the solar X-rays. This means, that the center line fit on the ionospheric base will not only remove the M2 layer, but in addition a small part of M1 from the residuals. The upper range for the M1 parameters is based on the error introduced by this partly removal of the M1 electron density. The four steps for the computation of the upper M1 parameter ranges is found below, a detailed derivation of the used Equation is found in Appendix B.

i.) The center straight line fit is conducted on the ionospheric base.

ii.) The center line is rotated around the projection of $n_{e,max}^{obs}(M2)$ (orange arrow in Figure 4.6) by the rotation angle $\theta + 3\sigma$, where

$$\theta(n_{e,max}^{obs}(M2)) = 4.77921537 \cdot 10^{-13}\ [m^{-3}] \cdot n_{e,max}^{obs}(M2) + 0.02456586\ [rad] \quad (4.8)$$
$$\sigma = 0.005174\ [rad].$$

3σ are added to the rotation angle in Equation 4.8, where σ is the determined error from the rotation angle calculation in Appendix B. Equation 4.8 has been determined by modeling the behavior of M2 and M1 for 50 MaRS observations with IonA-1 for full and reduced solar flux. Straight line fits are conducted on the resulting ionospheric bases and the rotation angle between the two line-fits is determined. The relation between the rotation angle θ and $n_{e,max}^{obs}(M2)$ is determined by conductiong a linear fit on the resulting rotation angles for the 50 MaRS observations.

iii.) The residuals derived by subtracting the rotated line from the smoothed n_e^{obs} are used to calculate the upper range parameters of M1 with the same subroutine used for the center M1 parameter determination.

In addition, the differences between the 50 modeled electron density profiles for full and reduced solar flux have been used to validate the described method. Subtracting the modeled electron densities for the full and the reduced solar flux from each other provides the 'real' M1 shape for each data set. Its absolute parameters have been determined and compared with the parameters derived with the above described method. It is found, that the described detection method works well for the M1 altitude and electron density. It slightly underestimates the 'real' vertical TEC, which is however still found within the derived lower and upper M1 boundaries. However, the method is not valid for absolute values of the M1 width, because the 'real' $h_{width}^{obs}(M1)$ is highly underestimated. The derived $h_{width}^{obs}(M1)$ are therefore only usable as a relative indicator for variations, but not as an estimate of absolute M1 widths.

4.2.4 Merged excess electron density

The parameters of the excess electron densities merged with the main ionosphere (Mm) are derived from the smoothed center fit M1 residuals (green residuals in Figure 4.6). For the Mm parameter determination, the used routines are similar to those used in the M1 parameter determination. The maximum first derivation $\left(n_{e,S}^{obs}\right)'$ is calculated for the new altitude range below $h_{max}^{obs}(M1)$ and the straight line fit is conducted on the $\left(n_{e,S}^{obs}\right)'_{max}$ to $0.7{\cdot}\left(n_{e,S}^{obs}\right)'_{max}$ range. This procedure yields the vertical TEC $n_{TEC}^{obs}(Mm)$, Mm maximum electron density $n_{e,max}^{obs}(Mm)$, altitude $h_{max}^{obs}(Mm)$ and width $h_{width}^{obs}(Mm)$ of the identified merged excess electron densities. While the other parameters are defined similar to the M1 parameters, the Mm width is defined as the altitude difference between the smoothed upper border of the Mm excess density $h_{U,smooth}(Mm)$ (linear interpolated altitude, where the smoothed residual electron density above $n_{e,max}^{obs}(Mm)$ falls below $3{\cdot}\sigma_{noise,UB}$ for the first time) and the earlier described smoothed lower border $h_{L,smooth}$. As illustrated in Figure 4.6 and 4.7, most Mm excess densities do not appear as pronounced layers. This indicates, that a part of the Mm excesses may be hidden in the M1 layer. Therefore the most reliable of the derived Mm parameters are the smoothed lower border $h_{L,smooth}$ and the vertical TEC $n_{TEC}^{obs}(Mm)$. $h_{L,smooth}$ is the only parameter not biased by the presence of M1 and $n_{TEC}^{obs}(Mm)$ provides an estimate for the visible Mm TEC. The maximum Mm electron density $n_{e,max}^{obs}(Mm)$ and altitude $h_{max}^{obs}(Mm)$ are less reliable, because the shoulder-like shape of the Mm excesses may disguise their true values.
It is not feasible to determine the errors for the Mm excess density parameters similar to those for the M1 layers due to the fact, that the origin of the Mm excess densities is not yet known. Therefore i.) the part of the Mm excess density hidden in the M1 layer and ii.) the influence of Mm on the base of M1 cannot be estimated from models in advance.

An error $\sigma^{obs}_{TEC}(Mm)$ for $n^{obs}_{TEC}(Mm)$ is estimated from the general noise level of the profile $\sigma_{noise,UB}$

$$\sigma^{obs}_{TEC}(Mm) = h^{obs}_{width}(Mm) \cdot \sigma_{noise,UB}. \tag{4.9}$$

The occurring merged excess electron densities are small compared to the main and secondary ionospheric regions. This makes their detection difficult and increases the possibility for misinterpretations. Large scale disturbances and high noise levels of the whole profile further complicate the detection. Two additional sources for uncertainties in the Mm parameter determination are the i.) the line-fitting method and ii.) the variability of the lower baselines in the MaRS observations.

Line-fitting method Figure 4.5 illustrates, that an undisturbed Chapman-layer shows a small deviation from a linear decrease in the lowest part of the electron density profile. The same behavior is found for the linear fit on the 10 - 95 nm solar flux results of IonA-1 in Panel (a) of Figure B.1 in Chapter B.1 of Appendix B. This behavior indicates, that a minimum boundary for the vertical TEC $n^{obs}_{TEC}(Mm)$ is required to avoid a misinterpretation of the chapmanesque absorption pattern in the lowest part of the ionosphere as a pronounced Mm.

Variability of the lower baseline In an ideal undisturbed and radial symmetric atmosphere and ionosphere it is expected from the description of the radio science method in Chapter 3, that the n_e^D profiles below the ionosphere and above the lowest valid altitude $h_{L,val}$ (called now lower baseline and is illustrated in Panel (a) of Figure 4.7) show either a zero value or a small negative drift. For the n_e^X profile, a zero baseline is expected if the neutral atmosphere is not yet strong enough to provide a significant effect on the X-Band. Individual disturbances in the upper and lower baselines of n_e^X are caused by unexpected movements of spacecraft or ground station, while additional plasma in the radio ray path disturbs the upper and lower baseline of the n_e^D profile. Those disturbances influence the appearance of the lower baseline of the individual n_e^D and n_e^X profiles, even if the electron density profile with the lower noise level is selected. Most disturbances found in the electron density profiles are individual for n_e^D and n_e^X, but some disturbances in the lower baseline are identified in both observed profiles.

While Panel (a) of Figure 4.7 contains an observation with mostly undisturbed lower baselines, the other Panels show observations with lower baseline disturbances visible in the n_e^D and n_e^X electron density profiles. Panel (b) contains an observation with a wavelike structure, Panel (c) shows a lower baseline shifted to negative electron density values and Panel (d) has lower baselines which are shifted to positive values. This behavior may be e.g. caused by deviations of the observed ionosphere from radial symmetry which add up during the Abel inversion procedure. Determining the real origins of the disturbed lower baselines is beyond the scope of this work, but yield potential for future projects.

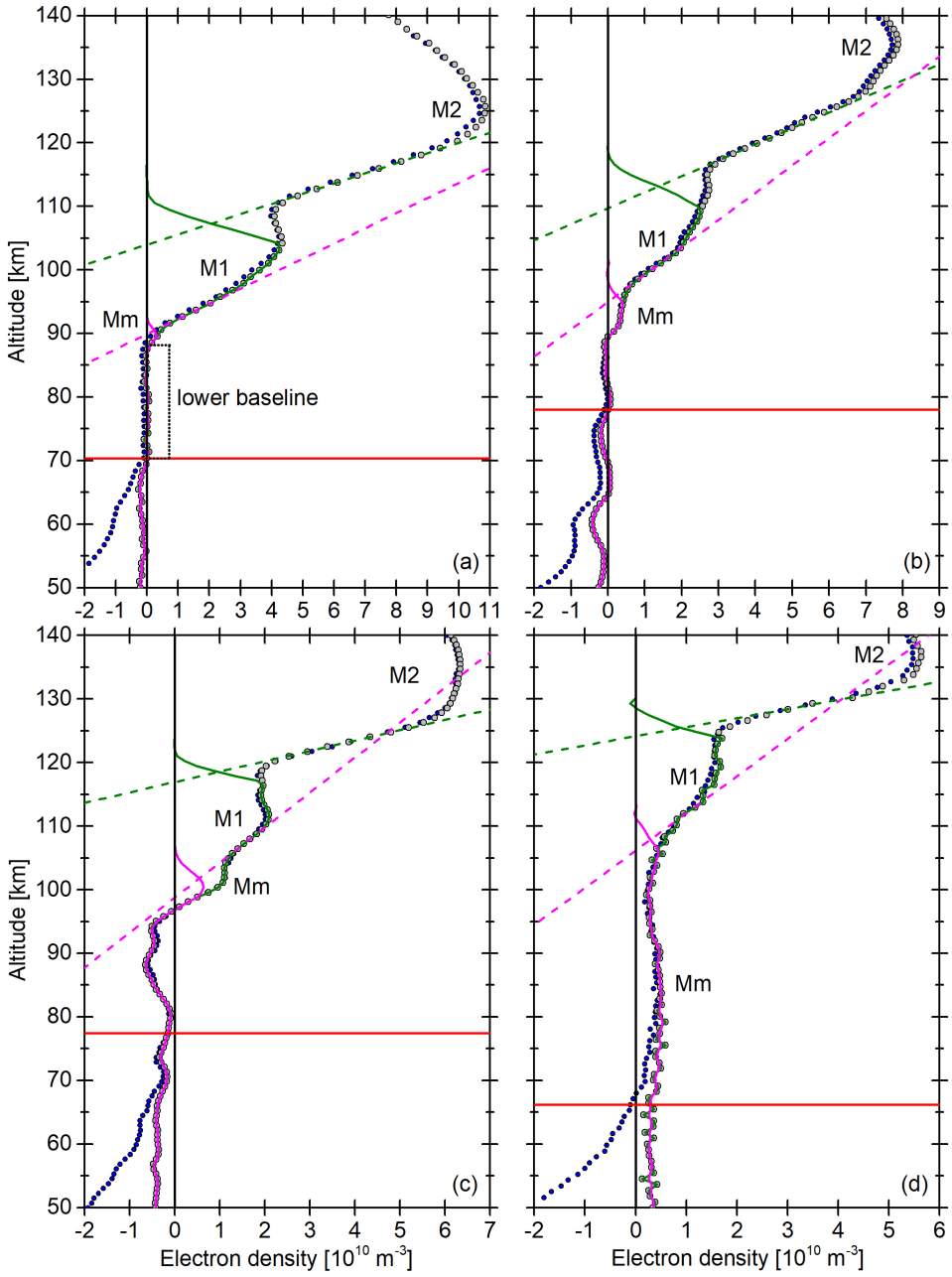

Figure 4.7: MaRS n_e^D (gray dots) and n_e^X (blue dots) observations of (a) DoY 107 (2006), L_S = 40.56°, Ω_{lon} = 91.80°, Ω_{lat} = 9.80°, χ = 57.90°, $h_{L,val}$ = 70.4 km, (b) DoY 342 (2005), L_S = 336.98°, Ω_{lon} = 69.93°, Ω_{lat} = 66.58°, χ = 77.00°, $h_{L,val}$ = 78.0 km, (c) DoY 331 (2005), L_S = 331.05°, Ω_{lon} = 306.15°, Ω_{lat} = 66.64°, χ = 80.51°, $h_{L,val}$ = 77.5 km and (d) DoY 14 (2014), L_S = 76.30°, Ω_{lon} = 77.03°, Ω_{lat} = 67.00°, χ = 87.08°, $h_{L,val}$ = 66.2 km. $h_{L,val}$ is indicated by the red line. The dashed green line indicates the center line-fit on the smoothed electron densities, while the solid green line indicates the residuals. The dashed and solid magenta lines indicate the line fit on the residuals and the identified Mm, respectively.

In this work, the uncertainties introduced into the determined Mm parameters by the Mm identification method and the variability of the lower observation baselines are considered by investigating two categories Mm_a and Mm_c of detected excess electron densities in two separate MaRS data sets MaRS_{quiet} and $\mathrm{MaRS}_{quiet,5km}$ (see overview in Figure 4.2). Merged excess electron densities with a large vertical TEC $n_{TEC}^{obs}(Mm)$ imply a good visibility independent of the merged excess depth, width or its maximum electron density. Therefore the amount of inherent $n_{TEC}^{obs}(Mm)$ is used as primary parameter for the identification of merged excess electron density below a M1 layer. The first category Mm_a in this work consists of all Mm detections for which the computed vertical TEC exceeds certain boundaries, which depend on the upper baseline noise $\sigma_{noise,UB}$. These boundary conditions have been chosen to assure, that the identified merged excess electron densities i.) exceed the vertical extent of the Fresnel-zone of the observation, ii.) are not caused by an increased noise level seen in the ionospheric upper baseline and iii.) are not misdetections caused by small chapmanesque absorption patterns not removed from the ionospheric profile by the straight line fit method. No reliable estimate for the $n_{TEC}^{obs}(Mm)$ uncertainties can be given in advance, because there is no sharp TEC boundary between the small chapmanesque absorption pattern and pronounced merged excess electron densities. Therefore two data sets MaRS_{quiet} and $\mathrm{MaRS}_{quiet,5km}$ have been selected on which different TEC boundary conditions are applied. This reduces the impact of a fixed boundary on the Mm occurrence rate correlation with environmental parameters in Chapter 7. In the MaRS_{quiet} data set all merged excess electron densities are contained in $\mathrm{Mm}_{a,3km}$ for which the computed vertical TEC meets the following condition

$$n_{TEC}^{obs}(Mm) > 3,000m \cdot 3 \cdot \sigma_{noise,UB}. \tag{4.10}$$

In the $\mathrm{MaRS}_{quiet,5km}$ data set all merged excess electron densities are contained in $\mathrm{Mm}_{a,5km}$ for which the computed vertical TEC meets the following condition

$$n_{TEC}^{obs}(Mm) > 5,000m \cdot 3 \cdot \sigma_{noise,UB}. \tag{4.11}$$

$3 \cdot \sigma_{noise,UB}$ is used here to cover disturbances already seen in the upper baseline of the electron density profile. The two boundaries of 3,000 m and 5,000 m are estimated to cover the uncertainty sources described above. The $\mathrm{MaRS}_{quiet,5km}$ data set is derived from the MaRS_{quiet} data set by removing the difference data set Mm_{diff} between $\mathrm{Mm}_{a,3km}$ and $\mathrm{Mm}_{a,5km}$. Using $\mathrm{MaRS}_{quiet,5km}$ in combination with the higher TEC boundary of $\mathrm{Mm}_{a,5km}$ is necessary to avoid a bias in the occurrence rates of the merged excess electron densities calculated in Chapter 7. The Mm occurrence rate is the percentage of Mm identifications in a given data set. Therefore the Mm occurrence rate depends on the number of observations in the data set. Using MaRS_{quiet} for both $n_{TEC}^{obs}(Mm)$ boundary conditions would always result in higher Mm occurrence rates for $\mathrm{Mm}_{a,3km}$ than for $\mathrm{Mm}_{a,5km}$. Removing Mm_{diff} from $\mathrm{MaRS}_{quiet,5km}$ removes that bias in the calculated occurrence rates.
The second category used in this work Mm_c is a subset of the derived Mm_a. Mm_c is

calculated for MaRS_{quiet} ($\text{Mm}_{c,3km}$) and $\text{MaRS}_{quiet,5km}$ ($\text{Mm}_{c,5km}$). This Mm category is applied to prove, that the merged excess electron densities are a real sporadic feature of the Mars ionosphere and not only caused by the reaction of the Abel inversion algorithm on deviations of the real ionosphere from radial-symmetric behavior. The Mm_c category does contain only those MaRS observations, where

- the range for the lower baseline parameter determination is at least 15 km.
  Panel(a) in Figure 4.7 illustrates the lower baseline range, which is the region between the lowest valid altitude $h_{L,val}$ and that altitude, where n_e^{obs} falls below $\sigma_{noise,UB}$ at the lower base of the ionosphere.

- $n_{TEC}^{obs}(Mm)$ is larger than $3000m \cdot 3{\cdot}\sigma_{noise,LB}$, where $\sigma_{noise,LB}$ is the standard deviation of the electron density in the lower baseline altitude range.

- the absolute value of the mean offset μ_{LB} of the lower baseline altitude range is lower than $6{\cdot}\sigma_{noise,UB}$ to avoid observations with extreme offsets.

Calculating $\text{Mm}_{c,3km}$ from MaRS_{quiet} and $\text{Mm}_{c,5km}$ from $\text{MaRS}_{quiet,5km}$ yields only those Mm identifications, where the amount of vertical TEC is larger than the disturbance of the lower baseline ($\sigma_{noise,LB}$) over the set altitude range. It is assumed, that $\sigma_{noise,LB}$ does contain not only the disturbances of the upper baseline, but additionally the disturbances caused by the deviation of the ionosphere from radial-symmetric behavior due to the fact, that the applied inversion algorithm works from the top of the profile down to the ionospheric base.

Chapter 5

Derived environmental parameters for the MaRS observations

This Chapter contains the environmental parameters derived for each observation in the MaRS_{quiet} data set. The input solar flux derivation and origin of the underlying neutral atmosphere for the IonA models (described in Chapter 6) are illustrated. The derivation of the solar flux proxies with boundaries for low, moderate and high solar flux is described and the underlying crustal magnetic field for the MaRS observations are determined. The flux proxies and magnitude of the crustal magnetic field are required in Chapter 7 for the determiation of potential formation processes of the merged excess electron densities from the MaRS observations.

5.1 Solar flux

Extreme ultraviolet, near ultraviolet, X-ray and others are terms for parts of the electromagnetic spectrum. Often those terms do not describe the same wavelength ranges, their meanings vary slightly from author to author. Therefore those terms shall be defined here for further use in this work, following *Woods and Rottman* (2002) in the ultraviolet, except for EUV. The definition for NIR and VIS is taken from the Solar 2000: ISO 21348 Definitions of Solar Irradiance Spectral Categories[1].

- Infrared
  - NIR: near infrared from 760 nm to 1400 nm
- Visible
  - VIS: visible from 380 to 760 nm

[1] *www.spacewx.com/pdf/SET_21348_2004.pdf*

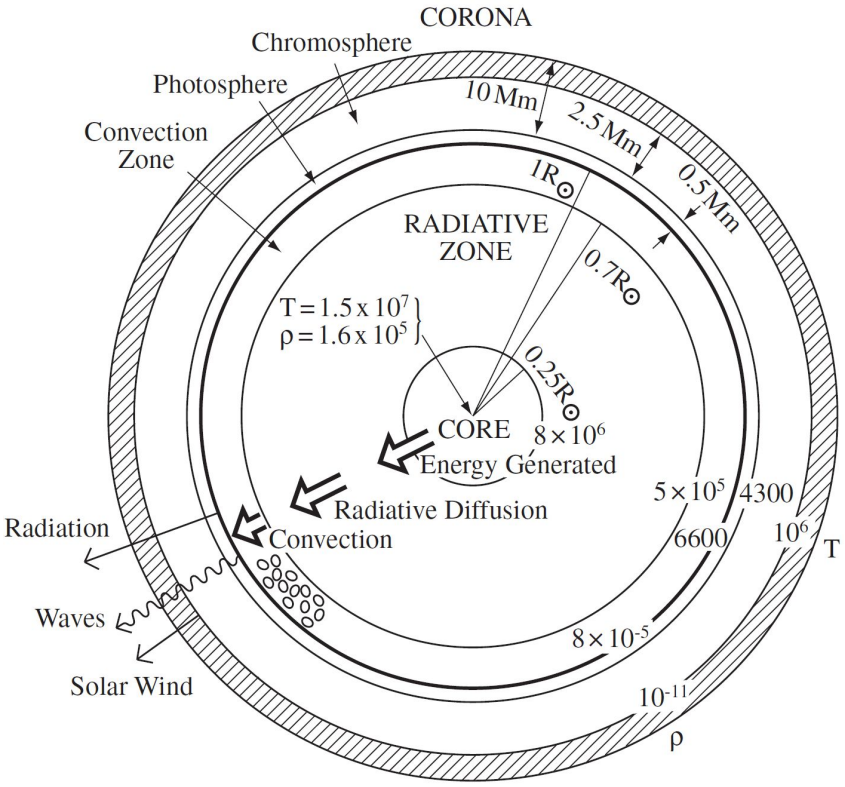

Figure 5.1: Internal structure of the Sun. The different sizes of the regions are approximated, but not drawn to scale. The shaded region indicates the boundary between chromosphere and corona and varies between $2.5 \cdot 10^6\,m$ *to* $15 \cdot 10^6\,m$*. Temperatures of the various regions are given in* K*, densities in* $kg\,m^{-3}$*, Mm in the Figure stands for* $10^6\,m$*. The Figure is taken from* Priest *(2014).*

- Ultraviolet
  - NUV: near ultraviolet from 300 - 400 nm
  - MUV: middle ultraviolet from 200 - 300 nm
  - FUV: far ultraviolet from 120 - 200 nm
  - EUV: extreme ultraviolet from 10 - 120 nm
- X-ray: radiation from 0.45 - 10 nm

5.1.1 The Sun: extrinsic and intrinsic solar flux variations

The Sun is a star of spectral type G2 and luminosity class V on the main sequence of the Hertzsprung-Russell diagram, which relates the stars spectral type and absolute

magnitude (*Unsöld and Baschek*, 2005). It has a mass of approximately $1.99 \cdot 10^{30}$ kg and a volumetric mean radius of 695,700 km. The photospheric composition consists mainly of hydrogen (90.965 %) and helium (8.889 %) with minor amounts of oxygen (774 ppm), carbon (330 ppm), neon (112 ppm), nitrogen (102 ppm), iron (43 ppm), magnesium (35 ppm), silicium (32 ppm) and sulphur (15 ppm)[2]. Most of the atoms are ionized due to the high solar temperatures.
Figure 5.1 illustrates the internal structure of the Sun. A thorough description of the Sun's features and magnetohydrodynamics is found in *Priest* (2014). The two main regions of the Sun are its interior, where the solar energy originates and travels outward by radiative transmission and convection, and its atmosphere, where the photons can escape directly into space. A division by dominant physical processes yields three main zones for the Sun's interior: the core, the radiative zone and the convection zone. The extreme conditions of highest pressure and temperature in the Sun's core provide the environment for thermonuclear reactions. Energy is generated by the fusion of four protons ${}^1H$ into a Helium core ${}^4He$, summarized by the equation

$$4^1H \rightarrow {}^4He + 2e^+ + 2\Theta + 26.7MeV. \tag{5.1}$$

Byproducts of the fusion process are two positrons e^+, two electron neutrinos Θ (0.5 MeV) and two gamma rays with a combined energy output of 26.2 MeV. As discussed in *Priest* (2014), the generated photons are slowly advancing outwards through the radiation zone, where they are absorbed and re-emitted by the dense local plasma. The radiative diffusion slowly reduces the energy of the photons from gamma rays to visible light. The convection zone is characterized by a temperature gradient which is too large, to keep the solar material in stable equilibrium. This causes plasma convection processes, which dominate the energy transport in this region.
The optical thickness/depth τ (for details see the Lambert-Beer law in Chapter 6 Eq. 6.7) is a measure for the transparency of a medium. If τ reaches 1, the available radiation is reduced by a factor $1/e$. The Sun's atmosphere consists of three main regions, the photosphere, chromosphere and corona. The photosphere is often called the Sun's visible surface, because it emits most of the Sun's radiation even if its only a few hundred km thick. The Sun's temperature decreases from approximately 6,600 K at the lower photosphere to a minimum of 4,400 K at approximately 500 km altitude. For the NUV to NIR continua its optical thickness is $\lesssim 1$ with high optical thickness for all but very weak spectral lines. This results in a continuum emission with superimposed absorption lines. The so-called Fraunhofer-lines appear, when the photospheric radiation is absorbed by species available in the overlying solar atmosphere (e.g. by forcing the electron of a hydrogen atom to a higher quantum level). Most absorption lines have their origin in the lower photosphere, but some arise in the chromosphere. In the chromosphere, the Sun's temperature rises slowly. It is optically thin for the NUV to the NIR continua

[2]derived from the NASA Sun fact sheet https://nssdc.gsfc.nasa.gov/planetary/factsheet/sunfact.html

and optically thick for the strong spectral lines. Between the chromosphere and corona, the Sun's temperature rises rapidly to a few million degrees in a less than 100 km thick transition region. The main radiative emission of this region is in the UV below 200 nm. Most spectral lines in the transition region and corona are emission lines. The corona emits in the UV, EUV and X-ray. It emits the continuous K-corona (scattered light from free electrons), F-corona (scattered light from dust) and certain lines, e.g. the red line (530.3 nm) and green line (637.4 nm) from forbidden transitions in highly ionized iron. The Sun's corona is optically thin for the full magnetic spectrum except for radio waves and few spectral lines.
A black body is an idealized object which absorbs 100 % of the incoming radiation independently of wavelength or incidence angle. Its photon flux emission Φ_λ at a certain wavelength λ depends only on its temperature T (*Unsöld and Baschek*, 2005)

$$\Phi_\lambda(T) = \frac{2\pi h_{Pl} c^2}{\lambda^5} \frac{1}{e^{h_{Pl}c/(k_B \lambda T)} - 1} \tag{5.2}$$

with the Planck's constant h_{Pl}, the speed of light in vacuum c and the Boltzmann constant k_B. As described in *Woods and Rottman* (2002), the general shape of the continuum solar emission resembles that of a black body with a temperature close to 5,800 K. The emission peak of the solar radiation is close to 600 nm and shows a slow and continuous decrease to the infrared wavelengths. For the shorter wavelengths of the ultraviolet, there is a steep decrease of the solar emission. The Fraunhofer absorption lines and absorption edges are superimposed on the ultraviolet continuum longward of 200 nm. Below 200 nm, the emission lines from the major species H, He and minor solar atmospheric species under the non-local thermodynamic equilibrium (non-LTE) conditions of the transition region and corona strongly influence the solar continuum and are very sensitive to the Sun's magnetic activity. The solar fluxes in Panel (a) of Figure 5.2 are from the Solar Irradiance Platform V2.38 (SIP V2.38), which is a database for the solar flux at Earth. A detailed description is found in the next Section. The solar fluxes in Panel (a) show, that the emission lines are more dominant than the continuum below than 130 nm.

The variation of the Sun's radiation depends on the observed frequency and occurs on all time-scales. The causes for the solar radiation variance are divided into extrinsic and intrinsic effects. Extrinsic effects are i.) radiation changes due to the planets position on its orbit (e.g. apocenter and pericenter) and ii.) radiation changes due to changes in the planetary field of view of the Sun due to the non-uniform distribution of the Sun's active regions. The first effect is illustrated in Panel (b) of Figure 5.2. The middle panel shows the integrated SIP V2.38 1 nm resolution photon flux up to 95 nm at the Mars position (detailed calculation description below). The planet-Sun distance variation between perihelion of 1.381 AU and aphelion of 1.666 AU causes large variations in the solar flux available at the Mars position. The second effect is not included, because SIP V2.38 provides fluxes for Earth and no regular observations of the solar flux at Mars is available before the arrival of the MAVEN spacecraft in the end of 2014. Intrinsic effects

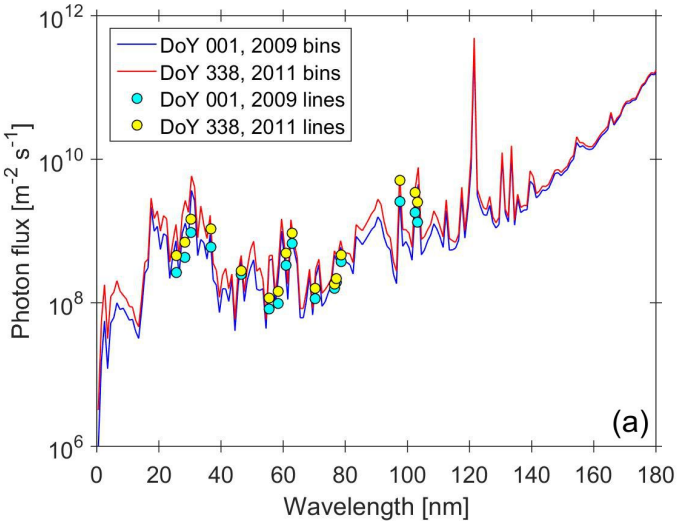

Figure 5.2: (a) SIP V2.38 solar photon flux in 1 nm bin resolution and bright solar lines from the 39 wavelength resolution at Earth for low (DoY 001, 2009) and high (DoY 338, 2011) solar activity. (b) Integrated SIP V2.38 solar flux up to 95 nm for Earth, integrated and time/distance calibrated solar flux for the Mars position and the radio emission 10.7 cm wavelength (F10.7 index) for Earth (which is a widely used indicator of the solar activity level). The light gray blocks indicate the MaRS occultation seasons, the dark gray lines the 266 observations in the $MaRS_{quiet}$ data set. The dashed lines indicate the lower and upper Φ_{SUM} and Φ_{EARTH} boundaries of Table 5.4.

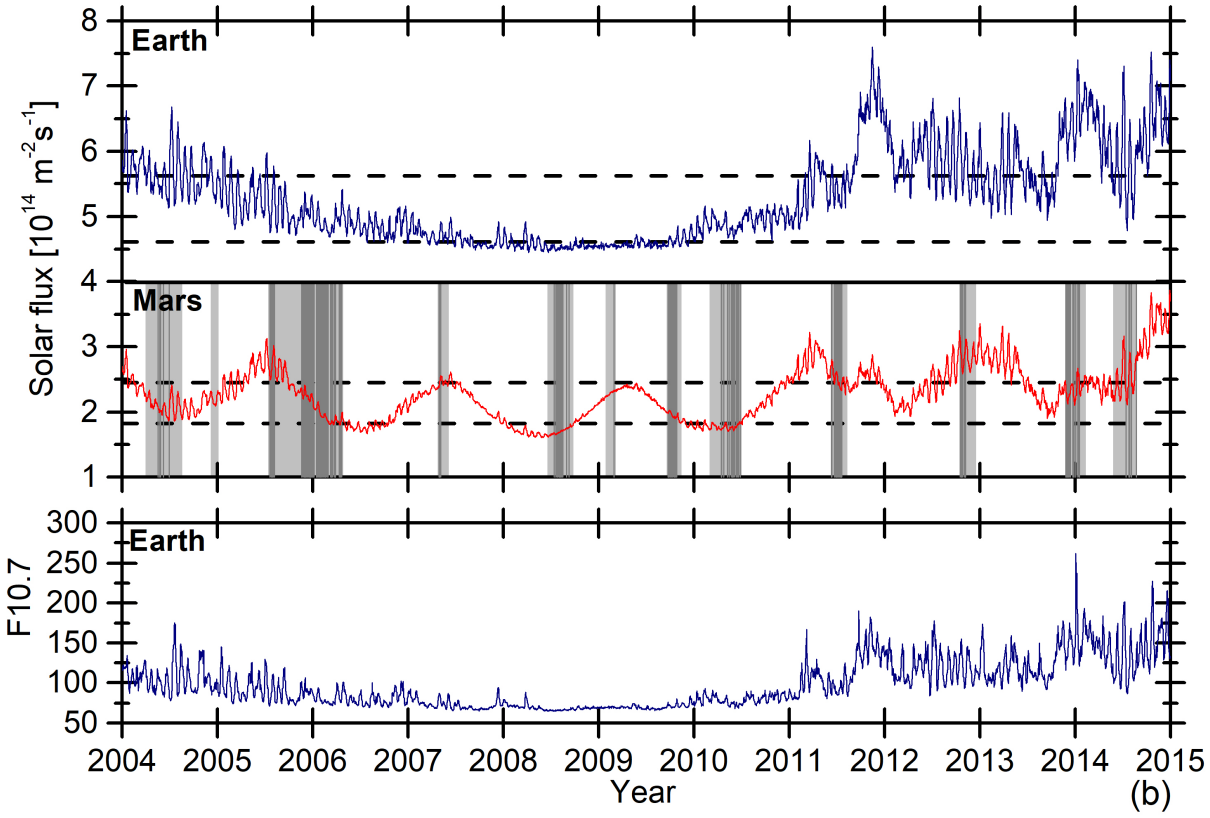

are caused by the Sun's internal processes. Their variation depends on the physical processes which trigger the radiation change. Long term variations are caused by the solar flux cycle. These variations are caused by the Sun's magnetic dynamo, whose full reversing cycle is approximately 22 years. Due to the fact, that the Sun's solar flux depends on the magnitude of its magnetic field and not on the orientation, the solar flux cycle is approximately 11 years, half the cycle of the Sun's magnetic dynamo. The effect of the solar cycle on the solar flux at Earth is illustrated in Panel (a) of Figure 5.2. The SIP V2.38 solar photon fluxes up to 180 nm in the 1 nm resolution with indicated fluxes in the bright solar lines from the 39 wavelengths resolution are given for Earth at solar minimum (DoY 001, 2009) and maximum (DoY 338, 2011) conditions. Medium term radiation variations are caused by the differential solar rotation with a mean of 27 days. Modulation of this effect are caused by the modification (appearance/disappearance) and slow evolution of the solar active regions over few months. Due to an increase in the number of active regions during solar maximum, the caused variation is higher during that time span. Short term variations are caused by solar eruption processes, e.g. solar flares, whose duration can be minutes to hours. *Woods and Rottman* (2002) give a variability of 15 % and less for solar radiation larger than 160 nm, a variability of 15 % - 70 % between 160 nm and 65 nm and a factor of 1.5 to 7 between 65 and 1 nm. The magnitude of the 27-day rotation is usually not more then 1/3 of the solar cycle variability and the solar flux variation along the Mars orbit is approx 16 %. The Sun's coronal emissions vary most, followed by the transition region emissions, the variations in the chromosphere and finally the variations of the photosphere with only 0.1 % for the longest UV wavelengths. This is caused by the increase in temperature and decrease in atmospheric density with increasing altitude and their associated instabilities. Solar radiation with wavelengths lower than 20 nm are dominated by emissions of the Sun's corona, e.g. from flares. The NOAA Geostationary Operational Environmental Satellites (GOES[3]) measurements in the 0.1 - 0.8 nm range observe several flares per month with an increase in solar irradiance by factors of 100 to 1000. *Hathaway* (2015) indicates the relation between the solar activity (sunspot number) and the occurrence rate of X- and M-class solar flares. The number of X- and M-class flares has a tendency to follow the sunspot number with more flares at the declining phase of the solar cycle. *Aschwanden* (1994) used the 0.5 - 0.8 Å soft X-ray monitored by GOES to investigate the behavior of the solar background X-ray and flares in solar cycle 21 and 22 ($\sim$ 1976 to 1993). He received the daily background flux from the GOES observations by either using the middle 8 hours of the day or interpolating from the other 16 hours to the middle of the day. A strong decrease in short X-ray background flux is found for low F10.7 and low monthly sunspot numbers compared to times of high solar activity. A lower number of flares ($>$ M1 class) is also found for those solar minimum activity conditions. *Gopalswamy* (2016) found a similar relationship between the low and high sun spot number and the SOHO rate of coronal mass ejections (CMEs) from 1996 -

[3]https://www.nasa.gov/content/goes

2015. Solar flares and coronal mass ejections are closely related and are both sources for solar energetic particles (SEPs).

5.1.2 Solar flux considered by the IonA models

The SIP data base (*Tobiska et al.*, 2000) provides historical, nowcast and forecast solar flux data and proxies for Earth with a publicly available resolution of one averaged data set per day with a variety of output model spectra with different resolutions. The SIP V2.38 data sets combine recent and current solar observations, e.g. from the Solar and Heliospheric Observatory SOHO (*Domingo et al.*, 1995) or the Solar EUV Experiment (SEE) on the Thermosphere Ionosphere Mesosphere Energetics Dynamics (TIMED) spacecraft (*Woods et al.*, 2005) with models of the solar spectral ranges. The solar photon flux ($photons/(s\,m^2\,\Delta\,\lambda)$) considered by the IonA models has a 1 nm resolution. For the validation of the IonA-2 model against the photo-chemical model of F. González-Galindo (GG-model - described in Chapter 6) the ASTM spectrum (static reference spectrum) is used. For computing the actual results in this work however, the VUV2002 FUV-UV spectrum is used, because it additionally contains the variability in the solar FUV (123 - 421 nm)[4]. For IonA-1, the upper wavelength limit is 95 nm, while for IonA-2 (see Chapter 6 for the detailed model descriptions) a wavelength range from 0.45 - 800 nm is used. Bright solar spectral emission lines at 256.3 Å (from *He II*, which is single ionized He, *Si X*), 284.15 Å (*Fe XV*), 303.31 Å (*Si XI*), 303.78 Å (*He II*), 368.07 Å (*Mg X*, *Mg VII*), 465.22 Å (*Ne VII*), 554.37 Å (*O IV*), 584.33 Å (*He I*), 609.76 Å (*Mg X*, *O IV*), 629.73 Å (*O V*), 703.36 Å (*O III*), 765.15 Å (*N IV*, *N III*), 770.41 Å (*Ne VIII*), 787.70 Å (*O IV*), 977.02 Å (*C III*), 1025.72 Å (*H I*) and 1031.91 Å (*O VI*) (*Warren et al.*, 1998; *Tian et al.*, 2008) are handled separately in both models. Their fluxes are taken from the SIP V2.38 39 wavelengths bin resolution. The lower wavelength border of 0.45 nm is chosen from the fact that the 1210 wavelength bin resolution (0.1 nm) (which will be used in a detailed calculation in Chapter 8) has no entries in the bins lower than 0.5 nm. The upper wavelength limit of 95 nm for IonA-1 is chosen, because the ionization potential of CO_2 with 13.777 eV[5] requires photons $<$ 90.04 nm. The upper wavelength border of 800 nm for IonA-2 is chosen, because not only photo-ionization processes but also the photo-dissociation of certain neutral molecules is considered in IonA-2 for which larger solar wavelengths are required.

As the solar flux output of the Sun is not isotropic, a correction of the SIP V2.38 solar flux at Earth in distance and time must be performed for each MaRS observation. The SIP V2.38 model provides the solar flux for Earth Φ_E. The solar flux input for IonA Φ_M is calculated for the planetary constellation at time t_{MARS}, the time when the radio sounding observations occurs at the planet. t_{MARS} defines $t_{SUN,rot}$, the time needed by

[4]recommended by Kent Tobiska, personal communication
[5]http://webbook.nist.gov

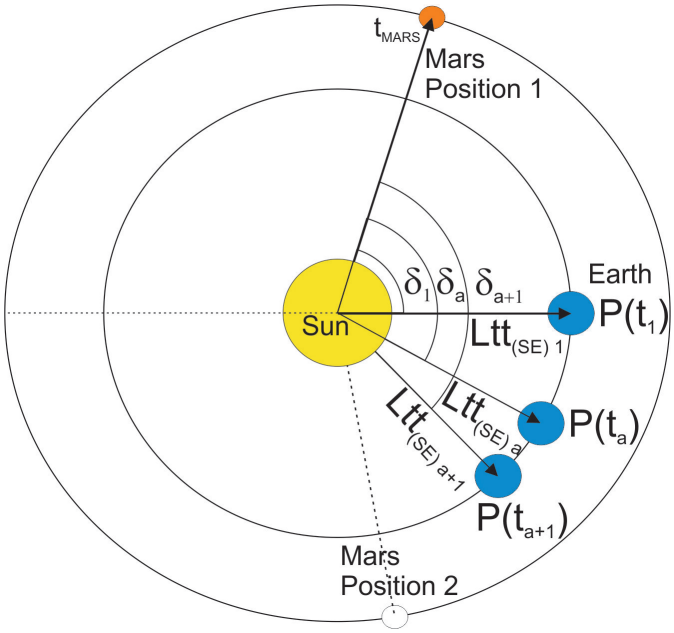

Figure 5.3: Iterative procedure for the determination of t_{EARTH}, the time where the SIP V2.38 solar flux is extracted for a given MaRS observations. The Figure is adapted from Peter *(2008).*

the Sun to rotate from the Earth position by the angle δ towards the planet position at t_{MARS}. $t_{SUN,rot}$ can be positive or negative, depending on the position of the Earth ahead (Mars Position 2) of or behind the planet (Mars Position 1). It is calculated with the space geometry information system SPICE[6] in an iterative procedure. Figure 5.3 illustrates the algorithm in which the position of Mars is fixed and the position of the Earth is varied, until t_{EARTH} - Ltt_{SE} + $t_{SUN,rot}$ + Ltt_{SM} = t_{MARS}, where Ltt_{SE} is the light time between Sun and Earth and Ltt_{SM} is the light time between Sun and Mars. The solar flux at t_{EARTH} is extracted from SIP V2.38 and calibrated to the actual Mars-Sun distance $r_{SUN,MARS}$ at the observation time

$$\Phi_M = \Phi_E \cdot \frac{(149,597,870,700m)^2}{r^2_{SUN,MARS}} \tag{5.3}$$

.

5.1.3 Definition of solar flux proxies and their boundaries for low, moderate and high solar proxy observations

The solar flux proxies are derived from the SIP V2.38 VUV2002 FUV-UV solar flux in 1 nm resolution. They are used as an easy way to categorize the MaRS ionospheric ob-

[6]development of NASA, the toolkit is freely available from
https : //naif.jpl.nasa.gov/naif/toolkit.html

	Integr. Range	Calibration	Units	low	moderate	high
Φ_{SUM}	0.45 - 95 nm	Mars	$[10^{14}\,s^{-1}m^{-2}]$	$\Phi < 1.83$	$1.83 \leq \Phi \leq 2.45$	$\Phi > 2.45$
Φ_{Xray}	0.45 - 10 nm	Mars	$[10^{12}\,s^{-1}m^{-2}]$	$\Phi < 2.09$	$2.09 \leq \Phi \leq 3.25$	$\Phi > 3.25$
$\Phi_{0.45\text{-}3nm}$	0.45 - 3 nm	Mars	$[10^{11}\,s^{-1}m^{-2}]$	$\Phi < 3.15$	$3.15 \leq \Phi \leq 4.95$	$\Phi > 4.95$
$\Phi_{0.45\text{-}1nm}$	0.45 - 1 nm	Mars	$[10^{10}\,s^{-1}m^{-2}]$	$\Phi < 6.99$	$6.99 \leq \Phi \leq 11.67$	$\Phi > 11.67$
Φ_{EARTH}	0.45 - 95 nm	Earth/none	$[10^{14}\,s^{-1}m^{-2}]$	$\Phi < 4.61$	$4.61 \leq \Phi \leq 5.63$	$\Phi > 5.63$

Figure 5.4: Boundaries for the solar flux proxies Φ_{SUM}, Φ_{Xray}, $\Phi_{0.45-1nm}$, $\Phi_{0.45-3nm}$ and Φ_{EARTH} calculated from the SIP V2.38 solar flux for the MaRS$_{quiet}$ data set observations.

servations for selected solar flux ranges. The solar flux proxies are derived by integrating certain SIP V2.38 solar flux ranges at the top of the planetary atmosphere. The solar flux integration boundaries for the solar flux proxies are given in Table 5.4. While Φ_{SUM}, Φ_{Xray}, $\Phi_{0.45-3nm}$ and $\Phi_{0.45-1nm}$ are integrated from the solar flux calibrated in time and distance for the Mars position, no calibration was done for Φ_{EARTH}.
Related solar flux proxies have been used by *Peter et al.* (2014) to show, that the magnitude of the M2 vertical TEC and main peak electron densities shows a positive correlation with the derived *SIP* solar flux at the Mars position. In this work, the low, moderate and high value proxy intervals are used to determine, if certain solar flux conditions during the MaRS observations provide a potential source for the merged excess electron densities. The dark gray lines in the middle plot in Panel (b) of Figure 5.2 show, that most of the MaRS observations used in this work are conducted during times of low solar flux at the Mars position. The solar proxy boundaries for the low, moderate and high value intervals are therefore not set in dependence of the solar flux variation during a full solar cycle, but in dependence of the SIP V2.38 solar flux associated with the MaRS$_{quiet}$ data set. This means, that low, moderate and high are no description of the real state of the Sun's activity, but a measure for the value of the solar proxy in relation to the solar proxies in the MaRS$_{quiet}$ data set.
The classical mean μ (see Eq. 4.3) and standard deviation σ (see Eq. 4.2) are calculated from all solar flux proxies for MaRS$_{quiet}$. For Φ_{SUM}, Φ_{Xray} and Φ_{EARTH}, $\Phi_{*,low}$ contains all those observations which are smaller than μ-σ, $\Phi_{*,mod}$ contains all observations for which the proxy value is found between μ-σ and μ+σ and $\Phi_{*,high}$ contains all observations for which the solar proxy is larger than μ+σ. For $\Phi_{0.45-3nm}$ and $\Phi_{0.45-1nm}$, $\Phi_{*,low}$ contains all those observations which are smaller than $\mu-0.5\cdot\sigma$, $\Phi_{*,mod}$ contains all observations for which the proxy value is found between $\mu-0.5\cdot\sigma$ and $\mu+0.5\cdot\sigma$ and $\Phi_{*,high}$ contains all observations for which the solar proxy is larger than $\mu+0.5\cdot\sigma$. The smaller boundaries are chosen for the $\Phi_{0.45-3nm}$ and $\Phi_{0.45-1nm}$ proxies due to their large variation, i.e. large

σ. The calculated boundaries for the solar proxy intervals are found in Table 5.4. Φ_{SUM} provides a measure for the variation of the solar flux range which is most important for the ionization of CO_2 at the Mars position. Φ_{Xray} is important for the M1 formation, while $\Phi_{0.45-3nm}$ and $\Phi_{0.45-1nm}$ cover the wavelength ranges which provide ionization close to the ionospheric base. Φ_{EARTH} is the solar flux at the top of the Earth atmosphere without further calibration. It provides a measure for the solar activity without the variation caused by the Mars orbit eccentricity.

5.2 The Mars Climate Database neutral atmosphere in ionospheric altitudes

The Mars Climate Database (MCD V5.2) is a database which contains statistical results of various model runs of a General Circulation Model (GCM) of the Mars atmosphere. The GCM is developed at the Laboratoire de Météorologie Dynamique du CNRS (Paris, France) in collaboration with the Open University (United Kingdom), Oxford University (United Kingdom) and the Instituto de Astrofisica de Andalucia (Spain). Additional support is given by the European Space Agency ESA and the Centre National d'Etudes Spatiales (CNES). The GCM is a 3-D model of the global atmospheric circulation of Mars. It includes physical processes as the radiative transfer through gas, dust and ice aerosols, the H_2O cycle, dust transport, and photochemical atmospheric, thermospheric and ionospheric composition calculations. The MCD V5.2 includes vertical profiles of the neutral temperature, pressure, atmospheric mass density and volume mixing ratios for CO_2, CO, O, O_2, O_3, H, H_2, N_2, Ar and the electron number density (*Forget et al.* (1999); *Millour et al.* (2015); *Forget et al.* (2015); *González-Galindo et al.* (2013)).
The atmospheric number densities n_s for the individual species s are computed from the ideal gas law (see e.g. (*Jacobson*, 2007))

$$n_N = \frac{p_N}{k_B T_N} \tag{5.4}$$

with the atmospheric density n_N, atmospheric pressure p_N, the Boltzmann constant k_B and the neutral atmospheric temperature T_N, in combination with the provided volume mixing ratios for each species s. The Mars Climate Database distinguishes five scenarios representing the atmospheric variability with dust load and with the solar cycle:

- "climatology" scenario
  Dust observations during Mars years without global dust storms (Mars year 24, 26, 27, 29, 30, 31 - 04/1999 to 07/2013) are combined and used for statistical studies on mean atmospheric behavior, day-to-day variability and large-scale variations. The Climatology scenario is available for low (MCDclim-low, F10.7 at Earth approx-

imately 70[7]), moderate (MCDclim-ave, F10.7 $\simeq$ 130) and high (MCDclim-high, F10.7 $\simeq$ 130) solar flux (*Forget et al.*, 2015; *Montabone et al.*, 2015).

- "cold" scenario
  The cold scenario (MCD-cold) contains an atmosphere with extremely low dust, topped by a thermosphere for low solar flux. As described in *Forget et al.* (2015), for every L_S, the model dust opacity at each planetary position is set to 50 % of the minimum observed during the Mars years 24 - 31. The thermosphere for this scenario is the low solar flux scenario (F10.7 $\simeq$ 70).

- "warm" scenario
  In the warm scenario (MCD-warm), the atmosphere is dusty, topped by a thermosphere for high solar flux. The dust opacity for every L_S at each planetary position is set to 150 % of the maximum observed values during the Mars years 24 - 31 (except for Mars years 25/28 global dust storms) (*Forget et al.*, 2015).

- "dust dtorm" scenario
  The dust storm scenario is available for solar longitudes ($180\,^\circ \leq L_S \leq 360\,^\circ$), when such phenomena are likely to happen on Mars. The optical depth is set to 5 for the whole planet. This scenario is available for low, moderate and high solar flux.

- "Mars Years" scenarios
  The Mars Years scenarios MY24 - MY31 (MCD-MY) contain the GCM model results for the planetary atmospheres of the associated Mars years. The scenarios include the day-to-day variability of the atmospheric dust load and solar flux.

All scenarios except the dust storm scenario (because it is a scenario for extreme atmospheric conditions) are used as input for IonA-1 and IonA-2. For each MaRS observation, the MCD V5.2 scenarios associated with the appropriate L_S, Ω_{lon}, Ω_{lat} and local time are extracted.

5.3 The Martian crustal magnetic field

The MGS-MAG/ER twin fluxgate magnetometer and electron reflection analyzer on board of MGS observed the small-scale crustal magnetic field in approximately 400 km altitude. The magnetic field data are binned into a $1\,^\circ$ grid over the Martian surface, where each bin contains a median of 14 measurement samples (*Connerney et al.*, 2001)[8].

[7] F10.7 itself is actually not used in the MCD V5.2, the value is only an approximation for the parametrized solar flux (*González-Galindo et al.*, 2005)

[8] The magnetic field vector data were downloaded from
http://mgs-mager.gsfc.nasa.gov/publications/grl_28_connerney/data/grl_28_connerney_map_data.txt

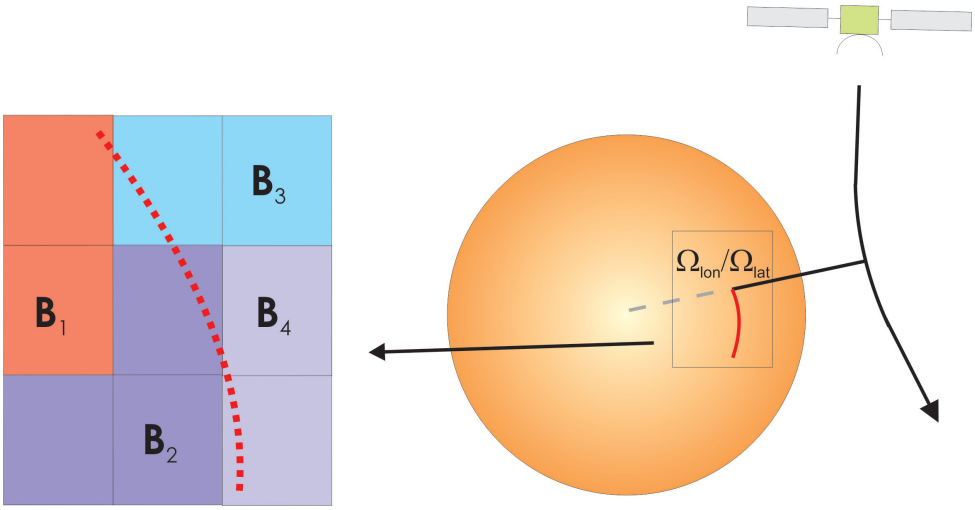

Figure 5.5: Illustration of the magnetic field parameter derivation for a MaRS observation from the movement of the footpoint over the surface of Mars. The Figure is adapted from Peter *(2008).*

As discussed earlier, the MaRS radio science observation is not completely vertical. Its footpoint, which is the intersection between the Martian surface and the vector between the Mars center and the point of closest approach of the radio-beam, is slightly moving during an occultation (illustrated in Figure 5.5). The strength of the magnetic field during a MaRS observation is estimated by i.) extracting the magnitudes of the crustal magnetic field for the footpoint coordinates when the radio ray is sounding the altitudes between 60 and 300 km above the areoid and ii.) determining the highest magnitude of the data set. The derived magnitudes of the crustal magnetic field are used to determine, if wind shear is a potential source for the merged excess electron densities (Chapter 7).

Chapter 6

Model development

Two one-dimensional models of the Mars ionosphere have been developed, Ionization in Atmospheres 1 (IonA-1) and 2 (IonA-2). IonA-1 is a fast steady-state model of the Mars dayside ionosphere. Its output are altitude profiles of the ionospheric O_2^+ and electron density for a certain solar zenith angle. It is used to estimate the error in the MaRS M1 layer detection method. IonA-2 is a further development of IonA-1. It is a time-marching photochemical model with a variable neutral-neutral and neutral-ion reaction scheme, minor neutral particle diffusion and ambipolar ion diffusion. IonA-2 provides altitude profiles of minor neutral densities and ion/electron densities for a full Martian Sol. The modeled neutral and ion densities will be compared with MaRS observations (Chapter 8) to investigate the role of O_2^+ and NO^+ in the formation of merged excess electron densities.

6.1 Theoretical background

This Section contains general information about the primary and secondary photo-production processes, chemical reactions and transport in the Mars upper neutral atmosphere and ionosphere. In addition, the operator splitting method for solving a system of 1-D photochemical reactions and transport equations is described.

6.1.1 Primary photo-production

The energy E_{ph}, wavelength λ and frequency ν of a photon are related by the Equation

$$E_{ph} = h_{Pl} \cdot \nu = h_{Pl} \frac{c}{\lambda} \tag{6.1}$$

with the Planck's constant h_{Pl} and the speed of light in vacuum c. The absorption of a photon by a molecule AB can initialize certain kinds of interactions depending on the

energy $h\nu$ of the photon

$$AB + h\nu \rightarrow A + B \qquad E_\lambda \geq E^s_{dt} \tag{6.2}$$
$$AB + h\nu \rightarrow AB^+ + e^- \qquad E_\lambda \geq E^s_{it} \tag{6.3}$$
$$AB + h\nu \rightarrow A + B^+ + e^- \qquad E_\lambda \geq E^s_{dit} \tag{6.4}$$
$$AB + h\nu \rightarrow AB^{++} + 2e^- \qquad E_\lambda \geq E^s_{Dit} \tag{6.5}$$
$$AB + h\nu \rightarrow A^+ + B^+ + 2e^- \qquad E_\lambda \geq E^s_{dDit}. \tag{6.6}$$

Photons with energies above the dissociation threshold E^s_{dt} of a species s dissociate a molecule by partly or fully breaking the bonds between the individual atoms (Eq. 6.2). Photons with energies above the species ionization threshold E^s_{it} can ionize atoms / molecules by producing free ion-electron pairs (Eq. 6.3). Photons with energies above the dissociative ionization threshold E^s_{dit} can cause dissociative ionization, where one or more of the molecule's fragments are ionized during the dissociation process (Eq. 6.4). Double ionization is possible for highly energetic photons with energies above the double ionization threshold E^s_{Dit} (Eq. 6.5) or the dissociative double ionization threshold E^s_{dDit} (Eq. 6.6). The total photon absorption by a species s at a certain wavelength λ is represented by its total photon absorption cross section $\sigma^s_{ta}(\lambda)$, which is assumed to be the sum of the total photo-dissociation σ^s_{td} and the total photo-ionization cross sections σ^s_{ti}. The calculation of radiative transfer through a gas is described by the Lambert-Beer law (*Schunk and Nagy*, 2009)

$$\Phi\left(h, \lambda, \chi\right) = \Phi_\infty\left(\lambda\right) e^{-\tau(h,\lambda,\chi)} \tag{6.7}$$

where $\Phi(h, \lambda, \chi)$ is the solar photon flux at wavelength λ for the solar zenith angle χ at altitude h and $\Phi_\infty(\lambda)$ is the solar photon flux for λ at the top of the atmosphere. τ is called the optical depth or thickness

$$\tau\left(h, \lambda, \chi\right) = \int_\infty^h \sum_s n_s\left(h\right) \cdot \sigma^s_{ta}\left(\lambda\right) dl_\lambda \tag{6.8}$$

where n_s is the number density of the neutral species s at altitude h and dl_λ is the incremental path length in the photon flux direction. dl_λ can be expressed as

$$dl_\lambda = -dh \cdot \mathrm{Ch}\left(h, \chi\right), \tag{6.9}$$

where $Ch\left(h, \chi\right)$ is the Chapman function for grazing incidence angle for a curved atmosphere. The function approaches $1/cos(\chi)$ for either a horizontally stratified atmosphere or if $\chi \rightarrow 0$. The fast numerical approach of *Smith and Smith* (1972) for $Ch\left(h, \chi\right)$ is used for the radiative transfer calculation in the IonA models.
The primary ion or neutral species u production $P^{pr}_{u,r}$ by reaction r from photo-dissociation, -ionization or dissociative ionization for solar zenith angle χ and at altitude h is given by

$$P^{pr}_{u,r}\left(\chi, h\right) = n_s\left(h\right) \int_0^{\lambda^s_{u,r}} \Phi\left(h, \lambda, \chi\right) \sigma^s_{ta} \cdot p^s_{u,r}\left(\lambda\right) d\lambda \tag{6.10}$$

where $\lambda^s_{u,r}$ is the dissociation, ionization or dissociative ionization threshold wavelength for species s in reaction r with the final state u, $\Phi(h,\lambda,\chi)$ is the number of available photons for wavelength λ at altitude h and solar zenith angle χ (calculated with Equation 6.7) and $p^s_{u,r}(\lambda)$ is the branching ratio for a given final ion/neutral state u of species s in reaction r for wavelength λ.
The total primary photo-production P^{pr}_u of species u is derived from the sum over all photo reactions r

$$P^{pr}_u(\chi,h) = \sum_r P^{pr}_{u,r}(\chi,h)\,. \tag{6.11}$$

The total primary electron production from photo-ionization P^{pr}_e used in IonA-1 is the sum of P^{pr}_u when only the ion species are considered.
The cross sections $\sigma^s_{raw}(\lambda)$ provided by a certain source are generally not available in the resolution of the solar flux bins provided by the SIP V2.38 database. Therefore the given cross sections need to be integrated to the correct flux bin width $\Delta\lambda$. The integration of the cross sections is done by the following steps

- Linear interpolation $\sigma^s_{eq}(\lambda)$ of the provided cross sections $\sigma^s_{raw}(\lambda)$ to an equidistant grid of $1\cdot10^{-4}$ Å, because the integration error of the trapezoidal numerical integration in the MATLAB[1] routine TRAPZ is smaller, if the input data are equidistant.
- Integration of the $\sigma^s_{eq}(\lambda)$ for the selected solar flux intervals by the MATLAB routine TRAPZ

  $$\sigma^s_x(\lambda,\Delta\lambda) = \frac{\int_{\Delta\lambda}\sigma^s_{eq}(\lambda)}{\Delta\lambda} \tag{6.12}$$

  where $\sigma^s_x(\lambda,\Delta\lambda)$ are the individual absorption, dissociation, ionization or dissociative ionization cross sections.

The cross sections for the bright solar lines are linear interpolated from the given $\sigma^s_{raw}(\lambda)$.

6.1.2 Electron impact ionization

Photoionization of a species can occur if the photon's energy E_{ph} is larger than the particle's ionization threshold E^s_{it}. The residual photon energy of the interaction is assumed to be carried by the electron due to the fact that its mass is much lower than that of the ion. Collision processes between the neutral atmospheric species and photo-electrons, e.g. for CO_2 (*Fox et al.*, 2009)

$$\begin{aligned} CO_2 + e^- &\rightarrow CO_2^+ + e^- + e^- \\ CO_2 + e^- &\rightarrow CO^+ + O + e^- + e^- \\ CO_2 + e^- &\rightarrow O^+ + CO + e^- + e^-, \end{aligned}$$

[1]The MATrix LABoratory (MATLAB) is a commercial software developed by MathWorks. The software is designed for solving numerical problems by the application of matrices.

can produce additional ion-electron pairs by electron-impact ionization if the residual energy carried by the electron is larger than the ionization threshold of ambient atmospheric species s. The detailed calculation of the ion and electron production from secondary impact ionization P_u^{sec} and P_e^{sec} is described in the correspondent IonA-1 and IonA-2 model section.

6.1.3 Chemical kinetic reactions

A detailed description of the following processes is found in *Jacobson* (2007). An elementary reaction is a chemical reaction without intermediate products. Where two bodies are involved, the elementary reaction is called bimolecular. For three bodies, a reaction is called termolecular. Those reactions mostly consist of pairs of bimolecular reactions with a third body M, which result in the given reaction equation. Examples for elementary bimolecular and termolecular collision reactions are

$$N + NO \rightarrow N_2 + O \qquad (ra)$$
$$O + O + M \rightarrow O_2 + M \qquad (rb)$$

Due to its high abundance in the Mars atmosphere, CO_2 is considered as third body M in the IonA-2 model. Chemical production rates $P_{u,r}^{rea}$ describe the change in the species number density over time for each individual reaction r. For the above reactions, they are written as

$$P_{N_2,ra}^{rea} = \frac{dn_{N_2}}{dt} = n_N \cdot n_{NO} \cdot k_{ra}$$
$$P_{O_2,rb}^{rea} = \frac{dn_{O_2}}{dt} = n_O \cdot n_O \cdot k_{rb}$$

with the N_2 and O production rates $P_{N_2,ra}^{rea}$ and $P_{O_2,rb}^{rea}$, the N, NO and O neutral number densities n_N, n_{NO} and n_O and the reaction coefficient k_r for each reaction r. k_{ra} is a bimolecular reaction coefficient, while k_{rb} is a termolecular reaction coefficient which already includes the third body's particle density n_{CO_2}.
The temperature dependence of the bimolecular reaction coefficient k_r is often estimated with the Arrhenius-equation

$$k_r = A_r \exp\left(-\frac{E_r}{R^* \cdot T}\right). \qquad (6.13)$$

A_r is the collisional or Arrhenius pre-factor, which is equal to the collision frequency multiplied by an efficiency factor. The activation energy E_r is the minimum energy which is required by the interacting particles to form an activated complex/transition state before forming the final reaction products. The temperature T is either the neutral T_N, ion T_i or electron temperature T_e, depending on the reacting bodies and R^* is the universal

gas constant. In reactions where E_r is close to zero, the Arrhenius pre-factor A_r becomes strongly dependent on the temperature. For those reactions Equation 6.13 changes to

$$k_r = A_r \left(\frac{300}{T}\right)^{B_r} \exp\left(-\frac{E_r}{R^* \cdot T}\right) \tag{6.14}$$

with the temperature factor B_r. If the temperature dependence of k_r is not known, k_r reduces to a single number.
Termolecular reactions are pressure dependent, because the third body number density [M] varies with the total pressure. Often, the pressure dependence of the reaction coefficient k_r is interpolated between a low-pressure limit $k_{0,T}$ and a high-pressure limit $k_{\infty,T}$

$$k_r = \frac{k_{\infty,T} k_{0,T}[M]}{k_{\infty,T} + k_{0,T}[M]} F_C^{\left[1+\left(\log_{10}\left(\frac{k_{0,T}[M]}{k_{\infty,T}}\right)\right)^2\right]^{-1}}. \tag{6.15}$$

where F_C is the so-called broadening factor (e.g. set to 0.6 in *Sander et al.* (2011)). Low and high pressure limits for the termolecular reaction coefficient calculations are often taken from *Sander et al.* (2011) in this work, where the low and high pressure limits are defined as

$$k_{0,T} = k_0(T) = k_0^{300} \left(\frac{T}{300}\right)^{-a} \tag{6.16}$$

$$k_{\infty,T} = k_\infty(T) = k_\infty^{300} \left(\frac{T}{300}\right)^{-b} \tag{6.17}$$

and k_0^{300}, k_∞^{300}, a and b are given.
The following reactions illustrate chemical processes of ionospheric impact (*Schunk and Nagy*, 2009)

$$CO_2^+ + O_2 \rightarrow CO_2 + O_2^+ \tag{6.18}$$

$$CO_2^+ + O \rightarrow O_2^+ + CO \tag{6.19}$$

$$O^+ + e^- \rightarrow O \tag{6.20}$$

$$O_2^+ + e^- \rightarrow O + O \tag{6.21}$$

$$N(^2D) + O_2 \rightarrow NO + O \tag{6.22}$$

$$N(^2D) \rightarrow N + h\nu. \tag{6.23}$$

Reactions 6.18 and 6.19 are examples for charge exchange processes. In simple charge exchange processes (r. 6.18), an electron is transferred from the neutral molecule or atom to the ion. Reaction 6.19 describes a more complex process, where the composition of both collision partners change during the collision. Reaction 6.20 and 6.21 describe recombination processes, which are important loss processes for ionospheric ions. Reaction

6.20 describes a simple recombination reaction (the inverse process to direct ionization), while 6.21 is an example for a dissociative recombination process, where the bond between the atoms is broken during the recombination process.
Reaction 6.22 and 6.23 are examples for excited state chemistry. Reaction 6.22 is a collisional de-excitation (also called quenching), while reaction 6.23 is called spontaneous emission, because a photon with the energy $h\nu$ is generated, when an electron of the excited atom, molecular or ion is falling on a lower energy level. As described in *Demtröder* (2010), molecules have four types of energy levels: translational, rotational, vibrational and electronic. Translational energy levels are very closely spaced, therefore the energy absorption into translational states (temperature increase) can be assumed to be continuous. The velocity of the molecules however leads to broadening of the absorption and emission lines by the Doppler shift. The rotational, vibrational and electronic transitions need certain quantized energies. The required photon energy increases from rotational transitions of the molecule, where the angular momentum around the molecule's rotation center changes, to vibrational transitions, where a combination of molecular bond stretching, angle bending and torsional motion occurs. The quantized photon energies needed for electronic transitions are even higher than that for the vibrational transitions. The Pauli principle states that an atomic state which is characterized by the set of four quantum numbers n_q, l_q, $m_{q,l}$ and $m_{q,s}$ can only be occupied by at most one electron. The principal quantum number n_q is always an integer. It defines the electronic shells of the atom. The innermost three shells are named K-shell for $n_q = 1$, L-shell for $n_q = 2$ and M-shell for $n_q = 3$. For every n_q, the angular momentum quantum number l_q can assume n_q possible values from 0 to (n_q-1). For each value of l_q, there are $2l_q + 1$ magnetic quantum numbers $m_{q,l}$ and for each $m_{q,l}$ two spin orientations with $m_{q,s}= \pm 1/2$ are possible. This yields

$$2 \cdot \sum_{l=0}^{n_q-1} 2l_q + 1 = 2n_q^2$$

positions for electrons with opposing spins. A short notation for the electronic state of an atom/molecule is given by

$$n_q^{2S_q+1} L_{q,J_q} \tag{6.24}$$

where S_q is the quantum number of the sum of all spins $\mathbf{S}_q$, L_q is the quantum number of the total angular momentum $\mathbf{L}_q$ (spin excluded) and J_q is the quantum number of the total angular momentum $\mathbf{J}_q = \mathbf{L}_q + \mathbf{S}_q$. For atoms, the quantum number L_q is replaced in Eq. 6.24 by latin letters, for molecules by greek letters, e.g.

- L= 0: S/Σ
- L= 1: P/Π
- L= 2: D/Δ.

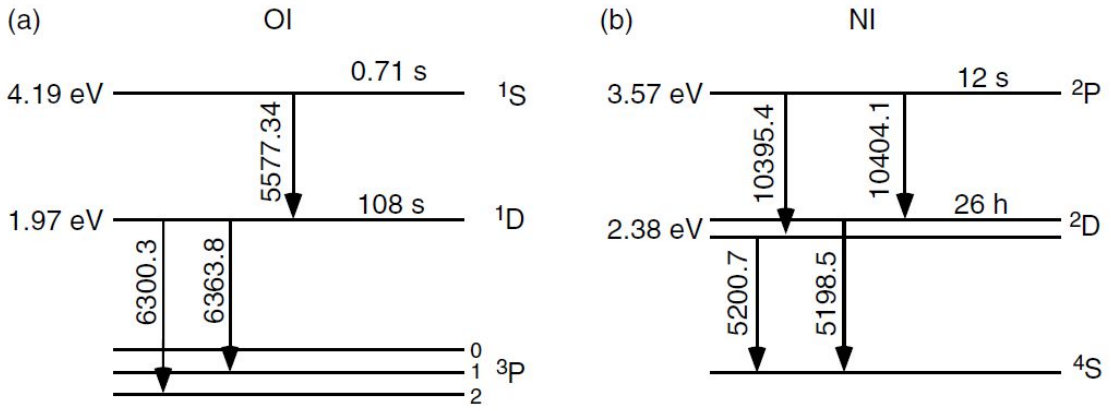

Figure 6.1: Low lying energy levels of (a) oxygen and (b) nitrogen. The energy levels are given in eV, while the photon energy emitted during the electron transition are given in Å. The Figure is taken from Schunk and Nagy *(2009).*

Figure 6.1 illustrates the low lying energy levels of oxygen and nitrogen. The neutral oxygen OI in the lowest energy state (ground state) is denoted $O(^3P)$, while the neutral nitrogen NI in the ground state is denoted $N(^4S)$. This notation is a shortened form of Relation 6.24 where n_q and J_q are neglected. The ground state atoms/molecules in this work are given without the electronic state description, additional terms are added for excited states only.

6.1.4 Transport of neutral and ion species in ionospheric heights

The Boltzmann equation (see e.g. Chapter 3 *Schunk and Nagy* (2009))

$$\frac{\partial f_s^B}{\partial t} + \mathbf{v}_s \cdot \nabla f_s + \mathbf{a}_s \cdot \nabla_v f_s = \frac{\delta f_s}{\delta t} \tag{6.25}$$

describes the temporal evolution $\partial f_s^B/\partial t$ of the velocity distribution function f_s^B of a species s under the influence of particle diffusion $\mathbf{v}_s \cdot \nabla f_s$, external forces $\mathbf{a}_s \cdot \nabla_v f_s$ and collisions $\delta f_s/\delta t$. The velocity distribution function $f_s^B(\mathbf{r}, \mathbf{v}_s, t)$ describes the number of particles of species s in a volume element d^3r at $\mathbf{r}$ with a velocity range d^3v_s about $\mathbf{v}_s$. $\mathbf{a}_s$ is the particle acceleration, ∇ is the Nabla or gradient operator in configuration space, while ∇_v is the gradient operator in velocity space. Equation 6.25 yields the base for different sets of transport equations. In a gas mixture which is dominated by collisions, f_s^B is driven to a Maxwelllian velocity distribution function. However, if collisions between similar particles are significant and the species in the gas have different drift velocities,

the velocity distribution function is driven to a local drifting Maxwellian function f_s^M

$$f_s^M(\mathbf{r}, \mathbf{v}_s, t) = n_s(\mathbf{r}, t) \left[\frac{m_s}{2\pi k_B T_s(\mathbf{r}, t)}\right]^{3/2} \cdot \exp\left\{-\frac{m_s\left[\mathbf{v}_s - \mathbf{w}_s(\mathbf{r}, t)\right]^2}{2k_B T_s(\mathbf{r}, t)}\right\} \tag{6.26}$$

at all positions and all times. n_s is the density of species s, m_s is the mass of the atom/molecule, T_s the temperature and $\mathbf{w}_s$ the drift velocity of species s. k_B is the Boltzmann constant. The 5-moment system of transport equations is basically derived from Equation 6.25 under the assumption of collision dominance for the velocity distribution function (Eq. 6.26). The name of the "5-moment" equation system relates to the number of parameters which are needed to describe each species in the gas: number density n_s (1 component), $\mathbf{w}_s$ drift velocity (3 components) and temperature T_s (1 component).
When it is assumed, that the velocity distribution functions of all species are described by drifting Maxwellians, stress and heat flow effects are zero in the calculations and the pressure tensor is diagonal and isotropic. Those closing conditions in combination with the species collision terms yield the 5-moment system of transport equations which consist of the continuity, momentum and energy equation for species s in interaction with other species u

$$\frac{\partial n_s}{\partial t} + \nabla \cdot (n_s \mathbf{w}_s) = 0 \tag{6.27}$$

$$n_s m_s \frac{D_s \mathbf{w}_s}{Dt} + \nabla p_s - n_s m_s \mathbf{g} - n_s q_s \left[\mathbf{E} + \mathbf{w}_s \times \mathbf{B}\right] = \sum_u n_s m_s \nu_{su} \Phi_{su} (\mathbf{w}_u - \mathbf{w}_s) \tag{6.28}$$

$$\frac{D_s}{Dt}\left(\frac{3}{2} p_s\right) + \frac{5}{2} p_s (\nabla \cdot \mathbf{w}_s) = \sum_u \frac{n_s m_s \nu_{su}}{m_s + m_u} \left[3k_B (T_u - T_s) \Psi_{su} + m_u (\mathbf{w}_s - \mathbf{w}_u)^2 \Phi_{su}\right]. \tag{6.29}$$

$D_s/Dt = \partial/\partial t + \mathbf{w}_s \cdot \nabla$ is the convective derivative, $\mathbf{g}$ the gravity acceleration, p_s is the pressure of species s, q_s is the charge of the species, $\mathbf{E}$ is the electric field, while $\mathbf{B}$ is the magnetic field. ν_{su} is the momentum transfer collision frequency, Φ_{su}^c and Ψ_{su}^c are velocity dependent correction factors, which are different for different collision processes. The momentum equation 6.28 yields the base for the transport of minor atmospheric neutrals by minor neutral diffusion and ambipolar diffusion of plasma.

Transport of minor neutral species

The main vertical transport process for neutral species in the Martian atmosphere is diffusion. *Poling et al.* (2001) describes diffusion as the net transport of material within a

single phase. Diffusion can result from gradients in pressure, temperature, external forces and species concentration. The 1-D relation between the diffusion flux $n_s \cdot w_s$ and the concentration gradient in z-direction of species s with the assumption, that the flux vector of species s has only a z-component ($w_s = w_{sz}$), is described by Fick's first law (see e.g. *Prölss* (2004))

$$n_s w_s = -D \cdot \frac{dn_s}{dz} \tag{6.30}$$

with the diffusion coefficient D. The 5-moment momentum equation 6.28 provides an approximation for the physical description of the two most important neutral diffusion processes in the lower and upper atmosphere of Mars, eddy diffusion and molecular diffusion. As described in *Prölss* (2004), the general composition of the lower atmosphere is dominated by the eddy diffusion. Eddy diffusion is a mathematical construct, which describes the mixing of the lower atmosphere by turbulent motion of air parcels in the form of a diffusion process. The eddy diffusion leads to a homogenization of the lower atmospheric composition and can be described in the form of Equation 6.30 with the eddy diffusion coefficient K. In the upper atmosphere, molecular diffusion becomes the dominant process. The low collision rates in the upper atmosphere in combination with an equilibrium between the downward flux caused by gravity and the expansion flux caused by molecular diffusion, allow each species to decay with its own individual scale height. The coefficient for molecular diffusion of species s is denoted D_s. The homopause region, where both effects are approximately equally strong has been found at Mars at $\sim 130\,km$ altitude for certain environmental conditions (see Chapter 2 and *Mahaffy et al.* (2015a)).

The mathematical approach for diffusion differs if the density of the modeled species is either comparable to or small compared to the whole atmospheric density at a certain altitude. For a comparable density, the diffusion process in the upper atmosphere is described by major diffusion (see e.g. mathematical approach of *Vlasov and Davydov* (1982)), while the diffusion of small number densities are described by minor molecular diffusion. Since major diffusion is not yet implemented in IonA-2, the following derivations relate to minor molecular diffusion. The minor molecular diffusion approximation is applicable, when the velocities of the neutral atmospheric species are small and show only a slow variation with time. This means, that waves are not considered in the diffusion approximation $\partial \mathbf{w}_s / \partial t \rightarrow 0$ and that the species flux needs to be subsonic $\mathbf{w}_s \cdot \nabla \mathbf{w}_s \rightarrow 0$. Under these circumstances, the convective derivative $D_s/Dt = \partial/\partial t + \mathbf{w}_s \cdot \nabla$ is neglected. The 1-D vertical minor neutral diffusion flux in the z-direction is derived from the momentum equation 6.28 of the 5-moment equation system for multiple gases. The equation is derived under the assumptions, that i.) the diffusion approximation is valid, ii.) the electron and magnetic field have no effect on the neutral species and iii.) there is only a small relative drift between the species ($\Phi^c_{su} = \Psi^c_{su} = 1$) and iv.) that the flux vectors of

species s and u have only a z-component ($w_s = \mathbf{w}_{sz}$, $w_u = \mathbf{w}_{uz}$). This yields

$$\frac{\partial p_s}{\partial z} - n_s m_s g = -\sum_{u \neq s} m_s n_s \nu_{su} (w_s - w_u)$$

$$n_s w_s = -\frac{1}{\sum_{u \neq s} m_s \nu_{su}} \left(\frac{\partial p_s}{\partial z} + n_s m_s g - \sum_{u \neq s} m_s n_s \nu_{su} w_u \right) \tag{6.31}$$

with $g = \mathbf{g}_z$. Defining the minor molecular diffusion coefficient D_s^m for species s

$$D_s^m = \frac{k_B T_s}{\sum_{u \neq s} m_s \nu_{su}}, \tag{6.32}$$

inserting Equation 6.32 into 6.31 and applying the ideal gas law $p_s = n_s k_B T_s$ yields

$$\begin{aligned} n_s w_s &= -\frac{D_s^m}{k_B T_s} \left(\frac{\partial p_s}{\partial z} + n_s m_s g - \sum_{u \neq s} m_s n_s \nu_{su} w_u \right) \\ &= -D_s^m \left(\frac{\partial n_s}{\partial z} + \frac{n_s}{T_s} \frac{\partial T_s}{\partial z} + n_s \frac{m_s g}{k_B T_s} - \frac{1}{k_B T_s} \sum_{u \neq s} m_s n_s \nu_{su} w_u \right). \end{aligned} \tag{6.33}$$

The collision term on the right side of the equation is set to zero, because the collision frequency ν_{su} is small.
The species velocity from eddy diffusion w_s^K in z-direction with the vertical eddy diffusion coefficient ($K = \mathbf{K}_z$) is

$$w_s^K = -K \frac{1}{n_s/n_N} \frac{\partial (n_s/n_N)}{\partial z} = -K \left(\frac{1}{n_s} \frac{\partial n_s}{\partial z} - \frac{1}{n_N} \frac{\partial n_N}{\partial z} \right) \tag{6.34}$$

where n_N is the neutral atmospheric density. The balance between the gravitational force and pressure gradient is the hydrostatic relation

$$\frac{dp}{dz} + n_N < m > g = 0 \tag{6.35}$$

where $< m >$ is the average atmospheric mass $< m >= \sum_s n_s m_s / n_N$. Replacing n_N in Equation 6.34 by Equation 6.35 and applying the ideal gas law for the neutral atmospheric density $p_N = n_N k_B T_N$ yields

$$n_s w_s = -K \left(\frac{\partial n_s}{\partial z} + \frac{n_s}{T_N} \frac{\partial T_N}{\partial z} + n_s \frac{< m > g}{k_B T_N} \right) \tag{6.36}$$

Combining the species flux from molecular diffusion (Eq. 6.33) with neglected collision term and the species flux from eddy diffusion (Eq. 6.36) yields

$$n_s w_s = -\left(K + D_s^m\right) \frac{\partial n_s}{\partial z} - n_s \left[K \left(\frac{< m > g}{k_B T_N} + \frac{1}{T_N} \frac{\partial T_N}{\partial z} \right) + D_s^m \left(\frac{m_s g}{k_B T_s} + \frac{1 + \beta_{corr}}{T_s} \frac{\partial T_s}{\partial z} \right) \right]. \tag{6.37}$$

β_{corr} is a correction factor to account for thermal diffusion of light species, which is used by *Colegrove et al.* (1966). In IonA-2 it is -0.25 for H and H_2 and otherwise zero.
The eddy diffusion coefficient is not well known in the Mars atmosphere (*Krasnopolsky*, 1986). The amplitudes of gravity waves in absence of dissipation increase with height as $1/\sqrt{n_N(h)}$. Due to the fact, that the gravity waves are involved in the atmospheric mixing, this relation is used for the calculation of K

$$K(h) = \frac{\zeta}{\sqrt{n_N(h)}}. \tag{6.38}$$

ζ is a pre-factor which is close to $1.4 \cdot 10^{13}$ for Venus, Mars and Earth, following the discussion in *Krasnopolsky* (1986) and *von Zahn et al.* (1980). This expression is similar to that used in *Fox* (2015).
The minor molecular diffusion coefficient D_s^m for the diffusion of species s through other gases u is calculated following *Colegrove et al.* (1966)

$$D_s^m = \frac{\sum_u n_u}{\sum_{u \neq s} \frac{n_u}{D_{su}^b}}, \tag{6.39}$$

where n_u is the gas number density of species u and D_{su}^b the binary diffusion coefficient. The binary diffusion coefficient D_{su}^b is calculated from the expression provided in Chapter 11 of *Poling et al.* (2001) and has been originally developed by Chapman and Enskog (e.g. (*Chapman and Cowling*, 1939))

$$D_{su}^b = \frac{3}{16} \frac{(2\pi k_B T_N / M_{su})^{1/2}}{n \pi \sigma_{su}^2 \Omega_D} f_D, \tag{6.40}$$

where T_N is the neutral temperature, because it is assumed, that all neutral species have similar temperatures. $M_{su} = M_s \cdot M_u/(M_s + M_u)$ is the reduced molecular/atomic weight of species s and u, M_s and M_u are the associated molecular/atomic weights, n is the number density of molecules/atoms in the mixture, σ_{su} is the characteristic length of the intermolecular force law between s and u, Ω_D is the collision integral for diffusion and f_D is the correction term for the molecular diffusion. f_D is in the order of unity if M_s and M_u are in the same order of magnitude. The value is between 1.0 and 1.1, if the masses of the molecules/atoms are very unequal and the light component is available only in trace amounts (*Marrero and Mason*, 1972). f_D is assumed to be 1 during the IonA-2 calculations. The intermolecular force law used in IonA-2 for the calculation is the 12-6 Lennard-Jones potential. The Lennard-Jones potential describes the interaction between uncharged and chemically unbound neutral atoms and molecules. The intermolecular energy between atoms/molecules Ψ^{lj} is described by

$$\psi^{lj}(r) = 4\epsilon^{lj} \left[\left(\frac{\sigma^{lj}}{r} \right)^{12} - \left(\frac{\sigma^{lj}}{r} \right)^{6} \right]. \tag{6.41}$$

r is the radial distance between the two particles, ϵ^{lj} is the characteristic energy, σ^{lj} the characteristic length in the Lennard-Jones potential. The parameters for the interaction between s and u are determined from the following expressions

$$\epsilon^{lj}_{su} = \left(\epsilon^{lj}_{s}\epsilon^{lj}_{u}\right)^{1/2} \qquad \sigma^{lj}_{su} = \frac{\sigma^{lj}_{s} + \sigma^{lj}_{u}}{2}. \tag{6.42}$$

An approximation for the collision integral for diffusion Ω_D is provided by *Neufeld et al.* (1972)

$$\Omega_D = \frac{A_1}{(T^*)^{A_2}} + \frac{A_3}{exp\,(A_4 T^*)} + \frac{A_5}{exp\,(A_6 T^*)} + \frac{A_7}{exp\,(A_8 T^*)} \tag{6.43}$$

with the values for T^* and A_x

$$T^* = k_B T_N/\epsilon^{lj}_{su} \qquad A_1 = 1.06036 \qquad A_2 = 0.15610$$
$$A_3 = 0.19300 \qquad A_4 = 0.47635 \qquad A_5 = 1.03587$$
$$A_6 = 1.52996 \qquad A_7 = 1.76474 \qquad A_8 = 3.89411$$

Plasma transport

As described in Chapter 5 and 11 of *Schunk and Nagy* (2009), ambipolar diffusion is the transport of ions and electrons together as a single gas under the influence of gravity, density and temperature gradients. Major ambipolar diffusion describes the movements of ions which are in the same order of magnitude as the available electron density. They are important for maintaining the plasma neutrality. Minor ambipolar diffusion describes the movements of ions, which are available in trace amounts in the ionosphere compared to the electron density. The major ambipolar diffusion used in this work is derived from momentum equation 6.28 the 5-moment approximation. In the derivation of the 1-D major diffusion equation, the diffusion approximation is used (no wave phenomena and subsonic flow). In addition, charge neutrality (where the electron density n_e equals the ion density n_i) and zero currents are assumed. Heat flow and stress effects are neglected similar to the derivation of the minor molecular diffusion. The ionosphere is assumed as unmagnetized, therefore $\mathbf{B}$ is neglected. $\mathbf{E}$ in Equation 6.28 is the small polarization electrostatic field which develops between the electrons and the ions due to a very slight charge separation. Its treatment is also neglected in the derivation of the ambipolar diffusion equation. Considering all the assumptions yields for the 1-D ambipolar diffusion equation

$$n_s w_s = -D^a_s \left[\frac{\partial n_s}{\partial z} + n_s\left(\frac{m_s g}{2k_B T_p} + \frac{1}{T_p}\frac{dT_p}{dz}\right)\right], \tag{6.44}$$

where D^a_s is the ambipolar diffusion coefficient for species s and T_p= $(T_i + T_e)/2$ is the plasma temperature. D^a_s is calculated from

$$D^a_s = \frac{2k_B T_p}{m_s \nu^{coll}_s}. \tag{6.45}$$

In IonA-2, ν_s^{coll} for species s is calculated as the sum of the neutral-ion ν_s^{in}, ion-ion ν_s^{ii} and ion-electron ν_s^{ie} collision frequencies. For the calculation of the elastic ion-neutral collision frequencies, Maxwell molecule collisions are applied. When the neutral approaches the ion, the neutral becomes polarized and the interaction potential between the two particles is that of an ion with an induced dipole. This yields for each ion i (after Eq. 9.73 and 9.40 of *Banks and Kockarts* (1973))

$$\nu_i^{in} = \sum_n \frac{m_n}{m_n + m_i} 2.6 \cdot 10^{-9} n_n \sqrt{\frac{\alpha_n^{pol}}{m_{red}}} \tag{6.46}$$

where the index n denotes the atmospheric neutral species. m_i and m_n are the ion and neutral species masses, n_n is the number density of the neutral species in cm^{-3}, α_n^{pol} is the polarizability of the neutral n in $10^{-24}\,cm^3$ and $m_{red} = (m_i m_n)/(m_i + m_n)$ is the reduced mass in amu. The neutral polarizabilities for IonA-2 were taken from *Mason and McDaniel* (1988).
For the ion-ion collisions, Coulomb interactions between the ions are relevant. The average ion-ion collision frequency for momentum transfer for each ion i with ions j in IonA-2 is taken from Eq. 4.140 of *Schunk and Nagy* (2009) in combination with Eq. 9.40 of *Banks and Kockarts* (1973))

$$\nu_i^{ii} = \sum_j \frac{m_j}{m_i + m_j} \frac{16\sqrt{\pi}}{3} \frac{n_j m_j}{m_i + m_j} \left(\frac{2 k_B T_{red}}{m_{red}} \right)^{-3/2} \frac{q_i^2 q_j^2}{m_{red}^2} \ln(\Lambda). \tag{6.47}$$

The species masses m_i and m_j are in g, n_j in cm^{-3}. The Boltzmann constant k_B is needed in $cm^2\,g\,s^{-2}\,K^{-1}$. $ln(\Lambda)$ is the Coulomb logarithm, the factor by which collisions with a small incidence angle are more efficient than large-angle collisions. It is ~ 15 for ionospheres (*Schunk and Nagy*, 2009). q_i and q_e are the ion and electron charges in esu. m_{red} is the reduced mass in g and $T_{red} = (m_i T_j + m_j T_i)/(m_i + m_j)$ is the reduced temperature in K.
The average ion-electron collision frequency for momentum transfer (Eq. 9.111 of *Banks and Kockarts* (1973)) yields

$$\nu_i^{ie} = \frac{4\sqrt{2\pi}}{3} \left(\frac{n_i q_e^4}{(k_B T_e)^{3/2} \sqrt{m_e}} \right) \ln(\Lambda). \tag{6.48}$$

The ion density n_i is in cm^{-3}, the electron mass m_e in g and the the electron charge q_e in esu.

6.1.5 Solving the 1-D continuity equation

The vertical 1-D continuity equation in the 5-moment approximation (Eq. 6.27) is

$$\frac{\partial n_u}{\partial t} + \frac{\partial}{\partial z}(n_u w_u) = P_u^{tot} - L_u^{tot}, \tag{6.49}$$

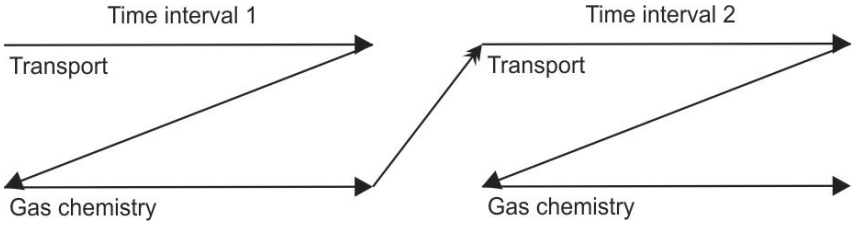

Figure 6.2: Illustration of the operator splitting method. Designed after Figure 6.1 in Jacobson *(2007)*

.

with the total photochemical production P_u^{tot} and total photochemical loss L_u^{tot} of species u. Equation 6.49 is solved in IonA-2 with the operator splitting method described in *Jacobson* (2007) and illustrated in Figure 6.2. Instead of solving the transport part and the photochemical part simultaneously, the processes are calculated in a sequential manner for each time step. The input parameters at the begin of the first time step are provided into the transport scheme. After the transport calculation for time step 1, the results are passed on to the photochemical scheme, which is solved for the same time step 1. The final results from time step 1 are then passed as input parameters into time step 2. The following Sections describe the calculation of the individual photochemical and transport schemes in IonA-2.

Solving the system of photo-chemical reactions

Without transport, the photochemical part of the continuity equation (Eq. 6.49) reduces to

$$\frac{\partial n_u}{\partial t} = P_u^{tot} - L_u^{tot}. \tag{6.50}$$

Equation 6.50 is a homogeneous differential equation of degree and order 1. A homogeneous differential equation has no separate term involving the independent variable (here time t). Due to the fact, that transport is neglected in the above equation, it is an ordinary differential equation (ODE). Its order is the highest derivative rank of the equation, while the degree is determined as the largest polynomial exponent of the highest order equation derivative (*Jacobson*, 2007). In an atmosphere/ionosphere with N species, chemical processes occur simultaneously between all available species. Therefore Equation 6.50 needs to be solved for N species simultaneously. This yields a system of N homogeneous differential equations, where P_u^{tot} and L_u^{tot} for each species u consist of the sums of the individual production and losses by the applied reactions. This system of ODEs has known initial densities for the N species at $t = 0$ and is therefore an initial value problem.

The overall lifetime τ_A^s of species s is defined as (*Jacobson*, 2007)

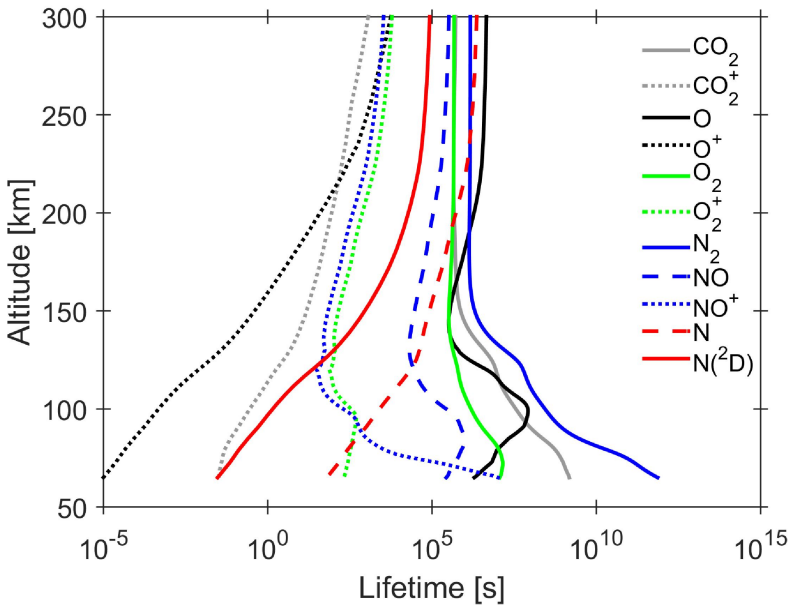

Figure 6.3: Lifetimes of selected species in the Mars atmosphere calculated with the IonA-$2_{var,flux}$ model setting for DoY 336 (2005) after six hours model run time.

$$\tau_A^s = \frac{1}{\frac{1}{\tau_{A,r1}^s} + ... + \frac{1}{\tau_{A,rN}^s}} \tag{6.51}$$

where $\tau_{A,r1}^s$ to $\tau_{A,rN}^s$ represent the e-folding lifetimes of species s (the time in which the original density of species s is reduced to $1/e$) in the individual loss reactions $r1$ to rN. The individual e-folding lifetimes of species s from each loss reaction depend on the kind of the reaction. For unimolecular reactions of species s, bimolecular reactions of species s with species v and termolecular reactions between species s, v and w, the following equations are used

$$\tau_{A,r1}^s = \frac{1}{k_{r1}} \tag{6.52}$$

$$\tau_{A,r2}^s = \frac{1}{n_v \cdot k_{r2}} \tag{6.53}$$

$$\tau_{A,r2}^s = \frac{1}{n_v \cdot n_w \cdot k_{r3}} \tag{6.54}$$

where n_v and n_w are the initial densities of species v and w. If the lifetimes of the species in a photochemical model differ by orders of magnitudes, the system of ODEs is called stiff. Certain ODE solver methods are better suited then others to cope with stiff photochemical systems. Figure 6.3 illustrates, that the system of ODEs for the

Mars atmosphere/ionosphere with the included reactions is a stiff ODE system due to the lifetime variations of several orders of magnitudes. The system of ordinary differential equations in this work is therefore solved with the Matlab function ODE15S, which is a solver for stiff ODEs.
The used version of the ODE15S is based on the Gear's method (*Gear*, 1971), for which *Jacobson* (2007) gives a good introduction. ODE solvers are based on explicit, implicit or semi-implicit time-stepping methods. In an explicit time-stepping procedure the newly calculated values, e.g. the number densities of the atmospheric species at time t are calculated from already existing values (e.g. from $t - \Delta t$, $t - 2\Delta t$). In implicit methods, additional and initially unknown terms at time t are solved in combination with the wanted variables. Explicit ODE solvers are not well suited for solving stiff problems. Their time step is limited by the species with the shortest lifetime. Larger time steps may lead to a destabilization of the ODE solution. Stiff ODEs are often and efficiently solved with semi-implicit methods, which are based on calculations for the actual time step, the start of the actual time step and sometimes additionally include the solutions at earlier time steps. The ODE15S solver is based on Gear's method, which is semi-implicit. Gear's method solves the backward differentiation formula (BDF). For that, the discretized first derivation of the individual species densities (denoted here as $\hat{n}$, which stands for the individual densities n_u of all species u))

$$\frac{d\hat{n}_t}{dt} \approx \frac{\hat{n}_t - \sum_{j=1}^{g} \alpha_{g,j} \cdot \hat{n}_{t-j\Delta t}}{\Delta t \cdot \beta_g}$$

$$0 \approx \Delta t \cdot \beta_g \frac{d\hat{n}_t}{dt} - \hat{n}_t + \sum_{j=1}^{g} \alpha_{g,j} \cdot \hat{n}_{t-j\Delta t} \tag{6.55}$$

yields the basis for the backward differentiation formula of order g. The values for the scalars $\alpha_{g,j}$ and β_g depend on the order g of the BDF method. Equation 6.55 is iteratively solved by replacing the left term of the equation by the predictor matrix $\boldsymbol{P}_t$ at time t and iteration m

$$\boldsymbol{P}_t \Delta\hat{n}_{t,m} = \Delta t \cdot \beta_g \frac{d\hat{n}_{t,m}}{dt} - \hat{n}_{t,m} + \sum_{j=1}^{g} \alpha_{g,j} \hat{n}_{t-j\Delta t}$$

$$\boldsymbol{P}_t \Delta\hat{n}_{t,m} = \hat{B}_{t,m} \tag{6.56}$$

where $\Delta\hat{n}_{t,m} = \hat{n}_{t,m+1} - \hat{n}_{t,m}$ and $d\hat{n}_{t,m}/dt$ is the first derivation of $\hat{n}_t$ at time t and iteration m. $\Delta\hat{n}_{t,m}$ in Eq. 6.56 is calculated with matrix decomposition/backsubstitution for each iteration m, which allows the calculation of $\hat{n}_{t,m+1}$. Updates of $\hat{B}_{t,m}$ for each iteration and regularly for $\boldsymbol{P}_t$ finally result in $\Delta\hat{n}_{t,m} \approx 0$. The convergence of the procedure is checked with a local and a global error test. The local error test is repeated after every iteration

with a normalized root-mean-square error (NRMS)

$$NRMS_{t,m} = \sqrt{\frac{1}{N}\sum_{u=1}^{N}\left(\frac{\Delta n_{u,t,m}}{R_{tol}n_{u,t,1} + A_{tol,t}}\right)^2} \tag{6.57}$$

where $\Delta n_{u,t,m}$ is the particle density change of species u at time step t for iteration m, N is the number of active species in the photochemical system, R_{tol} and A_{tol} are the relative and absolute error tolerance of the iteration procedure. $n_{u,t,1}$ is the number density of species u at the iteration start of the time step t. R_{tol} provides control of the procedure error relative to $n_{i,t,1}$. The absolute error tolerance A_{tol} provides control against fixed number densities. The local error test is passed, if $NRMS_{t,m}$ falls below a certain value which depends on the order of the method g. If the local error test does eventually not succeed after some iterations, the time step of the procedure is reduced until $NRMS_{t,m}$ falls below the defined value. After passing the local error test, a global error test is performed with a cumulative normalized root-mean-square error

$$NRMS_t = \sqrt{\frac{1}{N}\sum_{u=1}^{N}\left(\frac{\sum_m \Delta n_{u,t,m}}{R_{tol}n_{u,t,1} + A_{tol,t}}\right)^2} \tag{6.58}$$

where $\sum_m \Delta n_{u,t,m}$ is the sum of the changes in species u particle density during time step t. The $NRMS_t$ border value for the global error test is also dependent on the order of the method g. If the global error test does not succeed, the time step of the method is reduced. After every few successful time steps, the time step width and order of the method are newly estimated and updated.

Solving the system of transport equations

The solution for the 1-D system of transport equations is achieved in the operator splitting scheme by omitting the photochemical terms in the continuity equation 6.50

$$\frac{\partial n_u}{\partial t} = -\frac{\partial}{\partial z}\left(n_u w_u\right). \tag{6.59}$$

The calculation of the minor molecular diffusion and ambipolar diffusion are both based on Equation 6.59. For minor molecular diffusion, the flux term $n_u w_u$ is replaced by Equation 6.37, while for ambipolar diffusion Equation 6.44 is applied. Inserting Equation 6.37 into Equation 6.59 and assuming $T_u = T_N$ for all species u yields a second-order, parabolic, partial differential equation

$$\frac{\partial n_u}{\partial t} = J_1\frac{\partial^2 n_u}{\partial z^2} + J_2\frac{\partial n_u}{\partial z} + J_3 n_u \tag{6.60}$$

with the J_x parameters

$$J_1 = K + D_u^m \tag{6.61}$$

$$J_2 = \frac{\partial K}{\partial z} + \frac{\partial D_u^m}{\partial z} + K\left(\frac{1}{H_N} + \frac{1}{T_N}\frac{\partial T_N}{\partial z}\right) + D_u^m\left(\frac{1}{H_u} + \frac{1+\beta_{corr}}{T_N}\frac{\partial T_N}{\partial z}\right) \tag{6.62}$$

$$\begin{aligned} J_3 = &- K\left[-\frac{\partial}{\partial z}\left(\frac{1}{H_N}\right) + \frac{1}{T_N^2}\left(\frac{\partial T_N}{\partial z}\right)^2 - \frac{1}{T_N}\frac{\partial^2 T_N}{\partial z^2}\right] + \frac{\partial K}{\partial z}\left[\frac{1}{H_N} + \frac{1}{T_N}\frac{\partial T_N}{\partial z}\right] \\ &- D_u^m\left[-\frac{\partial}{\partial z}\left(\frac{1}{H_u}\right) + \frac{1+\beta_{corr}}{T_N^2}\left(\frac{\partial T_N}{\partial z}\right)^2 - \frac{1+\beta_{corr}}{T_N}\frac{\partial^2 T_N}{\partial z^2}\right] \\ &+ \frac{\partial D_u^m}{\partial z}\left[\frac{1}{H_u} + \frac{1+\beta_{corr}}{T_N}\frac{\partial T_N}{\partial z}\right]. \end{aligned} \tag{6.63}$$

Equation 6.60 is solved with an implicit and stable numerical method described in Appendix O of *Schunk and Nagy* (2009). For the solution of the second order differential equation, one set of initial conditions (the initial n_u density) and two boundary conditions (the flux $n_u w_u$) need to be applied.
The altitude range for the model is discretized into a set of vertical grid points with a width of Δz. The spatial derivatives in Equation 6.60 are replaced by space-centered spatial derivatives, while the time derivative is replaced by a forward time derivative

$$\frac{\partial^2 n}{\partial z^2} = \frac{n_{j+1}^{t+\Delta t} - 2n_j^{t+\Delta t} + n_{j-1}^{t+\Delta t}}{(\Delta z)^2} \tag{6.64}$$

$$\frac{\partial n}{\partial z} = \frac{n_{j+1}^{t+\Delta t} - n_{j-1}^{t+\Delta t}}{2(\Delta z)} \tag{6.65}$$

$$n = n_j^{t+\Delta t} \tag{6.66}$$

$$\frac{\partial n}{\partial t} = \frac{n_j^{t+\Delta t} - n_j^t}{\Delta t} \tag{6.67}$$

where t is the current time and $t + \Delta t$ the future time step, j is the grid index, which increases from lower model border to the upper border of the model. The species index u is omitted for clarity. Inserting these expressions into Equation 6.60 yields

$$-I_j^1 n_{j-1}^{t+\Delta t} + I_j^2 n_j^{t+\Delta t} - I_j^3 n_{j+1}^{t+\Delta t} = S_j^t \tag{6.68}$$

with the parameters I^x and S_j^t

$$I_j^1 = 1 - \frac{\Delta z}{2}\frac{J_2(j)}{J_1(j)} \tag{6.69}$$

$$I_j^2 = 2 + \frac{(\Delta z)^2}{(\Delta t)\, J_1(j)} - \frac{(\Delta z)^2\, J_3(j)}{J_1(j)} \tag{6.70}$$

$$I_j^3 = 1 + \frac{\Delta z}{2}\frac{J_2(j)}{J_1(j)} \tag{6.71}$$

$$S_j^t = \frac{(\Delta z)^2\, J_4(j)}{J_1(j)} + \frac{(\Delta z)^2}{(\Delta t)\, J_1(j)} n_j^t. \tag{6.72}$$

Equation 6.68 in combination with the flux boundary conditions is then iteratively solved for the future time step $t + \Delta t$ with the matrix decomposition algorithm described in *Schunk and Nagy* (2009) and yields the future densities $n_u^{t+\Delta t}$ for all species u. The transport equation for ambipolar diffusion is solved in a similar way.

6.2 IonA-1

IonA-1 (Ionization in Atmospheres 1) is a one-dimensional photochemical model of the Martian dayside ionosphere. The ionospheric calculations are conducted based on database inputs of the solar flux (SIP V2.38) and neutral atmosphere (MCD V5.2) from 50 to 250 km altitude. Included effects are the primary ionization of the neutral atmosphere by solar radiation and secondary ionization by a parameterized electron impact ionization. Dissociative recombination of O_2^+ is the included loss process for the generated ions. No transport effects are taken into account. This limits the usable altitude range of the model from the bottom of the ionosphere up to 160 km altitude, where the time between chemical reactions is short enough to neglect plasma transport. It is assumed, that the neutral temperature T_N, ion temperature T_i and electron temperature T_e are equal. Due to the underlying databases for solar flux and neutral atmosphere, environmental conditions can be easily changed in IonA-1 (e.g. changing solar flux by solar cycle/zenith angle or the neutral atmosphere at a certain longitudinal/latitudinal position of the planet). This allows a flexible modeling of the long MaRS observation periods with their changing environmental conditions. Another advantage of IonA-1 is the short model run time of a few seconds per ionospheric profile. The software architecture for IonA-1 is illustrated in Figure 6.4, a summary of the model parameters is found in Table 6.1.

6.2.1 Input parameters

For each MaRS observation, the observation time t_{MARS}, solar longitude L_S, planetary longitude Ω_{lon}, latitude Ω_{lat}, solar zenith angle χ and local solar time LST are extracted

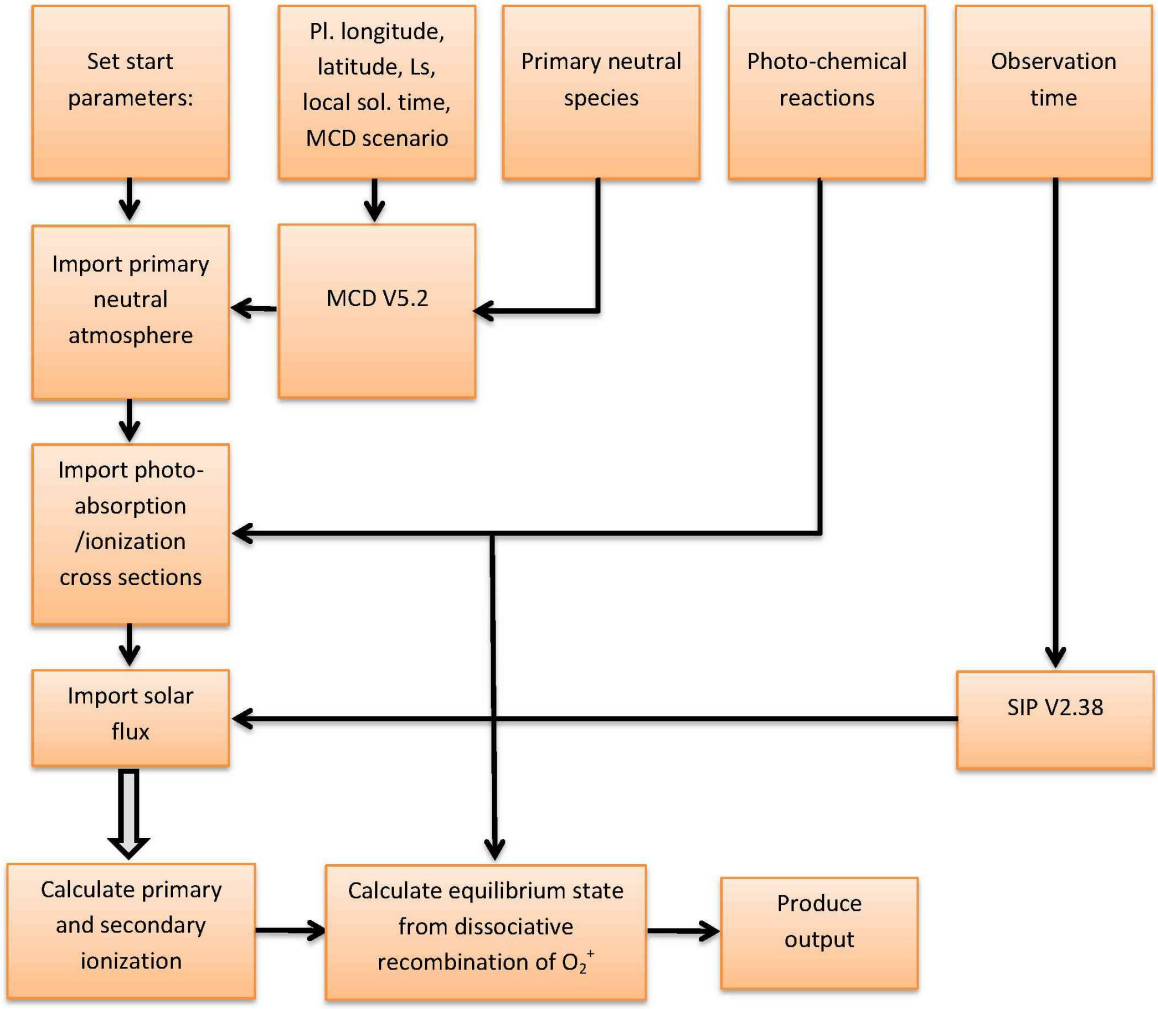

Figure 6.4: Flow diagram for the IonA-1 ionospheric model

	IonA-1	IonA-2 con validation	IonA-2 var/con
Model description	1-D steady-state model 50 - 160 km altitude adjustable altitude resolution	1-D time-marching model exit condition: passed model time 80 - 200 km altitude adjustable altitude resolution	1-D time-marching model exit condition: convergence/passed model time 65 - 300 km altitude adjustable altitude resolution
Planetary parameters	t_{MARS} and planetary coordinates derived from the selected MaRS observation	Ω_{lon}=0°, Ω_{lat}=0°, $L_S \simeq$15°	Planetary coordinates derived from the selected MaRS observation
Primary species	**MCD V5.2:** CO_2, N_2, O	**GG_2013:** CO_2, N_2, O_3, O, H_2O, O_2, H, Ar, CO, H_2, OH, HO_2, H_2O_2, O(^{1}D), N, N(^{2}D), NO, CO_2^+, O_2^+, O^+, CO^+, C^+, N_2^+, N^+, NO^+, H^+, HCO_2^+	**MCD V5.2:** CO_2, N_2, O_3, O, H_2O, O_2, H, Ar, CO, H_2
Temperature	$T_N = T_i = T_e$ T_N from MCD V5.2	$T_N = T_i$ from GG_2013 T_e: Rohrbough et al., (1979)	$T_N = T_i$ T_e: Rohrbough et al., (1979)
Solar flux	SIP V2.38 VUV2002 FUV-UV spectrum calibrated for the position of Mars at t_{MARS}	SIP V2.37 ASTM spectrum for DoY 012, 2004 calibrated for the position of Mars when L_S = 15°	SIP V2.38 VUV2002 FUV-UV spectrum calibrated for the position of Mars at t_{MARS}
Photo-absorption/-dissociation and -ionization cross sections	λ>5 nm: Schunk and Nagy (2009) λ<5 nm: Avakyan et al., (1999) ions are assumed to be directly converted into O_2^+	photo cross sections from Hubner and Mukherjee (2015) for all species except for O_3 (Sander et al., (2011)), CO_2 and N_2, references for the latter two species are found in the text	photo cross sections from Hubner and Mukherjee (2015) for all species except for O_3 (Sander et al., (2011)), CO2 and N2, references for the latter two species are found in the text
Secondary ionization	W-value approach (Wedlund et al., (2011))	Secondary ionization efficiency (Nicholson et al., (2009))	W-value approach (Wedlund et al., (2011))
Chemical reaction scheme	Dissociative recombination of O_2^+	**Reaction scheme 1:** detailed list in Table C.1 - C.4 in Appendix C	**Reaction scheme 2:** detailed list in Table C.5 - C.15 in Appendix C
Transport	None	None	Minor molecular diffusion and ambipolar diffusion
Time step	None - steady state	150 s	60 s

Table 6.1: Summary of the IonA-1 and IonA-2 input parameters and specifications

for that projected planetary surface position, when the sounded altitude above the areoid is 130 km (as described in Chapter 4). t_{MARS} is used to calculate the time t_{EARTH}, for which the solar flux between 0.45 and 95 nm in 1 nm resolution with separate bright solar lines is extracted from the SIP V2.38 data base and calibrated to the planetary position (details in Chapter 5). The MCD V5.2 CO_2, N_2 and O neutral densities and neutral temperature T_N from the selected database scenario yield the neutral atmosphere for the ionospheric calculations. The altitude resolution of the neutral atmospheric density and temperature is 0.2 km, calculated by MCD V5.2 internal interpolation routines. The altitude resolution of IonA-1 is likewise 0.2 km from 50 to 250 km altitude above the areoid.

6.2.2 Photochemical reaction scheme

The total photo-absorption σ^s_{ta} and -ionization σ^s_{ti} cross sections for CO_2, N_2 and O are taken from *Schunk and Nagy* (2009) between 5 and 95 nm (5 nm bin resolution with separate bright solar lines) and from *Avakyan et al.* (1998) below 5 nm (integrated to a resolution of 1 nm bins with Equation 6.12). No further branching ratios $p^s_{u,r}(\lambda)$ for differentiated ion states or dissociative ionization are applied. It is assumed that all produced ions from CO_2, N_2 and O are directly converted into the production of O_2^+. This assumption is based on the most important reactions in the Mars ionosphere for CO_2 (*Schunk and Nagy*, 2009)

$$CO_2 + h\nu \rightarrow CO_2^+ + e^- \tag{6.73}$$
$$CO_2^+ + O \rightarrow O_2^+ + CO \tag{6.74}$$
$$\rightarrow O^+ + CO_2 \tag{6.75}$$
$$O^+ + CO_2 \rightarrow O_2^+ + CO \tag{6.76}$$
$$O_2^+ + e^- \rightarrow O + O, \tag{6.77}$$

where ions other than O_2^+ are converted into this species. In addition, the reaction cycle of *Krasnopolsky* (2002)

$$CO_2 + h\nu \rightarrow CO^+ + O + e^- \tag{6.78}$$
$$\rightarrow C^+ + O_2 + e^- \tag{6.79}$$
$$C^+ + CO_2 \rightarrow CO^+ + CO \tag{6.80}$$
$$CO^+ + CO_2 \rightarrow CO_2^+ + CO. \tag{6.81}$$

shows, that additional products of the dissociative photo-ionization of CO_2 are also converted into O_2^+. Reaction 6.76 also yields a sink for the O^+ produced by the photo-ionization of O. However, the ion densities measured by the retarding potential analyzers on the Viking landers (*Hanson et al.*, 1977) in Figure 2.13 show, that the dayside ionospheric main peak of Mars consists mainly of O_2^+, with a smaller amount of CO_2^+. This

means, that not all CO_2^+ ions are converted into O_2^+. The remaining CO_2^+ mostly affects the ionospheric region at and slightly above the main peak. In addition, the dissociation/ionization model processes of N_2 yields small amounts of NO^+ in the lower ionosphere instead of O_2^+ (see model results of *Fox* (2015) and *González-Galindo et al.* (2013) in Figure 2.13). The assumption of $T_N = T_i = T_e$ changes the appearance of the electron density profile at that altitude, where the electron temperature and ion temperatures significantly deviate from the neutral temperature. These deviations are investigated in the more elaborated reaction scheme of IonA-2. No effects of double ionization are included in IonA-1.
In IonA-1, the solar flux $\Phi(h, \lambda, \chi)$ at altitude h is derived from the integration of the optical depth τ (Eq. 6.8) of the Lambert-Beer law (Eq. 6.7) by the trapezoidal numerical integration Matlab routine TRAPZ. Due to the discretization of the given SIP V2.38 solar flux into 1 nm bins, the primary O_2^+ production $P^{pr}_{O_2^+}$ in Equation (6.11) and (6.10) reduce to

$$P^{pr}_{O_2^+}(\chi, h) = \sum_s n_s(h) \sum_0^{\lambda^s_{u,r}} \Phi(h, \lambda, \chi)\, \sigma^s_{ti}(\lambda)\, d\lambda \tag{6.82}$$

for $s = CO_2$, N_2 and O.
The secondary ionization in IonA-1 is calculated by the W^s_E-value approach. Other descriptions for the W^s_E-value are the average energy loss per produced ion-electron pair or the mean energy per ion-electron pair. W^s_E is defined by

$$W^s_E = \frac{E^s_e}{< N_{pair} >} \tag{6.83}$$

where E^s_e is the energy of the photo-electron derived from the photoionization of species s and $< N_{pair} >$ is the average number of produced ion-electron pairs. As shown in Table 1 of *Wedlund et al.* (2011), the variation in the experiment and model values of W^s_E for the different species is quite large. The authors however present a sophisticated modeling approach for the W^s_E-value calculation for several species by applying a 1-D model of the TRANS-* family to solve the kinetic transport Boltzmann equation for suprathermal electrons, including electron/ion backscattering during the precipitation calculations. Among other species, they provide W^s_E-values for CO_2, N_2 and O in dependence of the photo-electron energy E^s_e. The secondary electron production $P^{sec}_{e,r}$ for the species CO_2, N_2 and O in IonA-1 is calculated in three steps

- The available energy distributions of the individual photo-electrons is derived by subtracting the energy of the first ionization potential E^s_{ip} of species s from the photon energy E_{ph} of the given interval center wavelengths λ (0.75 nm, 1.5 nm, 2.5 nm, ..., 94.5 nm)

$$E^s_e(\lambda) = E_{ph}(\lambda) - E^s_{ip}. \tag{6.84}$$

The lowest center wavelength is set to 0.75 nm instead of 0.5 nm, because as discussed in Chapter 4, the SIP V2.38 1210 wavelength (0.1 nm resolution) contains no flux in the 0.1 - 0.4 nm bins.

- In the next step, a mean value $W_E^{av}(h)$ is derived for each altitude h

$$W_E^{av}(h) = \frac{\sum_s n_s(h) \cdot W_E^s}{\sum_s n_s(h)} \tag{6.85}$$

- The total secondary electron production P_e^{sec}(h) at altitude h is then derived by the sum over all secondary ionization reactions r (one reaction available for each species s)

$$P_e^{sec}(h) = \sum_r \sum_\lambda P_{e,r}^{pr}(\lambda, h) \frac{E_e^s(\lambda)}{W_E^{av}(h)}. \tag{6.86}$$

This results in the total electron production by photo-ionization in dependence of the altitude above the areoid h

$$P_e(h) = P_e^{pr} + P_e^{sec}. \tag{6.87}$$

Under the assumption, that i.) the ionosphere consists of one dominant species O_2^+, ii.) the ionosphere is in equilibrium ($P_{O_2^+}^{tot} = L_{O_2^+}^{tot}$), iii.) the O_2^+ density is equal to the electron density e^- and iii.) the dissociative recombination of O_2^+ (Eq. 6.21) is the only loss process Equation 6.50 yields

$$P_{O_2^+}^{tot} = L_{O_2^+}^{tot} = n_{O_2^+} \cdot n_e \cdot k_r \tag{6.88}$$

$$P_e^{tot} = L_e^{tot} = n_e \cdot n_e \cdot k_r \tag{6.89}$$

$$n_e = \sqrt{\frac{P_e^{tot}}{k_r}} \tag{6.90}$$

where k_r is the reaction coefficient for dissociative recombination of O_2^+ (*Alge et al.*, 1983)

$$k_r = 1.95 \cdot 10^{-13} \left(\frac{T_{a,e}}{300}\right)^{-0.7} [m^3/s]. \tag{6.91}$$

where it is assumed, that T_e is equal to T_N.

6.2.3 Application

Figure 6.5 shows the IonA-1 results for the MaRS observation of DoY 348 (2005) based on the MCD-MY scenario. Panel (a) contains the altitudes, where the solar flux at a certain wavelength λ reaches $1/e$, while Panel (b) contains the comparison between the IonA-1 results and the MaRS observation. While most of the solar radiation is absorbed

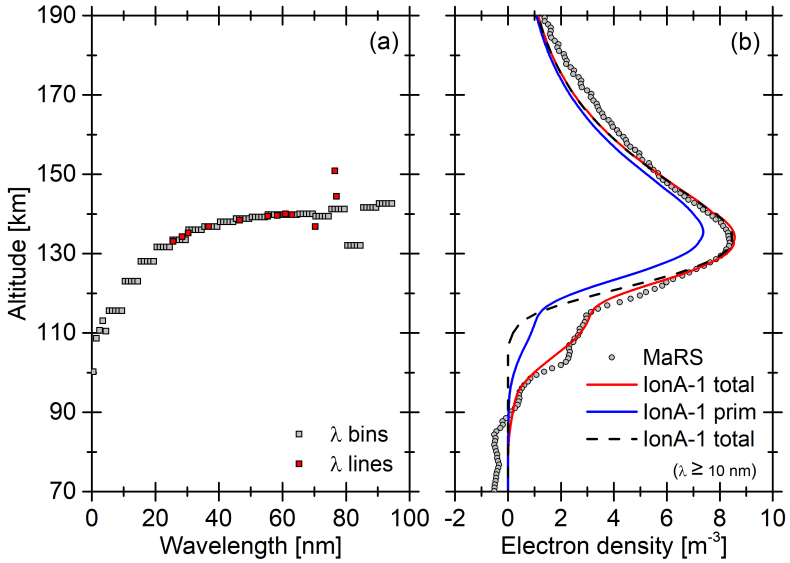

Figure 6.5: IonA-1 results for the MaRS DD observation of DoY 348, 2005 with L_S= 340.28°, Ω_{lon}= 70.10°, Ω_{lat}= 65.85° *and* χ= 74.90°. *(a) Altitude where* τ= 1 *(Eq. 6.7) for the solar bins and lines of SIP V2.38. (b) IonA-1 electron density derived from the primary electron production* P_e^{pr} *only (blue) and total electron production* $P_e^{tot}(\chi, h)$ *(red). The dashed line is the IonA-1 total electron density derived without solar wavelengths below 10 nm.*

in the main peak region, the M1 layer is mainly produced by solar radiation below 10 nm. Due to the absorption of the high energetic photons, secondary ionization is the major effect in the lower ionosphere. The steps in the τ= 1 altitudes for every five 1-nm-bins (for $\lambda \geq 10nm$) are caused by the photo-absorption/-ionization cross sections of *Schunk and Nagy* (2009), which are available in bins of 5 nm width. Even if the resolution of IonA-1 solar flux is 1 nm, the resolution of the cross section causes a clustering of the τ= 1 altitudes at certain heights.

The steady-state and single ion (O_2^+) IonA-1 model is sufficient for estimating the general ionospheric behavior in dependence of changing environmental conditions and for a rough error estimate of the M1 parameters derived from the MaRS data set. Its computational speed of few seconds per ionospheric profile enables the user to derive and compare ionospheric model results for many different observing conditions. IonA-1 is, however, not sufficient for modeling the processes possibly responsible for the small scale disturbances of the lower ionosphere. This is conducted with the IonA-2 model.

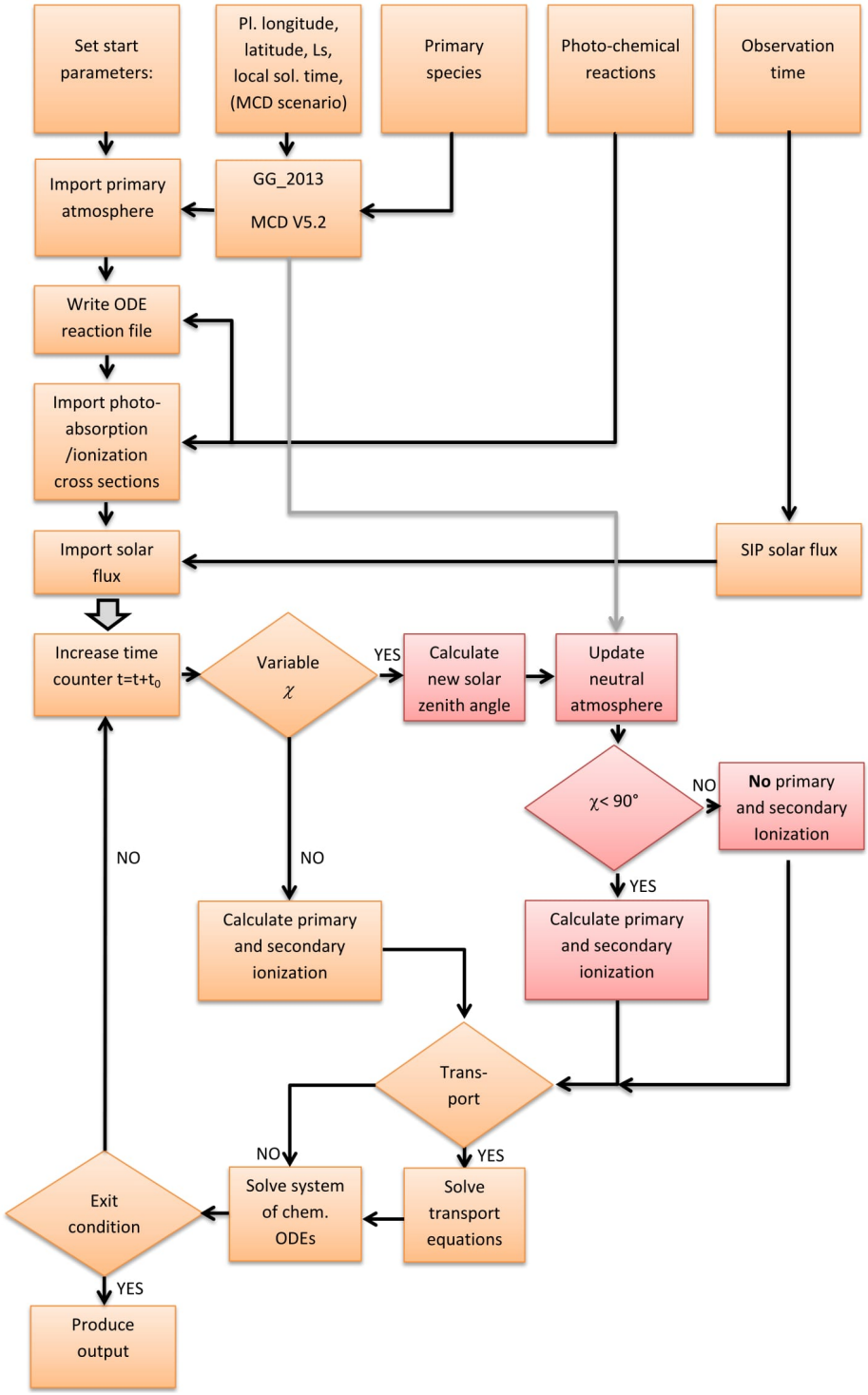

Figure 6.6: Flow diagram for IonA-2. Orange elements illustrate the IonA-2$_{con}$ core algorithm without external changes of the neutral atmosphere and solar flux. The combination of orange and red panels shows the flow diagram for IonA-2$_{var}$, where the neutral atmosphere/solar flux input changes over model run-time.

6.3 IonA-2

IonA-2 is a 1-D time-marching photochemical model for the Mars upper atmosphere and ionosphere from 65 - 300 km altitude. It includes a complete day-night photochemical cycle in combination with minor neutral diffusion and ambipolar transport processes. The flow diagram of the main IonA-2 features in Figure 6.6 illustrates the two available processing modes. The convergence mode (IonA-2_{con}) is illustrated by the orange elements. They represent the essential core algorithm of IonA-2, where the initial input solar flux and neutral atmosphere do not change during the model run. Exit conditions for the IonA-2_{con} model are either the convergence at a pre-selected local time or reaching a pre-set model run-time. IonA-2_{con} is basically used for the validation of the IonA-2 core algorithm. The combination of the orange and red elements in the flow diagram describes the variable (IonA-2_{var}) mode. IonA-2_{var} starts with initial solar flux and neutral atmospheric conditions for a given planetary longitude, latitude and local time. Exit conditions are also convergence at a certain solar time or a certain amount of passed model time. During the day-night cycle, the neutral atmosphere and solar zenith angle dependent solar flux are updated every 60 seconds. The following Sections describe the IonA-2 cross sections, the validation of the core algorithm and the input parameters and architecture of the variable IonA-2_{var} mode. A summary of the model input parameters and its software architecture is given in Table 6.1.

6.3.1 Photoabsorption/-dissociation and -ionization cross section derivation

Huebner and Mukherjee (2015) provide a data base of photoabsorption, -dissociation and -ionization cross sections from experimental and theoretical data sources, the PHoto Ionization/Dissociation Rates PhIDRates database. They calculated rate coefficients for the quiet/active Sun and black body radiation for more than 140 species and approx. 265 branches. The raw cross sections $\sigma^s_{raw}(\lambda)$ for the species Ar, CO, H, H_2, H_2O, H_2O_2, $O(^1D)$, N, NO, NO_2, O and O_2 are taken from their database, which is online available[2]. The O_3 cross sections are taken from *Sander et al.* (2011). The $\sigma^s_{raw}(\lambda)$ are integrated to the selected bin width of 1 nm by using Equation 6.12. The photo cross sections for CO_2 and N_2 are the most important for the lower Mars ionosphere and are therefore investigated here in detail. The numbering of the reactions is that of the reaction scheme 2 in the Tables C.5 to C.15 in Appendix C.

[2]http://phidrates.space.swri.edu

CO_2 photo cross sections

The seven branches considered for the photoabsorption, photodissociation and photoionization of CO_2 in PhIDRates are

$$CO_2 + h\nu \rightarrow CO + O(^1D) \qquad (IP002)$$
$$CO_2 + h\nu \rightarrow CO_2^+ + e^- \qquad (IP016)$$
$$CO_2 + h\nu \rightarrow CO^+ + O + e^- \qquad (IP018)$$
$$CO_2 + h\nu \rightarrow O^+ + CO + e^- \qquad (IP017)$$
$$CO_2 + h\nu \rightarrow C^+ + O_2 + e^- \qquad (IP019)$$
$$CO_2 + h\nu \rightarrow CO + O \qquad (IP001a)$$
$$CO_2 + h\nu \rightarrow CO(a^3\Pi) + O \qquad (IP001b)$$

The Cameron emission band system of CO arises from the spin forbidden transition of the metastable (approx. 7.5 ms (*Lawrence*, 1971)) lowest excited triplet state of $CO(a^3\Pi)$ to the singlet ground state $CO(X^1\Sigma^+)$. It is the strongest observed feature in the ultraviolet Martian dayglow emission (*Fox and Dalgarno*, 1979), which was first observed by the flybys of the Mariner 6 and 7 spacecrafts in 1969 - 1970 (*Barth et al.*, 1971; *Stewart*, 1972). The loss processes for $CO(a^3\Pi)$ included in the Cameron band emission of *Bhardwaj and Raghuram* (2011) and *Jain and Bhardwaj* (2012) are photodissociation/ionization, quenching by other species and radiative decay. The available PhIDRates photo cross sections for $CO(a^3\Pi)$ are similar to those for CO. The quenching or radiative decay of $CO(a^3\Pi)$ results in the ground state of CO. Therefore $CO(a^3\Pi)$ is handled in IonA-2 similar to the ground state CO and not as a different sub-species. This reduces the number of investigated CO_2 branches to six.
Above wavelengths of approx. 100 nm, the CO_2 absorption cross sections depend strongly on the temperature of the absorber gas. *Anbar et al.* (1993) show, that the use of temperature dependent CO_2 absorption cross sections in a model of the Mars atmosphere causes large differences in the CO_2 photodissociation rates. Therefore a linear temperature dependence of the CO_2 absorption cross sections between 195 K and 300 K is assumed in IonA-2. The raw CO_2 absorption cross sections for 300 K are taken from the compilation of *Huestis and Berkowitz* (2011) and *Keller-Rudek et al.* (2013). Additional absorption cross sections are available for 195 K from *Stark et al.* (2007) between 106.1 and 118.7 nm, from *Yoshino et al.* (1996) between 118.7 - 175.5 nm and from *Parkinson et al.* (2003) available in the observation range from 163 to 192.5 nm. All absorption cross section data are online available from the MPI-SA (*Keller-Rudek et al.*, 2013).
For the ionization processes, the thorough evaluation of partial absolute cross section of *Berkowitz* (2015) is used as a guide.

- 800 nm to 90 nm - $(IP002)$, $(IP001a)$
  The branching ratios for the two dissociation channels are calculated from the absolute cross sections available from PhIDRates.

- 90 nm to 74 nm - ($IP002$), ($IP001a$), ($IP016$)
  The first ionization potential of CO_2 is 89.99 nm, therefore ($IP016$) becomes available in this wavelength region. The ionization efficiency is extracted from the plots 1-3 of *Shaw et al.* (1995). This introduces an unpredictable, but small error, because approx. 20 data points are extracted from the plot for each 1 nm interval. Multiplying the ionization efficiency with the derived absorption cross sections yields the absolute cross sections for ($IP016$). The residual absorption cross sections are distributed to ($IP002$) and ($IP001a$) according to the PhIDRates branching ratios.

- 74 nm to 68 nm - ($IP002$), ($IP001a$), ($IP016$)
  Shaw et al. (1995) state a problem with the experiment in this wavelength region, which is obvious in their plot 4. Therefore the PhIDRates branching ratios for ($IP002$), ($IP001a$) and ($IP016$) are used instead.

- 68 nm to 64 nm - ($IP002$), ($IP001a$), ($IP016$), ($IP017$)
  The thermochemical threshold of 19.0701 eV ($\hat{\approx}$ 65.01 nm) (*Berkowitz*, 2015) indicates the onset of the dissociative ionization process ($IP017$) in this interval. The ionization efficiency is taken from *Shaw et al.* (1995), the branching ratios are taken from PhIDRates.

- 64 nm to 41 nm - ($IP002$), ($IP001a$), ($IP016$), ($IP017$), ($IP018$), ($IP019$)
  The thermochemical threshold of 19.4664 eV ($\hat{\approx}$ 63.69 nm) (*Berkowitz*, 2015) for ($IP018$) and the thermochemical threshold of 22.69 eV ($\hat{\approx}$ 54.64 nm) (*Masuoka and Samson*, 1980) for ($IP019$) indicate the onset of the dissociative ionization processes in this wavelength area. It is assumed, that all absorbed photon energy is going into photoionization below 62 nm (*Berkowitz*, 2015; *Shaw et al.*, 1995). The branching ratios above 62 nm are taken from PhIDRates, the branching ratios below from the branching ratios calculated on the basis of the absolute partial dissociative ionization cross sections of *Berkowitz* (2015).

- 41 nm to 13 nm - ($IP016$), ($IP017$), ($IP018$) ($IP019$)
  Branching ratios are calculated from the absolute ionization cross sections of *Masuoka* (1994) and used with the defined absorption cross sections. Double ionization effects in this interval are small compared to the cross sections for ($IP016$) and are therefore neglected.

- 13 nm - 4 nm - ($IP016$), ($IP017$), ($IP018$) ($IP019$)
  The absolute partial ionization cross sections of *Berkowitz* (2015) near the K-edge of the C atom (between approx. 6 and 4 nm), where the energetic photons are attacking the innermost (K-)shell of the atom, are used in combination with the absolute partial ionization cross sections of *Masuoka* (1994) (available down to 12.4 nm) to calculate branching ratios for the partial ionization processes.

- 4 nm - 0.45 nm - ($IP016$), ($IP017$), ($IP018$) ($IP019$)
  No absolute partial cross sections are available in this wavelength range. *Berkowitz* (2015) state, that ($IP016$) is one of the stronger channels, along with ($IP017$) – ($IP019$). Additionally, CO_2^{++} is present. The double ionization products are neglected in this work by assuming that CO_2^{++} dissociates fast. It is assumed, that all energy is equally distributed between the channels ($IP016$), ($IP017$), ($IP018$) ($IP019$).

N_2 photo cross sections

The three branches considered for the photoabsorption, photodissociation and photoionization of N_2 in PhIDRates are

$$\begin{aligned} N_2 + h\nu &\rightarrow N + N(^2D) && (IP006)\\ N_2 + h\nu &\rightarrow N_2^+ + e^- && (IP023)\\ N_2 + h\nu &\rightarrow N^+ + N + e^- && (IP024). \end{aligned}$$

A branching ratio of 50 % ground state N and 50 % excited $N(^2D)$ is assumed, (see *Richards et al.* (1981), *Shi et al.* (2017) and references therein). This assumption is e.g. used by *González-Galindo et al.* (2013). No cross section measurements for temperatures below 295 K are available, therefore this temperature range is used for the calculations. Again, the selection of measurements follows the discussion of *Berkowitz* (2002, 2015).

- 800 nm to 80 nm - ($IP006$)
  The photo-dissociation cross sections for this wavelength range are taken from the work of *Chan et al.* (1993). The data set is downloaded from the MPI-SA database. The onset of ($IP006$) in the data set is at 108 nm.

- 80 nm to 66 nm - ($IP006$), ($IP023$)
  The ionization potential for N_2 is at approx. 79.58 nm (*Berkowitz*, 2002), therefore ($IP023$) becomes available in this wavelength region. The cross sections in this wavelength region are those from *Shaw et al.* (1992). Their absorption cross sections are downloaded from MPI-SA and integrated to 1 nm bins. The ionization efficiency of *Shaw et al.* (1992) is not online available. It is therefore extracted from the plots in the publication. This introduces an unpredictable, but small error, because approx. 10 - 20 data points are extracted from the plot for each 1 nm interval. The ionization efficiency is integrated to 1 nm bins. Multiplying the ionization efficiency with the derived absorption cross sections yields the absolute cross sections for ($IP023$). The residual absorption cross sections is used for ($IP006$).

- 66 nm to 12 nm - ($IP023$), ($IP024$)
  Shaw et al. (1992) provide calculated photo-dissociation efficiency down to 68 nm.

Additionally, their ionization efficiency reaches 1 at approx. 66 nm. Therefore it is assumed, that all absorbed photon energy is going into ionization effects downward of 66 nm. The thermochemical threshold for ($IP024$) is approx. 51.04 nm (*Berkowitz*, 2002), therefore ($IP024$) becomes available in this wavelength region. The onset of double ionization $N2 + h\nu \rightarrow N^+ + N^+ + e^- + e^-$ has its threshold at approx. 31.87 nm. The cross sections in Table 2 of *Samson et al.* (1987) are used for this wavelength interval. The authors do not separate single and double ionization effects in their measurements. The double ionization cross sections of *Cole and Dexter* (1978) (extracted from the plot of *Samson et al.* (1987)) are used to separate the two effects. Double ionization is small in this interval compared to ($IP023$) and is therefore not further investigated.

- 12 nm to 2 nm - ($IP023$), ($IP024$)
  The photoionization and dissociative photoionization cross sections of *Stolte et al.* (1998) are used. Double (N^{++}) and triple (N^{+++}) ionization effects increase in this wavelength interval. The measured contribution of triple ionization to the absorption cross section is always lower than 1% and is therefore neglected. The contribution of double ionization increases up to approx. 25% at 1.55 nm. *Stolte et al.* (1998) made no effort, to separate the signals of N^+ and N_2^{++}, because N_2^{++} dissociates fast into $2N^+$. Therefore double ionization is not further investigated.

- 2 nm to 0.45 nm - ($IP023$), ($IP024$)
  When no or no reliable measurements for cross sections of a molecule in a certain wavelength range are available, atomic additivity is often used instead. In atomic additivity, the cross section for a molecule is assumed to be the sum of the cross sections of the individual atoms. In this wavelength interval, the absorption cross sections from *Henke et al.* (1993) for N are used. The branching ratios are taken from the measurement for the lowest available wavelength (1.55 nm) of *Stolte et al.* (1998).

6.3.2 Validation of the IonA-2 core algorithm

IonA-2_{con} represents the core algorithm of IonA-2 where all external variations of the neutral atmosphere, neutral temperature and solar flux from the change in local time and solar zenith angle with time are deactivated. IonA-2_{con} is used to validate the basic algorithm of IonA-2 by comparing its results to the output of the 1-D photochemical model of the Mars atmosphere and ionosphere of *González-Galindo* (2006) (called GG-model from now on) after 6 hours of run-time. The comparison of the IonA-2_{con} results with the GG-model output is done to determine the agreement between i.) the densities of the main species of the lower dayside ionosphere O_2^+, CO_2^+, NO^+ and O^+ and ii.) the nitrogen species cycle NO, N, $N(^2D)$, because those species are not provided in the

MCD V5.2 and are involved in the ionospheric NO^+ density. It is assumed, that the core algorithms and equations of IonA-2 are implemented correctly, when no large deviations in the results occur between the two models for mostly similar input parameters. For the comparison of the IonA-2_{con} and GG-model model outputs, similar input atmospheres, temperatures and a similar photochemical reaction scheme are used. The individual output densities are then derived by running both models for 6 hours of model time with constant solar flux. No transport effects are tested during the validation process and are therefore turned off in both models.

Input parameters

The input atmosphere for the comparison of IonA-2_{con} and GG-model consists of altitude profiles of the electron temperature[3], neutral temperature T_N and atmospheric/ionospheric densities for the species CO, CO_2, H, H_2, H_2O, H_2O_2, HO_2, N, $N(^2D)$, N_2, NO, NO_2, OH, O, $O(^1D)$, O_2, O_3, C^+, CO^+, CO_2^+, H^+, HCO_2^+, N^+, N_2^+, NO^+, O^+ and O_2^+ in a 2 km resolution between 80 and 200 km altitude. The input neutral temperature and atmospheric/ionospheric densities (including the altitude range and vertical resolution) are those from Figure 3a of *González-Galindo et al.* (2013)[4], which contains the output of the GCM of the Laboratoire de Météorologie Dynamique for the Mars ionosphere. The LMD-GCM is one of the input sources for the Mars Climate Database. The ionosphere of Figure 3a of *González-Galindo et al.* (2013) is shown in Figure 2.14 in Chapter 2, selected neutral species are found in Figure A.1 in Appendix A. The ionosphere described in Figure 3a of *González-Galindo et al.* (2013) is associated with Ω_{lon}= 0 °, Ω_{lat}= 0 ° and LST= 12h for a F10.7= 118.3 (the F10.7 value is only a solar flux indicator and not actually used in the GG-model or the GCM). The presented results are averaged data from model runs for the time period where L_S is between 0 ° and 30 °.
The photochemical reaction scheme used by both models is given in Table C.1 - C.4 in Appendix C and is similar to that used in *González-Galindo et al.* (2013). The electron impact ionization by photoelectrons used in both models is the secondary ionization efficiency parametrization of *Nicholson et al.* (2009). The photoabsorption/-dissociation/-ionization cross sections and input solar flux used in the IonA-2_{con} and GG-model differ. Due to the fact, that the publicly available and widely used photo cross sections and branching ratios differ, it was agreed to use mostly similar sources for two most important species for this work, CO_2 and N_2. For CO_2 it was agreed to use the *Huestis and Berkowitz* (2011) absorption cross section compilation and ionospheric branching ratios from *Schunk and Nagy* (2009) (available between 5 and 105 nm). Additionally, it is assumed, that below 167 nm, all CO_2 photo-dissociation is going into the production of CO and $O(^1D)$, while above 167 nm all photo-dissociation is going into the production of CO

[3]Digitalized by F. González-Galindo from the model results of *Rohrbaugh et al.* (1979) in *Kieffer et al.* (1992)

[4]provided by F. González-Galindo, personal communication

and O. For N_2, the absorption cross sections in the models were chosen individually, but it was agreed to use the branching ratios of *Schunk and Nagy* (2009) (5 to 105 nm) in both models. The GG-model computes the photo-absorption by a fast scheme, which i.) uses self-calculated tables of photo-absorption coefficients $\sigma_a^s \cdot n_s$ integrated over individual solar wavelength intervals for each absorbing species s as a function of their column densities and ii.) uses the assumption of equilibrium for the fastest species OH, $O(^1D)$ and HO_2. IonA-2 is applying the Lambert-Beer law (Eq. 6.8) with individual cross sections for 1 nm solar flux bins instead. The solar flux input for IonA-2_{con} is derived from the SIP V2.37 ASTM spectrum of the solar flux of DoY 012 in 2004 for a F10.7=118.3. The SIP solar flux spectrum is scaled for the appropriate Mars-Sun distance of 238,407,759 km[5] (approx. L_S= 15 °) with Equation 5.3. No equilibrium assumption is used. The termolecular reactions are multiplied with 2.5 to consider the effect of CO_2 as a collision partner compared to the lighter species where the original reactions where measured in (*Nair et al.*, 1994).

The IonA-2 core algorithm

The algorithm for IonA-2_{con} is described in the orange part of Figure 6.6. In the first step, the input configuration for the model is set: altitude resolution, primary input species (the species for which primary densities are provided) and the photochemical reaction scheme is selected from the pool of available reactions and secondary ionization parametrization modes. In the next step, the start densities for the neutral atmosphere (here additionally the start densities for the ionosphere), neutral temperature and electron temperature are imported. Afterwards, IonA-2 creates the ODE reaction file for the selected photochemical scheme. The file contains the system of ordinary differential equations for all species u (Equation 6.50)

$$\begin{aligned} \frac{\partial n_u}{\partial t} &= P_u^{tot} - L_u^{tot} \\ &= P_u^{pr} + P_u^{sec} + \sum_r P_u^{rea} \end{aligned} \tag{6.92}$$

where P_u^{rea} indicates the net production/loss from all reactions which contain species u. The automatic generation of the reaction file is a vast improvement compared to the manual file creation. In a model with more than 100 included reactions, the automatic file generation allows a fast change of the used reaction scheme, including efficient and consistent changes in reaction coefficients.
The calculation of the photoabsorption, -dissociation and -ionization production is conducted by the use of the trapezoidal numerical integration of the Lambert-Beer law (Eq. 6.7) by the Matlab routine TRAPZ. The primary photo-production P_u^{pr} of species u is

[5] calculated with SPICE

then derived from Equation 6.11.
The secondary ionization parametrization of *Nicholson et al.* (2009) is implemented in IonA-2_{con} for comparison purposes with the GG-model. *Nicholson et al.* (2009) provide analytic functions for the secondary ionization efficiency ϵ_u, which is the ratio of secondary to primary ion production for each individual species u. Their ϵ_u is based on the calculation of the primary and secondary ionization in the Mars ionosphere with a 1-D kinetic electron transport model coupled to the output of a 3-D Mars global circulation model. The secondary ionization production in IonA-2_{con} P_u^{sec} for ion u is derived by multiplying the direct and individual primary photo-production of u from its neutral species s with the secondary ionization efficiency ϵ_u

$$P_u^{sec} = P_{u,r}^{pr} \cdot \epsilon_u. \tag{6.93}$$

The system of ODEs (Eq. 6.92) is then solved by the Matlab ODE15s routine.
The combination of the absolute ODE solver error A_{tol}, relative ODE solver error R_{tol} and time step Δt determine the stability of the solver solution and the solver's speed. For a run time of 1 hour and a $A_{tol} = 10.0$ (which indicates, that the solver error for densities lower than 10.0 m^{-3} is not controlled by the solver), several configurations were tested with the highest resolution of $\Delta t = 30$ s and $R_{tol} = = 1.0 \cdot 10^{-12}$ and a lowest resolution of $\Delta t = 300$ s and $R_{tol} = 1.0 \cdot 10^{-6}$. It is found, that the difference caused by the change of R_{tol} is almost neglectable compared to the differences introduced by the increase of the model time step Δt. The calculation of P_u^{pr} and P_u^{sec} is not included in the ODE solver, but calculated in a separate routine. Therefore P_u^{pr} and P_u^{sec} are handled as constants in the solver and are only updated every model time step Δt. This behavior introduces a natural boundary on the model step width Δt. The solver conditions used in the comparison with the GG-model data are $\Delta t = 150$ s and $R_{tol} = = 1.0 \cdot 10^{-8}$. The data set computed with this solver setting has a maximum deviation of 0.13% (H^+ at 132 km altitude, the errors for the other densities are considerably smaller) compared to the data set with the highest resolution for 1 hour model run time. This is entirely sufficient for the computations in this work.

Comparing the IonA-2_{con} and GG-model results

Two wavelength ranges are investigated for the SIP V2.37 solar flux spectrum of DoY 012 (2004). The first scenario IonA-$2_{con,all}$ contains the solar flux from 0.45 - 800 nm, while IonA-$2_{con,part}$ contains the solar flux from 5 - 800 nm. The provided secondary ionization efficiency functions of *Nicholson et al.* (2009) are applied between 80 and 200 km altitude. This results in partly negative values for ϵ_u for few species u at low altitudes, which is caused by the closeness to the lower border of the given parametrization. Following F. González-Galindo[6], negative values are set to 0, while ϵ_u larger than 100 are set to 100.
Figure 6.7 illustrates the IonA-$2_{con,all}$ and IonA-$2_{con,part}$ results for DoY 012 in compari-

[6]personal communication

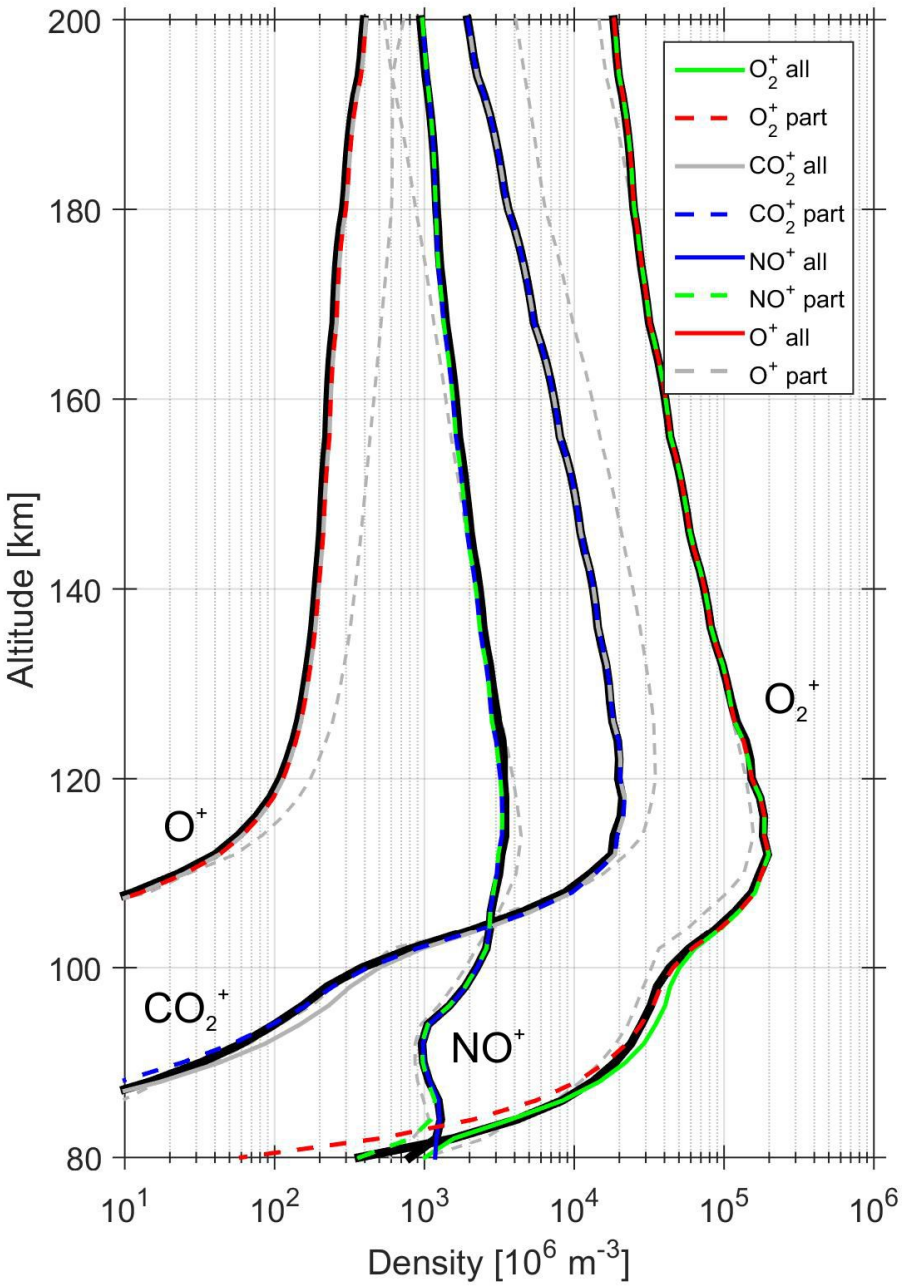

Figure 6.7: Comparison between the model input (thin dashed gray lines), GG-model (black lines), IonA-$2_{con,all}$ and IonA-$2_{con,part}$ results for DoY 012 (2004).

son with the initial ion densities and the GG-model results. The shown ionospheric species agree well above the ionospheric main peak. The individual densities are well met and important features as the altitude of the ionospheric main peak are in good agreement. Below the main peak region, the differences between IonA-2_{con} and the GG-model increase. Due to the fact, that the input atmosphere/ionosphere, the solar zenith angle, the neutral/electron temperatures and the chemical reaction scheme (including the reaction coefficients) are equal for this comparison, there are four sources for differences between the models:

i.) the input solar flux
The spectral intensity distribution may differ due to the use of different SIP database versions, underlying models (e.g. ASTM or VUV) or spectral resolution. The absolute intensity may differ due to different distance scaling (e.g. for a different L_S).

ii.) the photo calculations
The photoabsorption/-dissociation/-ionization cross sections and branching ratios for the individual species are mostly taken from different sources.

iii.) the secondary ionization parametrization and

iv.) different ODE-solver techniques.

The fast scheme of the GG-model makes it impossible to directly compare input solar fluxes or photoabsorption cross sections. Additionally, differences introduced by a different implementation of the secondary ionization (the strongest source of ionization for the main ionospheric species below 100 km altitude) or the use of other ODE solvers/integrators cannot be determined without having direct access to the GG-model. The differences between the IonA-$2_{con,all}$ (0.45 - 800 nm solar flux) and IonA-$2_{con,part}$ (5 - 800 nm solar flux) imply, that the differences between the CO_2^+, O_2^+ and O^+ densities are partly caused by a different handling of the solar radiation below 5 nm, but no exact source for the differences can be determined.

6.3.3 The IonA-2_{var} mode

The IonA-2_{var} mode extends the possibilities of IonA-2_{con} by providing a scheme for the ionospheric calculation for changing solar zenith angle, neutral atmosphere and temperature. Neutral atmospheric and ionospheric calculations for changing solar zenith angle and local time in this work are necessary for three reasons:

i.) The densities of certain nitrogen species are not available from the MCD V5.2 and need build-up time for the consistent computation of NO^+.

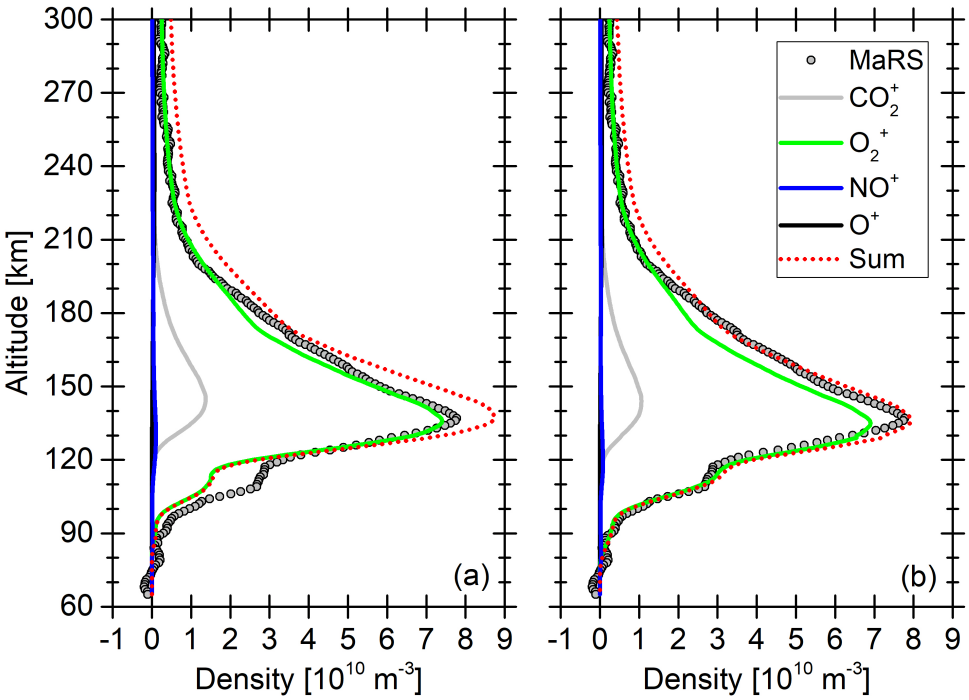

Figure 6.8: IonA-$2_{var,flux}$ results for DoY 336 (2005) for a start LST of 9 h and a model run time of 4 Mars hours. This results in a solar zenith angle of 78.78° *and a local solar time of 13 h. The secondary ionization in Panel (a) is calculated with the approach of* Nicholson et al. *(2009), while the secondary ionization in Panel (b) is calculated with the approach of* Wedlund et al. *(2011).*

ii.) Small amounts of O_2^+, NO^+, HCO^+, CO_2^+ and O^+ have been observed with MVN-NGIMS for solar zenith angles between 110° and 120° (*Girazian et al.*, 2017). In addition, the recombination of N and O to NO on the planetary nightside is an efficient source for NO (*Stiepen et al.*, 2015). Therefore the effect of the planetary day-night cycle is not neglected in this work.

iii.) The ionosphere is not in a complete equilibrium state due to the changing solar flux and is therefore not fully represented by equilibrium models.

Input parameters

The input atmosphere for IonA-2_{var} consists of altitude profiles of the neutral temperature T_N and atmospheric densities for the major atmospheric species Ar, CO, CO_2, H, H_2, H_2O, N_2, O, O_2 and O_3 from the MCD V5.2. The neutral atmospheric species and neutral temperature are extracted from the Mars Climate database in a 0.2 km resolution between 10 and 300 km altitude. The neutral atmosphere is extracted for the local time

resolution of 0.1 Mars hours for a complete cycle of 24 hours of Mars local time. The electron temperature is taken from *Rohrbaugh et al.* (1979). The input solar flux in 1 nm bin resolution with separate bright solar lines is derived from the SIP V2.38 similarly to the input for the IonA-1 model for each individual DoY. The photo cross section are taken from *Huebner and Mukherjee* (2015), except for O_3 (*Sander et al.*, 2011), CO_2 and N_2. Due to the importance of the CO_2 and N_2 cross sections for the model calculations, they have been investigated in detail for this work as discussed earlier in the text. In addition, SIP solar fluxes in a 1 Å resolution from the 1210 wavelength bin distribution and associated cross sections are available for the wavelength range between 0.45 - 10 nm. Those cross sections are needed for a detailed investigation of the origin of the merged excess electron densities. The IonA-2 densities are calculated with an altitude resolution of 1 km.
Figure 6.8 shows the IonA-$2_{var,flux}$ results (the term flux is explained later in the text). While the results in Panel (a) are calculated with the secondary ionization approach of *Nicholson et al.* (2009), the secondary ionization approach in Panel (b) is that of *Wedlund et al.* (2011). It is obvious, that the IonA-2 results in Panel (b) show a much better agreement with the main ionospheric region. In the approach of *Nicholson et al.* (2009), the M1 region is strongly underestimated. This might be caused by the fact, that the secondary ionization parametrization of *Nicholson et al.* (2009) is available for a solar zenith angle of $0\,^\circ$ only. Therefore, the secondary ionization parametrization used in this work is the W_E^s-value approach of *Wedlund et al.* (2011).

Variation of the solar flux and neutral atmosphere with time

The day-night cycle implemented in IonA-2 consists of the length of one Mars day (24.6597 hrs)[7], which is the synodic period of one Mars day (the rotation time of Mars until the Sun reaches the same position in the sky). One Mars hour therefore consists of 1.027 h. The initial model start local time is at 9 h LST. At the begin of each model time step, the major neutral atmospheric species and the neutral temperature are updated from the MCD V5.2 for the associated local time. The solar zenith angle χ is calculated from the current local time LST

$$\chi\left(LST\right) = \arccos\left(\cos\left(\frac{LST-12}{24}\cdot 2\pi\right)\cdot\cos\left(\phi_{inc}\cdot\sin\left(L_S\right)\right)\cdot\cos\left(\Omega_{lat}\right)+ \cos\left(\phi_{inc}\cdot\sin\left(L_S\right)\right)\cdot\sin\left(\Omega_{lat}\right)\right) \tag{6.94}$$

with the Mars axis inclination Φ_{inc}, solar longitude L_S and the planetary latitude Ω_{lat}. This equation is similar to that used in the LMD-GCM[8].

[7] Mars fact sheet at NASA https://nssdc.gsfc.nasa.gov/planetary/factsheet/marsfact.html
[8] personal communication with F. González-Galindo

Reaction scheme 2 and transport processes

The reaction scheme 2 of IonA-2_{var} is an updated version of reaction scheme 1 used for the validation of the core algorithm of IonA-2. It is found in Table C.5 to Table C.15 of Appendix C. The additional reactions in reaction scheme 2 are selected based on the work of *Fox and Sung* (2001) and *Fox* (2012, 2015) to test the effect of a wider range of reactions on the ionosphere of Mars. Figure 6.9 shows an example for the strongest CO_2^+, O^+, O_2^+ and NO^+ production/loss rates for the converged IonA-$2_{var,flux}$ reults for DoY 336 (2005).
Figure 6.10 shows example profiles for the vertical transport effects implemented in IonA-2. The neutral species C, H_2O_2, HO_2, $O(^1D)$, $N(^2D)$, N, NO, NO_2 and OH experience eddy diffusion and minor molecular diffusion. While the eddy diffusion is dominant in the lower atmosphere, molecular diffusion becomes the dominant process in the upper neutral atmosphere. Major diffusion of the major atmospheric species CO_2, N_2, O, O_2, O_3, H_2O, H, H_2, Ar and CO is not yet included in IonA-2. The variation of the major neutral species in the atmospheric day-night cycle during one Sol is provided by the Mars Climate Database. For the minor molecular diffusion an upper and a lower boundary condition are needed for each of the included species in IonA-2_{var}. For IonA-$2_{var,NOflux}$, the boundary fluxes for all minor neutral species in IonA-2 are set to zero. For IonA-$2_{var,flux}$, the lower flux boundary for N and NO is set to the limiting velocity at the homopause $w_u = K/H_N$ (*Hunten*, 1973), while the flux borders for all other minor species are set to zero. Ambipolar diffusion is calculated for the ions Ar^+, CO_2^+, CO^+, C^+, HCO_2^+, HCO^+, H^+, N_2^+, NO^+, N^+, O_2^+ and O^+. For ambipolar diffusion all boundary fluxes are set to zero.

The IonA-2_{var} time step and the convergence criterion

During the tests described earlier in this Chapter, a model time step of 150 s is found to provide an acceptable compromise between model speed and precision of the calculation. It is however found for IonA-2_{var}, that the model results also depend on the time step due to the regular update of the solar zenith angle, major neutral species, neutral temperature and the photoionization rate in the ODE solver. A smaller time step directly decreases the error introduced by the constant primary ionization rate in the ODE solver. However, for the major neutrals and T_N, a decrease of the model time step does not increase the accuracy of the results. The MCD V5.2 neutral atmosphere is only an interpolation between grid points of the 3-D GCM. Therefore a smaller time step does not automatically increase the precision of the computations in IonA-2 due to the interpolated MCD data. As a compromise, the model time step is set to 60 s for the IonA-2 model calculations. The problem with the external update of the major neutrals will be avoided in future computations by implementing the major molecular diffusion of *Vlasov and Davydov*

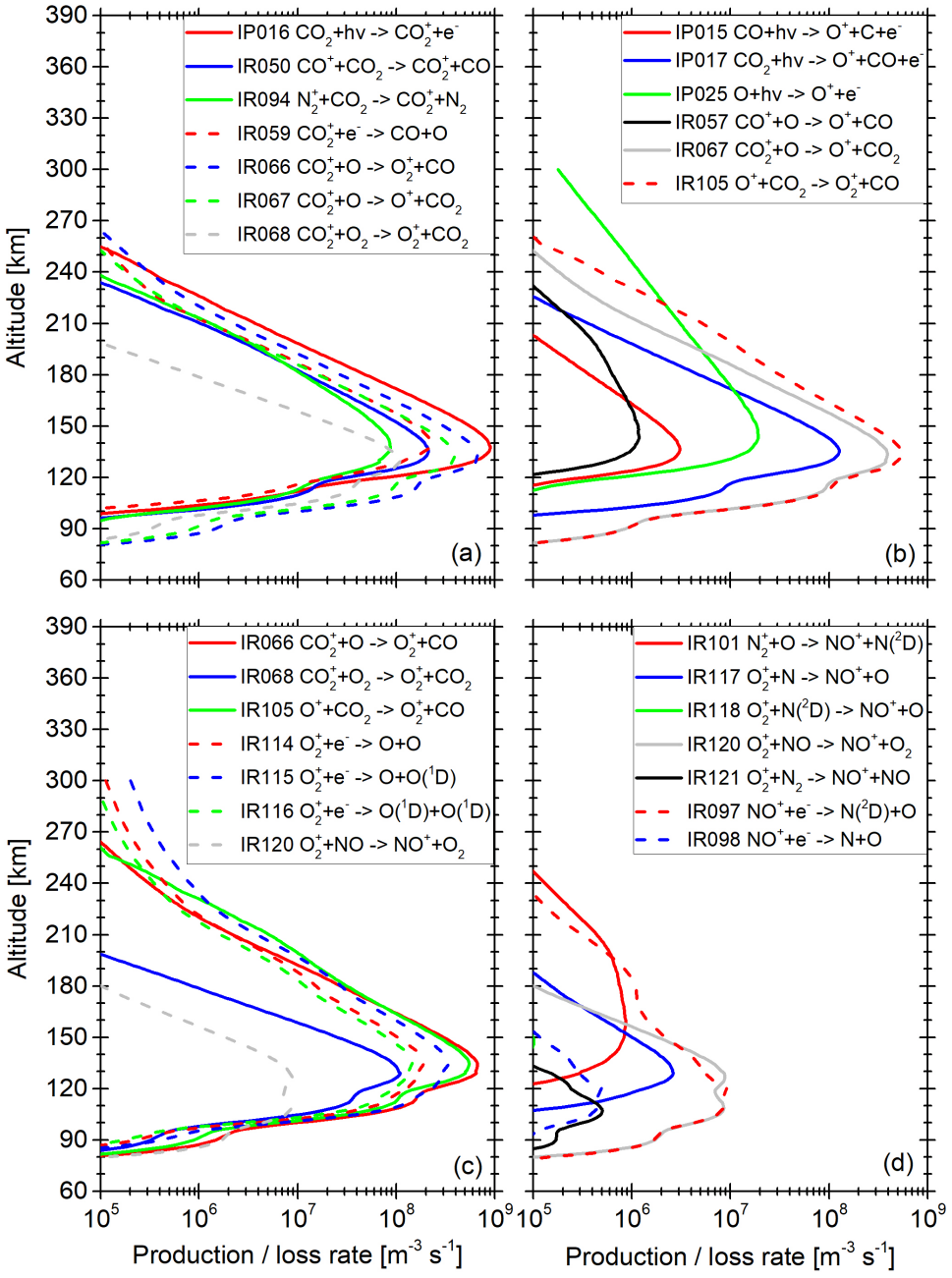

Figure 6.9: Production and loss rates of strong reactions for the converged IonA-2$_{var,flux}$ results for DoY 336 (2005) after 18 Sol and 13 h LST of model run time for (a) CO_2^+, (b) O^+, (c) O_2^+ and (d) NO^+.

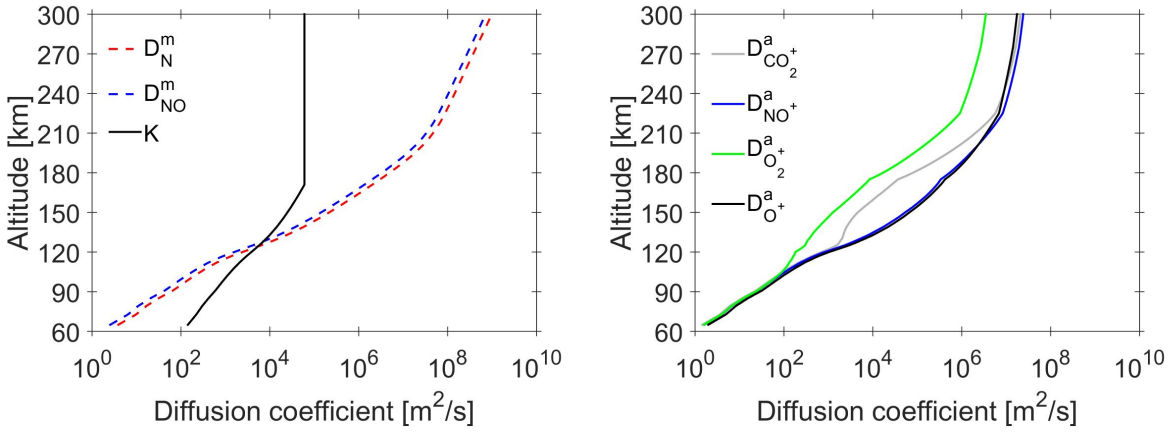

Figure 6.10: (left) Minor molecular diffusion coefficients D_N^m and D_{NO}^m and eddy diffusion coefficient K calculated with IonA-$2_{var,flux}$ for the conditions of the MaRS observation of DoY 336 (2005) also shown in Panel (2b) of Figure 8.2. (right) Ambipolar diffusion coefficients for N and NO for similar IonA-$2_{var,flux}$ conditions.

(1982).

The convergence criterion for the IonA-2_{var} mode is defined in dependence of the local solar time. Due to the changing external conditions over one Sol, the convergence cannot be measured from one time step to the next, because the atmosphere and ionosphere are always changing. Instead, the convergence is tested at a pre-defined local solar time. If the maximum change of the N, $N(^2D)$ and NO densities at each altitude falls below 3.5% from one Sol to the next at a preselected local solar time it is assumed, that the model has reached convergence.

6.3.4 Application

The improved CO_2 and N_2 absorption, dissociation and ionization cross section, the expanded reaction scheme 2 and transport effects in combination with the implemented day-night cycle result in a consistent 1-D model of the Mars upper atmosphere and ionosphere. The IonA-2 ion densities are compared to the in-situ ion observations of the Viking landers / the 1-D model results of *Fox* (2015) and the 3-D model atmosphere and ionosphere of the LMD-GCM in Chapter 8. The comparison between the MaRS ionospheric electron density profiles and the ion composition for the IonA-$2_{var,NOflux}$ and IonA-$2_{var,flux}$ boundary condition in Chapter 8 provide new insights on the potential production mechanisms and composition of the merged excess electron densities. In addition, the 1 Å high resolution solar flux and cross sections between 0.45 - 10 nm yield more information about the potential role of short solar X-ray in the Mm formation process.

Chapter 7

Effects of observational and environmental parameters on the merged excess electron densities

The undisturbed main structure of the Mars day side ionosphere consists of the photochemical region with the dominant M2 layer and the weaker M1 layer/shoulder. Below M1, additional features can be found merged (Mm) or detached (Md) from the main ionospheric region. In this Chapter, the parameters derived from the observed merged excess electron densities (Chapter 4) are compared with observational (Chapter 4) and environmental parameters (Chapter 5) to determine the potential origin of the Mm features. First, potential correlations between the derived environmental parameters and the main ionospheric features M2 and M1 are investigated. The found correlations yield not only information about the formation processes for M2 and M1, but also yield a chance for testing the reliability of the derived environmental parameters in combination with the MaRS observations (e.g. the obvious correlation between the vertical TEC of the ionosphere and the available solar flux). In the second step, potential correlations between the observational/environmental parameters and the identified Mm provide constraints for the potential formation processes of the merged excess electron densities in the Mars dayside ionosphere. Figure 7.1 shows the distribution of the 266 MaRS observation footpoints of the MaRS_{quiet} data set from 2004 - 2014 on the Mars surface with respect to the radial component of the crustal magnetic field. The 117 $\text{Mm}_{a,3km}$ observations with identified merged excess densities are highlighted as red triangles, while the white circles indicate the undisturbed MaRS electron density profiles.
The in-situ ion observations of the MVN-NGIMS experiment described in Chapter 2 show a dawn/dusk asymmetry of the upper ionosphere of Mars. The periapsis outside of the deep dips is approximately 150 km, therefore the information about a main peak asymmetry are sparse. The MaRS_{quiet} data set contains 36 (3) low Φ_{SUM} observations, 158 (31) moderate Φ_{SUM} observations and 15 (23) high Φ_{SUM} observations for afternoon (morn-

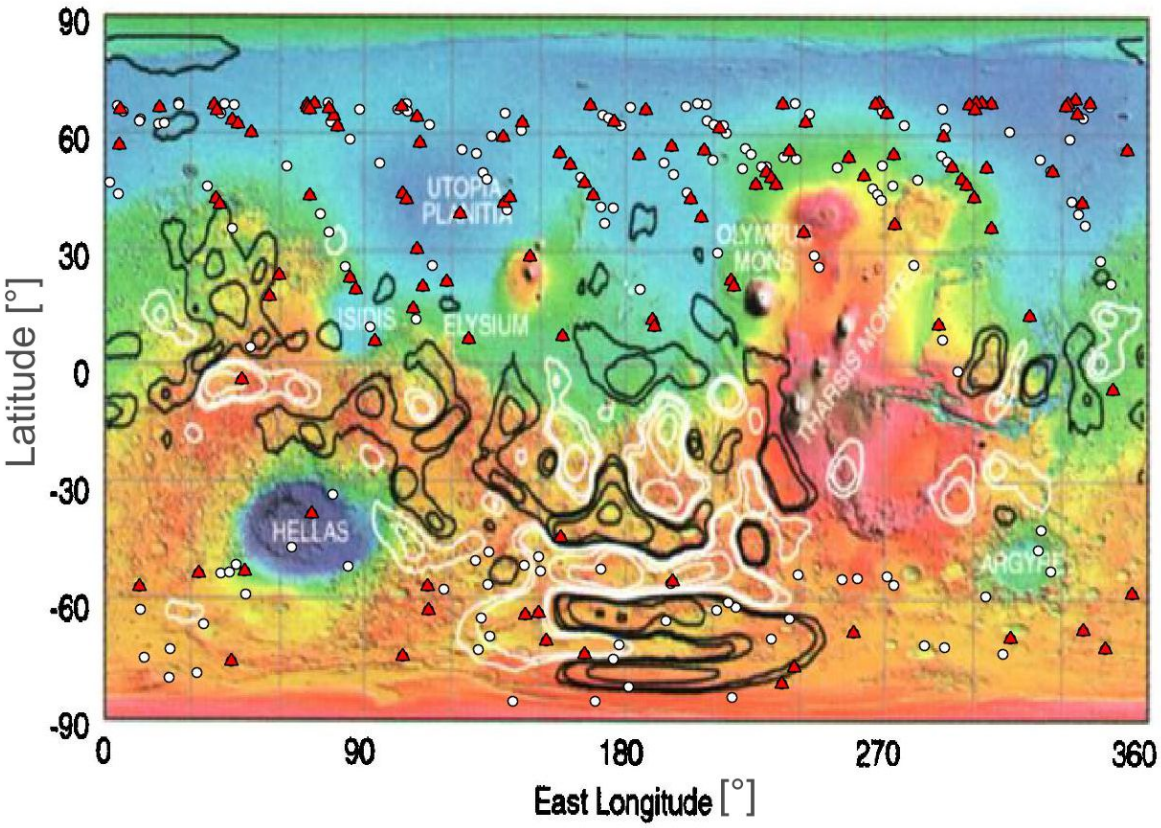

Figure 7.1: Distribution of the 266 $MaRS_{quiet}$ observation footpoints on the surface of Mars. The map is taken from Connerney et al. *(2001) and shows an overlay of the crustal magnetic field with the Mars topography. Black and white lines indicate isomagnetic contours of the radial field component at* (400 ± 30) *km altitude for* $B = \pm 10, 20, 50, 100, 200\,nT$*. Red triangles indicate the 117 observations containing merged excess electron densities ($Mm_{a,3km}$), white dots are the remaining 149 undisturbed MaRS observations.*

ing) local times. The data coverage of the quiet MaRS observations is therefore yet too sparse to identify this local time dependence for an undisturbed ionosphere. In addition, MaRS_{quiet} is too small to identify the separate effects of the changing solar activity, solar longitude L_S, planetary longitude Ω_{lon} and latitude Ω_{lat} on the state of the ionosphere. Therefore, the following correlations will cover most of the environmental parameters by investigating the effects of the changing solar radiation at the top of the atmosphere (covering the L_S Sun-planet distance variation) in dependence of the solar zenith angle (covering the solar flux variation due to Ω_{lat}) and crustal magnetic field at the observation location.

7.1 The M2 main peak region

The MaRS_{all} data set contains 451 observations. A part of those observations contain large scale noise caused by unexpected movement of the ground station/spacecraft, additional plasma in the radio ray path or other sources. Due to the fact, that the focus of this investigation is on the small scale Mm excess densities, instead of MaRS_{all}, only those 266 MaRS_{quiet} observation with small scale noise are further investigated. The smaller noise level of those observations provides more reliable parameters with less fluctuation induced by external sources.
Panel (a) of the Figures 7.2, 7.3, 7.4 and 7.5 contain the M2 parameters with their associated error bars derived from the MaRS_{quiet} data set. Panel (b) contains the weighted average $\overline{X}_w$

$$\overline{X}_w = \frac{\sum_{i=1}^{N} \frac{1}{\sigma_{X,i}} \cdot X_i}{\sum_{i=1}^{N} \frac{1}{\sigma_{X,i}}} \tag{7.1}$$

of each parameter X. $\overline{X}_w$ is calculated from all N data points X_i with associated error bar $\sigma_{X,i}$ in each 5 ° solar zenith angle bin of Panel (a). If asymmetric error bars are available for a given parameter, the mean error values are used for further calculation. The given error bars in Panel (b) are the weighted standard deviation $\overline{\sigma}_{X,w}$

$$\overline{\sigma}_{X,w} = \sqrt{\frac{N \cdot \sum_{i=1}^{N} \frac{1}{\sigma_{X,i}} \cdot \left(X_i - \overline{X}_w\right)^2}{(N-1)\sum_{i=1}^{N} \frac{1}{\sigma_{X,i}}}}. \tag{7.2}$$

Panel (a) of Figure 7.2 contains the electron content n_{TEC}^{obs} of the vertical MaRS electron density profiles computed from Eq. (4.4). The n_{TEC}^{obs} is subdivided into the three solar proxy intervals, low $\Phi_{SUM,low}$, moderate $\Phi_{SUM,mod}$ and high $\Phi_{SUM,high}$, which are

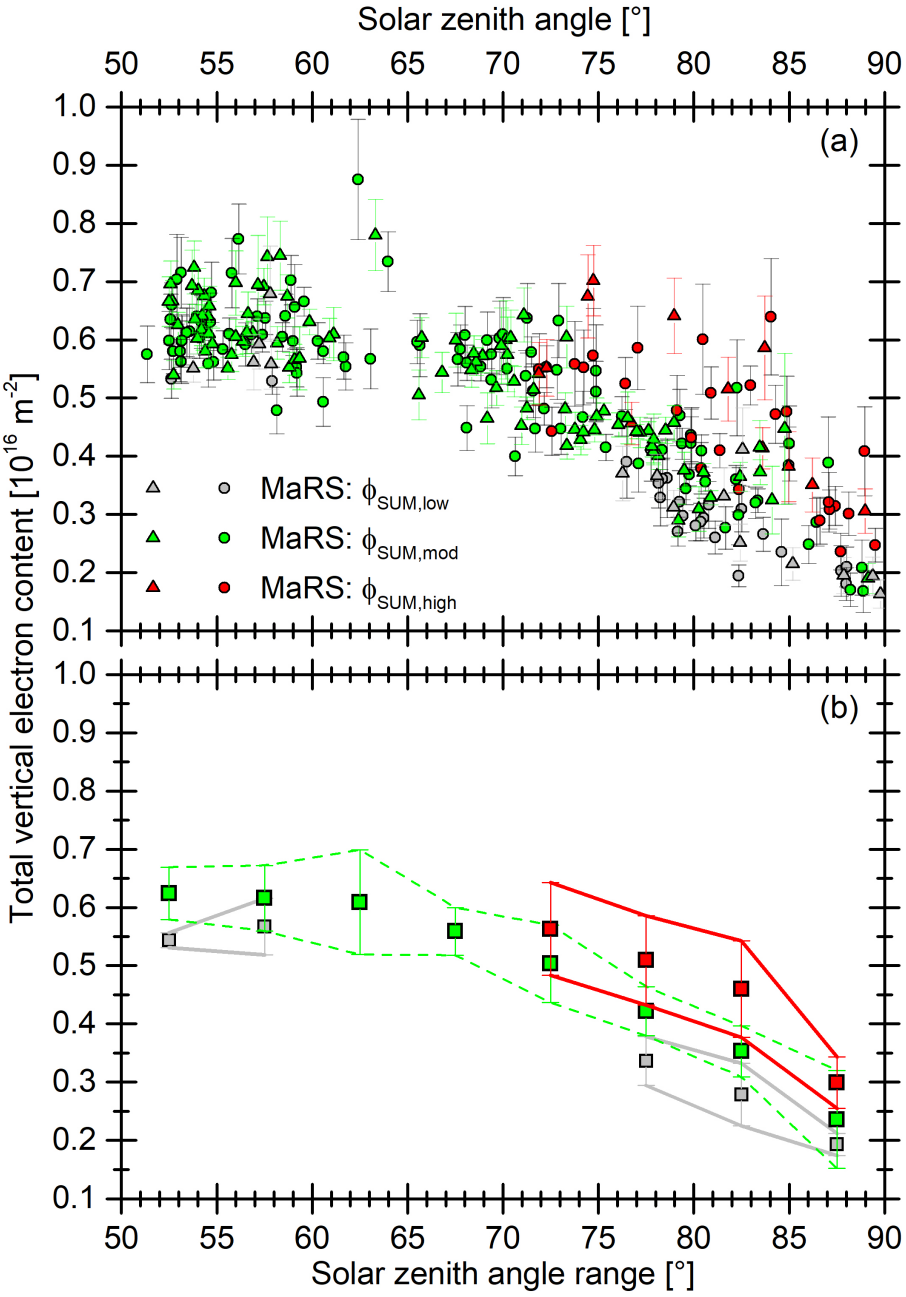

Figure 7.2: (a) Derived full vertical TEC n_{TEC}^{obs} with error bars for the $MaRS_{quiet}$ data set. Gray, green and red triangles indicate the $\Phi_{SUM,low}$, $\Phi_{SUM,mod}$ and $\Phi_{SUM,high}$ observations with detected merged layers, circles indicate the remaining observations. Colored error bars belong to the Mm, black error bars to the undisturbed observations. (b) 5° solar zenith angle weighted average $\overline{n}_{TEC}^{obs}$ for the three solar proxy intervals $\Phi_{SUM,low}$ (gray), $\Phi_{SUM,mod}$ (green) and $\Phi_{SUM,high}$ (red). The error bars indicate the calculated weighted standard deviation of the data points.

calculated from the SIP V2.38 model solar flux between 0.45 - 95 nm and are discussed in detail in Chapter 5. The gray, green and red triangles indicate observations with detected merged excess densities of the $\mathrm{Mm}_{a,3km}$ group for the three solar proxy intervals, while the undisturbed observations are represented by circles. For an ionosphere ideally controlled by solar radiation, the vertical TEC should vary with the solar zenith angle and the neutral scale height H_n as (*Withers*, 2009)

$$n_{TEC} \simeq 4.13 \frac{n_{e,max,0}(M2)}{\sqrt{\mathrm{Ch}\,(h,\chi)}} \cdot H_n \tag{7.3}$$

with

$$H_n = \frac{k_B T_N}{< m > g}, \tag{7.4}$$

where n_{TEC} is the vertical TEC, $n_{e,max,0}(M2)$ the M2 peak density for solar zenith angle $\chi = 0\,^\circ$ and $Ch\,(h,\chi)$ the Chapman function for grazing incidence angle. The $Ch\,(h,\chi)$ function (*Chapman*, 1931b; *Smith and Smith*, 1972) is a geometrical correction for the difference between a horizontally layered and a spherical atmosphere. It reduces to $1/\cos(\chi)$ for small solar zenith angles. The scale height H_n of the neutral atmosphere is calculated from the Boltzmann constant k_B, the atmospheric neutral temperature T_N, the average $< m >$ (homosphere) or molecular/atomic (heterosphere) mass and the gravity acceleration g. As expected from Eq. 7.3, the observations in Fig. 7.2 show a strong solar zenith angle dependence. In addition, the observed TEC is strongly related to the SIP V2.38 model solar flux (found in Eq. 7.3 by the $n_{e,max,0}(M2)$ variable, which is also dependent on the available solar flux in Chapman-theory). The difference between the vertical TEC in the three flux levels is even better visible in Panel (b). Here, the weighted average TEC $\overline{n}^{obs}_{TEC}$ and weighted standard deviation are calculated from all data points in each $5\,^\circ$ solar zenith angle bin, independent of the availability of Mm. For solar zenith angles larger than $75\,^\circ$ the calculated weighted standard deviation of the $\Phi_{SUM,low}$ and $\Phi_{SUM,high}$ has no overlapping part.

Panel (a) of Figure 7.3 contains the observed M2 peak densities $n^{obs}_{e,max}(M2)$ of MaRS_{quiet} subdivided into the $\Phi_{SUM,low}$, $\Phi_{SUM,mod}$ and $\Phi_{SUM,high}$ solar proxy intervals. The peak density of an ionosphere ideally controlled by solar radiation should vary with the solar zenith angle and is usually compared with the Chapman relation (*Chapman*, 1931a)

$$n_{e,max,\chi}\,(M2) = n_{e,max,0}\,(M2) \cdot \cos^{\epsilon_{ch}}(\chi)\,, \tag{7.5}$$

where $n_{e,max,\chi}\,(M2)$ is the peak density at the solar zenith angle χ and $\epsilon_{ch} = 0.5$ is the exponent for perfect agreement with the Chapman theory. The observed data in Fig. 7.3 demonstrate the decrease of $n^{obs}_{e,max}(M2)$ with increasing solar zenith angle, as predicted from the Chapman relation. Equation (7.5) is fit to the moderate solar proxy interval $\Phi_{SUM,mod}$ to illustrate the obvious influence of the changing solar flux on the Mars ionosphere. For solar zenith angles lower than $85\,^\circ$, almost all of the M2 densities within

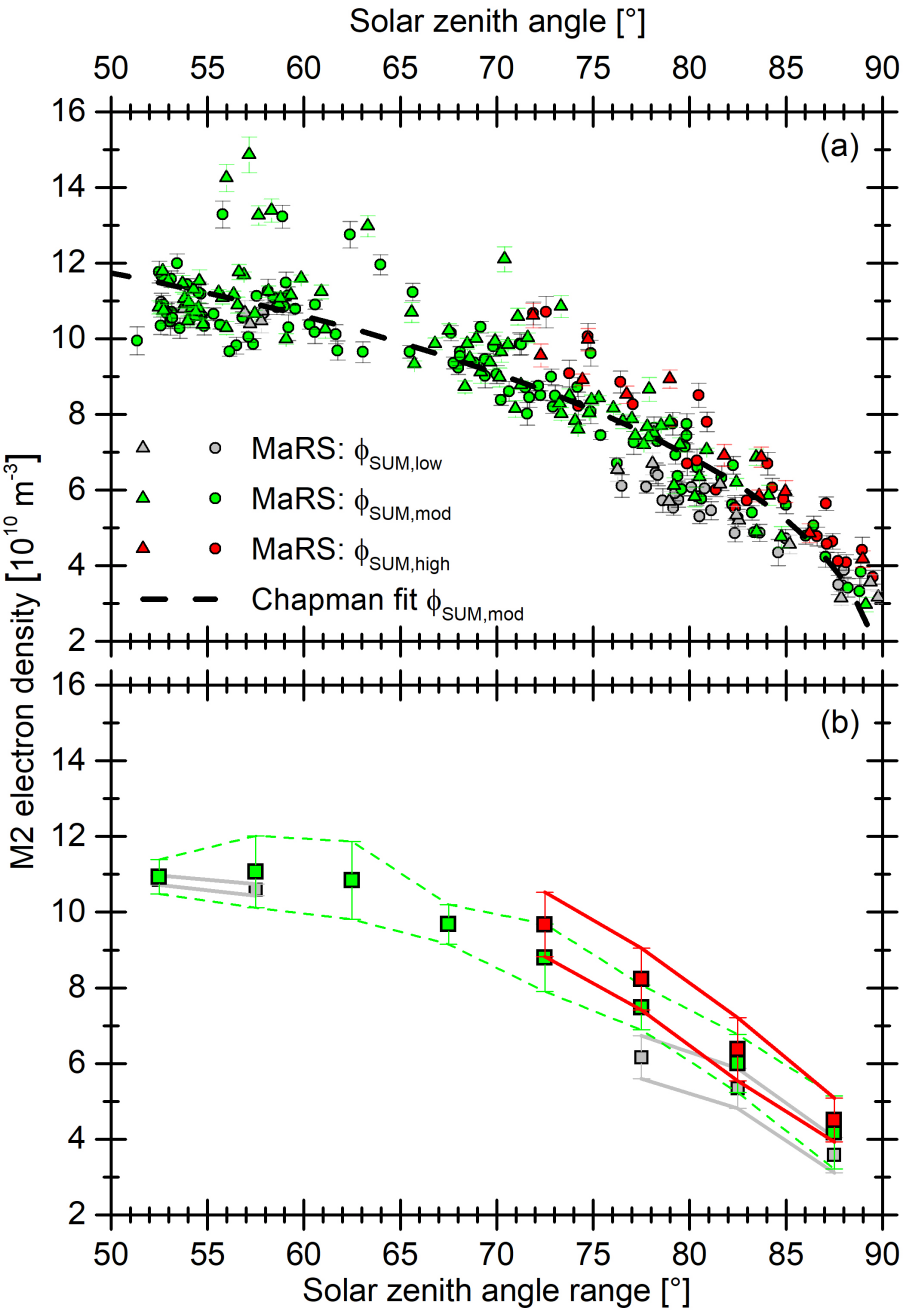

Figure 7.3: (a) Derived M2 electron density with error bars for the $MaRS_{quiet}$ data set. (b) 5° solar zenith angle weighted average $\overline{n}^{obs}_{e,max}(M2)$ and weighted standard deviation $\overline{\sigma}^{obs}_{n_{e,max}}(M2)$ of the all data in Panel (a). The color code is similar to that in Figure 7.2. The dashed line illustrates the fit of the Chapman relation (7.5) on the $\Phi_{SUM,mod}$ proxy data range. The derived parameter is $\epsilon_{ch} = 0.407 \pm 0.002$, which does not include the ideal value of $\epsilon_{ch} = 0.5$.

the solar proxy interval $\Phi_{SUM,low}$ are below the Chapman relation fit (dashed line in Fig. 7.3), while most of the M2 densities of interval $\Phi_{SUM,high}$ are found above. For higher χ, the $\Phi_{SUM,high}$ data are found still above the $\Phi_{SUM,low}$ data, but they are not separated by the Chapman-fit any more. This is explained by the fact, that Eq. 7.5 is based on idealized conditions. E.g. the assumption of a locally radial symmetric atmosphere is less probable to be fulfilled in the more variable atmosphere and ionosphere near the planetary terminator. The effect of the varying solar radiation on the ionospheric state is more easily seen in Panel (b), where the weighted average M2 electron density data $\overline{n}^{obs}_{e,max}(M2)$ of $\Phi_{SUM,low}$ are found below and the weighted average data of $\Phi_{SUM,high}$ are found above the weighted average data of $\Phi_{SUM,mod}$ for all solar zenith angles. The influence of the solar flux on the $n^{obs}_{e,max}(M2)$ observations is less strong than for the n^{obs}_{TEC} data. The calculated weighted standard deviation error bars of the $\Phi_{SUM,low}$ and $\Phi_{SUM,high}$ overlap except for the $75\,^\circ - 80\,^\circ$ solar flux interval. The vertical TEC of an observation is stronger affected by solar radiation changes than the $n^{obs}_{e,max}(M2)$ behavior, because n^{obs}_{TEC} is additionally influenced by the M2 peak width $h^{obs}_{width}(M2)$ (see Figure 7.5 below). The $h^{obs}_{width}(M2)$ for $\Phi_{SUM,high}$ increase for increasing χ, which is not the case for the low solar flux $h^{obs}_{width}(M2)$, where only the scatter of the data points widens. Due to the double increase in $n^{obs}_{e,max}(M2)$ and $h^{obs}_{width}(M2)$ for the high solar zenith angles, the difference between the $\Phi_{SUM,low}$ and $\Phi_{SUM,high}$ TEC is more pronounced than for the $n^{obs}_{e,max}(M2)$ or $h^{obs}_{width}(M2)$ alone. It is expected to find the observed trend of increasing M2 densities for increasing solar flux continued for the $\Phi_{SUM,high}$ data for lower χ.

The derived M2 peak altitudes $h^{obs}_{max}(M2)$ are shown in Figure 7.4. The Chapman relation (*Chapman*, 1931a) for the peak altitude is

$$h_{max,\chi}\,(M2) = h_{max,0} - H_n \cdot \ln(\cos\chi)\,, \tag{7.6}$$

where $h_{max,\chi}$ is the peak altitude for the solar zenith angle χ, $h_{max,0}$ is the peak altitude for $\chi = 0\,^\circ$ and the H_n the neutral scale height. Despite the large variation of the observed M2 peak altitudes in Fig. 7.4, an altitude/solar zenith angle dependence, as expected from the Chapman theory, is evident for higher solar zenith angles. The change in solar flux during the observation periods from 2004 to the end of 2014 and its impact on the Martian ionosphere is not as clear as for the M2 densities. The Chapman relation (7.6) was fit to the observations assigned to the moderate solar proxy interval $\Phi_{SUM,mod}$. The influence of the varying solar flux on the Mars ionosphere, already found for the full profile TEC (Fig. 7.2) and peak electron density (Fig. 7.3), is confirmed and reflected in an increase of the peak altitude for increasing values of the solar flux for solar zenith angles between 75 and $85\,^\circ$ (Panel (b) of Fig. 7.4). For higher χ, there is no clear division between the low and high solar flux data by the fit, even if the $\Phi_{SUM,high}$ $\overline{h}^{obs}_{max}(M2)$ values are still found found above the $\Phi_{SUM,low}$ $\overline{h}^{obs}_{max}(M2)$ data points in this interval. The problem with the Chapman fit is caused by the i.) low number of the $\Phi_{SUM,mod}$ data points in this solar zenith angle interval and ii.) the proximity to the terminator. For lower χ, close to none

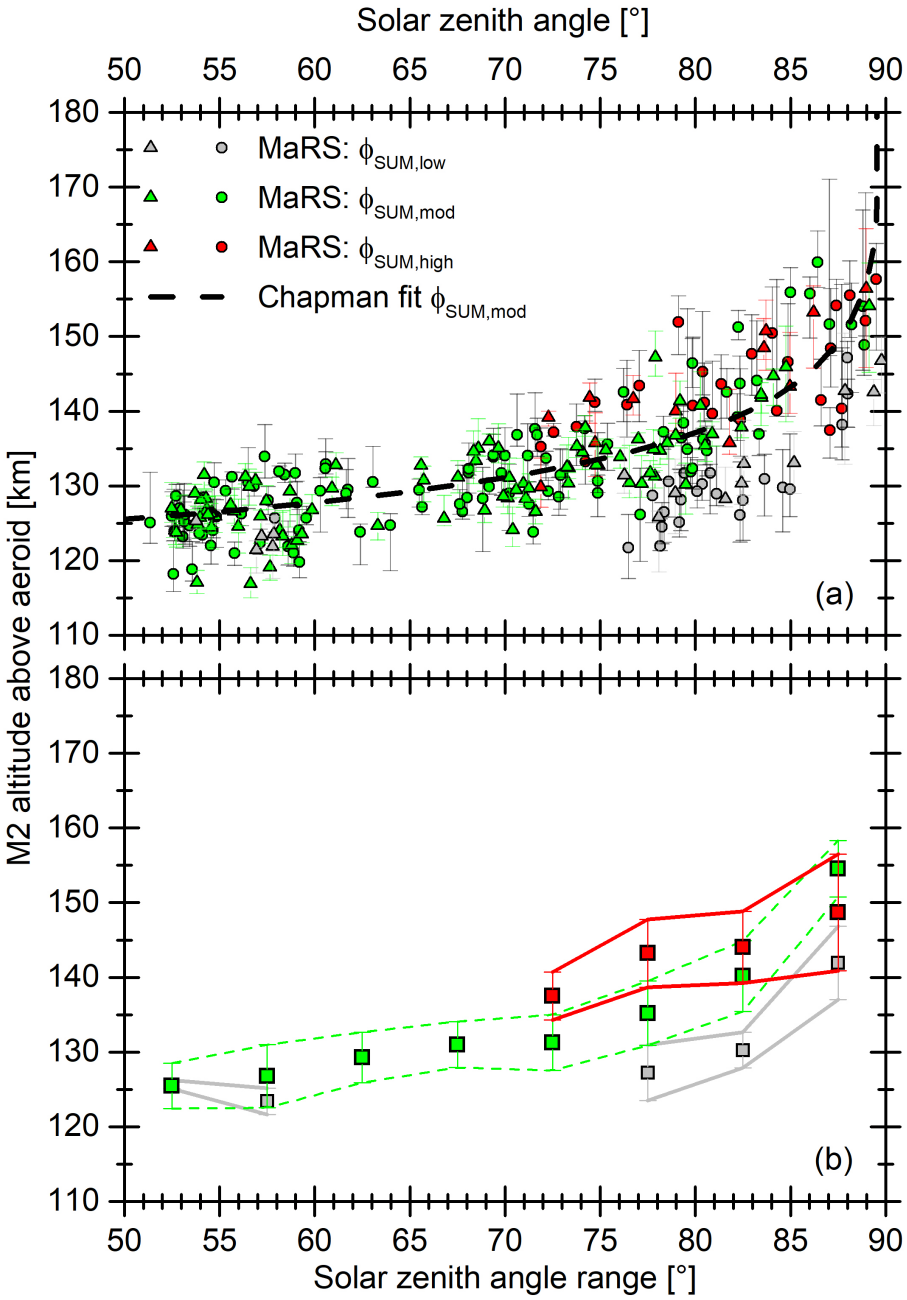

Figure 7.4: (a) Derived M2 altitude $h_{max}^{obs}(M2)$ with error bars for the $MaRS_{quiet}$ data set. (b) 5° solar zenith angle weighted average $\overline{h}_{max}^{obs}(M2)$ and weighted standard deviation of the all data in Panel (a). The color code is similar to those in Figure 7.2. The dashed lines illustrates the fit of the Chapman relation (7.6) on the moderate solar flux data. The derived parameter is $H_n = 8.8 \pm 0.3$ km.

	Slope M2 width vs. χ (km/°)	Slope $\Phi_{S,SUM}$ vs. χ [s^{-1} m^{-2}/°]
$\Phi_{SUM,low}$	- 0.002 ± 0.026	- 0.0035 ± 0.0015
$\Phi_{SUM,mod}$	0.093 ± 0.008	0.0103 ± 0.0007
$\Phi_{SUM,high}$	0.419 ± 0.094	0.0180 ± 0.0030

Table 7.1: Slopes of the M2 width and solar flux in dependence of the solar zenith angle derived from the fits in Figure 7.5 and 7.6.

high solar flux observations are available.

Figure 7.5 shows the observed M2 layer widths $h^{obs}_{width}(M2)$ with associated error bars. The linear fits illustrate the behavior of the M2 width due to the varying solar flux. The fit-slopes are listed in Table 7.1. In an ionosphere, developing in a single-species atmosphere by monochromatic radiation, with only locally constant H_n, an increase in M2 width with solar zenith angle can be caused by two effects:

i.) Increasing/decreasing solar flux between ionospheric observations can cause the neutral atmospheric temperature to rise/fall, generating higher/lower scale heights H_n by an expanding/collapsing atmosphere (Eq. 7.4).

ii.) The increasing M2 peak altitude for increasing zenith angle (see Fig. 7.4) may cause the formation of the M2 layer in altitude regions with a higher neutral scale height H_n.

Fig. 7.6 shows the Φ_{SUM} vs. χ dependence for the used MaRS observations, grouped into the three solar flux intervals. The resulting fit-slopes are listed in Table 7.1. There is only a very slight decrease in M2 width with increasing solar zenith angle for the $\Phi_{SUM,low}$ interval. This indicates, in combination with the decreasing Φ_{SUM} in Fig. 7.6, that the atmosphere cooled down slightly for the higher zenith angle observations. This would explain the absent M2 width increase for higher zenith angle data. For the $\Phi_{SUM,mod}$ and $\Phi_{SUM,high}$ intervals, the M2 width is increasing, as is the solar flux Φ_{SUM} with increasing χ. Therefore the increase in M2 width can be caused by higher neutral scale heights, by increasing Φ_{SUM}, and by the increase in M2 peak altitude, i.e. a main peak in regions of potential higher H_n.

7.2 The secondary layer M1

This Section correlates the behavior of the derived M1 parameters (Chapter 4) with selected environmental parameters (Chapter 5). For the M2 parameter comparison earlier

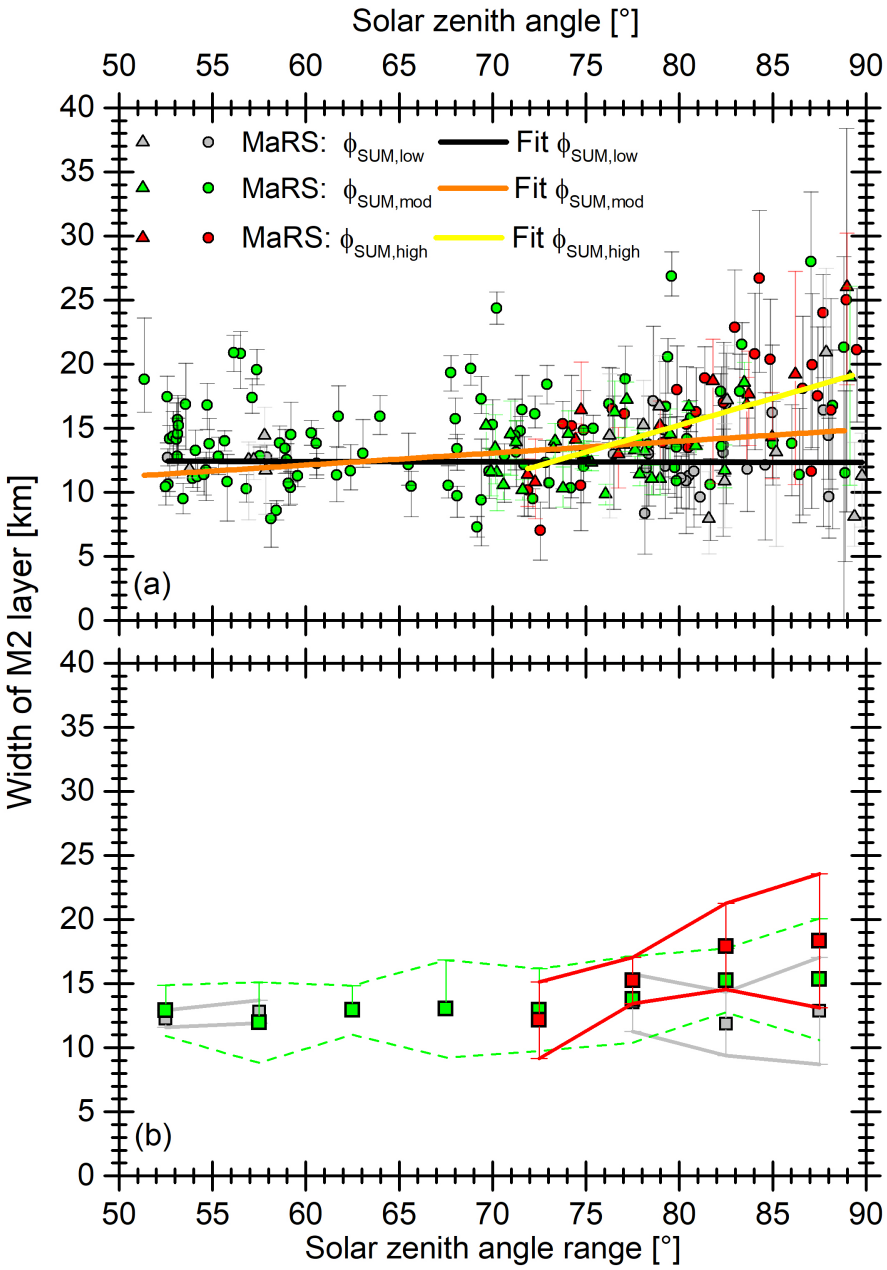

Figure 7.5: (a) Derived M2 width $h^{obs}_{width}(M2)$ with error bars for the $MaRS_{quiet}$ data set. (b) 5° solar zenith angle weighted average $\overline{h}^{obs}_{width}(M2)$ and weighted standard deviation of the data in Panel (a). The color code is similar to those in Figure 7.2. The slopes of the fitted lines can be found in Table 7.1.

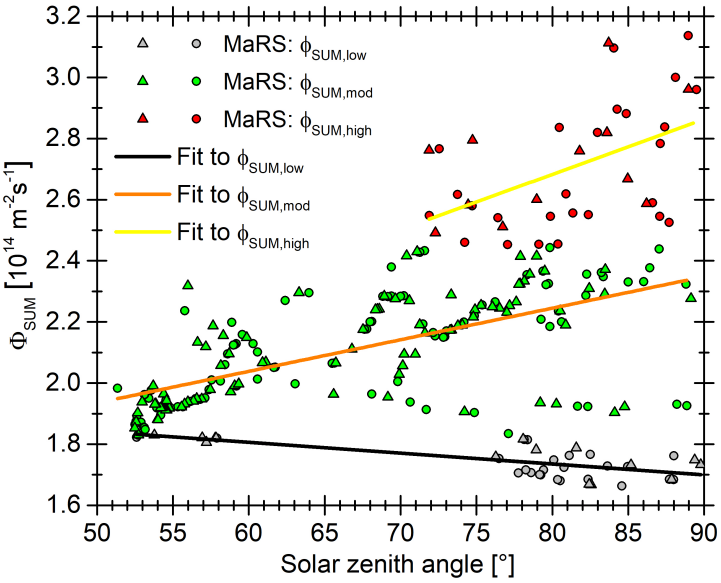

Figure 7.6: Derived Φ_{SUM} solar flux distribution for the $MaRS_{quiet}$ data set. The color code is similar to that in Figure 7.2.

in this Chapter, the selected MaRS observations are divided into the three defined intervals of the solar flux proxy Φ_{SUM}. However, the computations with IonA-1 show (Figure 6.5 in Chapter 6), that the model M1 layer is mostly produced by photoionization and secondary impact ionization by solar radiation with wavelength below 10 nm. Therefore the solar flux proxy Φ_{Xray} is used here for the correlations, which consists of the integrated SIP V2.38 model solar flux from 0.45 - 10 nm. The weighted average and weighted standard deviation are calculated from Eq. (7.1) and (7.2). Data points with only one visible error bar contain only the error in the indicated direction. The error detection method shows no variation of the M1 parameter in the opposite direction. For few M1 detections the variation in the M1 parameter shows no variation at all. For other M1 detections, the automatic error approximation did not work correctly (e.g. due to strong underestimation of the lower range of the M1 parameters by the automated M1 detection method). Those M1 parameters are not used for the calculation of the weighted average.

Panel (a) of Figure 7.7 contains the electron content $n_{TEC}^{obs}(M1)$ of the M1 layer. As for the vertical TEC of the full ionospheric profile n_{TEC}^{obs}, it is computed from Eq. (4.4), but here for the residual M1 layer after the linear fit. No Chapman-relation (Eq. 7.3) is fit to the M1 data, because a large factor in the M1 formation is secondary impact ionization which is not included in the classical Chapman-theory (*Chapman*, 1931a). This argument is valid for the subsequent M1 correlations. From the behavior of the full vertical TEC n_{TEC}^{obs} in Figure 7.2 it is exptected, that the M1 TEC also decreases with increasing χ. The MaRS data in Panel (a) of Figure 7.7 confirm this predicted behavior in general. The weighted average TEC values with the weighted standard deviation error bars in Panel

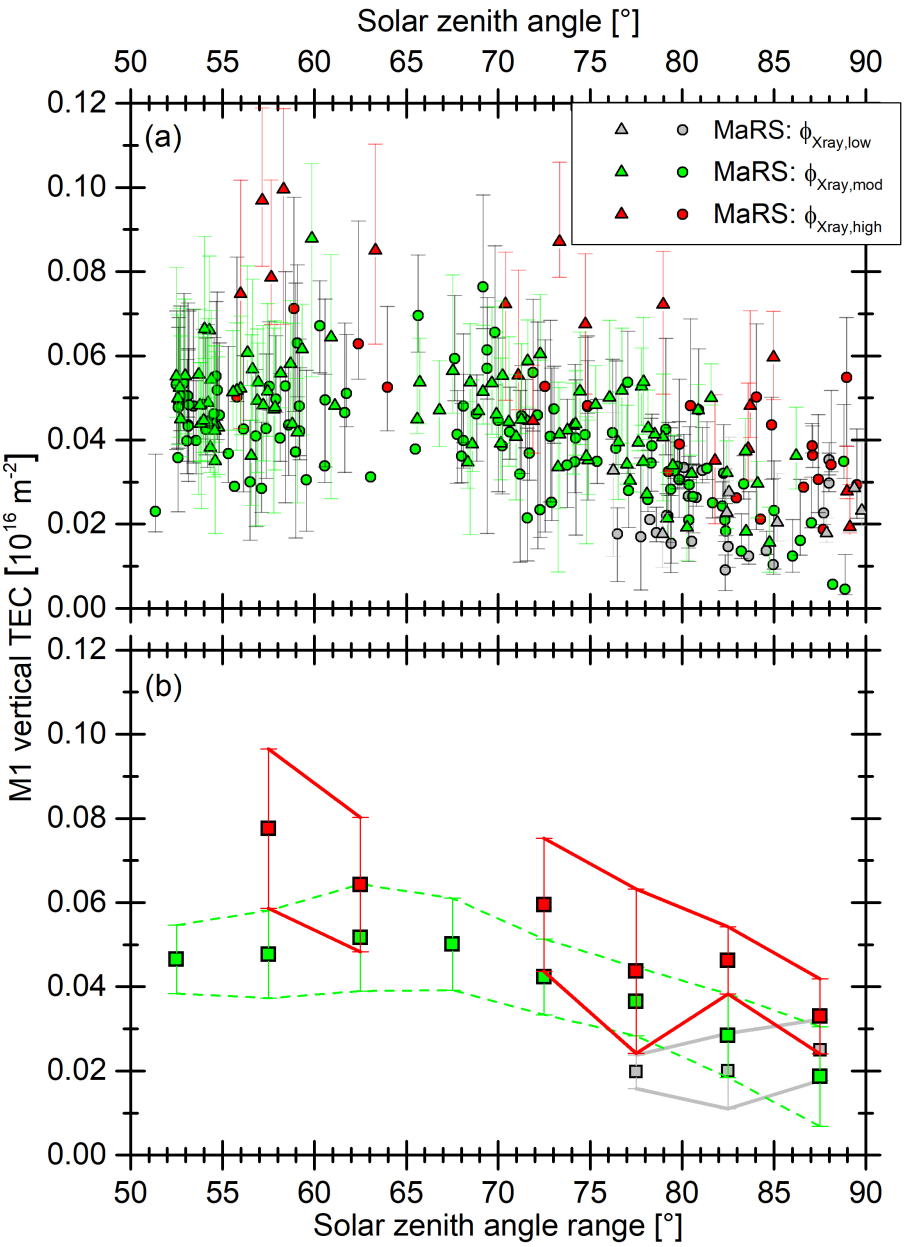

Figure 7.7: (a) Derived M1 TEC $n_{TEC}^{obs}(M1)$ with error bars for the $MaRS_{quiet}$ data set. Gray, green and red triangles indicate the $Mm_{a,3km}$ observations with detected merged layers. The respective colored circles indicate the remaining observations. (b) 5 ° solar zenith angle weighted average $\overline{n}_{TEC}^{obs}(M1)$ for the three solar proxy intervals $\Phi_{Xray,low}$ (gray), $\Phi_{Xray,mod}$ (green) and $\Phi_{Xray,high}$ (red). The error bars indicate the calculated weighted standard deviation of the data points. For 17 detected M1 electron densities, the automatic error approximation did not work. These data points are not included in the $\overline{n}_{TEC}^{obs}(M1)$ calculation and show no error bars.

(b) indicate, that the effect of the changing solar radiation on $n_{TEC}^{obs}(M1)$ is similar but slightly less clear than for n_{TEC}^{obs}. There are four possible explanations:

i.) Additional dynamic physical effects play a role in the M1 formation which is not important for the M2 main peak region.

ii.) The solar proxies are determined from the SIP V2.38 model flux for Earth calibrated for the Mars position. Due to the fact, that the solar flux has a higher variability in the X-ray than in the EUV, the Φ_{Xray} proxy might be less reliable for Mars than the Φ_{SUM} proxy.

iii.) The method for deriving the M1 parameters might weaken the relation between the solar flux proxy intervals and $n_{TEC}^{obs}(M1)$. The test with the 50 IonA-1 model electron density profiles in Panel (c) of Figure B.2 in Appendix B shows a slight underestimation of the derived center TEC compared to the "real" model TEC, even if the "real" model TEC is still found within the derived error bars.

iv.) The large derived error bars of the M1 TEC might diminish the derived M1 TEC dependence on the solar flux proxy intervals.

The M1 peak electron densities are derived in a similar way as the M2 peak electron densities, but for the M1 residual electron density. Panel (a) of Figure 7.8 contains the observed M1 peak densities $n_{e,max}^{obs}(M1)$ subdivided into the three Φ_{Xray} solar proxy intervals. Panel (b) contains the weighted average $\overline{n}_{e,max}^{obs}(M1)$ values with the weighted standard deviation error bars of the MaRS_{quiet} data in Panel (a). The M2 peak shows a decrease in peak electron density for decreasing solar flux when the solar zenith angles are equal. This behavior is found even stronger for the M1 peak electron density. However, the above discussed reasons for a dampening of the correlation between the solar proxy intervals and the M1 parameters are still valid. As shown in Panel (b) of Figure B.2 in Appendix B, the derived IonA-1 center M1 electron densities (determined with the M1 detection method from the IonA-1 model electron densities) slightly overestimate the "real" model M1 electron densities for approximately half of the data set. The "real" model electron densities are however still found in the derived M1 ranges.

The derived M1 peak altitudes $h_{max}^{obs}(M1)$ are shown in Figure 7.9. The clear increase for the M2 peak altitude with increasing solar zenith angle is also found for the M1 peak altitude. However, the M1 altitude increase from $\Phi_{Xray,low}$ to $\Phi_{Xray,high}$ solar proxy observations for similar solar zenith angles is less pronounced. The $\Phi_{Xray,mod}$ data even show a strange and inhomogeneous altitude behavior compared to the relation between the low and high solar flux proxy observations. Panel (a) of Figure B.2 in Appendix B shows, that the M1 altitude derived from the IonA-1 model ionospheres is close to the altitude of the "real" model ionosphere for most cases. Due to the fact, that the M1 TEC and M1 peak electron density are still correlated with the solar flux proxies similar to the M2 parameters, the found behavior is not easily explained. Using the solar flux proxy Φ_{SUM} for

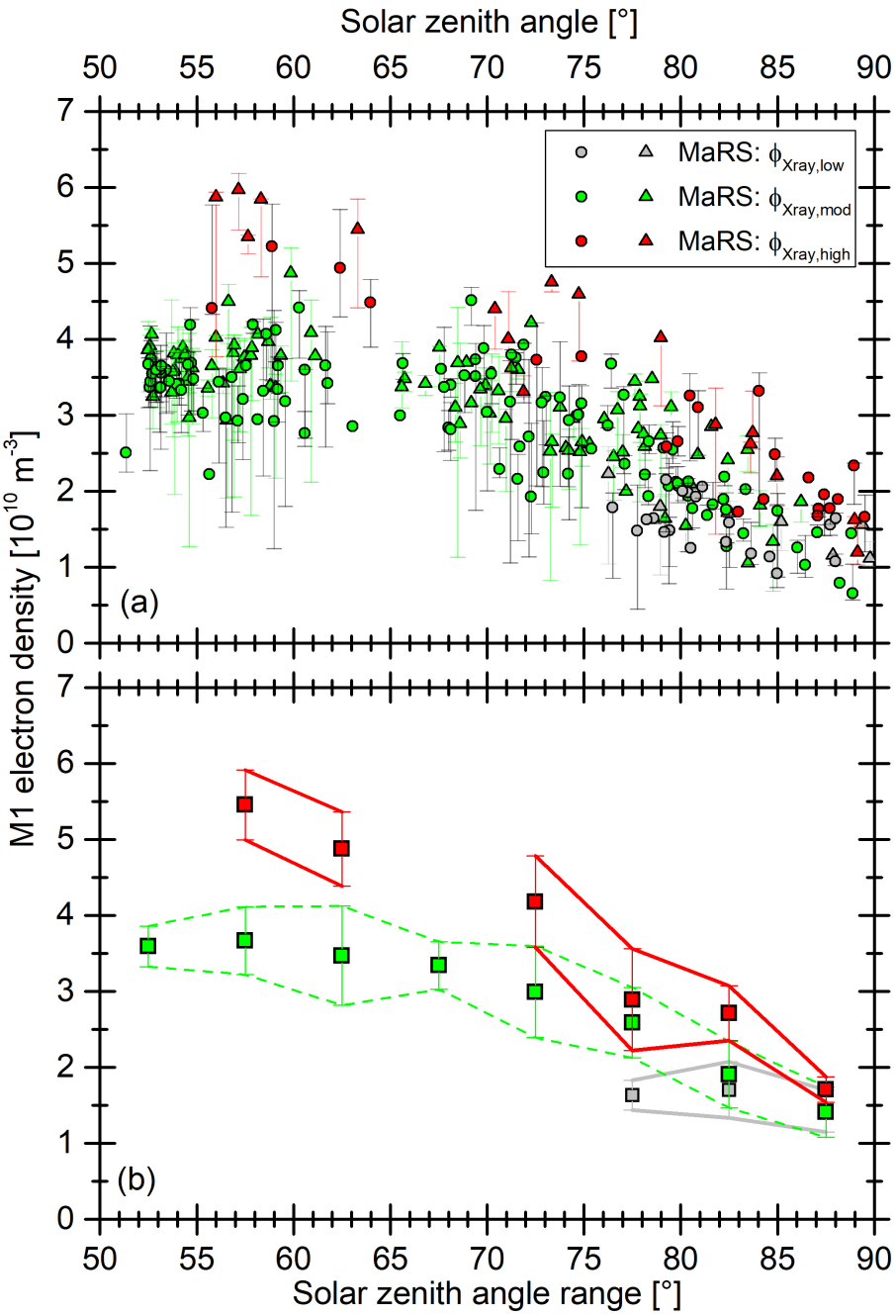

Figure 7.8: (a) Derived $n_{e,max}^{obs}(M1)$ *with error bars for the* $MaRS_{quiet}$ *data set. (b)* $5\,^{\circ}$ *solar zenith angle weighted average* $\overline{n}_{e,max}^{obs}(M1)$ *and weighted standard deviation of all data in Panel (a). The color code is similar to Figure 7.7. The error approximation did not work for 17* $n_{e,max}^{obs}(M1)$*, which are not included in the* $\overline{n}_{TEC}^{obs}(M1)$ *calculation. 23* $n_{e,max}^{obs}(M1)$ *show no variation in the M1 electron density. They are included in the weighted average with an assumed error of* $1 \cdot 10^9 m^{-3}$.

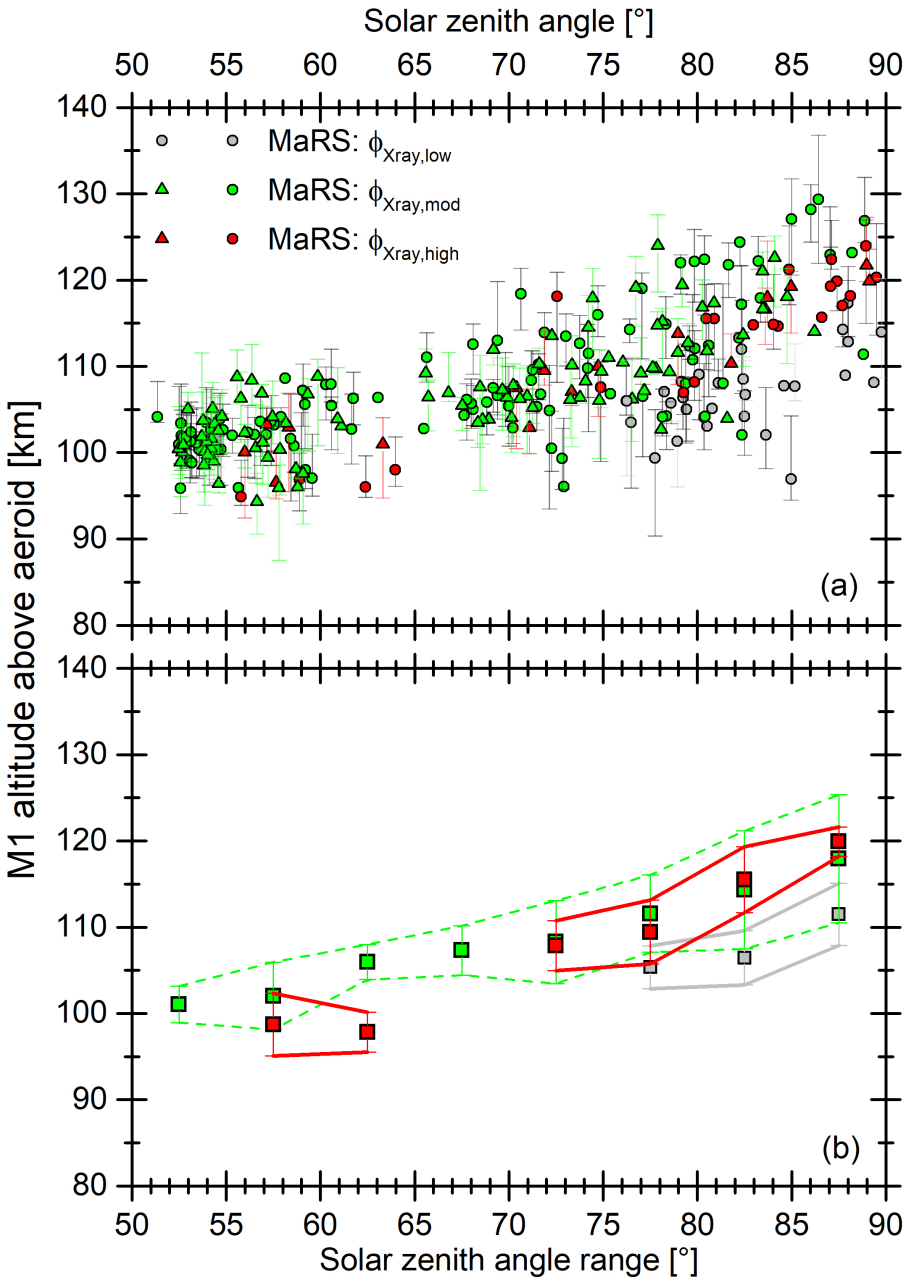

Figure 7.9: (a) Derived M1 altitude $h_{max}^{obs}(M1)$ with error bars for the $MaRS_{quiet}$ data set and Φ_{Xray} solar proxy. (b) 5° solar zenith angle weighted average $\overline{h}_{max}^{obs}(M1)$ and weighted standard deviation of all data in Panel (a). The color code is similar to Figure 7.7. The error approximation did not work for 17 $h_{max}^{obs}(M1)$, which are not included in the $\overline{h}_{max}^{obs}(M1)$ calculation. 24 $h_{max}^{obs}(M1)$ show no M1 altitude variation. They are included in the weighted average with an assumed error of 1 km.

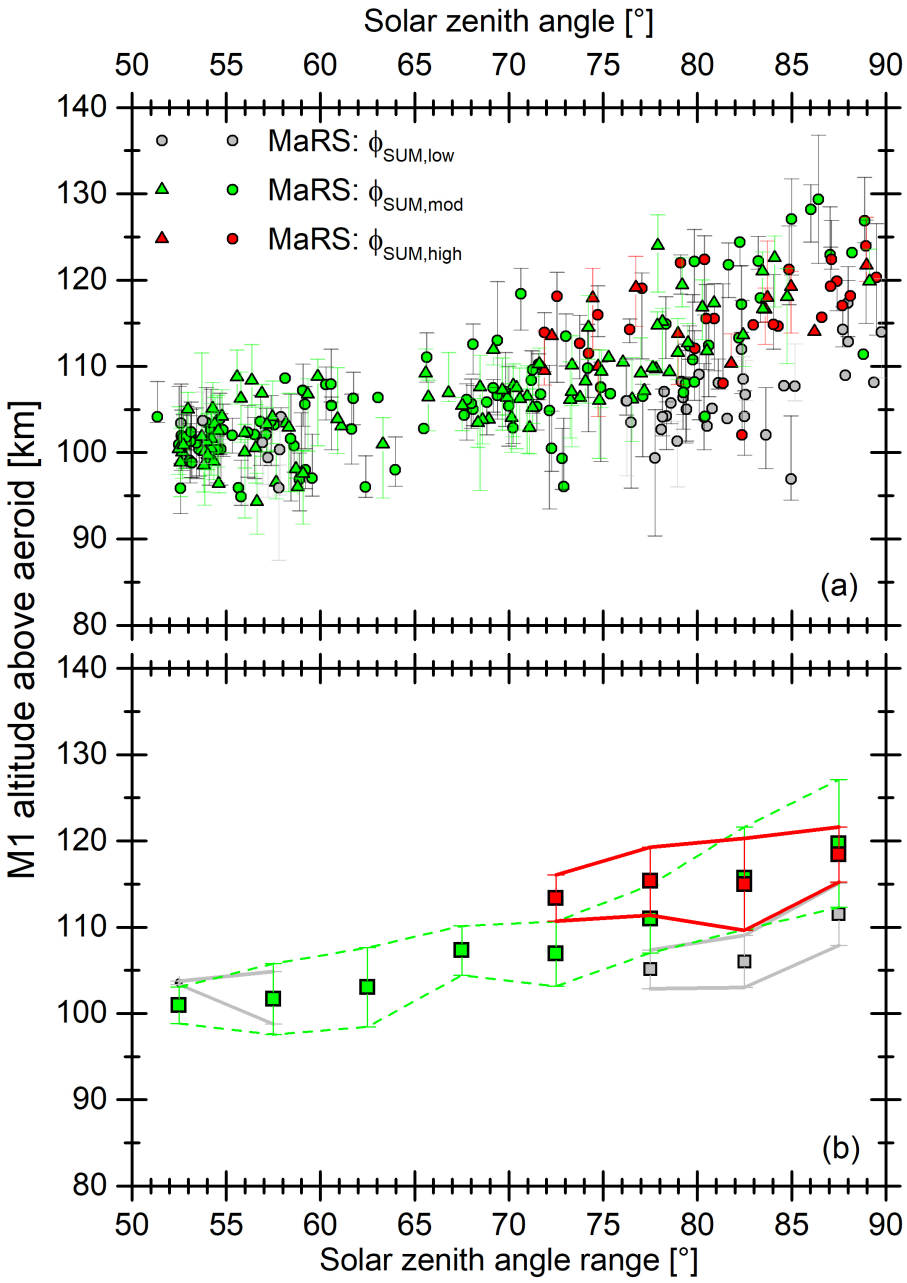

Figure 7.10: (a) Derived M1 altitude $h_{max}^{obs}(M1)$ with error bars for the $MaRS_{quiet}$ data set and Φ_{SUM} solar proxy intervals. (b) 5° solar zenith angle weighted average $\overline{h}_{max}^{obs}(M1)$ and weighted standard deviation of all data in Panel (a). The color code is similar to Figure 7.7. The error approximation did not work for 17 $h_{max}^{obs}(M1)$, which are not included in the $\overline{h}_{max}^{obs}(M1)$ calculation. 24 $h_{max}^{obs}(M1)$ show no M1 altitude variation. They are included in the weighted average with an assumed error of 1 km.

	Slope M1 width vs. χ (km/°)	Slope Φ_{Xray} vs. χ [s^{-1} m^{-2}/°]
$\Phi_{Xray,low}$	0.59 ± 0.15	0.0000 ± 0.0066
$\Phi_{Xray,mod}$	0.03 ± 0.01	0.0002 ± 0.0009
$\Phi_{Xray,high}$	0.07 ± 0.03	0.0002 ± 0.0021

Table 7.2: Slopes of the M1 width and solar proxies in dependence of the solar zenith angle derived from the fits in Figure 7.11 and 7.12.

$h^{obs}_{max}(M1)$ in Figure 7.10 yields slightly better results, especially for the low solar zenith angles. The M1 vertical TEC and M1 peak electron density are directly correlated with the X-ray solar flux. The altitude of the M1 peak however shows a better correlation with Φ_{SUM}, because the M1 altitude depends on the composition and temperature of the underlying neutral atmosphere, which is determined by the whole solar flux output of the Sun.

Figure 7.11 shows the observed M1 layer widths $h^{obs}_{width}(M1)$ with associated error bars. $h^{obs}_{width}(M1)$ is calculated as the difference between the upper and lower altitude where the M1 electron density reaches 50 % of $n^{obs}_{e,max}(M1)$. As discussed in Chapter 4, the M1 width determined by the M1 detection procedure does not provide information about the absolute state of the ionosphere as it is for the M2 layer. As shown in Panel (d) of Figure B.2 in Appendix B, the M1 width determined from the IonA-1 model is generally underestimated by the straight line procedure used for the M1 parameter detection. Therefore the width of the M1 layer can only be used to determine relative changes of $h^{obs}_{width}(M1)$ in dependence of environmental parameters, but not for determining the absolute state of the ionosphere. As for the M2 layer, the linear fits in Panel (a) of Figure 7.11 illustrate the behavior of the M1 width, but here in dependence of the Φ_{Xray} solar proxy. The fit-slopes are listed in Table 7.2. Figure 7.12 shows the Φ_{Xray} vs. χ dependence for the MaRS_{quiet} data set, grouped into the three solar proxy intervals. The resulting fit-slopes are listed in Table 7.2. The slopes for $\Phi_{Xray,low}$, $\Phi_{Xray,mod}$ and $\Phi_{Xray,high}$ are small compared to their error bars. The fluctuation of the parameters for $\Phi_{Xray,low}$ and $\Phi_{Xray,mod}$ is even higher than for their Φ_{SUM} equivalents. This is caused by the high variability in the solar X-ray output of the Sun. The small increase of the fit slope for the M1 width in the $\Phi_{Xray,mod}$ and $\Phi_{Xray,high}$ intervals and the strong increase of the fit slope for $\Phi_{Xray,low}$ indicate, that the increase in M1 width is caused by the increase of the M1 main peak altitude to higher altitudes, where the temperature is higher for the highest solar zenith angles. This is due to the fact, that the $\Phi_{Xray,low}$ M1 widths consist only of observations for high solar zenith angles, while the fit on the other two solar proxy intervals covers the full observable solar zenith angle range.

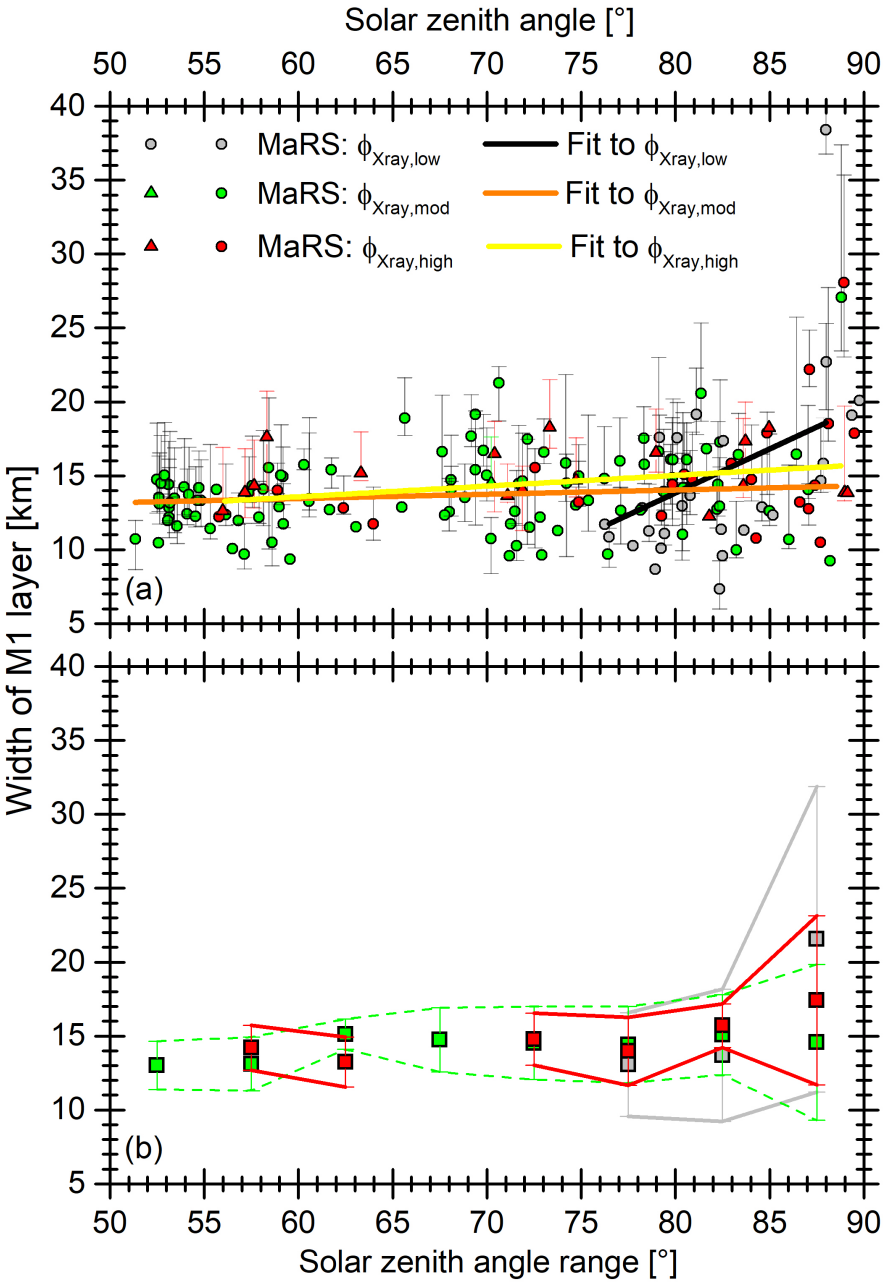

Figure 7.11: (a) Derived M1 width $h^{obs}_{width}(M1)$ with error bars for the $MaRS_{quiet}$ data set. (b) 5° solar zenith angle weighted average $\overline{h}^{obs}_{width}(M1)$ and weighted standard deviation of all data in Panel (a). The color code is similar to those in Figure 7.7. For 20 detected M1 parameters, the automatic error approximation did not work. Those data points are not included in the $\overline{h}^{obs}_{width}(M1)$ calculation.

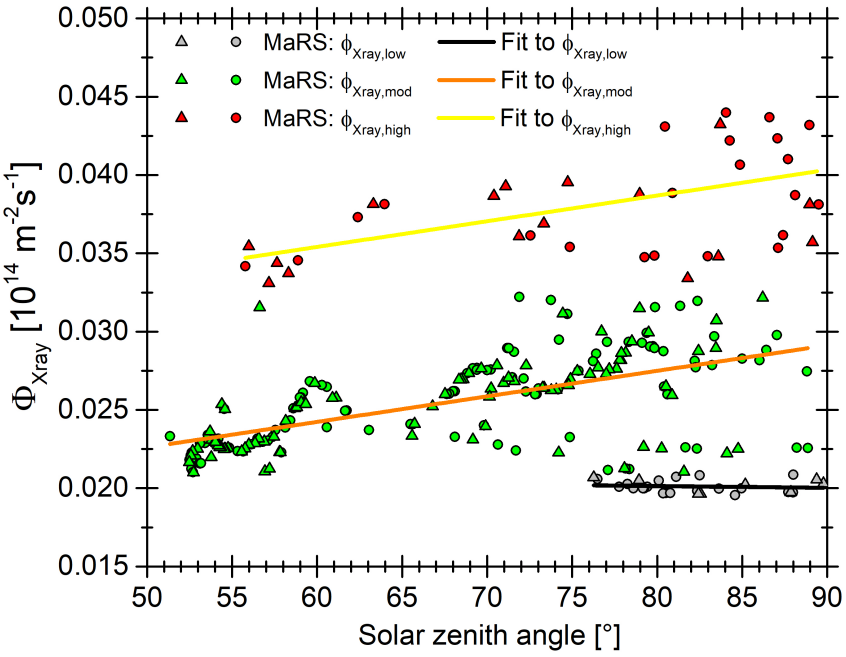

Figure 7.12: Derived Φ_{Xray} solar proxy distribution for the $MaRS_{quiet}$ data set. The color code is similar to that in Figure 7.7.

7.3 Merged excess electron density

The merged excess electron densities (Mm) derived in Chapter 4 are compared to a selection of observational (Chapter 4) and environmental parameters (Chapter 5) to draw conclusions about their potential formation processes. The vertical Mm TEC is based on the visible part of the merged excess density and is therefore (together with the lower altitude limit of the ionospheric profile h_L) its most reliable feature. Two categories of merged excess electron densities Mm_a and Mm_c have been defined in Chapter 4 based on this parameter. The Mm_a category is used to identify potential origins of the merged excess electron densities by investigating potential correlations with environmental parameters. The Mm_c category is a subcategory of Mm_a. It is used to prove that the sporadic Mm exist independently of disturbances introduced by the Abel inversion of ionospheric deviations from a radial-symmetric behavior. The plots found here are those for the $\mathrm{Mm}_{a,3km}$ and $\mathrm{Mm}_{c,3km}$ categories, while the plots for the $\mathrm{Mm}_{a,5km}$ and $\mathrm{Mm}_{c,5km}$ categories are found in Appendix D. Deviations between the $\mathrm{Mm}_{a,3km}/\mathrm{Mm}_{c,3km}$ and $\mathrm{Mm}_{a,5km}/\mathrm{Mm}_{c,5km}$ groups are discussed in the text if they occur.

7.3.1 Detectability of the merged excess electron densities

The merged excess electron density occurrence rate P_x

$$P_x = \frac{N_x}{N} \cdot 100.0 \tag{7.7}$$

is the number of Mm identifications N_x in all MaRS observations in the data set for a given interval N. P_x is used in this Section to show that the selected vertical TEC limit for the $\mathrm{Mm}_{a,3km}$ category (which is the lower TEC limit of $\mathrm{Mm}_{a,3km}$ and $\mathrm{Mm}_{a,5km}$) is chosen small enough to avoid the introduction of an unwanted bias by the detection method. For that, P_x is determined in dependence of the upper baseline noise level $\sigma_{noise,UB}$, the lower baseline noise level $\sigma_{noise,LB}$ and the lower baseline mean μ_{LB}.
Figure 7.13 shows the effect of the observational noise in the upper baseline $\sigma_{noise,UB}$ and the Mm identification process on the occurrence rate of the merged excess electron densities. Panel (a) contains the Mm occurrence rates for $\mathrm{Mm}_{a,3km}$ (called $P_{Mm,a}$) and $\mathrm{Mm}_{c,3km}$ (called $P_{Mm,c}$) in dependence of the upper baseline noise level $\sigma_{noise,UB}$. In additon, the occurrence rates of the potential merged excess electron densities (P_{pot}) are shown. They contain all potential Mm identifications of the detection algorithm described in Chapter 4, independent of their $n_{TEC}^{obs}(Mm)$. If the occurrence rates with $\sigma_{noise,UB} > 12 \cdot 10^8\, m^{-3}$ are neglected due to the low number of observations in those intervals, P_{pot} is decreasing for increasing $\sigma_{noise,UB}$. The same trend is found for $P_{Mm,a}$, but not for $P_{Mm,c}$. This might either be caused by the low number of only 31 Mm_c identifications in the MaRS_{quiet} data set due to the very strict applied boundaries or by a dominating other effect (e.g. spacecraft orbital geometry) caused by the additionally applied boundary conditions. Panel (b) of Figure 7.13 contains the individual TEC $n_{TEC}^{obs}(Mm)$ of the potential and detected merged excess electron densities. The red squares and error bars are the weighted mean $\overline{n}_{TEC}^{obs}(Mm)$ (Eq. 7.1) and weighted standard deviation $\overline{\sigma}_{TEC}^{obs}(Mm)$ (Eq. 7.2) of the $\mathrm{Mm}_{a,3km}$ data set, which includes the $\mathrm{Mm}_{c,3km}$ observations due to the fact that they are a subgroup of $\mathrm{Mm}_{a,3km}$. It is found, that the $\overline{n}_{TEC}^{obs}(Mm)$ values are increased at very low and high $\sigma_{noise,UB}$. Two explanations are found for the increased TEC at very low $\sigma_{noise,UB}$:

i.) The low number of only four MaRS observations in this interval might provide a non-representative sample of the available TEC (e.g. only detections for a certain solar flux) or

ii.) the extremely low upper baseline noise introduces no fake small merged excess densities (which would bias the $n_{TEC}^{obs}(Mm)$) into the observations.

The higher $\overline{n}_{TEC}^{obs}(Mm)$ for increasing $\sigma_{noise,UB}$ are explained by the bias introduced into the Mm groups during the identification process. Only those merged excess densities are included into $\mathrm{Mm}_{a,3km}$, which have a $n_{TEC}^{obs}(Mm)$ value larger than the limit defined in Relation 4.10. This limit depends on $\sigma_{noise,UB}$ and therefore causes an increase in $\overline{n}_{TEC}^{obs}(Mm)$

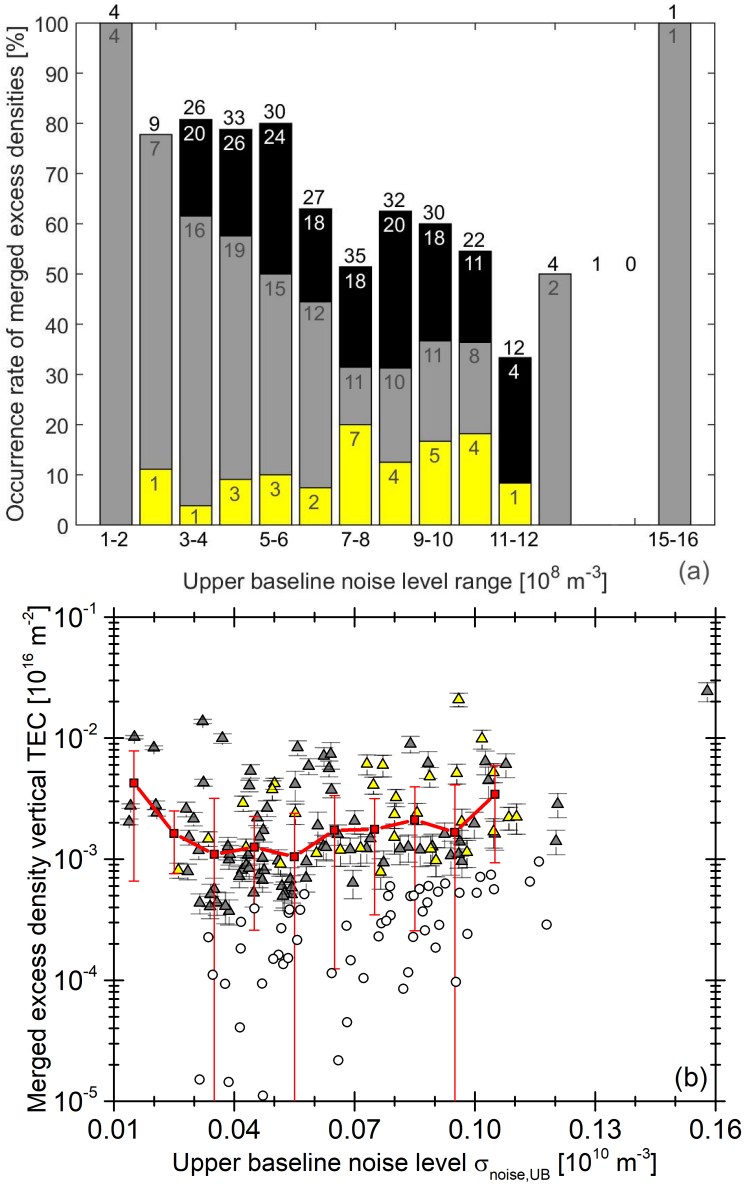

Figure 7.13: (a) P_x of all potential Mm (black), $Mm_{a,3km}$ (gray) and $Mm_{c,3km}$ (yellow) in dependence of $\sigma_{noise,UB}$. Numbers on top of the bars indicate all $MaRS_{quiet}$ observations in an interval. Numbers within the bars indicate the identifications in the respective Mm categories. (b) $n^{obs}_{TEC}(Mm)$ with error bars $\sigma^{obs}_{TEC}(Mm)$ for the potential Mm (black circles), $Mm_{a,3km}$ (gray triangles) and $Mm_{c,3km}$ (yellow triangles) in dependence of $\sigma_{noise,UB}$. Red squares and error bars are the respective weighted average and weighted standard deviation of $Mm_{a,3km}$. The deviation of the $n^{obs}_{TEC}(Mm)$ distribution/error bars from a regular Gaussian behavior cause some of the error bars to include negative values which cannot be fully shown in a logarithmic plot. Weighted average and standard deviations are calculated for intervals with more than 3 Mm detections only.

for increasing $\sigma_{noise,UB}$. The potential bias introduced in further correlations by the Mm identification method is accepted to avoid Mm misdetections caused by increased observational noise. It could be assumed, that the increased $\overline{n}^{obs}_{TEC}(Mm)$ for higher $\sigma_{noise,UB}$ is proof that the Mm identification method might partly cause the decrease of $P_{Mm,a}$ for increasing noise, but the effect of decreasing occurrence rates for increasing $\sigma_{noise,UB}$ is also visible in P_{pot}, where all merged excess densities are included independently of their level of $\sigma_{noise,UB}$. It is therefore assumed, that the decrease of $P_{Mm,a}$ for increasing $\sigma_{noise,UB}$ is mostly caused by the disguise of Mm with small $n^{obs}_{TEC}(Mm)$ by enlarged observational noise and not by the selected identification method.
It is therefore concluded, that

(1) an increased upper baseline noise level may obscure available merged excess densities.
Therefore only correlation tests with positive Mm detections are valid, correlation tests with the negative (no Mm excess densities detected) Mm occurrence rates are not feasible.

(2) merged excess densities are real features of the ionosphere.
The regularly occurring Mm in the $\mathrm{Mm}_{c,3km}$ group, which contains Mm with larger $n^{obs}_{TEC}(Mm)$ than $3,000m \cdot 3{\cdot}\sigma_{noise,LB}$ indicates, that merged excess densities exist independently of the additional electron density introduced by the Abel-transform of inhomogeneities of the above ionosphere / deviations from radial symmetry.

Figure 7.14 shows, that there is a correlation found between the upper baseline noise $\sigma_{noise,UB}$ and the lower baseline mean μ_{LB}. Therefore the dependence of the merged excess density occurrence rates on $\sigma_{noise,UB}$ might be passed on to the relation of P_x and $n^{obs}_{TEC}(Mm)$ with the lower baseline mean μ_{LB}. Panel (a) of Figure 7.15 contains the occurrence rates P_{pot}, $P_{Mm,a}$ and $P_{Mm,c}$ in dependence of the lower baseline mean μ_{LB}. Instead of the complete MaRS_{quiet} dataset, only those 175 MaRS observation of the data set are considered here as basic data for the P_x calculation, which have a minimum lower baseline of 15 km. This is done to avoid the introduction of bias into the calculation of μ_{LB} by extremely short lower baselines. While no clear linear dependence between the calculated occurrence rates and μ_{LB} is found, there are two distinct aspects visible in the plot. The first obvious feature is the accumulation of observations in the $[-1.0 \cdot 10^9\, m^{-3}$ to $0\, m^{-3}]$ and $[0\, m^{-3}$ to $1.0 \cdot 10^9\, m^{-3}]$ intervals. This is explained by the fact, that the lower baseline of an undisturbed ionospheric profile is expected to be close to $\mu_{LB} = 0$, with a small negative deviation for the lower baseline electron density derived from the differential Doppler. The maximum of $P_{Mm,c}$ at the $[0\, m^{-3}$ to $1.0 \cdot 10^9\, m^{-3}]$ interval is explained by a combination of the Mm_c group selection effect and the relation between μ_{LB} and $\sigma_{noise,UB}$. Only those merged excess densities are included into Mm_c, which have an absolute value of μ_{LB} smaller than $6{\cdot}\sigma_{noise,UB}$. As shown in Figure 7.14, the most negative μ_{LB} correspond with the lowest $\sigma_{noise,UB}$. Those observations therefore do not

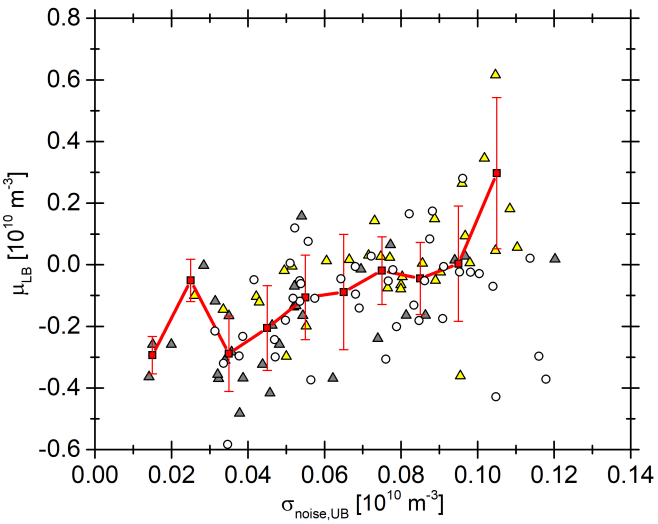

Figure 7.14: Lower baseline mean μ_{LB} in dependence of the upper baseline noise level $\sigma_{noise,UB}$. Only those Mm identifications from the 175 observations in the $MaRS_{quiet}$ data set are shown which have a lower baseline range > 15 km. The red squares are the calculated mean, the error bars and the standard deviation of the Mm_a fulfilling the above criterion. The color code of the dots/triangles is similar to that in Figure 7.13.

fulfill the boundary conditions and are not included in the Mm_c group. Figure 7.14 shows, that μ_{LB} increases for increasing $\sigma_{noise,UB}$. As long, as the increase in $\sigma_{noise,UB}$ is similar to the increase in μ_{LB} more observations are identified as Mm_c, which leads to a higher $P_{Mm,c}$. When the increase of μ_{LB} is stronger than that of $\sigma_{noise,UB}$, the observations are no longer included in Mm_c. Therefore a maximum must occur in $P_{Mm,c}$.
The second obvious feature in the bar plot is, that the potential Mm with the highest negative μ_{LB} have very low $n_{TEC}^{obs}(Mm)$ in comparison with the $n_{TEC}^{obs}(Mm)$ of the two Mm detections with the highest positive μ_{LB}. The explanation for that is found in the relation between the $n_{TEC}^{obs}(Mm)$ and the average deviation of the lower baseline from the zero line μ_{LB}. The effect which causes a positive μ_{LB} does also influence the area where the Mm occur. Therefore an increase in μ_{LB} should cause an increase in $n_{TEC}^{obs}(Mm)$, while a decrease in μ_{LB} is expected to lead to a a decrease in μ_{LB}. The behavior seen in the extreme examples is not obvious for the full data set in Panel (b) of Figure 7.15. The effect might be weak compared to other influences which play a role in the amount of available $n_{TEC}^{obs}(Mm)$.
It is therefore concluded, that

(3) no clear correlation effect is found between the Mm_a occurrence rates and μ_{LB}.

(4) the Mm_c category is not used for further correlation with environmental parameters.

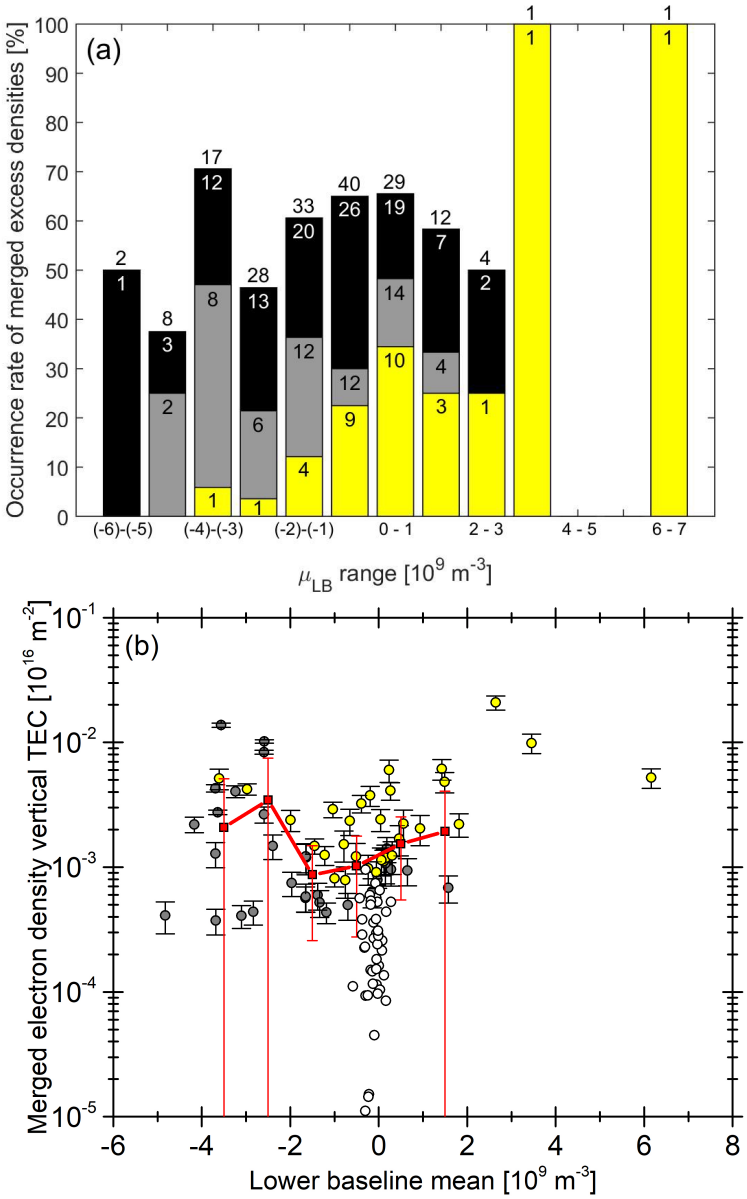

Figure 7.15: (a) P_{pot}, $P_{Mm,a}$ and $P_{Mm,c}$ for the 175 Mm from $MaRS_{quiet}$ where the range of the lower baseline exceeds 15 km in dependence of $1.0 \cdot 10^9\,m^{-3}$ bins of μ_{LB}. (b) $n_{TEC}^{obs}(Mm)$ with error bars $\sigma_{TEC}^{obs}(Mm)$ for the potential Mm (black circles), $Mm_{a,3km}$ (gray triangles) and $Mm_{c,3km}$ (yellow triangles) groups in dependence of μ_{LB}. Red squares and error bars are the calculated weighted average and weighted standard deviation in the intervals defined in Panel (a). The deviation of the $n_{TEC}^{obs}(Mm)$ distribution/error bars from a regular Gaussian behavior cause some error bars to include negative values which cannot be fully shown in a logarithmic plot. The weighted average and standard deviation are calculated for intervals with more than 3 Mm detections. The color code and numbering is similar to that in Figure 7.13.

The low number of observations in this category in combination with the bias caused by the chosen category conditions prevent this application.

7.3.2 The dependence of the merged excess electron densities on observational and environmental parameters

The previous Section showed, that the merged excess electron densities are real features of the Mars dayside ionosphere and that the feasible category for further investigations is the Mm_a category. In this Section correlations of $Mm_{a,3km}$ are conducted with further observational and environmental parameters. The $Mm_{c,3km}$ results are shown for completeness. Significant plots for the $Mm_{a,5km}$ and $Mm_{c,5km}$ categories are provided in Appendix D and are discussed in the text.
Figure 7.16 illustrates the solar zenith angle χ distribution of $Mm_{a,3km}$ and $Mm_{c,3km}$. Panel (a) contains the Mm occurrence rate distribution with χ, while Panel (b) contains the $\sigma_{noise,UB}$ level of the $MaRS_{quiet}$ data set in dependence of their associated solar zenith angles. While $P_{Mm,a}$ shows a weak decrease for increasing χ, no clear dependence of $\sigma_{noise,UB}$ on χ is found except for the fact, that for solar zenith angles above 85 ° no observations with $\sigma_{noise,LB} < 5 \cdot 10^8 m^{-3}$ are found.
The important facts from the above investigations are:

(1) 117 $Mm_{a,3km}$ observations out of the 266 $MaRS_{quiet}$ observations contain merged excess densities, which is approximately 44%.
90 $Mm_{a,5km}$ observations of the 239 $MaRS_{quiet,5km}$ observations contain merged excess densities, which is approximately 38%.

(2) The merged excess electron densities show a wide range of shapes already illustrated in Figure 4.7 of Chapter 4.

(3) Merged excess densities are identified for all solar zenith angles on the planetary dayside accessible with MaRS.

(4) A small decrease in $P_{Mm,a}$ is found for decreasing solar zenith angle.

The crustal magnetic field of Mars may play an important role in the formation of the Mm excess densities. On Earth (details in Chapter 2), sporadic E layers occur below the ionospheric main peak which can have peak magnitudes similar to those in the F region. The most widely accepted theory for the sporadic E layer formation on Earth is the wind-shear theory. When charged particles are dragged along with neutral winds in the Earth global magnetic field, the combination of wind-shear regions and Lorentz-force can cause the accumulation of long-lived ions into sporadic E layers. The influx of meteoric material on Mars in combination with the photochemical ionization reactions and the crustal magnetic field might cause the local formation of sporadic E layers on Mars. This

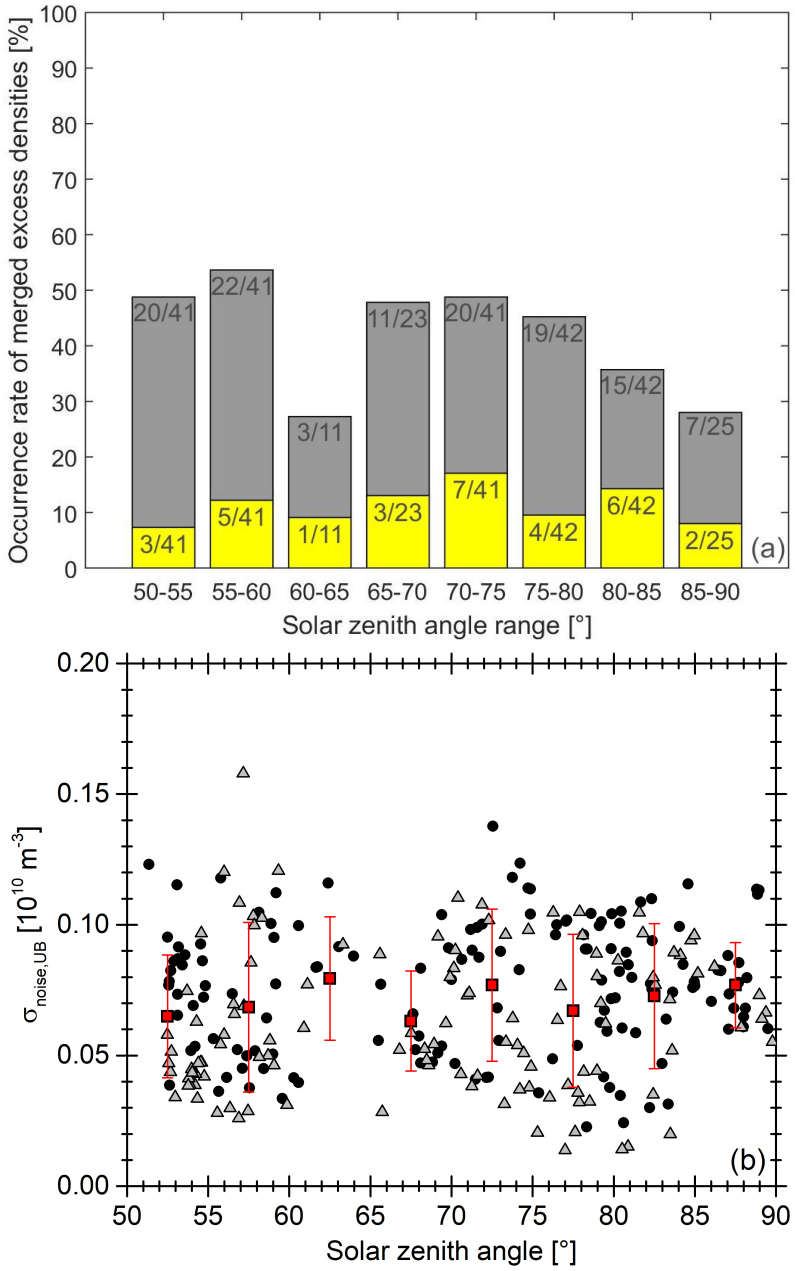

Figure 7.16: (a) Occurrence rates of $Mm_{a,3km}$ and $Mm_{c,3km}$ in dependence of 5° solar zenith angle bins. The color code and numbering is similar to that in Figure 7.13. (b) $\sigma_{noise,UB}$ distribution in dependence of the solar zenith angle χ for the $MaRS_{quiet}$ data set. $Mm_{a,3km}$ data are illustrated by filled gray triangles, the remaining $MaRS_{quiet}$ observations without merged excess density detections as filled black dots. Red squares and error bars are the average and standard deviation of the $MaRS_{quiet}$ data sets for 5° solar zenith angle intervals.

B_{tot} [nT]		observations			B_{tot} [nT]		observations		
low	up	all [#]	Mm [#]	Mm [%]	low	up	all [#]	Mm [#]	Mm [%]
0	10	199	95	47.7	80	90	1	0	0.0
10	20	37	13	35.1	90	100	1	1	100.0
20	30	9	2	22.2	100	110	0	0	0.0
30	40	2	0	0.0	110	120	2	1	50.0
40	50	8	3	37.5	120	130	0	0	0.0
50	60	5	1	20.0	130	140	0	0	0.0
60	70	1	1	100.0	140	150	0	0	0.0
70	80	0	0	0.0	150	160	1	0	0.0

Table 7.3: Occurrence rates of $Mm_{a,3km}$ in dependence of the total crustal field strength B_{tot}. The first two columns contain the lower and upper B_{tot} interval limits, column 3 contains all $MaRS_{quiet}$ observations in the given interval, column 4 contains the number of $Mm_{a,3km}$ detections and column 5 the Mm occurrence percentage.

hypothesis is tested by investigating if the occurrence rate of $\mathrm{Mm}_{a,3km}$ is correlated with the total strength of the Mars crustal magnetic field B_{tot} in 400 km altitude. Table 7.3 contains the number of MaRS_{quiet} observations binned into 10 nT intervals of B_{tot}. As it it already visible from Figure 7.1, almost 75 % of the MaRS_{quiet} observations are from regions with B_{tot} lower than 10 nT. Those are very small magnitudes, because the crustal magnetic field vectors derived by *Connerney et al.* (2001) for the Martian surface are rarely zero. Including all observations below 20 nT increases the percentage to almost 89% and including all observations below 30 nT yields more than 92% of the MaRS_{quiet} data set. No clear increase in the Mm occurrence rate is found for increasing magnitude of B_{tot}.
This leads to the following results:

(5) The investigation of the correlation between the occurrence rate of merged excess electron densities and strong crustal magnetic fields is inconclusive.
The low number of available MaRS_{quiet} observations for high B_{tot} makes it impossible to draw reliable conclusions about the occurrence rate of merged excess electron densities for higher magnetic field strength B_{tot}. More observations above the high crustal magnetic field regions, especially on the southern hemisphere, are required.

(6) Mm excess densities are available above regions with very low crustal magnetic field. This implies, that the formation mechanism for the identified merged excess electron densities may differ from the wind-shear theory on Earth.

The integrated vertical TEC of the whole ionospheric profile n_{TEC}^{obs} and the main peak electron density $n_{e,max}^{obs}(M2)$ show a dependence on the Φ_{SUM} solar proxy intervals, while

	all	$Mm_{a,3km}$		$Mm_{c,3km}$			all	$Mm_{a,3km}$		$Mm_{c,3km}$	
	[number]	[number]	[%]	[number]	[%]		[number]	[number]	[%]	[number]	[%]
Φ_{SUM}						Φ_{EARTH}					
low	39	15	**38.5**	7	**17.9**	*low*	26	7	**26.9**	5	**19.2**
moderate	189	90	**47.6**	17	**9.0**	*moderate*	207	92	**44.4**	19	**9.2**
high	38	12	**31.6**	7	**18.4**	*high*	33	18	**54.5**	7	**21.2**
Φ_{Xray}											
low	28	8	**28.6**	5	**17.9**						
moderate	199	92	**46.2**	19	**9.5**						
high	39	17	**43.6**	7	**17.9**						
$\Phi_{0.45\text{-}3.0}$						$\Phi_{0.45\text{-}1.0}$					
low	100	41	**41.0**	13	**13.0**	*low*	97	40	**41.2**	12	**12.4**
moderate	125	57	**45.6**	12	**9.6**	*moderate*	131	60	**45.8**	13	**9.9**
high	41	19	**46.3**	6	**14.6**	*high*	38	17	**44.7**	6	**15.8**

Table 7.4: Occurrence rate of $Mm_{a,3km}$ and $Mm_{c,3km}$ in the low, moderate and high Φ_{SUM}, Φ_{Xray}, $\Phi_{0.45-3nm}$, $\Phi_{0.45-1nm}$ and Φ_{EARTH} solar proxy intervals. For each parameter, the first column contains all $MaRS_{quiet}$ observations in a given solar proxy interval, the second column contains the number of Mm occurrences, the third column the occurrence percentage, while the fourth and fifth columns contain the number and percentage of $Mm_{c,3km}$ observations in each solar proxy interval.

the M1 TEC $n_{TEC}^{obs}(M1)$ and maximum electron density $n_{e,max}^{obs}(M1)$ are related with the Φ_{Xray} solar parameter. Therefore the question arises, if the occurrence rate of the merged excess densities depends on the amount of solar flux available at Mars and/or on the general solar activity cycle (e.g. by the number of occurring flares). This is investigated in Table 7.4 for the solar parameters Φ_{SUM}, Φ_{Xray}, $\Phi_{0.45-3nm}$, $\Phi_{0.45-1nm}$ and Φ_{EARTH}. While the SIP V2.38 integrated solar flux for Φ_{SUM}, Φ_{Xray}, $\Phi_{0.45-3nm}$ and $\Phi_{0.45-1nm}$ is calibrated for the position of Mars, the values for Φ_{EARTH} are taken directly from the solar flux model without any time or distance calibration. A potential correlation between the Mm occurrence rate and the Mars solar flux parameters indicates a connection of the excess densities with the amount of SIP V2.38 solar flux available at the Mars position. A potential correlation with Φ_{EARTH} indicates a correlation with the Sun's general solar activity level. As discussed in Chapter 5, the Sun's activity level cannot be directly inferred from Φ_{SUM} due to the eccentricity of the Mars orbit (see solar flux variation at the Mars position in the middle Figure of Panel (b) in Fig. 5.2). The results in Table 7.4 indicate no correlation between the Mm occurrence rate and the Φ_{SUM} solar flux ranges. As shown in Chapter 6, solar X-ray radiation below 10 nm is penetrating deepest into the Mars atmosphere. This is the part of the solar radiation spectrum primarily responsible for the formation of the M1 layer. If transport processes and the effects of

precipitating solar energetic particles are neglected, only this radiation range is capable of producing ions in the lowest ionospheric altitude region. So the lower wavelength solar proxies might yield a better base for a correlation. The Mm occurrence rates for the solar flux intervals of Φ_{Xray}, $\Phi_{0.45-3nm}$ and $\Phi_{0.45-1nm}$ show a partial increase for increasing solar flux. This correlation is, however, quite weak. Small decreases/increasing of the detected Mm in the high solar flux intervals would already change the found correlations due to the low number of observations in those intervals. For the Φ_{EARTH} solar flux intervals, the correlation is much more stable. The behavior of the Mm identifications in the $\mathrm{Mm}_{a,5km}$ (Appendix D, Table D.1) is similar.
The found results indicate the following:

(7) The activity level of the Sun may play a key role in the origin of the Mm excess densities.
The strong correlation between the Mm occurrence rate and Φ_{EARTH} indicates a relation of the Mm formation with the Sun's activity level. As discussed in Chapter 2, eruption processes (e.g. solar flares) are a source for short solar X-ray, which increases for an increasing solar activity level. Short solar X-ray is therefore a potentially important source for the formation of the merged excess electron densities in the otherwise undisturbed planetary atmosphere.

(8) The solar radiation spectrum provided by the SIP V2.38 with a resolution of one data set per day for the Earth orbit might not be sufficient to reproduce the short solar X-ray at the Mars position at all times.
Even if the calibrated proxies Φ_{SUM} and Φ_{Xray} show a correlation with the vertical TEC and peak densities of the M2 and M1 layers, Φ_{EARTH} seems to be a better indicator for the amount of available short solar X-ray at the Mars position. The range of Φ_{Xray} might be too wide to provide a correlation with the electron density at the lower boundary of the dayside ionosphere. The spatial and temporal variability of the Sun's short X-ray output is too high as that SIP V2.38 can be a reliable indicator at the Mars position. The MVN-LPW-EUV photometers (see Chapter 2) provide the soft solar X-ray and EUV irradiance (0.1-3 nm and 17-22 nm, 0.1-7 nm, 121-122 nm) for Mars from the end of 2014 until today. These observations will be used to correlate the occurrence of merged excess electron densities with the short X-ray solar radiation at Mars for the upcoming occultation seasons.

The vertical TEC and peak electron density of the M2 and M1 regions show a dependence on the solar flux proxies in combination with the solar zenith angle. Panel (a) of Figure 7.17 shows $n_{TEC}^{obs}(Mm)$ in dependence of χ, with color coded low, moderate and high $\Phi_{0.45-3nm}$ ranges. The comparison with the $\Phi_{0.45-3nm}$ proxy is shown here, because it provides the clearest correlation with the Mm occurrence rate (see Table 7.4). The plots for the correlation with the $\Phi_{0.45-1nm}$ and Φ_{Xray} proxies are provided in the Appendix for $\mathrm{Mm}_{a,3km}$ and $\mathrm{Mm}_{a,5km}$ (Figure D.1 to D.5). Panel (b) of Figure 7.17 contains the weighted

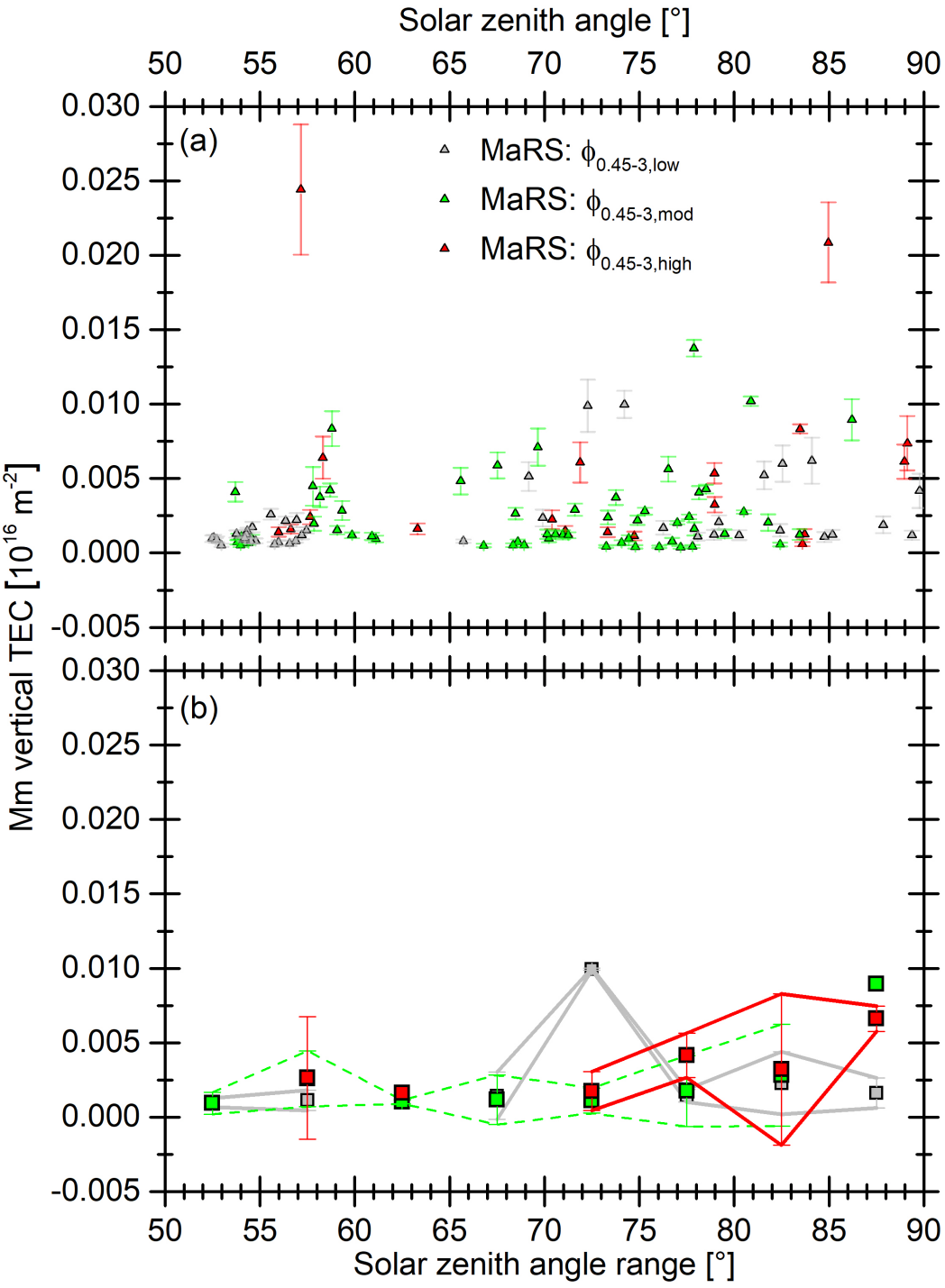

Figure 7.17: (a) $Mm_{a,3km}$ vertical TEC in dependence of the solar zenith angle χ. (b) The weighted average Mm TEC $\overline{n}^{obs}_{TEC}(Mm)$ (squares) and weighted standard deviation (error bars) calculated for 5° solar zenith angle bins and the $\Phi_{0.45-3nm}$ proxy levels used in Panel (a).

average $\overline{n}^{obs}_{TEC}(Mm)$ (Eq. 7.1) and weighted standard deviation (Eq. 7.2) of the data in Panel (a) to provide a clearer view of potential $n^{obs}_{TEC}(Mm)$ dependences on the SIP V2.38 model solar flux. The weighted standard deviation in the $55\,^\circ - 60\,^\circ$ bin and the $80\,^\circ - 85\,^\circ$ bin includes negative values due to the included high TEC outliers in those solar zenith angle bins. It is obvious, that no clear difference is found for the $n^{obs}_{TEC}(Mm)$ for low and high proxy values. Similar results are found for $\mathrm{Mm}_{a,3km}$ and $\mathrm{Mm}_{a,5km}$ in combination with the $\Phi_{0.45-1nm}$ and $\Phi_{0.45-3nm}$ solar proxies. An explanation for the lack of correlation between the $n^{obs}_{TEC}(Mm)$ and the derived SIP V2.38 model solar flux parameters is already discussed in the preceding paragraph. Another explanation is provided by the fact, that not the full merged excess density layer is visible due to the presence of the M1 layer.

Panel (a) of Figure 7.18 shows the Mm maximum altitudes $h^{obs}_{max}(Mm)$ and their upper $h_{U,smooth}(Mm)$ and lower $h_{L,smooth}(Mm)$ borders in comparison to the smoothed lower border of the undisturbed profiles $h_{L,smooth}$. Panel (b) shows the data of Panel (a) separately averaged in $5\,^\circ$ solar zenith angle bins. The average $h_{L,smooth}$ values of the Mm profiles are found lower in the atmosphere than the average $h_{L,smooth}$ values of the undisturbed profiles. However, the error bars of the averaged Mm and undisturbed profiles still overlap, except for the highest solar zenith angle data. This implies, that the effect of the Mm excess densities is relatively weak compared with the variation of the lower ionospheric border. The altitude differences between $\mathrm{Mm}_{a,5km}$ and the associated undisturbed profiles is even larger than for the $\mathrm{Mm}_{a,3km}$ category (see Fig. D.6 in the Appendix).
This leads to the following results:

(9) The merged excess electron densities are found in an altitude region between approximately 70 to 110 km altitude.

(10) The smoothed lower borders of the merged excess electron densities in MaRS_{quiet} are on average found in lower altitudes than the smoothed lower borders of the undisturbed profiles.
This is another indication, that the source for the merged excess electron densities in the undisturbed dayside ionosphere is short solar X-ray ray radiation, which causes the primary ionization at the lower base of the ionosphere.

(11) The increase of the lower ionospheric base for the undisturbed profiles is mirrored by the observations containing merged excess electron densities.
This is an expected behavior if the primary source for the Mm region is short solar X-ray.

After investigating the altitude distribution of the merged excess densities, it will be tested, if the physical processes causing the Mm excess densities are restricted to the altitude region of the visible excess density or if the effect extends up into the M1 layer or even alters the full ionospheric profile. Panel (a) of Figure 7.19 compares the reduced full profile TEC (n^{obs}_{TEC}-$n^{obs}_{TEC}(Mm)$) of the $\mathrm{Mm}_{a,3km}$ excess densities with the

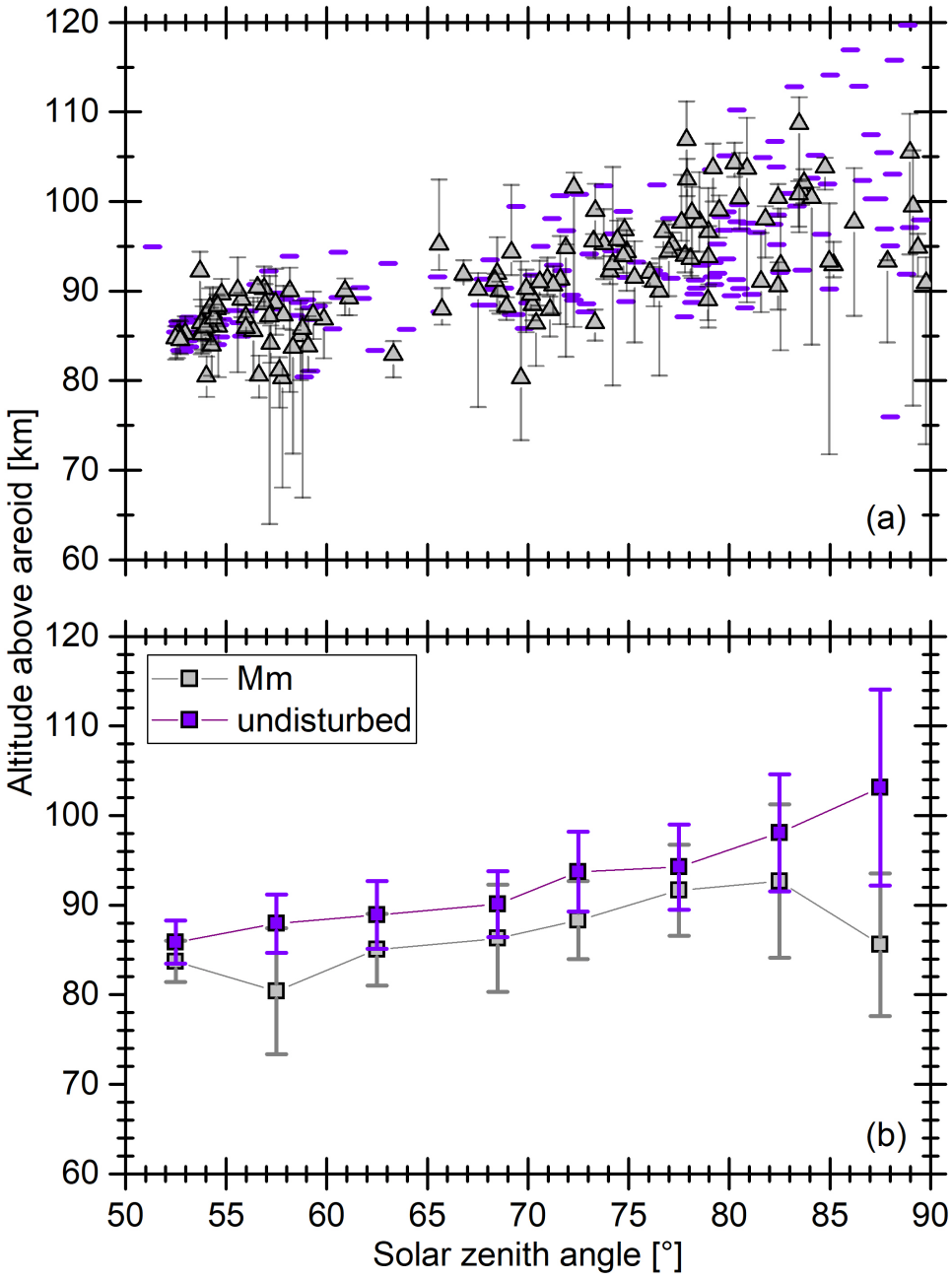

Figure 7.18: Comparison between the $Mm_{a,3km}$ altitude ranges and the smoothed lower border of the undisturbed $MaRS_{quiet}$ observations. (a) Gray triangles indicate the Mm altitude $h^{obs}_{max}(Mm)$. The upper and lower error bars indicate the smoothed upper $h_{U,smooth}(Mm)$ and lower $h_{L,smooth}(Mm)$ borders of the Mm excess density. The violet minuses indicate the smoothed lower borders $h_{L,smooth}$ of the undisturbed $MaRS_{quiet}$ profiles. (b) $h_{L,smooth}$ of the Mm and undisturbed profiles, separately averaged in 5° solar zenith angle bins. The given error bars indicate the calculated standard deviation of the data points.

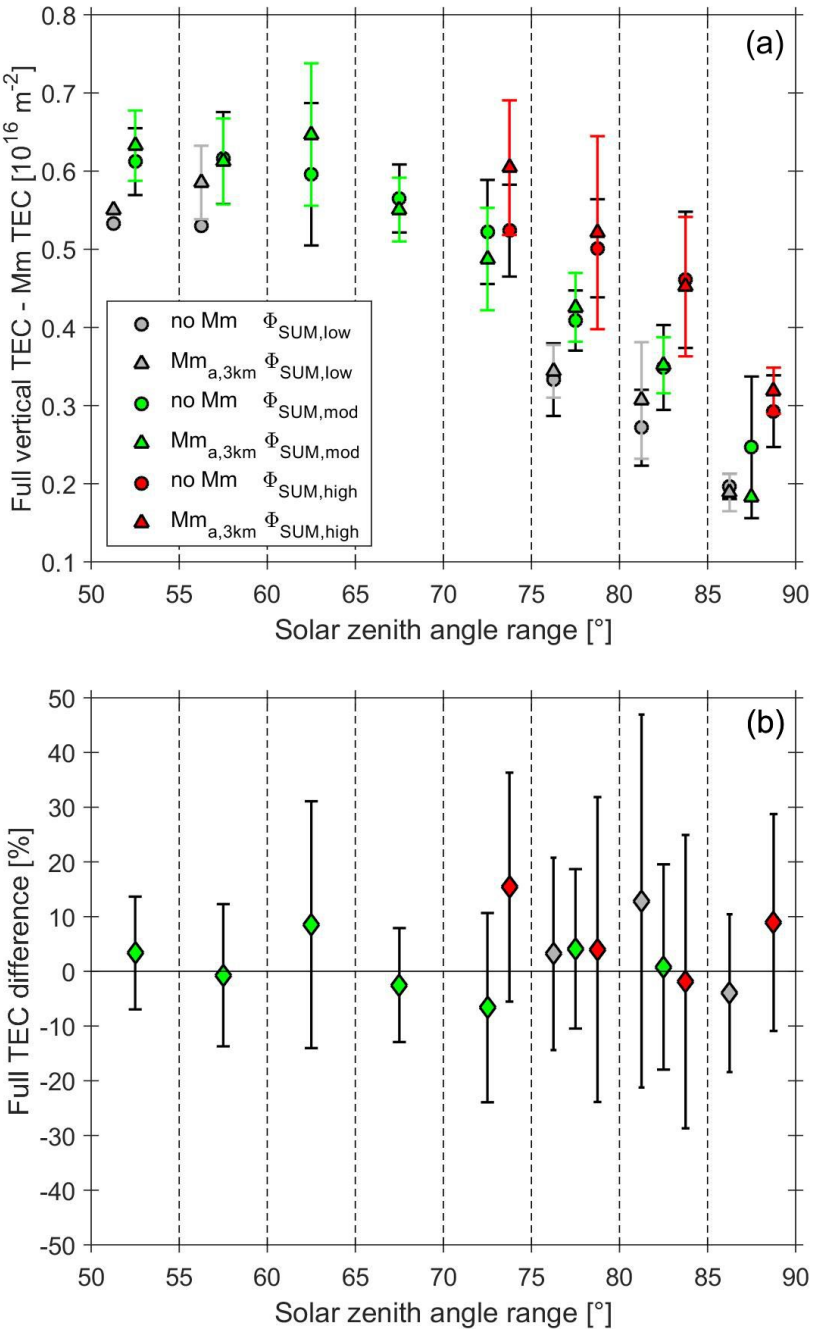

Figure 7.19: (a) Weighted average (circles) and weighted standard deviation (error bars) of the $MaRS_{quiet}$ TEC separately calculated for observations with (n^{obs}_{TEC}-$n^{obs}_{TEC}(Mm)$) and without Mm (n^{obs}_{TEC}) in the Φ_{SUM} proxy intervals. The colored error bars are associated with the triangles. (b) Differences between the averaged TEC values of Panel (a) in percent of the undisturbed TEC. The error bars are calculated with the classical error propagation.

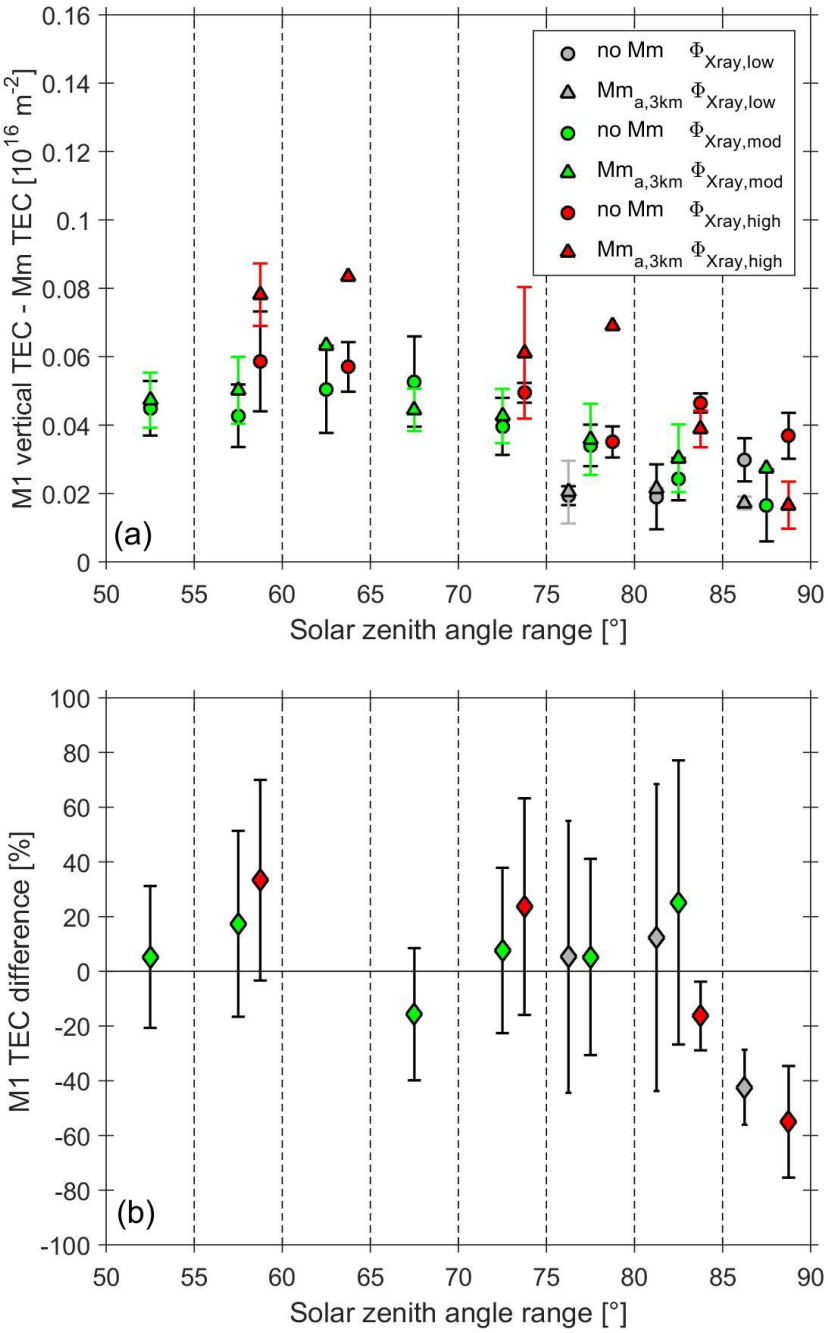

Figure 7.20: (a) Weighted average (circles) and weighted standard deviation (error bars) of the $MaRS_{quiet}$ M1 TEC separately calculated for observations with ($n_{TEC}^{obs}(M1)$-$n_{TEC}^{obs}(Mm)$) and without Mm ($n_{TEC}^{obs}(M1)$) in the Φ_{Xray} proxy intervals. The colored error bars are associated with the triangles. (b) Differences between the averaged TEC values of Panel (a) in percent of the undisturbed TEC. The error bars are calculated with the classical error propagation.

n_{TEC}^{obs} values of the undisturbed observations in MaRS$_{quiet}$. The reduced full profile TEC is used here to eliminate the Mm TEC as potential source for enhanced n_{TEC}^{obs} values. The weighted average and weighted standard deviation are calculated separately for the MaRS observations containing Mm ($\overline{n}_{TEC}^{obs,red}$) and the undisturbed profiles ($\overline{n}_{TEC}^{obs,u}$) in 5° solar zenith angle bins and for the three Φ_{SUM} solar flux proxy intervals. Error bars are only calculated for a bin, if more than one observation is available. The observations are grouped due to their Φ_{SUM} fluxes and solar zenith angles bins, because n_{TEC}^{obs} depends on both parameters (see Figure 7.2). Panel (b) of Figure 7.19 contains the difference $\overline{n}_{TEC}^{obs,diff}$ of $\overline{n}_{TEC}^{obs,red}$ and $\overline{n}_{TEC}^{obs,u}$ from Panel (a) in percent of the associated $\overline{n}_{TEC}^{obs,u}$

$$\overline{n}_{TEC}^{obs,diff} = \frac{\overline{n}_{TEC}^{obs,red} - \overline{n}_{TEC}^{obs,u}}{\overline{n}_{TEC}^{obs,u}} \cdot 100.0. \tag{7.8}$$

The error bars are calculated with classical error propagation from the error bars in Panel (a). Figure 7.20 shows a similar calculation for the M1 TEC $n_{TEC}^{obs}(M1)$, grouped for the Φ_{Xray} X-ray flux ranges and solar zenith angle bins, due to their dependence on those parameters (see Figure 7.7). The plots for the MaRS$_{quiet,5km}$ data set are found in the Appendix (Fig. D.7 for the full vertical TEC and Fig. D.8 for the M1 TEC). The comparison of the weighted average TEC for the disturbed and undisturbed MaRS$_{quiet}$ observations provides similar results for the whole ionospheric profile and the M1 layer. Most calculated TEC differences have positive values. This indicates a relation between the occurrence of the merged excess electron densities and an increase in TEC for n_{TEC}^{obs} and $n_{TEC}^{obs}(M1)$. However, the error bars of the TEC differences include the zero line in all/most of the intervals in Figure 7.19 and 7.20.
This shows that

(12) indications for a weak correlation between the occurrence of merged excess electron densities and n_{TEC}^{obs} and $n_{TEC}^{obs}(M1)$ are available, but obscured by the necessary binning of the variable ionospheric observations.

For completeness, Figure 7.21 shows the variation of the Mm electron density $n_{e,max}^{obs}(Mm)$. The M2 and M1 maximum density both show a dependence on χ as it is expected for a layer based on simple Chapman-theory. This is not the case for $n_{e,max}^{obs}(Mm)$. Similar results are found for the MaRS$_{quiet,5km}$ data set (see Fig. D.9 in the Appendix). Two explanations are provided:

i.) The line fit used for the $n_{e,max}^{obs}(Mm)$ determination may not provide the correct value due to the general shoulder shape of the merged excess densities.

ii.) Additional physical processes, independent of χ, may disguise a possible solar zenith angle dependence.

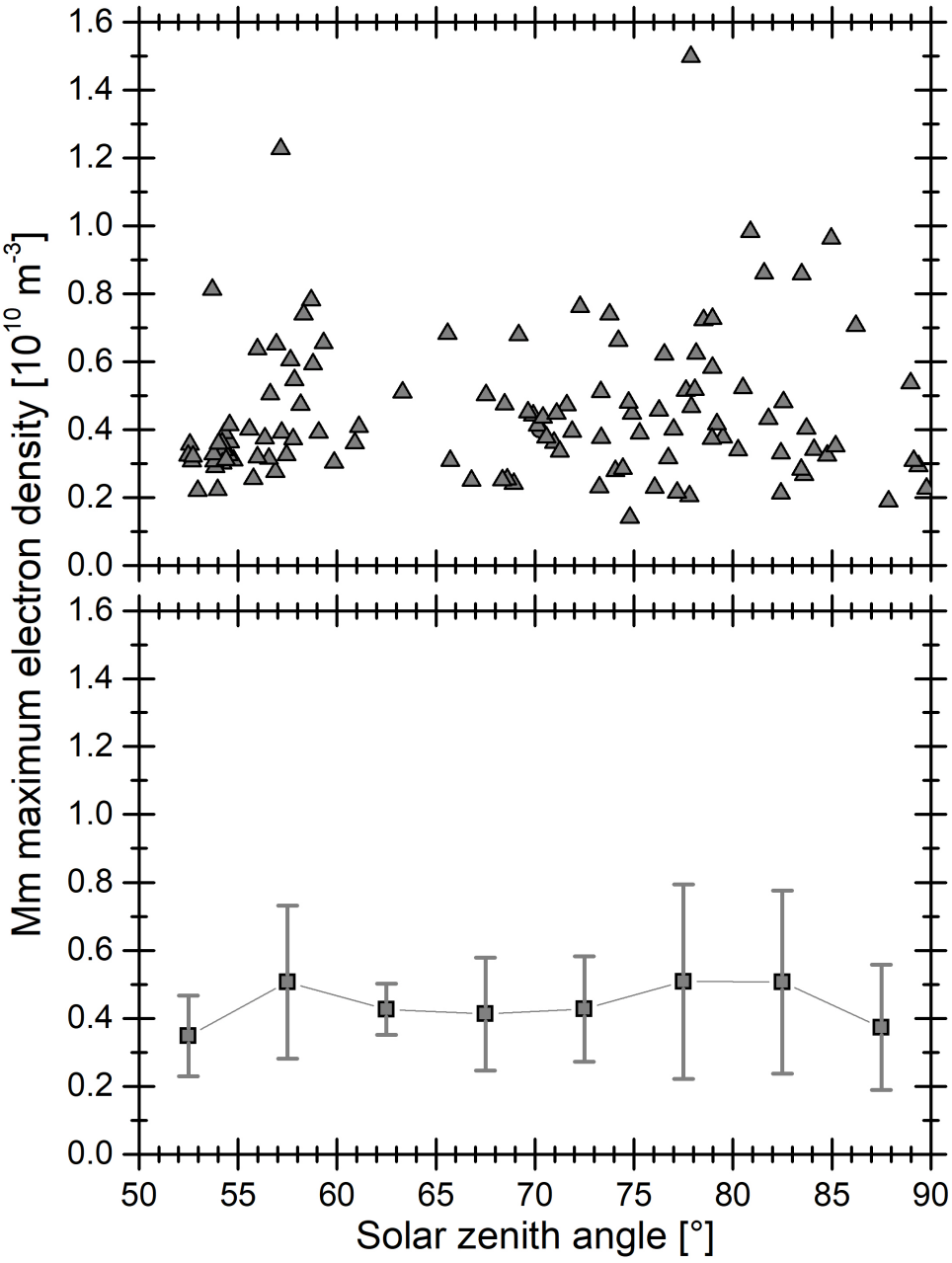

Figure 7.21: Mm maximum electron density. (a) The gray triangles indicate the Mm maximum electron density $n_{e,max}^{obs}(Mm)$ of $MaRS_{quiet}$. (b) $n_{e,max}^{obs}(Mm)$ averaged in 5° solar zenith angle bins. The given error bars indicate the calculated standard deviation of the data points.

Chapter 8

Exploration of the potential origins of the merged excess electron densities

In the previous Chapter it was determined from the MaRS_{quiet} data set that the occurrence of the merged excess electron density affects the ionospheric base in the altitude region between 70 and 110 km. The remaining part of the ionosphere shows no significant enhancement of electron densities compared to the ionospheric variability. Short solar radiation and solar energetic particles (SEPs) are potential sources for the merged excess electron densities and their possible role in the formation of the merged excess electron densities will be discussed in the following Chapter.
Solar photons with high energies are absorbed at the described altitude region while high energetic SEPs might also reach that height, especially along open crustal field lines. The most quiet MaRS observations of the ionospheric dayside have been selected for this work

i.) to investigate if merged excess electron densities do occur in otherwise undisturbed observations or if they are only a side product of the strongly disturbed ionosphere and

ii.) to derive the essential variability of the merged excess electron densities in otherwise undisturbed ionospheric observations.

This work focuses on the derivation of the characteristics for the merged excess electron density in otherwise undisturbed ionospheric observations and on the role of solar radiation in the formation of Mm. Solar photons at a certain altitude can either ionize the local atmospheric neutrals or, if present, particles of extraplanetary origin. The first Section of this Chapter investigates the effect of short solar X-ray on the local atmospheric neutrals. First, the role of the local neutral atmospheric composition in the formation/composition of the merged excess electron densities will be investigated, followed by the comparison of the potential merged excess electron densities derived from IonA-2 with the identified Mm parameters of the MaRS observations. Subsequently, the sporadic nature of the merged

electron densities will be discussed in combination with the variability of their observed shapes. Other potential sources for merged excess electron densities, which comprise local metal ions of meteoric origin, internal atmospheric waves, and the influx of SEPs, are discussed at the end of this Chapter.

8.1 Local ionospheric ions as potential source for merged excess electron densities

In this Section, the 1-D time-marching photochemical model IonA-2 is used to investigate, if the ionization of local neutral atmospheric species by short solar X-ray and impact ionization is sufficient to produce merged excess electron densities in the observed altitude region with the appropriate magnitude of vertical TEC and electron density.

8.1.1 The effect of the local composition of the neutral atmosphere on the potential merged excess electron densities

As discussed in Chapter 6, IonA-2 in the IonA-2_{var} mode is based on the MCD V5.2 neutral atmosphere (CO_2, N_2, O_3, O, H_2O, O_2, H, Ar, CO and H_2 - now called major neutral species) of a full Martian Sol, extracted for the L_S, Ω_{lon} and Ω_{lat} parameters of a selected MaRS observation. The solar flux is provided by the SIP V2.38 model for Earth and then calibrated to the Mars position at the time of the MaRS observation. The photochemical reactions of IonA-2_{var} provide additional neutrals (C, H_2O_2, HO_2, $O(^1D)$, $N(^2D)$, N, NO, NO_2 and OH - now called minor neutral species) and ion (Ar^+, CO_2^+, CO^+, C^+, HCO_2^+, HCO^+, H^+, N_2^+, NO^+, N^+, O_2^+, O^+) species. Ambipolar diffusion is computed for all ions, while minor neutral diffusion transport is calculated for the minor neutrals. No minor diffusion is computed for the major neutrals. Their transport requires major neutral diffusion, a physical effect not yet included in IonA-2. Instead, the major neutral species of the Mars upper atmosphere are regularly updated based on the vertical neutral density profiles the Mars Climate Database for the changing local solar time conditions. IonA-2 uses time steps of 60 s and a variable solar flux input to simulate the changing solar zenith angle conditions at the selected position on the planet. IonA-2_{var} always starts at 9 h LST with the start densities for the major neutrals derived from the MCD. The densities of all minor species are set to zero, except for NO. Start densities for NO are taken from the neutral atmospheric densities[1] of the LMD-GCM for which the ionosphere is given in Figure 3 of *González-Galindo et al.* (2013) for 9 h local solar time. The correspondent Figure for the Mars ionosphere is shown in Chapter 2 as Figure 2.14, the neutral atmospheres are found in Appendix A as Figure A.1. It was decided to use NO start densities above zero to reduce the model run-time until convergence. It

[1] provided by F. González-Galindo, personal communication

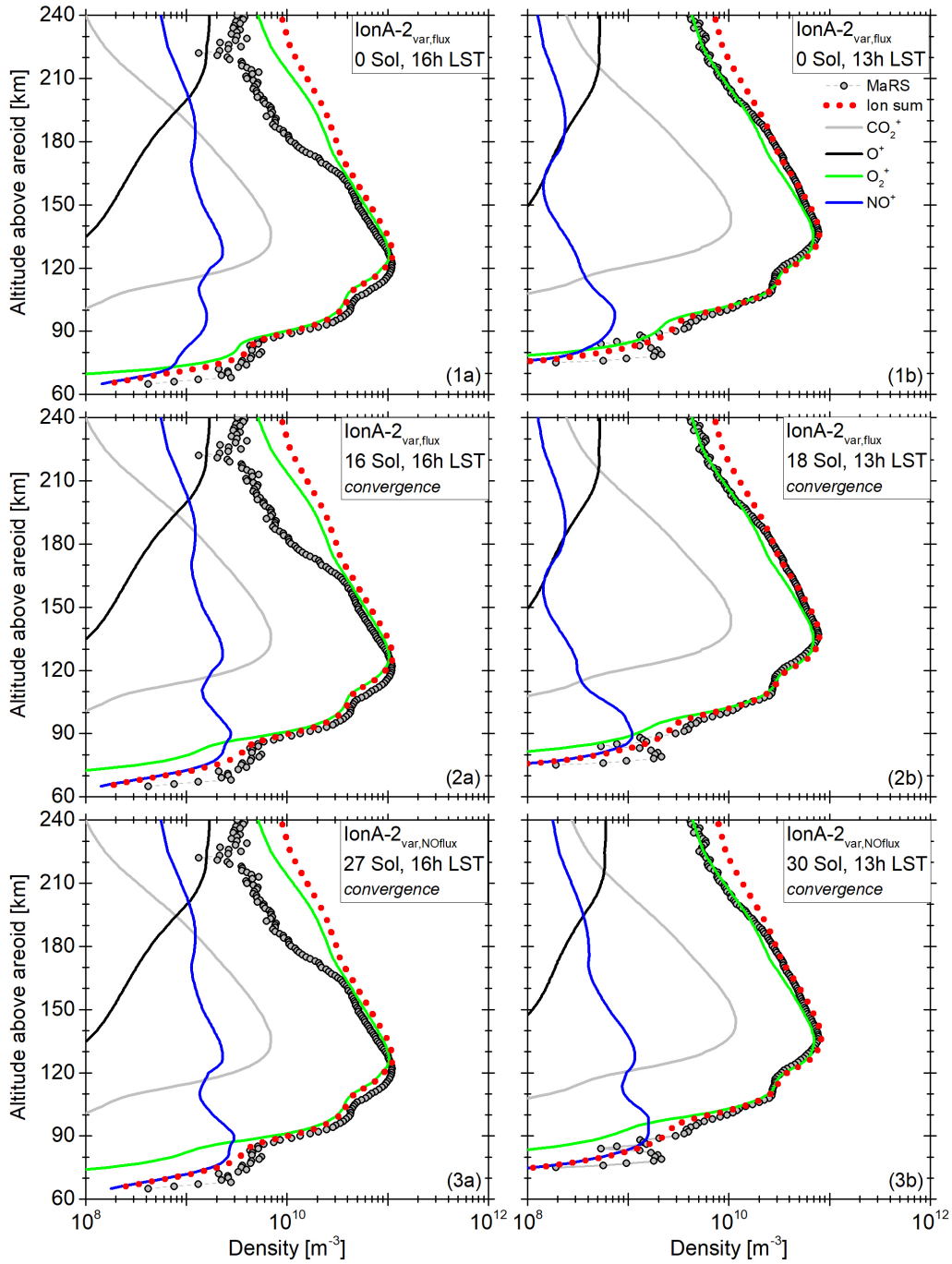

Figure 8.1: IonA-2_{var} results for (a) DoY 111 (2006) for 16 hrs local time and $\chi = 59.22°$ and (b) DoY 336 (2005) for 13 hrs local time and $\chi = 78.78°$. Panel 1 (a,b) contain the IonA-$2_{var,flux}$ ionospheric composition after 7 (for 1a) and 4 (for 1b) Mars hours model run time, respectively. Panel 2 (a,b) contain the IonA-$2_{var,flux}$ ionosphere after convergence. Panel 3 (a,b) contain the IonA-$2_{var,NOflux}$ ionosphere after convergence. The IonA-2 model assumes plasma neutrality. Therefore the shown model ion densities and ion sum correspond to the model electron densities.

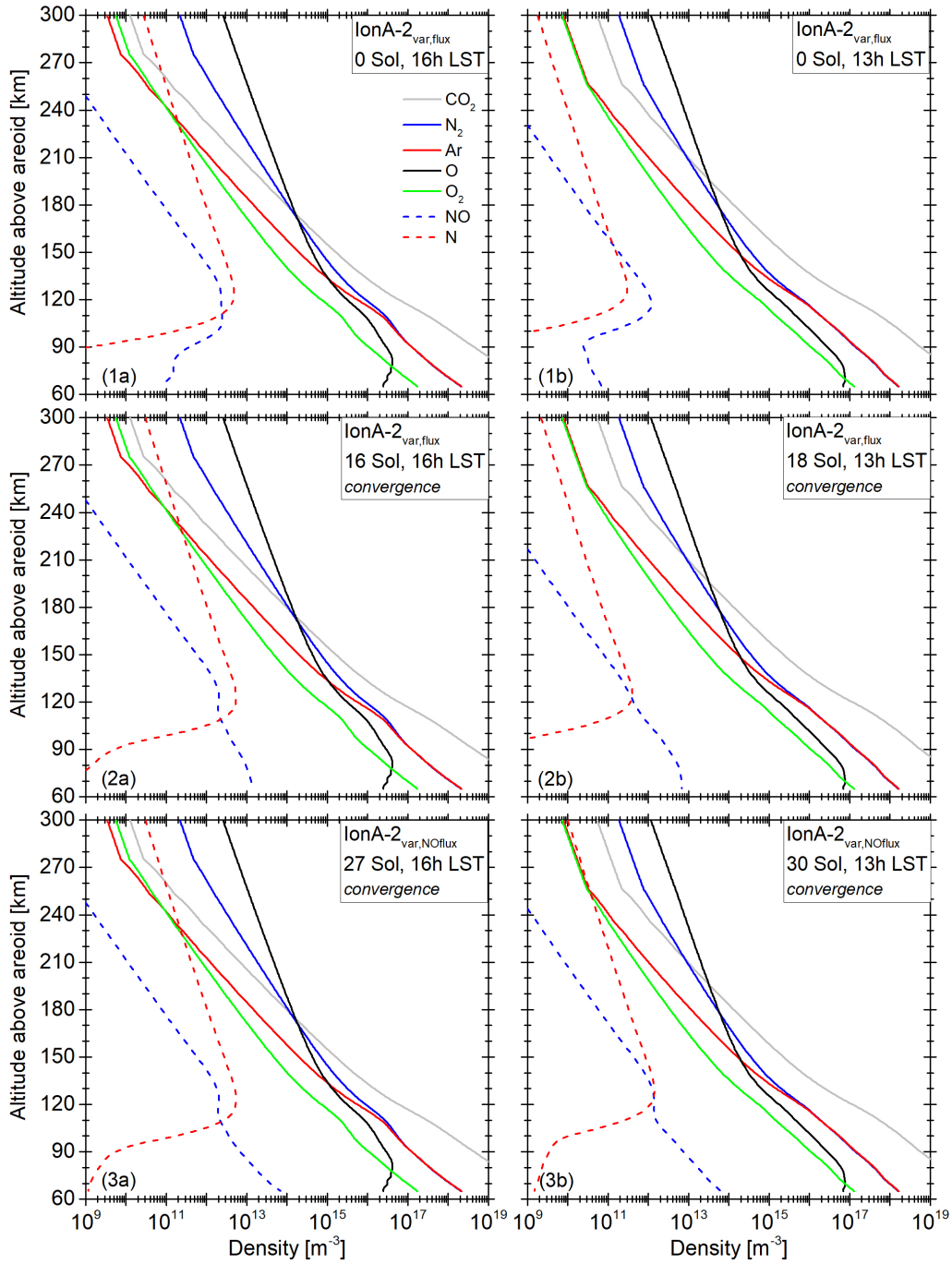

Figure 8.2: IonA-2_{var} results for (a) DoY 111 (2006) for 16 hrs local time and $\chi = 59.22°$ and (b) DoY 336 (2005) for 13 hrs local time and $\chi = 78.78°$. Panel 1 (a,b) contain the IonA-$2_{var,flux}$ neutral atmosphere after 7 (for 1a) and 4 (for 1b) Mars hours model run time. Panel 2 (a,b) contain the IonA-$2_{var,flux}$ neutral atmosphere after convergence. Panel 3 (a,b) contain the IonA-$2_{var,NOflux}$ neutral atmosphere after convergence.

is assumed that IonA-2_{var} has achieved convergence, if the maximum change of the N, $N(^2D)$ and NO densities at each altitude falls below 3.5% from one Sol to the next at a preselected local solar time. A test calculation with zero start densities for all minor neutrals shows a difference to the regular calculation of zero above 150 km altitude and < 2 % below 150 km altitude, which is well below the convergence criterion of the model. However, the internal model run time (Mars Sols) until convergence was similar for both model runs. This was caused by the small amount of NO in the input lower neutral atmosphere.
While general model convergence is achieved fast above 120 km, many Sols of model run time are needed until the lower atmosphere achieves a convergent state. This is caused by the slow downward diffusion of NO, especially at the lowest altitudes of the model. Future convergence computations will be faster, because the now available N, $N(^2D)$ and NO densities can be used as new start parameters.
Figure 8.1 contains the IonA-2_{var} model ion densities based on the MCD-MY scenario and calculated with reaction scheme 2 in comparison with the observations from DoY 111 (2006) with a model local solar time of 16.0 h (the time of the observation is at 16.0 LST) and DoY 336 (2005) for a model LST of 13.0 h (the observation LST is 13.1 h). Full hours LST have been chosen for the model output due to the later discussed symmetry of the solar zenith angle to 12 h LST. The MaRS observation of DoY 111 (2006) was chosen for comparison with the IonA-2 model, because of its very pronounced V-shaped merged excess density. It is found though ((a) Panels of Figure 8.1), that the combination of the derived MCD neutral atmosphere and SIP solar flux for the observational conditions of DoY 111 with IonA-2_{var} do not perfectly reproduce the altitude of the observed ionospheric main peak. This indicates an input neutral atmosphere which is too dense compared to the observation. In this case, the altitude where the optical depth τ reaches unity (see Eq. 6.8) is found at higher altitudes since the atmosphere is more dense. However, the agreement between the observation and the model altitudes of the lower ionospheric base is good. The MaRS observation of DoY 336 (2005) has been chosen for comparison, due to the more complex shape of the merged excess electron density compared to the V-shape of DoY 111. Both MaRS observations took place above low crustal fields with a B_{tot} of approx. 11 nT for DoY 111 and approx 2 nT for DoY 336. Panel (1) and (2) of Figure 8.1 and 8.2 show the IonA-$2_{var,flux}$ results for the approximate solar zenith angles of the observations. The IonA-$2_{var,flux}$ mode uses a net downward flux velocity of K/H_n (see Chapter 6 for details) for N and NO as a lower boundary condition at 65 km altitude. While Panel (1) shows the IonA-$2_{var,flux}$ results after the first few hours of calculation, Panel (2) shows the convergence distribution of N and NO at the given local times. Panel (3) shows the convergence distribution in the IonA-$2_{var,NOflux}$ mode, where a zero flux lower boundary condition for the minor diffusion of N and NO is applied. The increase of the NO density at the lower model altitudes from Sol 0 in Panel (1) to the convergence after several Sols in Panel (2) of Figure 8.2 is caused by the net production of NO in the thermosphere and its downward transport.

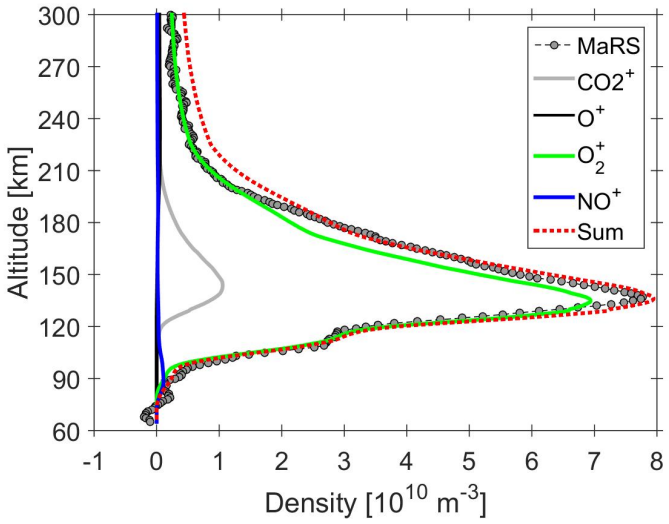

Figure 8.3: IonA-$2_{var,flux}$ convergence results for DoY 336 (2005) on a linear scale.

Due to the lower boundary flux velocity of K/H_n for Panel (2), the NO density for Panel (3) with zero downward flux is even larger than in Panel (2).
The following conclusions can be drawn:

(1) All model electron density profiles (red dots) for DoY 111 (2006) and DoY 336 (2005) in Figure 8.1 could reproduce the observed V-shaped merged excess electron density feature. This occurred without artificial enhancement of the SIP V2.38 X-ray fluxes.

(2) The electron density of the modeled potential Mm stays almost similar for the three computed scenarios (low NO, high NO, very high NO). Only its composition changes from predominantly O_2^+ in Panel (1) to predominantly NO^+ in Panel (3). This is caused by the larger abundance of NO in the lower atmosphere for the convergence scenarios.

Figure 8.3 shows a comparison between the convergent IonA-$2_{var,flux}$ model results for DoY 336 (2005) from Panel (2b) of Figure 8.1 with the observed MaRS electron density on linear scale. Without any adjustments to the model input parameters, the agreement between the modeled and observed peak densities is excellent. The width of the model main peak is only slightly too wide, which is an indicator for a slight overestimation of the model electron temperature (T_e) around the main peak compared to the T_e at the time of the observation. The observed ionospheric base with the M1 region and the merged excess electron density are well met by the IonA-$2_{var,flux}$ electron densities, except for the small scale structure in Mm at the lower boundary. However, the MaRS radio science experiment can only observe the ionospheric electrons, but not the ions. Therefore the

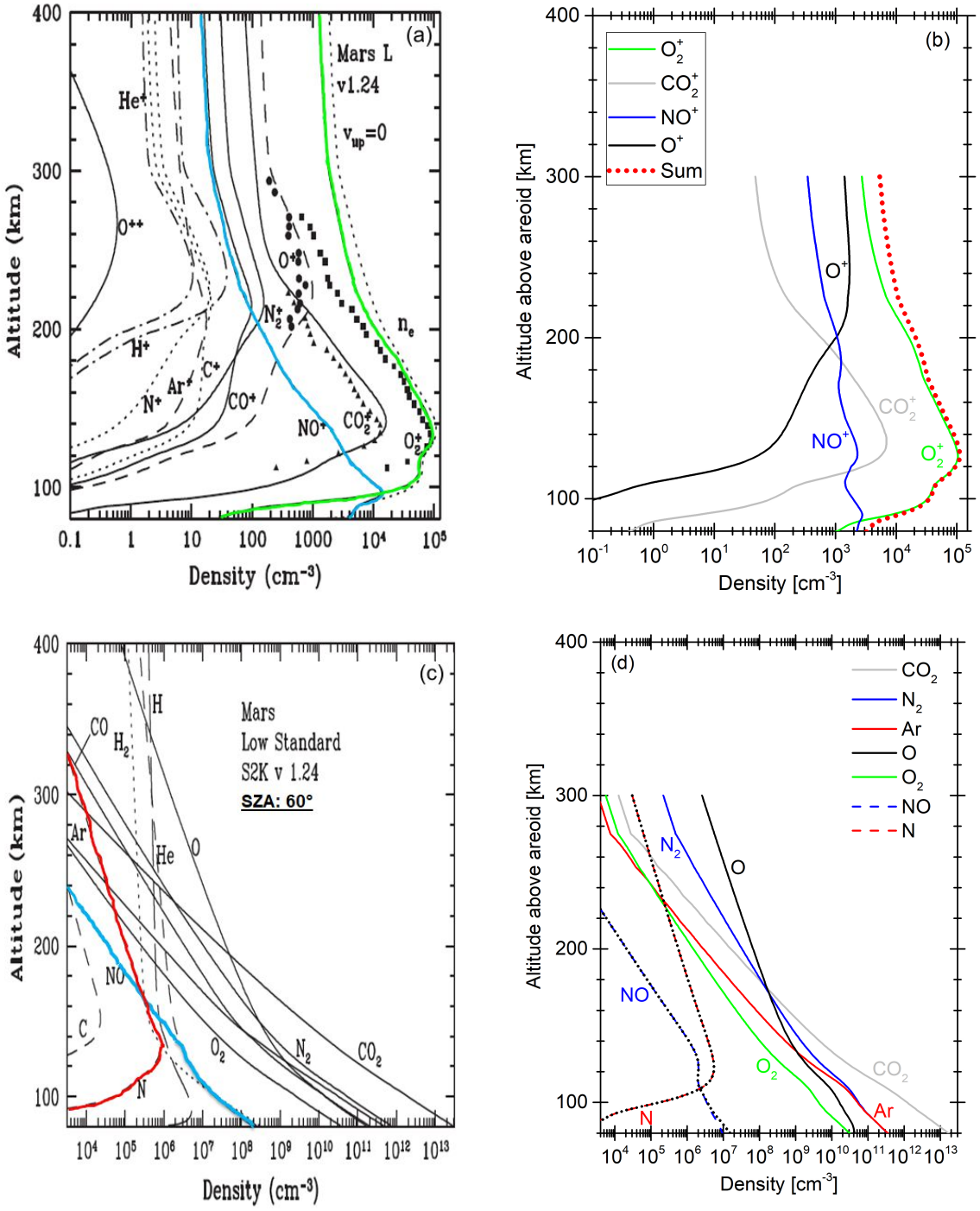

Figure 8.4: The left Panels (a,c) are taken from Fox *(2015) and show the Martian ionosphere and neutral atmosphere calculated with the low solar flux standard model for $\chi = 60°$ (lines) and the results of the Viking 1 lander Viking-RPA (symbols) from* Hanson et al. *(1977). The right Panels (b,d) show the convergent IonA-$2_{var,flux}$ results for DoY 111 (2006) in similar scale. In addition, Panel (d) contains the convergent IonA-$2_{var,NOflux}$ results for N and NO as black dotted lines.*

IonA-2_{var} ion densities need to be compared to other observations/models for validation of the general ion distribution in the model results. Figure 8.4 shows the comparison between the converged IonA-$2_{var,flux}$ results for DoY 111 (2006) and the model results of the 1-D photochemical/transport model of *Fox* (2015) (now called Fox-model). In addition, Panel (a) of Figure 8.4 contains the Viking-1 lander Viking-RPA ion results for the Mars ionosphere. Even though the environmental conditions of the Viking-RPA observations and input parameters for the Fox-model differ from those of the MaRS observation of DoY 111 (2006), the available ion densities are sufficient to evaluate the general ion distribution of the IonA-2 model results. While the Viking-RPA observations, the Fox-model and the IonA-$2_{var,NOflux}$ model results for DoY 111 (2006) have similar solar zenith angles, they differ widely for other parameters.

- The F10.7 parameter at Earth for the Viking observations is 70. The solar input for the Fox-model is taken from the SIP V1.24 for an F10.7 of 68 at Earth, while the SIP V2.38 F10.7 at Earth is 106.1 for the solar flux used in IonA-2_{var}.

- The Viking-RPA observations took place at $L_S = 97\,^\circ$ which is close to aphelion, the Fox-model is calculated for the average Mars-Sun distance of 1.524 AU. The MaRS observation took place at an L_S of approx. $42\,^\circ$.

- The neutral atmosphere of the 1-D convergence model of *Fox* (2015) was originally designed to explain the Viking-RPA observation, the IonA-2_{var} model uses the neutral atmosphere of the Mars Climate Database for a Martian Sol derived for the conditions of the MaRS observation.

- The Fox-model and IonA-$2_{var,flux}$ both use a downward flux for N and NO during their computations. While the downward flux in the Fox-model is 100 $cm^{-2}s^{-1}$ for N and $2 \cdot 10^7$ $cm^{-2}s^{-1}$ for NO, the flux in the IonA-2 model is variable and depends on the available density of the species at the lower boundary ($n_u \cdot K/H_n$).

Despite all described differences between the Viking-RPA observations and the two models, the agreement between the Viking-RPA observation and the Fox-model on the one hand and the IonA-2_{var} results on the other hand is quite good. The shape and position of the individual O_2^+, CO_2^+ and O^+ IonA-2_{var} ions are in general agreement with the Viking-RPA observations and the Fox-model. However, the altitude of the ionospheric main peak differs slightly. This might either be caused by differences in altitude calibration or by the higher density of the neutral atmosphere in the Fox-model (see lower Panels in Figure 8.4). The electron density in the lower ionosphere is slightly larger for the Fox-model than for IonA-2_{var}. The same is found for the CO_2^+ peak densities of the Fox-model, but cannot be investigated for the O_2^+ of the main peak due to the logarithmic presentation of the Fox ion densities. Differences in the electron densities of the two models are most probably caused by the different versions of the SIP model. The larger electron density

of the Fox-model in combination with the larger NO density at 80 km altitude explains the larger NO^+ densities below 100 km altitude in comparison with the IonA-2_{var} results. The general shape of the neutral N and NO are similar in both models, but their altitude dependent N/NO ratio differs. The exact reason for this deviation remains unclear due to the large differences in the model input parameters and model scheme. The variation of the N/NO ratio in the IonA-2_{var} results during the day is illustrated in Figure 8.6. A discussion of the balance between N and NO in the lower thermosphere and upper mesosphere of Mars is found later in this text.
The above discussion allow to draw the following conclusions:

(3) Despite the differences between the Viking-RPA environmental and the *Fox* (2015) model conditions on the one hand and the IonA-$2_{var,flux}$ model parameters for DoY 111 (2006) on the other hand, an overall good agreement is found between the IonA-$2_{var,flux}$ ion distribution and the other independent results. This good agreement allows to be confident, that the IonA-$2_{var,flux}$ model results are physically and chemically reasonable.

8.1.2 The modeled potential merged excess electron densities in comparison with the MaRS observations

The IonA-2 results in the previous Figures depict the modeled potential Mm for the approximate solar zenith angle and local time of the associated MaRS observations. However, IonA-2_{var} is no convergence model for a single solar zenith angle, but relies on the major neutral atmosphere of the 3-D Mars Climate Database of a full Martian Sol. For every day/night cycle of passed model time, IonA-2_{var} provides 24 neutral atmospheric and ionospheric states, one for every Mars hour. Those additional model results for DoY 111 (2006) and DoY 336 (2005) provide a larger coverage of solar zenith angles than the single atmospheric/ionospheric result for the time of the MaRS observation. During a Martian Sol of model run time, all local solar times are covered by IonA-2_{var}, but usually not all solar zenith angles. The planetary latitude Ω_{lat} and solar longitude L_S of the selected MaRS observation geometrically constrain the possible solar zenith angles due to the inclination of the Mars rotation axis in combination with the planet's position on its orbit around the Sun. This is illustrated in the variation of the solar zenith angles associated with the local solar times in Figure 8.5. For the MaRS observation of DoY 336 (2005) the lowest solar zenith angle reached by the model is 78.01° at 12 h LST. The model outputs for the shown morning and afternoon local times have similar solar zenith angles (χ). Due to geometrical reasons, χ is always symmetric to 12 h LST and the IonA-2_{var} results have been produced in 1 h LST intervals. This also results in a similar solar input flux for the morning and afternoon model ionospheres with the same temporal distance to 12 h LST. This might however not be the case for the major neutrals from the Mars Climate Database, if a different parametrization of the solar flux is applied in

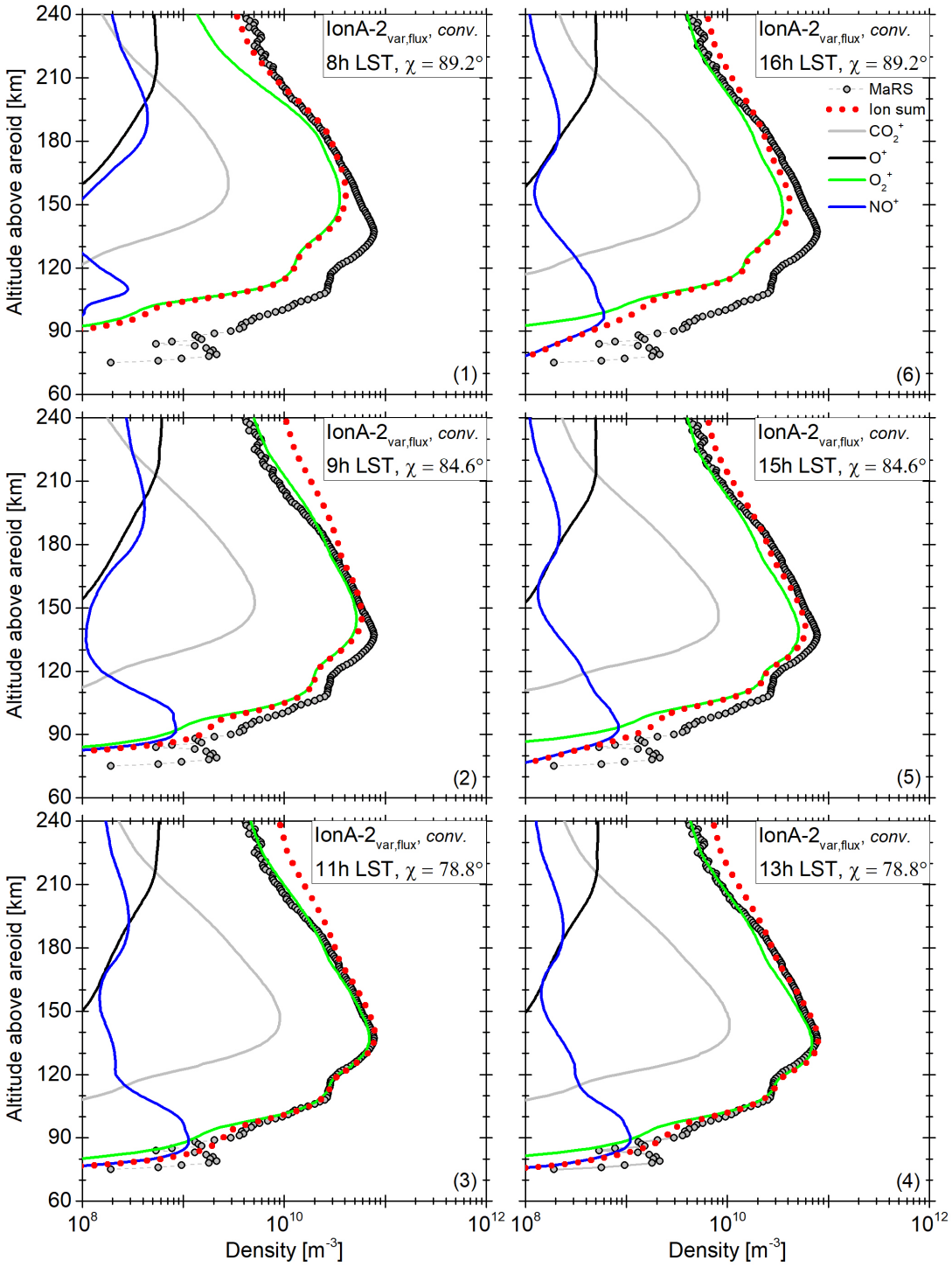

Figure 8.5: Convergent IonA-$2_{var,flux}$ ionospheric results for DoY 336 (2005) for 8 - 16 h local solar time.

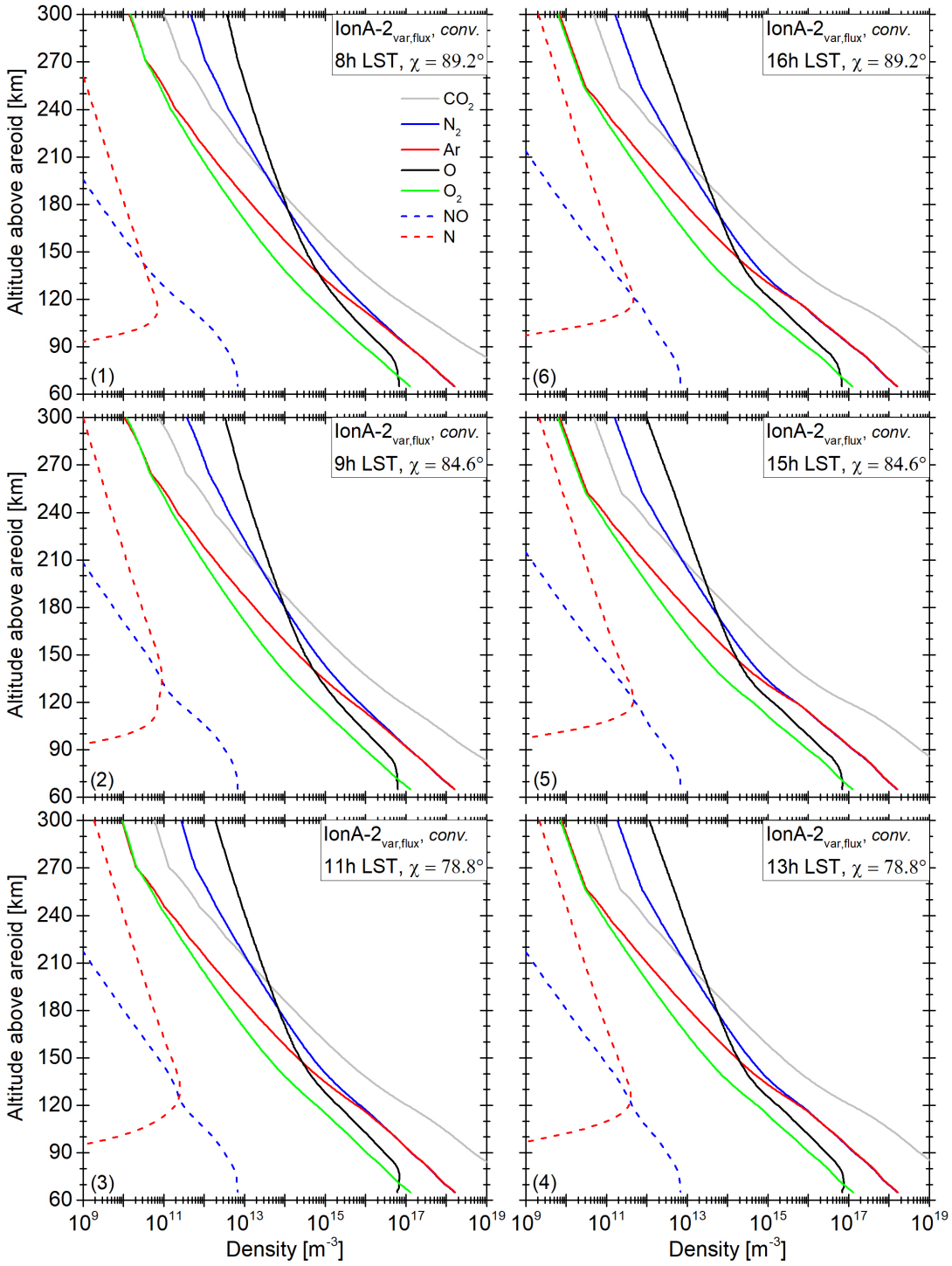

Figure 8.6: Convergent IonA-$2_{var,flux}$ neutral atmospheric results for DoY 336 (2005) for 8 - 16 h local solar time.

the underlying GCM.
Figure 8.5 shows the variability of the modeled Martian ionospheric dayside for DoY 336 (2005), while Figure 8.6 contains the associated neutral atmosphere. The evolving ionosphere is affected by the change in solar flux, neutral temperature and underlying neutral atmospheric densities during the course of the day. Even if the solar input into the planetary atmosphere is symmetric to 12 h LST, the resulting ionospheres are not. The lowest region of the afternoon ionosphere is predominantly composed of NO^+, while the morning ionosphere contains a higher amount of O_2^+. This is explained by the longer lifetime of NO^+ at lower altitudes in comparison with O_2^+ (see Figure 6.3). The altitude where the optical depth τ reaches unity rises to higher altitudes for an increasing solar zenith angle. This reduces the production of O_2^+ at the lowest ionospheric altitudes from noon to dusk. NO^+ is produced by the interaction between O_2^+ and NO (r. IR120) and withstands the photochemical processes in IonA-2 slightly longer than O_2^+ and therefore provides the remaining "excess" in the lowest ionospheric region when the production of O_2^+ ceases. The assymetry between morning and afternoon ionosphere is also seen by *González-Galindo et al.* (2013) (see lower Panels of Fig. 2.14). The general shape of the LMD-GCM NO^+ for $\chi \sim 90\,^\circ$ (18 h LST) is quite similar to the IonA-2_{var} result for 16 h LST. Differences in the extent of the M1 layer are explained by the different parametrization of the secondary ionization in the two models and the different solar flux input. While the LMD-GCM results were calculated with the impact ionization parametrization of *Nicholson et al.* (2009), the IonA-2 model is using the parametrization of *Wedlund et al.* (2011). This might also cause some of the differences between the LMD-GCM morning results at 6 h LST and the IonA-2_{var} results for 8 h LST. The exact reason for the additional structure in the upper part of the IonA-2_{var} NO^+ profiles remain unclear due to the different input parameters, position on the planet and used reaction scheme. The most important difference in the underlying neutral atmosphere, the ratio between N and NO, will be discussed later in this Chapter.
The subsequent comparisons of the model results with the identified Mm contain only the parameters of the potential Mm derived from the convergent IonA-$2_{var,flux}$ results. The derived parameters for the potential Mm from the convergent IonA-$2_{var,NOflux}$ ionospheres are very similar to those derived from the IonA-$2_{var,flux}$ model results and therefore omitted in the plots to provide a better view on the differences between the morning and afternoon ionosphere. The modeled potential merged excess electron densities have been identified with the same procedures which were used for the determination of the Mm in the MaRS observations (see Chapter 4 for details). Smoothing of the model results is neglected in this process, because the model electron densities do not contain observational noise. Panel (a) of Figure 8.7 contains the altitude of the derived maximum electron density of the Mm of the converged IonA-$2_{var,flux}$ results for DoY 111 (2006) and DoY 336 (2005) in comparison with the identified $\mathrm{Mm}_{a,3km}$ of the MaRS_{quiet} data set of Figure 7.18. The "error" bars in this Figure indicate no real error bars of observation or model, but the extent of the merged excess electron density. The model altitudes are in good

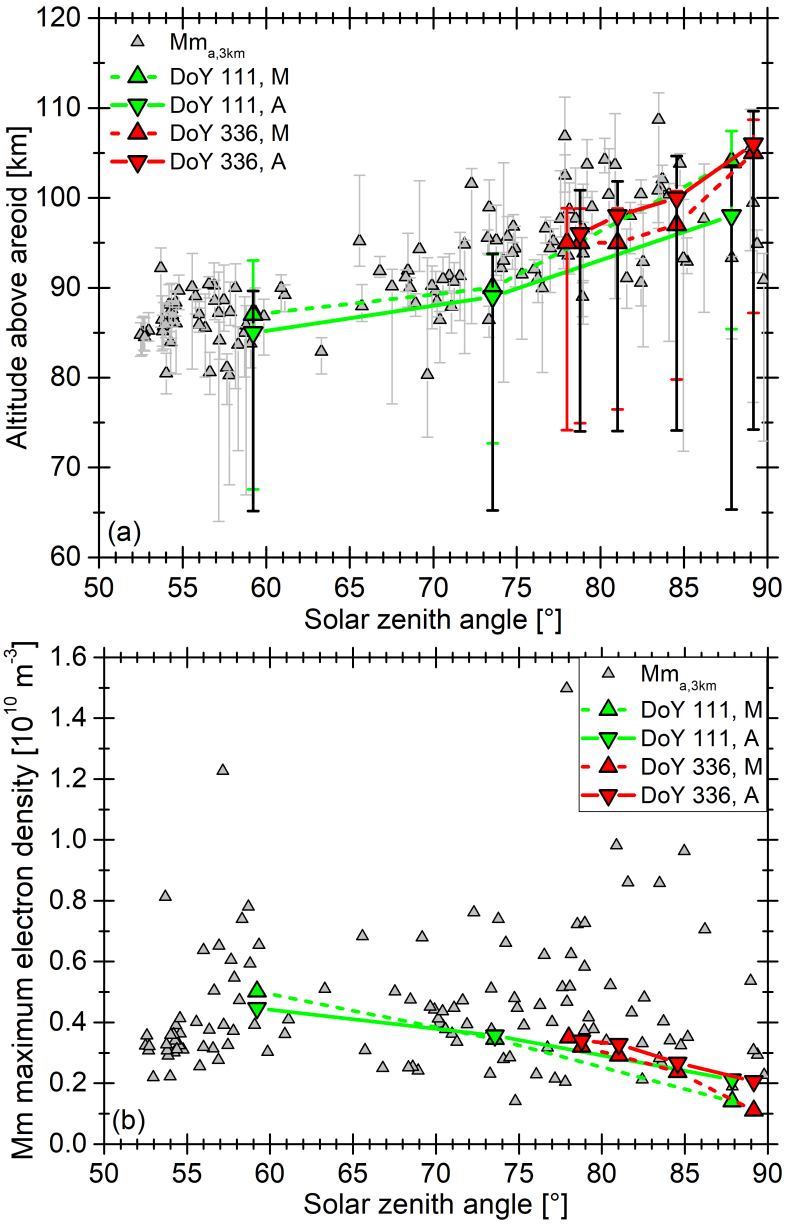

Figure 8.7: Altitude of the maximum Mm electron density (a) and maximum electron density (b) of the modeled IonA-2$_{var,flux}$ potential merged electron densities for DoY 111 (2006) (green) and DoY 336 (2005) (red) for the (M)orning and (A)fternoon neutral atmospheres in comparison with the Mm parameters derived from the MaRS$_{quiet}$ data set.

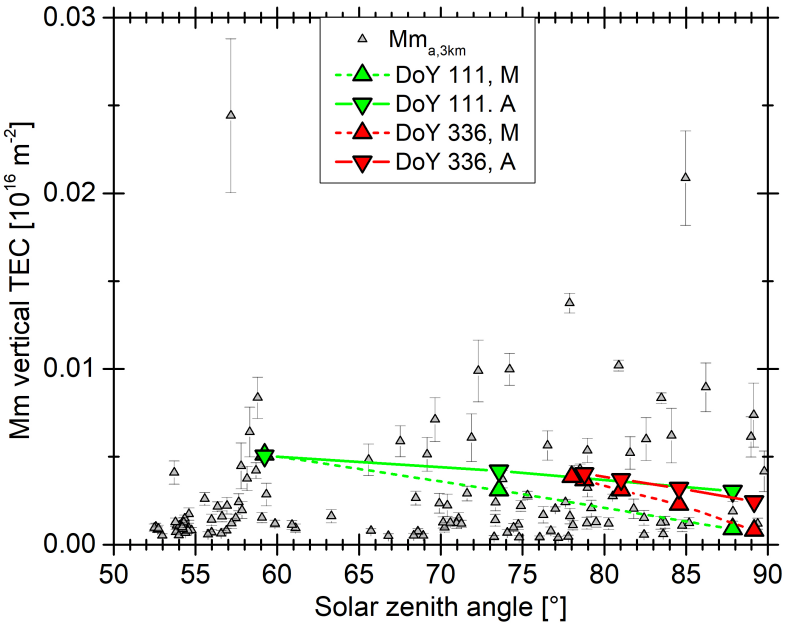

Figure 8.8: Vertical TEC of the modeled IonA-2$_{var,flux}$ potential merged electron densities for DoY 111 (2006) (green) and DoY 336 (2005) (red) for the (M)orning and (A)fternoon neutral atmospheres in comparison with the Mm parameters derived from the MaRS$_{quiet}$ data set.

agreement with the altitude range of the identified Mm, except for the interval between 85 and 90 degree solar zenith angle, where only very few identified Mm are available. The lower extent of the modeled potential Mm is obviously larger than the average lower altitude extent of the observed Mm. This is an expected result, because the model data are not affected or constraint by observational noise. The altitude increase of the Mm maximum for higher solar zenith angles found for the observed Mms is reproduced by the model. This behavior is also visible for the observed M2 and M1 peaks. It is explained for all absorbable solar radiation by the increase of the altitude where the optical depth τ reaches 1 with increasing solar zenith angle. Panel (b) of Figure 8.7 contains the comparison between the maximum electron density of the modeled potential Mm and the identified Mm from Figure 7.21. The identified Mm maximum electron densities show no pronounced solar zenith angle dependence. As already discussed in Chapter 7, a potential trend in the identified Mm may be obscured by the pronounced scatter in the data set. This might be caused by problems with the line-fitting method or additional physical processes whose combined effects disguise a potential trend. The model potential Mm shows a decrease for increasing solar zenith angle similar to the one observed in the MaRS measurements for the main peaks of M2 and M1. This decrease is different for the morning and the afternoon ionospheres. In IonA-2$_{var}$, the only change in solar flux is provided by the change in solar zenith angle. Therefore the morning and afternoon ionospheres

with a similar temporal distance to 12 h LST experience the same solar input flux. While the general decrease of the maximum electron density of the potential Mm for increasing solar zenith angle is caused by the decrease in available solar radiation at a certain altitude, the differences between the morning and afternoon ionospheres are caused by photochemical processes including the underlying neutral atmosphere. Figure 8.8 shows the vertical TEC $n_{TEC}^{obs}(Mm)$ of the identified Mm in comparison with the vertical TEC of the model potential Mm. Neither a clear trend is found in the $n_{TEC}^{obs}(Mm)$ in relation to the solar zenith angle, nor a clear correlation with the short solar X-ray proxies $\Phi_{0.45-3nm}$ and $\Phi_{0.45-1nm}$. The latter is attributed to an enlarged variability in the Suns short X-ray output, that would lead to a decrease in the validity of the SIP V2.38 short X-ray flux for the Mars position. The derived potential model TEC is well in agreement with the vertical TEC of the identified Mm. The model TEC shows a decrease for increasing solar zenith angle and differences between the morning and afternoon ionospheres. The decrease in the modeled vertical TEC is explained by similar arguments already explained above in the discussion of the maximum electron density. The differences between the morning and afternoon ionospheres provide additional information about the correlation with the solar flux proxies. For DoY 111 (2006), the $\Phi_{0.45-1nm}$ solar flux proxy is $9.2 \cdot 10^{10} s^{-1} m^{-2}$, while $\Phi_{0.45-3nm}$ yields $3.9 \cdot 10^{11} s^{-1} m^{-2}$. This corresponds to the moderate solar flux proxy range in Table 5.4 of Chapter 5. For DoY 336, $\Phi_{0.45-1nm}$ is $1.2 \cdot 10^{11} s^{-1} m^{-2}$, while $\Phi_{0.45-3nm}$ yields $5.1 \cdot 10^{11} s^{-1} m^{-2}$. This corresponds to the high solar flux proxy range. The short solar X-ray used for the proxies is also used as an input solar flux for IonA-2. Therefore it would be expected, that the modeled vertical TEC for DoY 336 is always higher than that for DoY 111. Nevertheless, the given data points in Figure 8.8 indicate, that this is not the fact, but no results were available for a similar χ in both observations. Therefore, either the uncertainties introduced by the underlying neutral atmosphere or those given by the line fitting method are too large to allow the identification of the TEC variation introduced by the tested range of short solar X-ray fluxes.
This leads to the following results:

(4) The change in the short solar X-ray input for IonA-2 from DoY 111 (2006) to DoY 336 (2005) is not strong enough to provide a significant difference in the modeled potential Mm vertical TEC in comparison to the variability introduced by the underlying neutral atmosphere and the applied detection method.

(5) The IonA-2 results show an ionospheric dawn/dusk asymmetry, which agrees well with the findings of *González-Galindo et al.* (2013). There is a good agreement between the NO^+ behavior in the lower ionosphere for the dusk terminator, but large deviations at the dawn terminator. Some of the differences can be explained by the different approaches for the parametrization of the secondary impact ionization. The chosen parametrization in the IonA-2 model shows an excellent agreement with the MaRS observations of the M1 peak, which is also strongly affected by the secondary ionization.

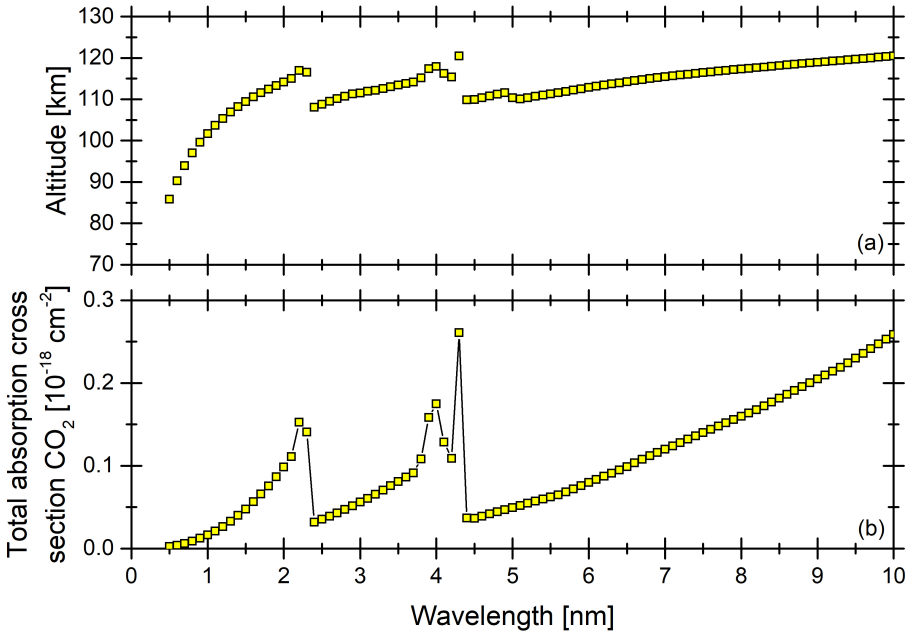

Figure 8.9: (a) Altitude where the optical depth τ reaches unity, based on the convergent DoY 336 (2005) IonA-$2_{var,flux}$ results with 1 Å resolution in the 0.45 - 10 nm range. (b) 1 Å resolution CO_2 absorption cross sections.

(6) The altitude range, maximum electron density, and vertical TEC derived from the IonA-2_{var} potential Mm agree well with the observed Mm.

The good agreement between model and observational results provides additional confidence in the IonA-2 model and shows that it can be used to reveal the underlying physical and chemical processes leading to the observed excess electron densities.

8.1.3 The effect of the short solar X-ray variability on the occurrence rate and shape of the potential Mm

The derived altitude range, maximum electron density and vertical TEC from the IonA-2_{var} potential Mm agree well with the parameters of the identified Mm. However, the SIP V2.38 solar input flux for the modeled MaRS observations of DoY 111 (2006) and DoY 336 (2005) was not enhanced in any way. But if Mm is a persistent feature in the IonA-2_{var} model, why aren't Mm identified in more/all MaRS observations? This topic is explored by investigating the effect of a variable short solar X-ray radiation on the IonA-2 model ionosphere. In a first step, the wavelength range is determined which generates the potential Mm in IonA-2_{var}. In the second step, this wavelength range is varied and the temporal response of the ionosphere is investigated. The variation of the short solar X-ray also provides an estimate of the possible shapes of the potential Mm with the physical

and photochemical processes implemented in IonA-2. For this investigation, the original SIP V2.38 input solar flux in 1 nm resolution between 0.45 and 10 nm is replaced by the SIP V2.38 1 Å solar flux (from the SIP V2.38 1,210 wavelength spectrum). In addition, the cross sections in the 0.45 - 10 nm range are replaced by the 1 Å bin cross sections for all species.

Panel (a) of Figure 8.9 illustrates the atmospheric altitude at which the optical depth τ is unity in the 0.45 - 10 nm solar radiation range. The distribution of τ is calculated for DoY 336 (2005) based on the IonA-$2_{var,flux}$ results. The optical depth for DoY 111 (2005) is almost similar, but slightly shifted downwards due to the lower solar zenith angle of the observation compared to DoY 336. The structure in the absorption altitudes is explained by Panel (b) of Figure 8.9, which shows the used total absorption cross sections of CO_2 between 0.45 and 10 nm. The structure in the absorption cross sections is mirrored by the altitude where τ reaches unity. It is caused by the so called K-edge, which is the binding energy of an electron at the innermost shell (called the K-shell) of an atom. Photons with energies slightly above the binding energy of the electron have a higher probability of being absorbed than photons with an energy slightly below that border. This causes a sudden increase in the absorption cross section just above the electron binding energy. The peak between 6 and 4 nm wavelength is caused by the K-edge of the C atom, while the peak below 4 nm is caused by the K-edge of the O atom of CO_2 (see Chapter 6). From the altitude distribution of the optical depth it is deduced, that for DoY 336 (2005) the solar radiation below 1.5 nm is primarily responsible for the potential merged excess electron densities in IonA-2_{var}.

Panel (1) of Figure 8.10 and 8.11 contain the IonA-$2_{var,flux}$ and IonA-$2_{var,NOflux}$ convergence results for DoY 336 (2005) shown in Panel (1b) and Panel (3b) of Figure 8.1 with a focus on the merged excess electron densities. Those data are the input neutral atmosphere and ionosphere for the IonA-2_{var} model. In addition, the solar flux below 1.5 nm was set to zero at the beginning of the calculations. The IonA-2_{var} results after 20 min of model time are given in Panel (2), while Panel (3) shows the results after 40 min of model time. The electron density in the lowest part of the ionosphere shows a continuous decrease with time for both modeled scenarios. Complex structures as seen in the observation of DoY 336 are neither found in the O_2^+ dominated potential Mm of Figure 8.10 nor in the NO^+ dominated potential Mm of Figure 8.11. The decrease of the potential Mm in both model scenarios is further explored by determining the difference between the reduced solar flux results from Panel (3) of both Figures with the associated IonA-2_{var} results for a full solar flux input after 40 minutes of model time. Using the IonA-2_{var} model results for the full solar flux input after 40 minutes of model time as baseline is necessary, because the ionosphere is a temporally evolving structure and using the original input data at 13 h LST as a baseline would distort the calculated differences. Figure 8.12 shows the difference between the respective results for full and reduced solar flux in percent of the full solar flux results. -100 % means a complete reduction of the potential Mm in that altitude, while 0 % indicates no change compared to the full solar

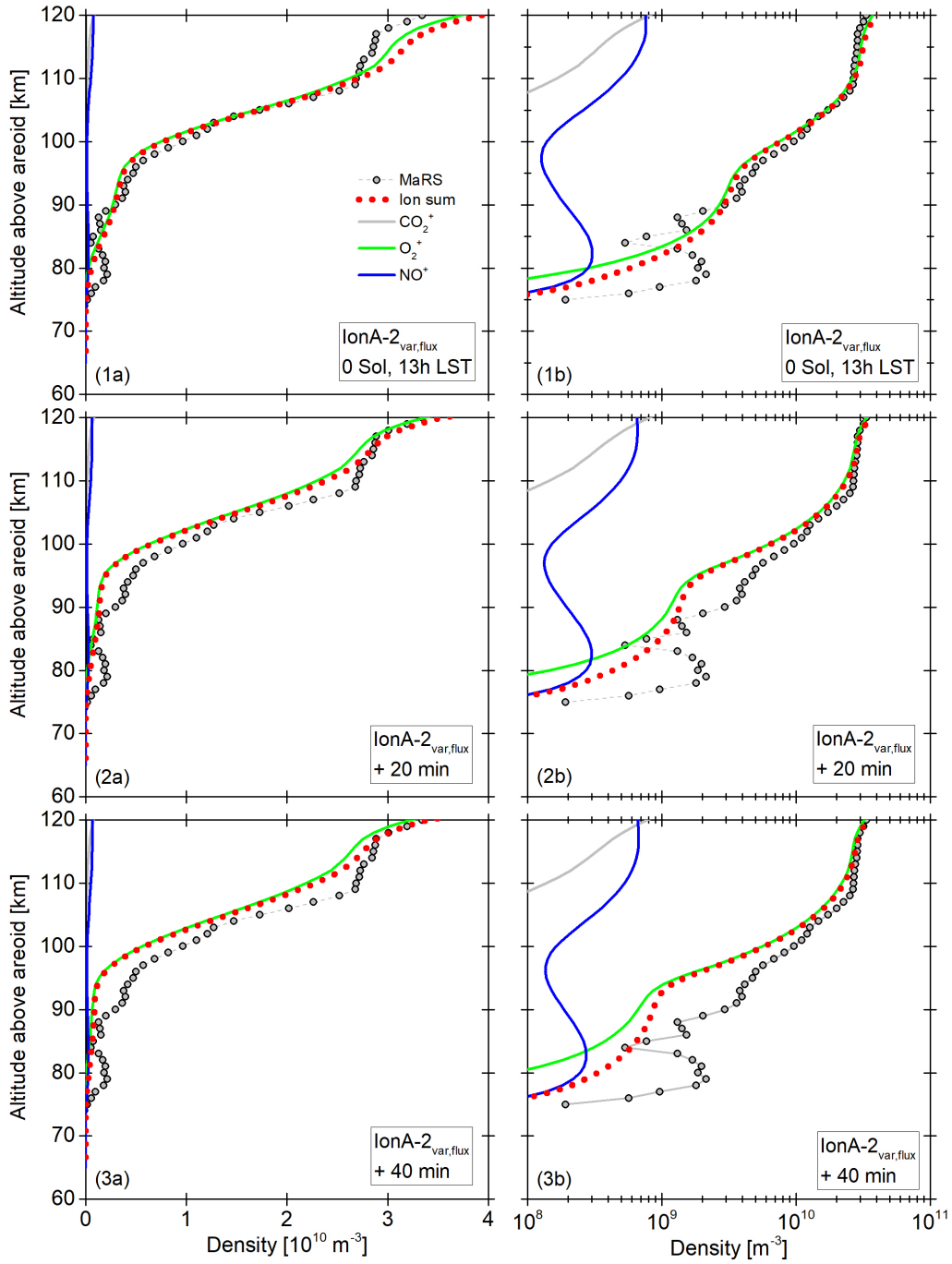

Figure 8.10: Panel (1) contains the linear (a) and logarithmic (b) representation of the IonA-$2_{var,flux}$ results of DoY 336 (2005) in Panel (1b) of Fig. 8.1 as starting point for the calculations. Panel (2) contains the IonA-$2_{var,flux}$ results calculated with the solar flux > 1.5 nm after 20 min of run time. Panel (c) contains the IonA-$2_{var,flux}$ results with the solar flux > 1.5 nm after 40 min of run time.

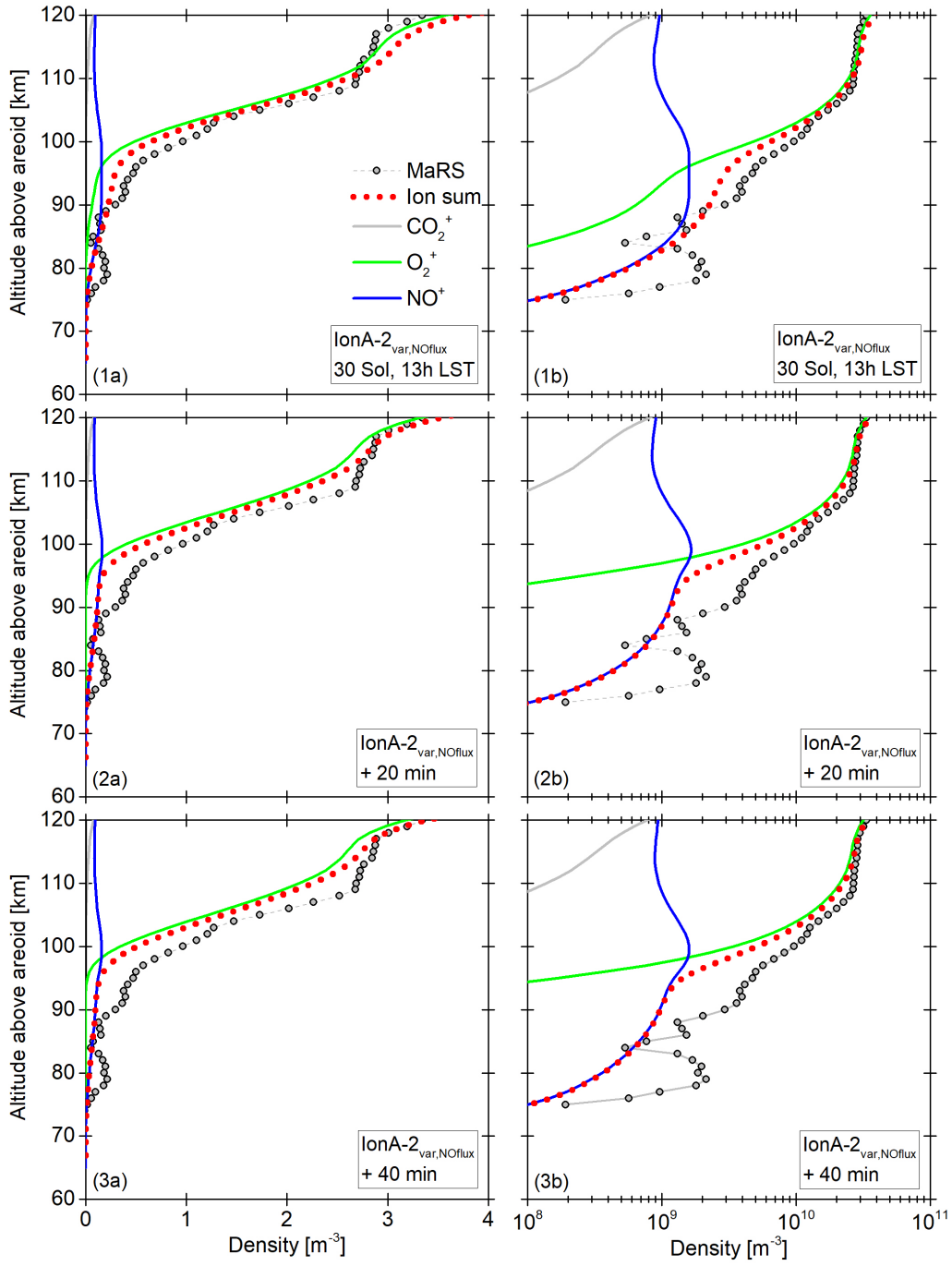

Figure 8.11: Panel (1) contains the linear (a) and logarithmic (b) representation of the IonA-$2_{var,NOflux}$ results of DoY 336 (2005) in Panel (3b) of Fig. 8.1 as starting point for the calculations. Panel (2) contains the IonA-$2_{var,NOflux}$ results calculated with the solar flux > 1.5 nm after 20 min of run time. Panel (c) contains the IonA-$2_{var,NOflux}$ results with the solar flux > 1.5 nm after 40 min of run time.

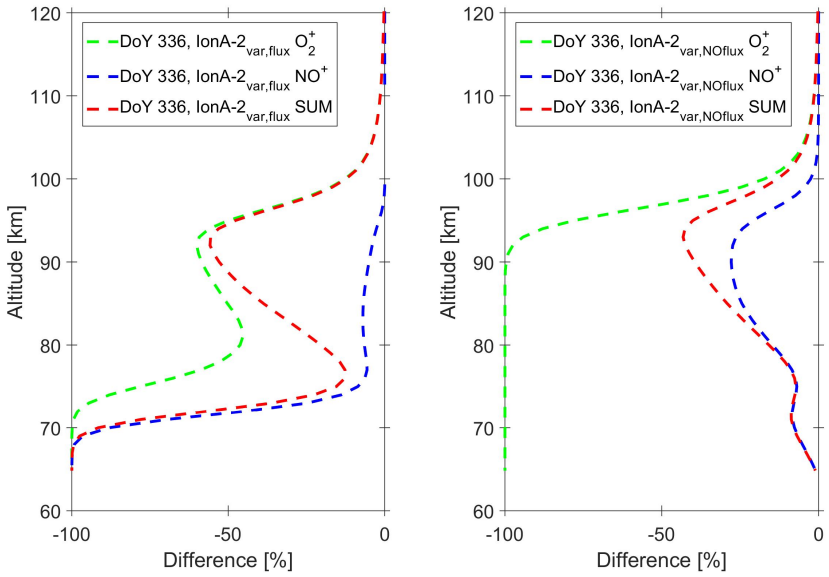

Figure 8.12: Difference between the IonA-2_{var} results for DoY 336 (2005) for the flux range 1.5 - 800 nm and 0.45 - 800 nm after after 40 min of model time in percent of the full solar flux results. (left) derived from the converged IonA-$2_{var,flux}$ results, (right) derived from the converged IonA-$2_{var,NOflux}$ results.

flux results. It is found, that the potential merged excess electron density decreases faster when it consists mostly of O_2^+ and slower for the NO^+ dominated part. This can be explained by Figure 6.3, where the different lifetimes of the species are illustrated in dependence of altitude. It is shown, that the lifetime of NO^+ exceeds those of O_2^+ below an altitude of approximately 80 km. An increase in solar flux from 0.45 - 10 nm by a factor 10 was also tested, but could not explain the observed complex potential Mm structure. Only a further increase of the V-shape was achieved (not shown).

In the next step, an extreme model scenario is created to test the capability of IonA-2_{var} to produce a complex structure in a potential Mm. For that, the SIP V2.38 wavelength bins between 0.55 and 1.55 nm are set to zero, while the solar flux of the lowest available SIP interval (0.45 to 0.55 nm) is increased by a factor 1,000. The neutral atmosphere and ionosphere of Panel (2b) of Figure 8.1 are again used as the input scenario. IonA-$2_{var,flux}$ is executed for 5 and 20 minutes of model time. Surprisingly, the model results did not lead to an enhancement of electron density in the lowest part of the ionosphere, but show a wide layer structure in the altitude range of the identified merged excess electron densities (see Figure 8.13). This behavior is explained by the absorption/ionization range of the lowest SIP solar flux bin. Figure 8.14 illustrates the ionization range of the solar radiation from 0.45 - 0.55 nm in the IonA-2_{var} model. The input parameters for this scenario are the neutral atmosphere of Panel (2b) of Figure 8.2 (similar to the earlier

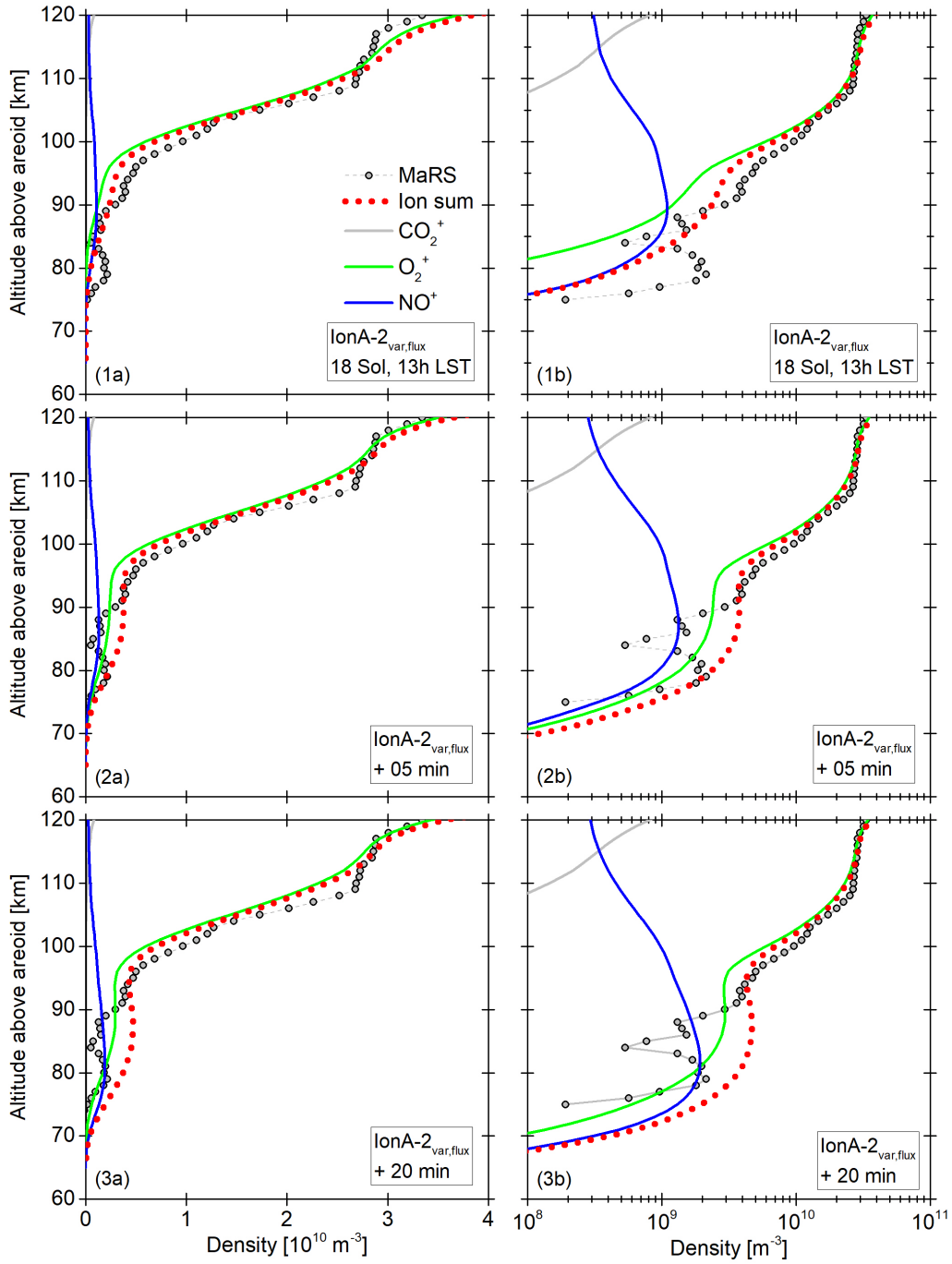

Figure 8.13: Panel (1) contains the linear (a) and logarithmic (b) representation of the IonA-$2_{var,flux}$ results of DoY 336 (2005) in Panel (2b) of Fig. 8.1 as starting point for the calculations. Panel (2) contains the IonA-$2_{var,flux}$ results calculated with the enhanced flux from 0.45 - 0.55 nm after 5 min of model time. Panel (c) contains the IonA-$2_{var,flux}$ results with the enhanced solar flux after 20 min of model time.

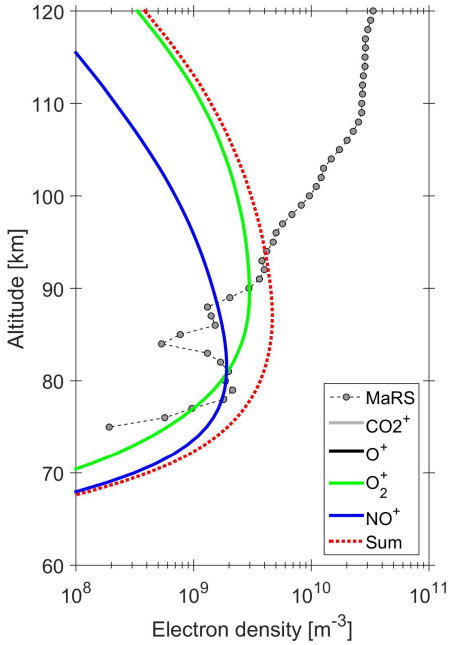

Figure 8.14: IonA-$2_{var,flux}$ results for the neutral atmosphere of Panel (2b) of Figure 8.2 with the enhanced solar input flux between 0.45 - 0.55 A and a model run time of 20 minutes.

calculations for enhanced solar flux), but the ionospheric densities are all set to zero. The only remaining input solar flux for this calculation is the SIP solar flux between 0.45 and 0.55 nm, enhanced by a factor of 1,000. IonA-$2_{var,flux}$ was then executed for 20 minutes of model time. The resulting ionosphere shows the wide layer structure in the altitude range of the merged excess electron densities, which is also seen in Figure 8.13. Due to the wide area of the absorption of the solar flux between 0.45 - 0.55 nm, no small scale structures are produced with IonA-2 in the range of the potential merged excess electron densities.
These investigations allow to draw the following conclusions::

(7) The solar radiation $<$ 1.5 nm is the main source for the potential Mm in IonA-2_{var}.

(8) The higher the NO^+/O_2^+ ratio in a potential merged excess electron density, the longer is the lifetime of the potential Mm if the short solar X-ray is decreased.

(9) An increase/decrease in solar flux $<$ 1.5 nm leads to an instant (in minutes) increase/decrease of the potential Mm, respectively. No complex structures occur during this process.

(10) IonA-2_{var} is not capable of producing other than V-shaped potential merged excess electron densities. The absorption region for the 1 Å solar radiation bins in the

neutral atmosphere is too wide.

(11) The variability of the solar flux, which is not properly mirrored in the averaged solar spectrum of the SIP, provides an explanation for the sporadic occurrence of the merged excess electron densities in the ionospheric dayside obervations of MaRS.

8.1.4 Discussion of the uncertainties in the IonA-2$_{var}$ results

The comparison of the IonA-2 potential merged excess electron densities with the identified Mm shows, that the interaction between short solar X-ray below 1.5 nm with the local Martian atmosphere is sufficient to explain the presence of the V-shaped merged excess electron densities in the dayside ionosphere of Mars. The model potential Mm consist of a combination of O_2^+ and NO^+, depending on the locally available amount of NO. The rate between O_2^+ and NO^+ also determines the lifetime of the potential merged excess electron densities. The additional small scale structure observed in the Mm of DoY 336, however, is not explained by the model.
Potential sources for uncertainties in the derived results comprise the input neutral atmosphere, the input solar flux, uncertainties in cross sections/secondary impact ionization/reaction rates and temperatures in combination with the sparse coverage of the investigated altitude region by other experiments and the neglection of multidimensional atmospheric/ionospheric effects in the 1-D IonA-2 model. These uncertainties will be discussed in the following Section.

The MCD V5.2 neutral atmosphere The Martian atmosphere provided by the MCD V5.2 is the result of a sophisticated GCM. While the model has been validated against several data sets for the lower atmosphere (e.g. *Lewis et al.* (1999)), exospheric temperatures (e.g. *González-Galindo et al.* (2015)) and ionospheric electron densities (e.g. *González-Galindo et al.* (2014)), it is unclear how closely the provided atmospheres reproduce the conditions at the time of a selected MaRS observation. In addition, the input solar fluxes for the MCD and the IonA-2 model are always different. The major neutrals, provided by the MCD, are therefore dependent on a different solar flux than the minor neutrals/ionosphere.
Due to the fact, that our knowledge about the Martian atmosphere is limited by a low number of observations compared to Earth, the Mars Climate Database yields one of the most reliable sources for individual calculations over a full Martian Sol. The MCD-MY scenario used in this work is designed to roughly mimic the observed planetary conditions (atmospheric dust load and solar variability) for the Mars years 24 to 31. The IonA-2 calculations over a full Martian Sol are necessary for the recombination of N and O (r. IR016) on the Martian night side. The self-consistent calculation of the major diffusion and the neutral, ion and electron temperatures from one input flux will make IonA-2 independent of the Mars Climate Database neutral atmosphere in future calculations.

The SIP V2.38 solar flux The SIP V2.38 solar flux model is based on observations for the position of Earth. The underlying models, which translate the observed solar features into full solar spectra might over- or underestimate the Suns output in certain solar flux ranges. The SIP resolution of one average solar spectrum per day may not be sufficient to provide a realistic X-ray variability at Mars.
Before the arrival of MAVEN at Mars at the end of 2014, no solar flux monitor for the planet was available. The SIP V2.38 solar spectra are therefore a tool widely used in the modeling community of the Mars ionosphere (e.g. *Mendillo et al.* (2011), *González-Galindo et al.* (2013) or *Fox* (2015)). Future inputs for IonA-2 will include the observations of the MVN-LPW-EUV EUV and soft X-ray monitor on board of MAVEN.

Uncertainties in cross sections, impact ionization, reaction rates and ion/electron temperatures in combination with the sparse observation coverage of the region of interest The most important ionization cross sections in the atmospheric region of interest are those for CO_2. CO_2 provides the highest ionization rate in the lower ionosphere due to its high volume mixing ratio. The difficulties in the CO_2 cross section derivation have been already discussed in Chapter 6. The most important error source introduced in IonA-2 for the region of interest are the branching ratios for the CO_2 absorption cross sections for solar flux below 4 nm. In this particular wavelength range, no exact values exist for the partial ionization cross sections. In IonA-2, the branching ratios for the available ionization channels are equally distributed instead of attributing all photo-ionization to CO_2^+, even if it is one of the stronger channels (*Berkowitz*, 2015). In addition, double ionization effects are neglected. The branches of the reaction provide CO_2^+, O^+, C^+ and CO^+. However, as discussed in Chapter 6, there are reactions which can convert the latter ions back into CO_2^+. Therefore the difference caused by the branching ratios is assumed to be small. The potential error source might cause a slight underestimation of the full extent of the potential Mm.

The secondary impact ionization is an important feature in the altitude region of interest. In IonA-2 it is parametrized with the W-value approach of *Wedlund et al.* (2011) and not based on a direct physical approach. This neglects the possible vertical transport of the energetic electrons. As shown in Chapter 6, the use of the approach of *Nicholson et al.* (2009) largely underestimates the electron density of the M1 region, which is not the case for the approach of *Wedlund et al.* (2011). The parametrization of the secondary impact ionization will be replaced by a physical approach in a future version of IonA-2.

Not all reaction rates used in the IonA-2 model (or other models of the Mars ionosphere) are well constraint by measurements. An example is the factor of 2.5, which is widely used as a correction factor for termolecular collision reactions of two species with CO_2 and was first introduced by *Nair et al.* (1994). Most reaction rates have been mea-

sured for lighter collision partners in comparison to CO_2 and the factor of 2.5 is used to adapt the reaction rate to the larger CO_2 molecule. A second problem is the availability of the required reaction constants and temperature dependences for the Mars atmosphere and ionosphere. Some reactions (e.g. r. IR001) are only upper limits for possible reactions, while others are theoretical estimates (e.g. r. IR086). For some reactions, no temperature dependence is known (e.g. r. IR019), while other measured reaction constants contain large error bars (e.g. r. IR057). This situation is especially difficult if the experimental coverage of the region of interest is sparse and the model results can only be validated against a small number of different instrument data sets. The input neutral atmosphere and solar flux in combination with the reaction scheme and transport of IonA-2 provide an excellent agreement with the electron density of the MaRS observation of DoY 336 (2005). But even if the photochemical cycle of the dayside ionosphere of Mars seems to be roughly understood, there are still many open questions. One of them is the nitrogen cycle at Mars and the associated N/NO ratio in the lower thermosphere and upper mesosphere, which is not well constraint by observations. The Viking Landers observed neutral NO down to approximately 120 km altitude with a density of approximately 10^{13} m^{-3} and $\sim 2 \cdot 10^{12}$ m^{-3} in 130 km altitude (see Figure 2.1 in Chapter 2), but no N densities could be derived. In addition, no NO^+ could be uniquely determined from the ion measurements (*Hanson et al.*, 1977).
The model ionospheres of e.g. *Krasnopolsky* (2002), *Fox* (2004), *González-Galindo et al.* (2013) or *Fox* (2015) all contain the major ionospheric features. In addition, NO^+ is always present, as is a potential Mm (stronger or weaker, depending on the underlying neutral atmosphere, the solar flux and the secondary ionization in the models). The model of *Fox* (2015), the LMD-GCM, and IonA-2 all contain NO^+, especially in the lower ionosphere, but while the Fox-model and IonA-2 show a dominance of NO over N in the upper mesosphere, the neutral atmosphere of the LMD-GCM (see Figure A.1 in Appendix A) shows a dominance of N over NO in the full provided data range of 80 to 200 km altitude. This difference shows, that the nitrogen cycle in the upper atmosphere of Mars and the associated ratio between N and NO require a thorough discussion. More information about the nitrogen cycle of Mars is found e.g. in *Krasnopolsky* (1993) and *Lefèvre and Krasnopolsky* (2017).
The predominant production mechanism for N and $N(^2D)$ in the Mars dayside thermosphere is the photo-dissociation of N_2

$$N_2 + h\nu \rightarrow N + N(^2D). \qquad \text{(r. IP006)}$$

The electron impact dissociation

$$N_2 + e^- \rightarrow N + N(^2D)$$

might provide an additional amount of N and $N(^2D)$, but this effect is not yet included in IonA-2 due to the parametrization of the impact ionization by the approach of *Wedlund*

et al. (2011). It will be investigated in a future version of IonA-2. De-excitation or quenching of $N(^2D)$ during collisions (r. IR020 and r. IR021) with ambient atoms or molecules changes the ratio between the production of N and $N(^2D)$. In the thermosphere, NO is mainly formed by

$$N(^2D) + CO_2 \rightarrow NO + CO. \qquad \text{(r. IR019)}$$

The production of N and NO is balanced by the sink equation

$$N + NO \rightarrow N_2 + O. \qquad \text{(r. IR014)}$$

In addition, the reaction

$$NO^+ + e^- \rightarrow N(^2D) + O. \qquad \text{(r. IR097)}$$

plays an important role in the production of $N(^2D)$. At night, N and O recombine to NO (r. IR016). During this reaction, the NO ultraviolet nightglow is produced by the spontaneous and fast de-excitation of the excited NO product. Those and many other processes in the IonA-2 reaction scheme provide the balance between the production of N and NO in the day and night cycle of the Martian atmosphere and ionosphere. The nitrogen species with the higher net production from the described processes is transported downwards from the thermosphere into the upper mesosphere, because photochemistry in that altitude region is much faster than transport.
In IonA-2 NO dominates over N in the model lower altitudes. In the following Section it is shortly investigated with an extreme model scenario, if and how the IonA-2 model is capable to reproduce the dominance of N over NO shown by the neutral atmosphere of the LMD-GCM. For this purpose, reaction IP006 is changed to

$$N_2 + h\nu \rightarrow N + N$$

instead of the so far assumed output of 50% N and 50% $N(^2D)$ (see Chapter 6). In addition, the reaction

$$N + CO_2 \rightarrow NO + CO \qquad \text{(r. IR012)}$$

is disabled. A IonA-2 test run for the MaRS observation of DoY 336 (2005) yields a dominance of N over NO after 34 Mars hours of model time. Figure 8.15 shows the resulting neutral atmosphere and ionosphere after 2 Sol and 4 Mars hours of model time. This time frame was chosen to resemble the solar zenith angle conditions of the observation. Suppressing reaction IR012 plays an important role in the process of achieving the dominance of N over NO in the upper mesosphere. This reaction mechanism provides only an upper limit and no reaction has been observed between the species so far (*Fernandez et al.*, 1998). Therefore, the suppression of this reaction is physically/chemically reasonable. The effect of a change in the photo-dissociation branching ratio for N_2 on the dominance between N and NO in the upper mesosphere is described by *Krasnopolsky* (1993). The author found, that small changes in the production rate of N and $N(^2D)$

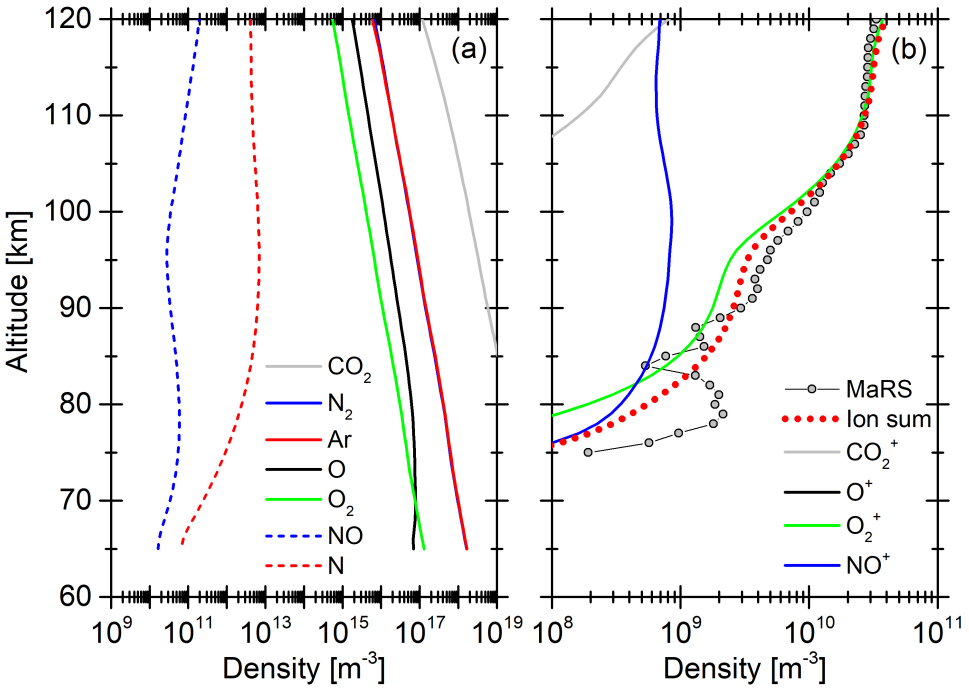

Figure 8.15: Neutral atmosphere (a) and ionosphere (b) derived in the IonA-$2_{var,flux}$ mode from the MCD V5.2 major neutral species input for DoY 336 after 2 Sol + 4 Mars hours run time.

from photo-dissociation of N_2 are able to change the dominance of either N or NO at 80 km altitude.

The frequent remote and in-situ observations of the upper neutral atmosphere and ionosphere of Mars by MAVEN down to approximately 150 km altitude in combination with deep dips down to approximately 120 km altitude will provide new observational insight in the model chemistry of the poorly constraint region of the upper mesosphere. Panel (a) of Figure 2.13 shows the averaged altitude profiles of the Mars ionospheric composition derived from MVN-NGIMS observations for a solar zenith angle of 60 °. The NO^+ density of approximately $3 \cdot 10^8\, m^{-3}$ is in excellent agreement with the IonA-$2_{var,flux}$ results for the MaRS observation of DoY 336 (2005). The Martian neutral atmosphere shown in the right Panel of Figure 2.9 for a solar zenith angle of 45 ° however shows a N density of $\sim 2 \cdot 10^{14}$, which is orders of magnitudes larger than the IonA-2_{var} N densities, even for the case, where N dominates. (the shown IonA-2_{var} atmosphere is only an example and has not yet reached convergence). An equilibrium calculation can be used to estimate the expected NO^+ densities from the reported MVN-NGIMS N density

$$NO^+ = \frac{n_{O_2^+} \cdot n_N \cdot 1 \cdot 10^{-16}}{n_e \cdot 2 \cdot 10^{-14} \left(\frac{300K}{T_e}\right)^{0.8}}. \tag{8.1}$$

Using the approximate densities given in the Figures 2.9, 2.13 (MVN-NGIMS) and Figure 8.16 (MVN-LPW) ($n_{O_2^+} \sim 2 \cdot 10^{10}\, m^{-3}$), ($n_N \sim 2 \cdot 10^{14}\, m^{-3}$), ($n_e \sim 2.5 \cdot 10^{10}\, m^{-3}$), ($T_e \sim 800\, K$) yields $n_{NO^+}(155km) \sim 1.8 \cdot 10^{12}\, m^{-3}$. This is extremely large in comparison to the $n_{NO^+}(155km) \sim 1.3 \cdot 10^{8} m^{-3}$ measured by the MVN-NGIMS instrument and unrealistic compared to the M2 main peak electron densities in Figure 7.3. Some of the discrepancies may be explained by the variance of N due to the different solar zenith angles in the neutral atmosphere and ionospheric observations and a potential different solar flux during these observations. Another large part of the discrepancies might be caused by the high observed MVN-LPW electron temperature used in the equilibrium calculation. Figure 8.16 shows the average electron temperatures T_e derived with the MVN-LPW experiment. Those are the first direct measurements of T_e below 200 km altitude. These electron temperatures are much higher at the altitudes of the ionospheric main peak than the model results provided by *Rohrbaugh et al.* (1979), which are used in IonA-2. This model is based on the Viking lander results. The Viking landers could not observe T_e at altitudes below 200 km, but the model extrapolates these measurements to the required altitude range. Including the recently reported MVN-LPW T_e into IonA-2 results in a large overestimation of the electron density in the ionospheric main peak region, not in agreement with the MaRS observations. MVN-LPW observed this T_e close to the subsolar point, which might partially explain the high temperatures. In addition, the authors state, that the given electron temperature at lower altitudes might be over- but not underestimated. These controversal results show, that the region of interest is still poorly understood. Models like IonA-2 are therefore urgently required to gain more insight into the underlying processes.

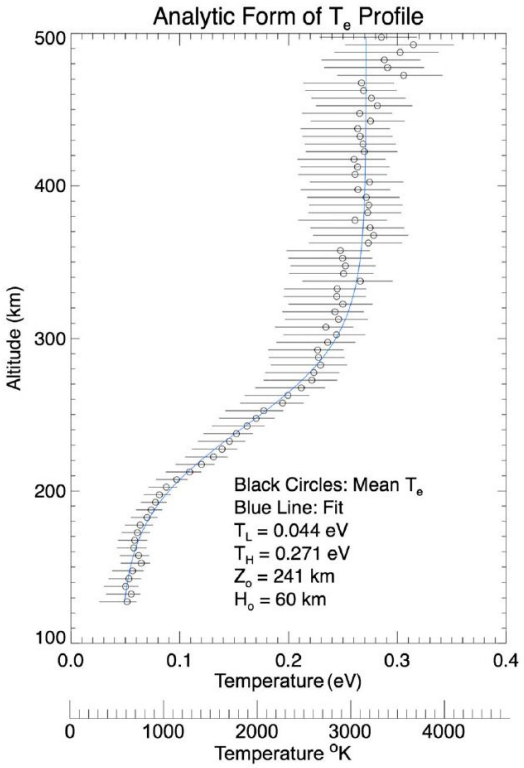

*Figure 8.16: Electron temperature T_e variation derived from the inbound leg of the MVN-LPW observations during the deep dip campaign in April 2015 (*Ergun et al., *2015) . The average solar zenith angle at periapsis is* 12°. *The mean T_e is illustrated by circles, the horizontal lines are the T_e uncertainties, the connecting line is a fit to the data.*

Multidimensional transport IonA-2 is a 1-D model which does not include the effects of horizontal transport. The comparison of the *NO* nightglow observations of MEX-

SPICAM and MVN-IUVS with results of the LMD-GCM (*Gagné et al.*, 2013; *Stiepen et al.*, 2017; *González-Galindo et al.*, 2015) show a global transport pattern, which tends to accumulate light species as N and O at the planetary poles. Those effects are neglected in IonA-2, but might play a role in the balance between N and NO in the upper mesosphere and thermosphere. The strength of this effect will be investigated with a future version of IonA-2, where altitude profiles of the NO nightglow are included and compared with the MEX-SPICAM and MVN-IUVS observations.

The discussion of the potential sources of uncertainty in the IonA-2 model shows, that the overall photochemical scheme of the Mars dayside ionosphere is roughly understood, but many open questions remain. As shown by comparisons with the MaRS electron density observations, IonA-2 provides the approximately correct altitude for the included absorption/ionization processes. This makes short solar X-ray below 1.5 nm wavelength a highly probable source for the V-shaped Mm. The dominant ion in the identified merged excess electron densities remains unclear due to the large uncertainties in the applied reaction rates and local temperatures. A wealth of new information about the upper atmosphere is continuously provided by the Mars Express and the MAVEN spacecraft and presents new challenges for the existing models. The new data will be a great help for constraining the Martian atmospheric and ionospheric composition and variability. Models like IonA-2, on the other side, are required to interpret and understand these observations.

8.2 Other potential sources for merged excess electron densities

Figure 8.17 shows six examples of observed MaRS electron density profiles which contain merged excess electron densities. Panel (a) and (b) show the two Mm from Figure 7.21 with a maximum electron density above $10^{10}\,m^{-3}$. The merged excess electron density in Panel (a) consists of a very pronounced V-shape, for which an enlarged flux in short solar X-ray yields a probable explanation. The observation in Panel (b) shows a strong Mm directly below M1. Other physical processes than the enhanced short solar X-ray are needed to explain this shape. The electron density profiles in Panel (c) and (d) contain examples for complex wavelike structures in the lower baseline below the Mm features. The MaRS observations in Panel (e) and (f) have been conducted on the same Earth day, approximately 24 h apart. The observation footpoints vary in longitude, but are observed at almost the same latitude and solar zenith angle. While the first observation in Panel (e) shows only a very pronounced Mm but an otherwise undisturbed ionosphere, the electron density profile in the second observation (Panel (f)) is largely disturbed. The potential sources for the shown disturbances are shortly discussed in this Section. In

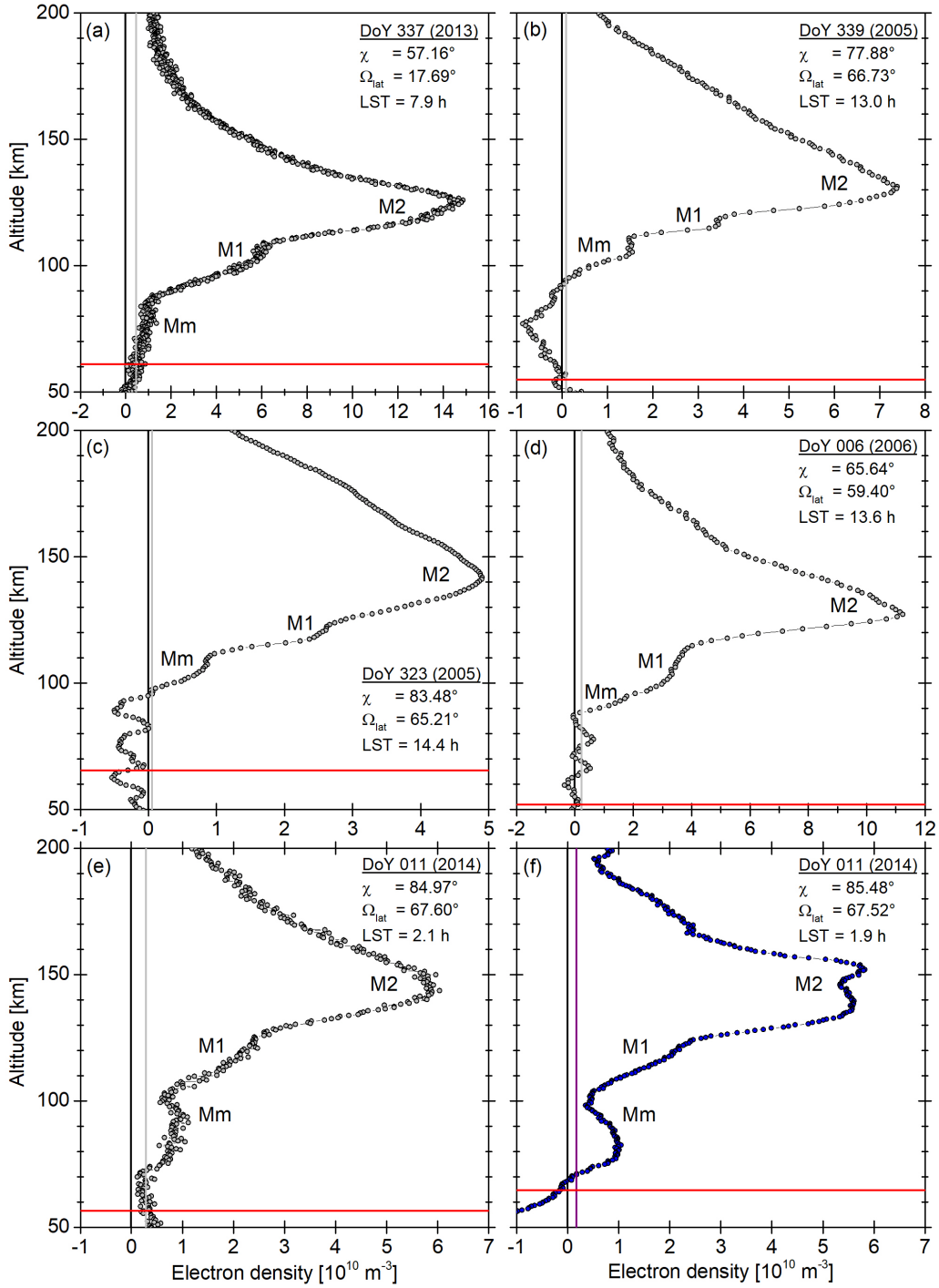

Figure 8.17: MaRS electron densities for (a) DoY 337 (2013), (b) DoY 339 (2005), (c) DoY 323 (2005), (d) DoY 006 (2006), (e) DoY 011 (2014) 2:35 a.m. UTC at Earth and (f) DoY 011 (2014) 11:40 p.m. UTC at Earth. Gray dots indicate observations derived from diff. Doppler, while blue dots indicate electron density derived from X-band. Gray/purple lines indicate the noise level $3{\cdot}\sigma_{noise,UB}$, the red line indicates the lowest valid altitude $h_{L,val}$.

addition, a short summary of the current observation status for the metallic ions in the lower ionosphere of Mars is given. Other potential sources for the merged excess electron densities cannot be ruled out but will be topic of future investigations.

Internal waves in the Mars upper atmosphere Both MaRS observations in Panel (c) and (d) of Figure 8.17 show a merged excess electron density structure below the M1 layer. Underneath Mm, the lower baselines of both profiles contain wavelike structures. The lower baseline disturbance in Panel (c) could even be identified as a possible detached excess electron density feature. Short solar X-ray alone is an unlikely source for these features. The lowest available wavelength interval in the SIP model is 0.45 - 0.55 nm. The altitude, where τ reaches unity for this wavelength interval is $\sim 72\,km$ for DoY 111 (2006) with an solar zenith angle of 58.80 ° and $\sim 86\,km$ for DoY 336 (2005) with a χ of 78.96 °. Shorter solar wavelengths might penetrate deeper into the Martian atmosphere, but the investigations with IonA-2 show, that the absorption range for an 1 Å bin is much too wide to explain the small scale structure in DoY 336 (2005). Another potential explanation for the observed disturbances is provided by a combination of internal waves in the Mars upper atmosphere and the movement of the projected footpoint of the observation over the surface of Mars. Upward traveling waves play an important role in the vertical coupling of the atmosphere/ionosphere system on Earth and gravity waves have been also identified in the upper atmosphere of Mars (see Chapter 2 for a detailed discussion). *Fritts et al.* (2006) determined typical spatial scales of 20 - 200 km in 100 - 130 km altitude. Density fluctuations vary from approx. 5 to 50 %. The spatial scale of these waves might provide an explanation for the wavelike structures in the lower baseline of the shown MaRS profiles. In an radio occultation ingress observation, the ionosphere and neutral atmosphere are successively sounded from top to bottom. During that time, the projected footpoint of the observation moves slightly over the surface of Mars. The observed profiles are therefore not completely vertical. When the radio ray is passing through the region of a small gravity wave, the horizontal radial symmetry of the neutral atmosphere and the radial symmetry of the ionosphere is disturbed. The Abel-transform of the received signals, which assumes radial symmetry, might react to such local horizontal disturbances with the production of the seen wavelike structures.

Solar energetic particle precipitation The MEX-MARSIS instrument observed considerable ionospheric electron density structures over regions of strong and predominantly vertical crustal magnetic fields. They extent as much as 50 km above the surrounding ionosphere, with an average of 19 km (*Gurnett et al.*, 2005; *Duru et al.*, 2006; *Gurnett et al.*, 2008). *Duru et al.* (2006) used the (*Cain et al.*, 2003) magnetic field model (based on MGS-MAG/ER observations) for correlations with the position of hyperbola-shaped traces in the ionograms of the MEX-MARSIS ionosounder. It was found, that many structures occur over highly magnetized regions of Mars for a magnetic field strength larger

than 150 nT at 150 km altitude and a field orientation within 20° from the vertical. The authors connect the structures with solar wind electrons, which reach the base of the ionosphere along the open field lines and heat the ionosphere. Solar wind electrons penetrating deep into the Mars ionosphere are another possible cause of Mm excess densities. The MaRS_{quiet} data set contains only 5 observations over crustal fields with a magnitude larger than 20 nT (roughly estimated by converting the 150 nT value to 400 km altitude by the simple assumption of an inverse quadratic distance dependence of the magnetic field) and a deviation angle from vertical of at most 30° (it is assumed, that the deviation angle from vertical will increase for higher altitudes). These five observations comprise two observations with and three observations without Mm excess density, for which the TEC however is found well within the scatter of all observations (not shown here). Due to the low number of MaRS observations over stronger crustal magnetic fields, no valid conclusion about the influence of the crustal magnetic field on the MaRS TEC can be drawn. The atmosphere of Mars is directly exposed to the precipitation of solar energetic particles (SEPs) due to the lack of an intrinsic magnetic field. This causes impact ionization and the production of secondary electrons (see e.g. *Lillis et al.* (2012)). While the MaRS observation at 2:35 a.m. UTC Earth time of DoY 011 (2014) (Panel (e) in Figure 8.17) shows obvious disturbances in the lower part of the electron density profile only, the MaRS observation later on the same day (11:40 p.m. UTC, Panel (f) in Figure 8.17) shows an overall strongly disturbed ionosphere, indicating a long lasting event. No SEP monitor was present at Mars during the time of observation, but *Ulusen et al.* (2012) correlated Mars Global Surveyor radio science observations with the MGS-MAG/ER Electron Reflectometer as an indicator for SEP events. A similar comparison was done for this day with the MEX-ASPERA3 electron spectrometer (*Barabash et al.*, 2004) which shows a strong and slowly decreasing solar event in the days before the MaRS observation. Around 2:30 a.m., a slight increase in the electron spectrometer data[2] is found, while no data are available for the strong event at 11:40 p.m.[3]. Further investigations and comparison with other instruments are therefore needed. Future simultaneous observations of MaRS and the MVN-SEP instrument will put further constraints on the interactions between SEPs and the lower dayside ionosphere of Mars.

Metallic ions in the lower ionosphere of Mars The discovery of the sporadic electron density structure below the M1 layer by *Pätzold et al.* (2005) in the MaRS observations intensified the investigation of this topic by modelers and observers (e.g. *Molina-Cuberos et al.* (2008); *Withers et al.* (2008); *Whalley and Plane* (2010); *Pandya and Haider* (2014)). However, due to a missing monitor for interplanetary dust particles at Mars, the input flux of meteoric particles for the models was poorly constraint. The comet Siding Spring (discovered at the Siding Spring observatory in Australia by R. McNaught (*Mc-*

[2]provided by M. Fränz, personal communication

[3]This work was presented as a poster on the EGU 2016 in Vienna - abstract EGU2016-1040.

Naught et al., 2013)) passed within 141,000 km of Mars on the 19. October 2014 (*Espley et al.*, 2015). During this rare opportunity the comets coma and plasma interacted directly with Mars and allowed the direct observation by Mars Express and MAVEN (e.g. (*Gurnett et al.*, 2015; *Restano et al.*, 2015; *Benna et al.*, 2015b). During the passage of Siding Spring, the MVN-IUVS experiment detected Mg^+ in the range from $5 \cdot 10^9\, m^{-3}$ to $3 \cdot 10^{10}\, m^{-3}$ at 120 km altitude (*Schneider et al.*, 2015). The remote identification of Mg^+ is conducted by detecting the resonant scattering of solar UV photons by Mg^+. Mg^+ is reliably detected, if the detection region is lit and if the solar disturbance of the instrument is not too pronounced. *Crismani et al.* (2017) used the MVN-IUVS observations of one Martian year to investigate the parameters of the observed Mg^+. A main peak concentration of $\sim 2.5 \cdot 10^8\, m^{-3}$ was found at approximately 90 km altitude with an uncertainty of ∼2.5 km. Variability of the Mg^+ at a fixed altitude of 90 km was identified and attributed to the seasonal warming and cooling of the Martian atmosphere. At the equator, the Mg^+ density decreases up to a factor 5 towards the dawn and dusk terminators. This effect is weaker at the poles, due to the less pronounced diurnal cycle in these regions. No correlation between the Mg^+ density and predicted meteor showers were found during the investigated Martian year. Even if Mg^+ is detected in the Mars atmosphere, the only detection of the associated Mg was found by MVN-IUVS during the passage of Siding Spring. This yields a big challenge for the existing meteor-ionosphere interaction models, which predict a large Mg layer in combination with the Mg^+.
The mean peak altitude of the Mg^+ layer in the MVN-IUVS observations is in good agreement with the altitude range of the merged excess electron densities in the MaRS observations. However, the mean peak density is too small to be regularly seen by MaRS due to the inherent noise level of the observations. Only strong positive deviations from the mean could be detected by MaRS. Mg^+ obviously contributes to the observed merged excess electron densities at 90 km altitude but is most probably not the only source. The absorption of short solar X-ray by the planetary neutral atmosphere in IonA-2 is therefore the major source for ionization in the investigated altitude region. *Whalley and Plane* (2010) assume, that the main source for the ionization of Mg in that altitude range is charge exchange with ambient O_2^+. This implies for MaRS radio science, that the ratio between the ambient Mg^+ and O_2^+ (and probably NO^+) is indistinguishable in the observed electron density. At Earth, the wind shear mechanism is assumed to provide the strong metallic sporadic E-layers in the lower ionosphere. This mechanism does however require the presence of a magnetic field. Only few MaRS observation are available over strong crustal fields. Therefore no correlations with this parameter is currently possible. The majority of merged excess electron densities is however found over weak magnetic fields. It is therefore expected, that an enhancement of the Mg^+ densities by wind shear is not the primary source for the identified merged excess electron densities in the MaRS_{quiet} data set.

Chapter 9

Summary of the derived results and future prospects of the developed data base and software

The lower dayside ionosphere of Mars consists of two major features, the main ionospheric layer M2 and the lower and weaker M1 region. In 2005, *Pätzold et al.* (2005) discovered small scale sporadic electron density structures beneath M1 in the observations of the Mars Express radio science experiment (MaRS). Radio science experiments can only sense the electron density distribution but not the ions, therefore the origin and composition of these features remained unknown. Until today, no in-situ observations of the atmospheric and ionospheric composition have been conducted in the altitude region between 70 and 110 km. The large number of radio science observations with Mars Global Surveyor were conducted in X-band only. The resulting electron density profiles provide no possibility to distinguish between real small scale structures and features introduced by unexpected movement of the spacecraft or the ground station. In contrast, the radio science experiment MaRS provides dual-frequency ionospheric observations. This technique allows to distinguish between disturbances introduced by unexpected movement and frequency shifts caused by plasma along the radio ray path. The observations conducted by MaRS therefore allow a thorough analysis of the small scale variability of the lowest part of the Martian dayside ionosphere with unprecedented accuracy.
Potential energy sources for the ionization processes in the region of interest are short solar X-ray or solar energetic particles. Potential targets for these ionization processes are either local neutral species of planetary origin or metallic neutrals of extraplanetary origin (interplanetary dust particles/remnants of meteoroids). Another potential source for those features are internal gravity waves. For this work, the small scale sporadic electron density structures are divided into two categories. The features merged with the main ionospheric body are called merged excess electron densities (Mm), while the features detached from the main ionospheric body are called detached excess electron densities

(Md). This work focuses on the question, if the ionization of the ambient neutrals by short solar X-ray is sufficient to explain the occurrence rate and characteristics of the merged excess electron densities. The first of the following two Sections gives a summary of the conducted work and the achieved results, while the second Section provides a brief summary of the future prospects and potential applications of this work.

9.1 Summary of the derived results

More than 10 years of Mars Express MaRS radio science observations (2004 - 2014) provide a profound data base for this exploration of the potential origins of the merged excess electron densities. From the wealth of information, only those MaRS observations with the smallest amount of large scale observational noise have been selected for this work. They are used to investigate, if merged excess electron densities form in otherwise undisturbed observations of the ionospheric dayside or if they are only a by-product of a strongly disturbed ionosphere. The MaRS_{quiet} data set consists of 266 dayside observations of the ionospheric electron density. The combination of the MaRS dual-frequency observations in X- and S-Band provide a third product, the differential Doppler. While the X-Band is more sensitive to unexpected movement of spacecraft or ground station, the differential Doppler shows a higher sensitivity to additional plasma caused by solar wind disturbances along the radio ray path.
Statistical correlations between the occurrence rate/characteristics of the identified Mm and the observational and environmental parameters of the observation provide information about potential formation processes. For each observation in the MaRS_{quiet} data set, characteristics of the ionosphere, observational parameters (Chapter 4) and environmental parameters (Chapter 5) at the time of the observation have been derived. Characteristics of the ionosphere consists of the M2, M1 and Mm vertical TEC, peak electron density, altitude and width with error bars where possible. The error bars for M1 are derived with the help of a fast 1-D equilibrium model (Chapter 6). Observational parameters comprise the areocentric position of the MaRS observation, the altitude calibration of the observations (areoid), parameters of the electron density profiles (noise level and offset of the upper baseline, upper and lower altitude borders of the electron density profile, the lowest valid altitude of an observation, the noise level and offset of the lower baseline). Environmental parameters are the SIP V2.38 solar flux proxies and the crustal magnetic field strength in 400 km altitude.
Radio science experiments can only sense electrons, but they can not provide any information about the corresponding ionospheric ions, therefore a model of the Mars ionosphere is needed to investigate the potential Mm formation by solar X-ray and explore the effect of a changing neutral atmosphere on the Mm composition. Chapter 6 describes the development of the IonA-2 model, which is a 1-D time-marching photochemical transport model with an implemented diurnal cycle. For the simulation of the diurnal cycle, IonA-2 uses

the MCD V5.2 major neutral species and neutral temperature for a full Sol in combination with the SIP V2.38 Earth solar flux spectra calibrated for the Mars position. The photochemical scheme in combination with eddy and minor diffusion of the minor neutrals and ambipolar diffusion of the ions provides vertical profiles of several minor neutral species and major ions for a full Martian Sol. This work focuses on the ionospheric dayside, no nightside profiles are shown. The comparison between the IonA-2 and the MaRS electron density profile from DoY 336 (2005) shows an excellent agreement between model and observation. The IonA-2 ion distribution shows a surprisingly good agreement with the Viking-RPA in-situ observations and other independent model ion densities of *Fox* (2015), despite the differences between the Viking-RPA environmental and the *Fox* (2015) model input conditions. This good agreement between IonA-2, the MaRS measurements, other independent observations, and other "state-of-the-art" model results provides confidence in the physical and chemical validity of the developed ionospheric model. It builds a powerful tool for the investigation of possible formation processes of the merged excess electron densities.
Chapter 4 to 6 provide a solid base for the investigation of possible formation mechanisms. Results based on these investigations are subsequently discussed in Chapter 7 and 8. Chapter 7 describes the derivation of the Mm occurrence rates and characteristics and correlates them with observational and environmental parameters. These investigations provide information about potential formation processes of the merged excess electron densities. The influence of the solar flux and the underlying neutral atmosphere is discussed in Chapter 8. It contains the comparison between the model potential Mm derived for changing solar flux conditions and underlying compositions of the Mars neutral atmosphere and the MaRS identified Mm. The results discussed in Chapter 7 and 8 are summarized in the following two Sections.

9.2 Mm characteristics deduced from the MaRS observations

The MaRS_{quiet} data set yields a profound base for the derivation of the Mm occurrence rates and characteristics. Correlations of the derived Mm attributes with observational and environmental parameters yield information about potential formation processes of the merged excess electron densities.

Existence of the merged excess electron densities A very first step requires the confirmation of the physical existence of these ionospheric features. If the external noise introduced by unexpected movement or plasma is low enough, merged excess electron densities are found in the electron density profiles derived from X-Band and those from differential Doppler for the same MaRS occultation. This shows, that the Mm are more

than a feature caused by external disturbances of the observation. The further investigation of the effect of the upper baseline noise level $\sigma_{noise,UB}$ and deviations from a radial symmetric atmosphere on the identified merged excess electron densities in Chapter 7 confirms, that the Mm are real features in the Mars ionosphere. However, an increased $\sigma_{noise,UB}$ may obscure existing merged excess electron densities. Approximately 44% of the MaRS$_{quiet}$ data set contain pronounced identified merged excess electron densities. Additional potential Mm have been detected in the observations, but are neglected in the statistics to avoid a bias by including the weak detections. It is now obvious from the conducted investigations, that there is no clear border between a pronounced merged excess electron density and the weaker "dips" at the lower base of the ionosphere, they most probably share the same origin. The identified merged excess electron densities show a wide variety of shapes.

Correlation of the identified Mm characteristics with observational and environmental parameters Merged excess electron densities are found for all solar zenith angles of the ionospheric dayside accessible in the MaRS$_{quiet}$ data set (50 ° to 90 °). The bulk of Mm has been identified over regions with low crustal magnetic fields. However, a correlation between the occurrence rate of the merged excess electron densities and strong crustal magnetic fields remains inconclusive due to the low number of available MaRS$_{quiet}$ observations for high B_{tot}. The occurrence rate of the merged excess electron density strongly correlates with the Sun's activity level. This is a first indicator for the importance of the Sun's emissions in the formation process of the Mm. Solar events, which provide potential energy sources for the Mm in the form of background short X-ray flux, are rare for low solar activity, as are CMEs and solar flares. The merged excess electron densities are found in an altitude range of approximately 70 to 110 km altitude, only accessible by short solar X-ray flux. In addition, the smoothed ionospheric base of the merged excess electron densities is on average found lower in the Martian atmosphere then the base of the smoothed undisturbed observations. This indicates a Mm formation process, which requires energy sources that are capable to penetrate the Mars ionosphere deeper than usual (e.g. short solar X-ray or SEPs). However, neither the vertical TEC nor the maximum electron density of the Mm show a correlation with the solar zenith angle or the short X-ray solar flux proxies $\Phi_{0.45-1nm}$ and $\Phi_{0.45-3nm}$. Those solar flux proxies are calculated from the calibrated SIP V2.38 solar flux model, which originally provides solar flux spectra for Earth with one average solar spectrum per day. The Sun's variability in the short solar X-ray at the Mars position during the time of a Mars observation might therefore not be sufficiently well represented by the proxies. The mean value and standard deviation for the vertical TEC and the maximum electron density are $2.569 \cdot 10^{13} \pm 2.562 \cdot 10^{13}\, m^{-2}$ for the vertical TEC and $0.44 \cdot 10^{10} \pm 0.20 \cdot 10^{10}\, m^{-3}$ for the maximum electron density, respectively. Those values neglect the two strongest

TEC observations in Figure 7.17. The standard deviation in the vertical TEC is almost as strong as the associated mean, even when the two outliers are not taken into account. This is caused by the non-Gaussian distribution of the data. An additional merged excess electron density does not significantly increase the vertical TEC of the entire profile or the M1 layer. A potential trend is obscured by the high TEC variability in the MaRS_{quiet} data set.

9.3 Comparison of the IonA-2 potential Mm with the identified MaRS merged excess electron densities

Modeling the ionosphere electron density exemplarily for two selected MaRS observations with different solar zenith angles and Mm shapes provides additional insight into the atmospheric and ionospheric processes in the Mm region.

The effect of short solar X-ray on the local neutral atmosphere The characteristics of the potential Mm derived from the IonA-2 model electron density depend directly on the SIP solar radiation below 1.5 nm. The model produces V-shaped merged excess electron densities without artificial enhancement of the SIP V2.38 X-ray fluxes, if the solar flux distribution below 1.5 nm is taken into account in 1 and 0.1 nm resolution. A direct comparison between two MaRS observations and the associated IonA-2 results for the approximate position and time of the observation yield a good agreement between the general V-shape structure of the observed and modeled Mm. An increase/decrease in solar flux $<$ 1.5 nm yields a prompt (in minutes) increase/decrease of the potential Mm, which might partially explain the sporadic appearances of the Mm structure in the MaRS observations. The higher the NO^+/O_2^+ ratio of a potential merged excess electron density, the longer is its lifetime during a decrease in short solar X-ray. IonA-2 is not capable of producing substructures in the V-shaped Mm. The atmospheric absorption region for the 1 Å solar radiation bins is too wide to produce ionospheric small scale structures without the implementation of any further physical processes. The characteristics of the model potential Mm for all analyzed profiles agree well with those of the identified Mm with regard to altitude range, maximum electron density and TEC.

The effect of the poorly constraint nitrogen cycle on Mars on the model results The actual ratio between the N and NO species in the lower thermosphere and upper mesosphere of Mars is still unknown due to the lack of in-situ observations of the local composition and due to the currently poorly constraint reaction schemes and atmospheric input parameters. The IonA-2 model provides a dominance of NO over N in the lower model altitudes, similar to the results of *Fox* (2015). On the other hand, N dominates over NO in the LMD-GCM. The dominance of N over NO is reproducible with IonA-2

with small changes of the reaction scheme. Both IonA-2 model scenarios however result in a certain amount of NO^+ in the lower ionosphere. During the dominance of NO over N, the main reaction for the production of NO^+ is the charge exchange between O_2^+ and NO (r. IR120). If N dominates over NO, the main production mechanism for NO^+ is the charge exchange between O_2^+ and N (r. IR117). Therefore NO^+ (in combination with O_2^+) is a probable candidate for the merged excess electron densities.

Final results The merged excess electron densities identified in the MaRS observations show a positive correlation with the Sun's activity. Their base is on average found deeper in the atmosphere, than the base of the averaged undisturbed MaRS electron density profiles. This indicates a dependence of the formation process on energy sources which penetrate deep into the atmosphere. Short solar X-ray which ionizes the local neutral atmosphere provides a satisfying explanation for the identified V-shaped merged excess electron densities in the MaRS observations. This result is in contrast to previous model predictions who assumed a meteoric origin of the sporadic layers. However, other potential sources might provide an additional electron density contribution (meteoric Mg^+), additional sub-structures (gravity waves) or strong Mm enhancements with large disturbances in the ionosphere (SEPs). The sporadic occurrence of the merged excess electron densities in the MaRS observations is assumed to be a combination of observational (increased observation noise level, shift of the lower baseline by ionospheric deviations from radial symmetry) and environmental (solar flux variation, changes in the neutral atmospheric composition) factors.

9.4 Outlook

The subsets of the MaRS observations, MaRS_{all} and MaRS_{quiet} with their derived observational and environmental parameters yield a promising data base for further investigations of the still poorly understood lower ionosphere of Mars. The 1-D time-marching IonA-2 model is already a powerful tool with large potential for further investigations.

MaRS observations 2004 - 2014 The MaRS_{quiet} data set provides an excellent data base for the derivation of statistical characteristics for the detached excess electron densities.
The interaction between solar energetic particles and the lower atmosphere and ionosphere of Mars can be investigated by a correlation between the Mm derived from MaRS_{all} and the observations of the MEX-ASPERA3 electron spectrometer. The observations of the electron spectrometer yield a rough indicator for SEP activity at Mars.

MaRS observations 2015 - ongoing The derivation of the Mm characteristics and occurrence rate from these new MaRS observations with the already existing software tools

will provide an excellent data base for comparison with the observations of the MAVEN spacecraft. The MVN-LPW-EUV solar monitor observes certain solar flux bins directly at Mars, which will provide a realistic database for the comparison with the identified merged excess electron densities. A similar approach is possible with the MVN-SEP Solar Energetic Particle instrument. The MVN-IUVS instrument provides the possibility of a direct comparison of the Mg^+ density with the available ionospheric electron density.
The upcoming occultation season at the end of February 2018 will provide observations over the southern hemisphere of Mars, where the strongest crustal fields are available. For the very first time, these observations will give the opportunity to explore if wind shear in combination with the meteoric Mg^+ is a source for pronounced merged or detached excess electron densities over strong crustal fields.

Interplanetary comparison In 2009, *Pätzold et al.* (2009) discovered electron density features in the lower ionosphere of Venus, which resemble the excess electron densities in the Mars dayside ionosphere. A similar analysis of the electron density profiles derived with the Venus Express Radio Science Experiment VeRa with already existing tools will provide a good opportunity for the interplanetary comparison of the feature.

Applicability of the current IonA-2 model IonA-2 in its current development status is well suited for the investigation of the role of gravity waves in the formation of substructures in the V-shaped merged excess electron density. The IonA-2 diurnal atmospheric and ionospheric densities can be used as input for further calculations of the errors introduced in the ionospheric electron density profiles by deviations from radial symmetry.

Potential future development stages for IonA-2

- Constrain the IonA-2 reaction scheme by comparing the results directly with MAVEN observations of the composition, neutral, ion and electron temperatures in the upper atmosphere.

- Include a simple approach for the determination of the NO night glow produced by the recombination of N and O on the planetary night side for a comparison with the night glow observations of MEX-SPICAM (*Stiepen et al.*, 2015).
  The resulting night glow intensities will provide constraints for the N/NO ratio in the Mars upper atmosphere.

- Integrate the MSDM (Meteor Simple Diffusion Model)[1] into the software architecture of IonA-2.

[1] Basic version provided by G. Molina-Cuberos

Except for the model used by *Crismani et al.* (2017), the current meteor layer models for Mars are based on 1-D neutral atmospheres and ionospheres for a certain solar zenith angle. Including the MSDM into IonA-2 will provide a valuable tool for the comparison between the Mg^+ observations of MVN-IUVS and the MaRS electron density observations.

- Include major species diffusion (see e.g. *Vlasov and Davydov* (1982))
  The implementation of major species diffusion will provide independence from the major neutral densities of the Mars Climate Database. However, the input of external temperatures remains necessary. An application to the Venus ionosphere is possible, if reasonable neutral, ion and electron temperatures for a full Sol are provided.

- Self consistent computation of impact ionization, electron, ion and neutral temperature
  The implementation of these features will make IonA-2 completely independent of external temperature input.

This work could provide valuable insight into atmospheric processes in the poorly understood lower ionosphere and upper atmosphere of Mars. So far, ionospheric models predicted that the observed excess electron densities are produced predominantly by meteor infall from the interplanetary space, a concept which is challenged based on the new findings. The thorough analysis of the MaRS observations and the development of the IonA-2 model provided the possibility, for the very first time, to unravel the underlying formation processes. This is a significant step towards the understanding of the Martian atmospheric coupling.

Appendix A

Supporting information Chapter 2

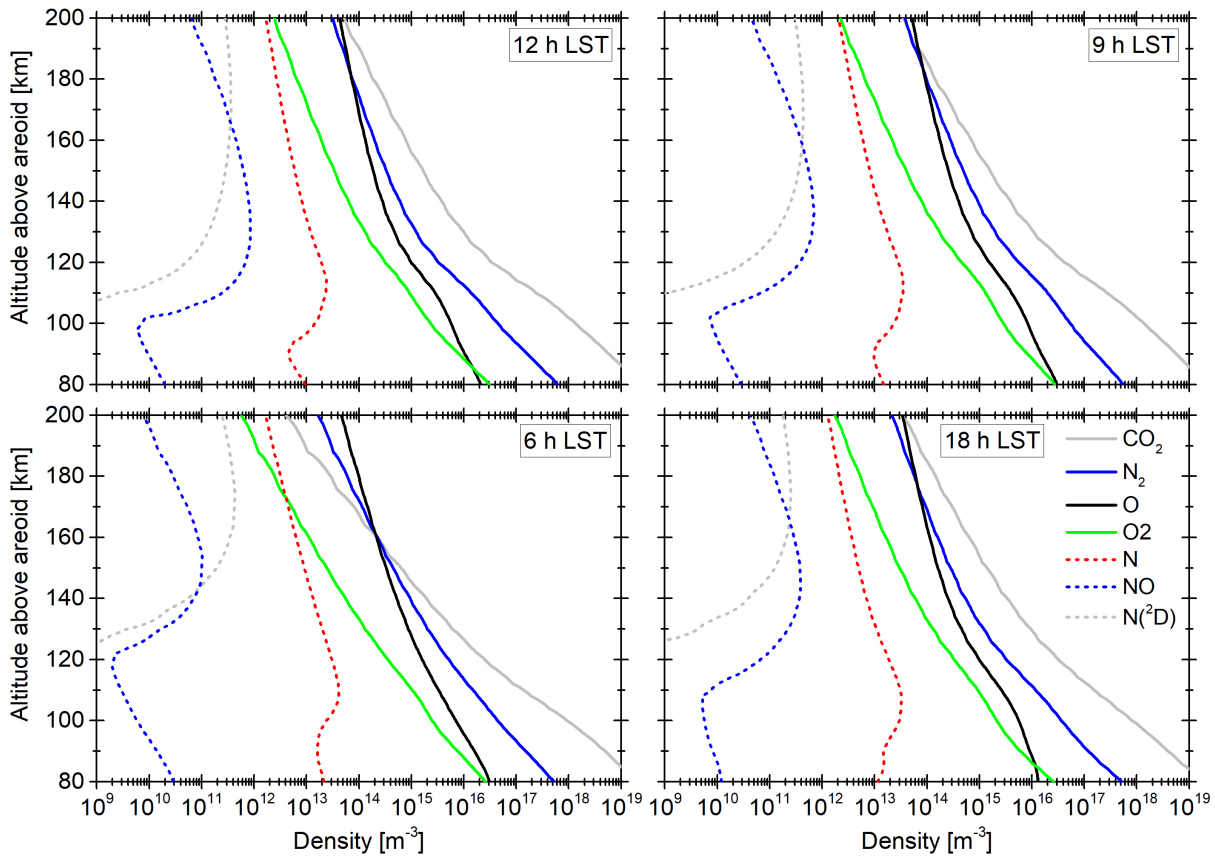

Figure A.1: LMD-GCM CO_2, N_2, O, O_2, N, NO and $N(^2D)$ neutral atmospheric species associated with the ionospheres given in Figure 3 of González-Galindo et al. *(2013) and shown in this work as lower Panels in Figure 2.14 of Chapter 2. The data were provided by G. González-Galindo.*

Appendix B

Supporting information Chapter 4

B.1 Derivation of the M1 upper parameter range

Panel (a) of Figure B.1 shows the IonA-1 model (see Chapter 6) results for DoY 263 (2009) for the wavelength range 0.5 - 95 nm and 10 - 95 nm. While the model result for the full wavelength range shows a pronounced M1 layer, it is completely erased for the reduced wavelength range. A second effect of the wavelength reduction is a small rise of the ionospheric base for the reduced wavelength profile. The M1 parameter derivation from the residuals of a linear fit on the base of the ionosphere therefore introduces an error to the calculated parameters, because a part of the M1 feature is automatically removed by the line fit. Limits for this effect are estimated from 50 selected MaRS observations. IonA-1 model runs were conducted for all MaRS_{quiet} observations for the wavelength range of 0.5 - 95 nm and the MCD V5.2 scenarios MCDclim-low, MCDclim-ave, MCDclim-high, MCD-cold, MCD-MY and MCD-warm (see Chapter 5). 50 observations have been selected for which the IonA-1 results approximately fit the base of the ionosphere. This rough match indicates those profiles for which the differences between the real neutral atmosphere / solar flux and the chosen MCD V5.2 atmospheric scenario and SIP V2.38 solar flux is not too large.
After computing the IonA-1 model results for both wavelength ranges, line fits are conducted on both model profiles in the altitude range from the maximum first derivation of the IonA-1 electron density below the main peak $\left(n_e^{I1}\right)'_{max}$ to $0.7{\cdot}\left(n_e^{I1}\right)'_{max}$ (orange arrows on the purple line in Panel (a)). The fitted straight line is then extrapolated to the $n_{e,max}^{I1}(M2)$ value, indicated in Panel (a) of Figure B.1 with two orange arrows. This point yields the rotation basis for the later rotation angle θ determination. The second line fit is done on the reduced solar flux profile for the same altitude range used for the full solar flux profile. In addition, the fitted straight line is forced through the determined rotation point. Both line fits therefore include the rotation angle θ in dependence of the maximum electron density $n_{e,max}^{I1}(M2)$ of the full solar flux IonA-1 result.

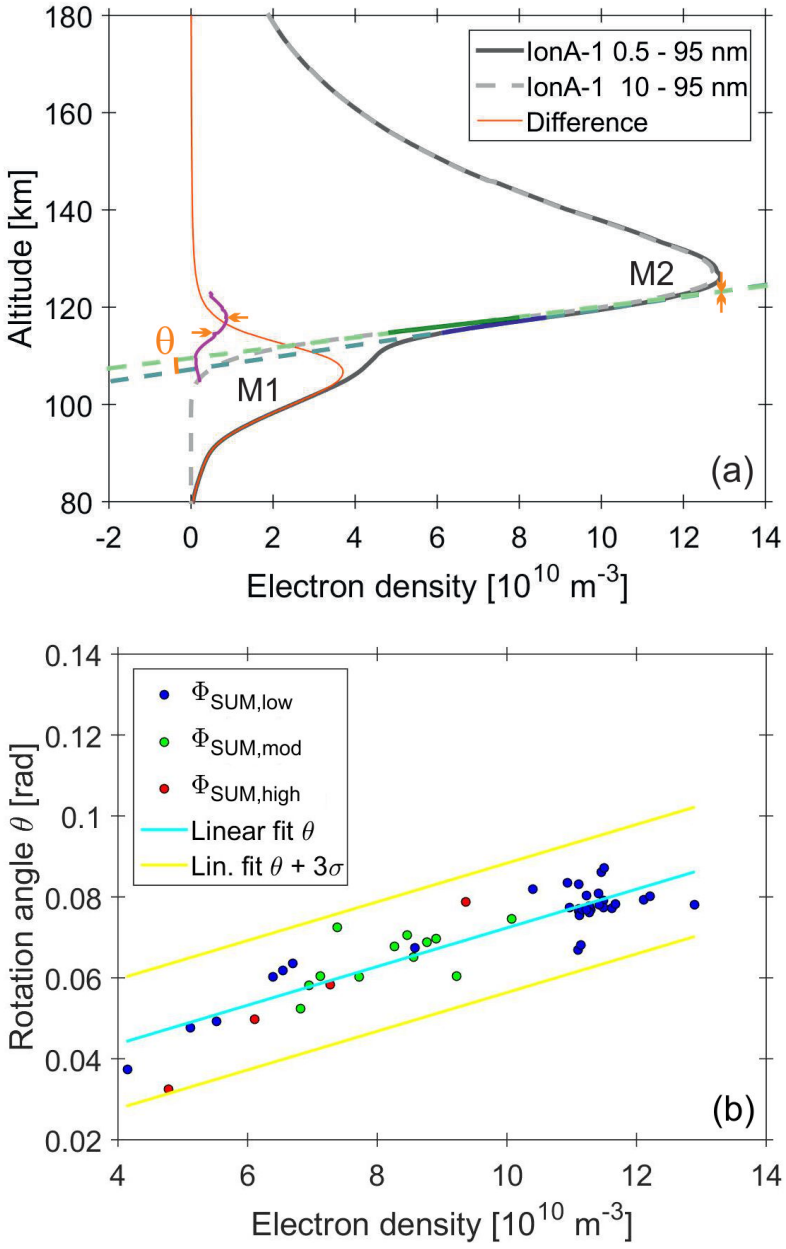

Figure B.1: (a) IonA-1 results for DoY 263 (2009) for the MCD V5.2 MCDclim-low scenario. The purple line is the first derivation of the 0.5 - 95 nm model data. The dashed blue line is the fit on the dark blue part of the 0.5 - 95 nm profile, the dashed green line the fit on the dark green part of the 10 - 95 nm profile. θ is the rotation angle between both line fits. The orange arrows are explained in the text. (b) θ for the 50 modeled MaRS observations, the solar flux proxy intervals $\Phi_{SUM,low}$, $\Phi_{SUM,mod}$ and $\Phi_{SUM,high}$ are defined in Chapter 5.

Panel (b) of Figure B.1 shows the rotation angles θ for the 50 selected profiles in dependence of $n_{e,max}^{I1}(M2)$. Other methods, e.g. a rotation point fixed at $1.0{\cdot}10^{11}m^{-3}$ or the dependence of θ on the solar zenith angle χ were tested, but did not lead to a better parameterization of the results. Therefore the rotation angle θ is determined in dependence of the M2 peak electron density by a straight line fit

$$\theta(n_{e,max}^{obs}) = 4.77921537 \cdot 10^{-13}\ [m^{-3}] \cdot n_{e,max}^{obs}(M2) + 0.02456586\ [rad]$$
$$\sigma = 0.005174\ [rad],$$

where σ is the error of the fit slope.
The upper range of the M1 parameters is then determined for a MaRS observation in four steps:

i.) A straight line fit is conducted on the base of the ionosphere from $\left(n_{e,S}^{obs}\right)'_{max}$ to $0.7{\cdot}\left(n_{e,S}^{obs}\right)'_{max}$.

ii.) The rotation point is determined by extrapolating the straight line to the value of $n_{e,max}^{obs}(M2)$.

iii.) The straight line is rotated around the projection of $n_{e,max}^{obs}(M2)$ by $\theta{+}3{\cdot}\sigma$.

iv.) Subtracting the rotated straight line from the smoothed n_e^{obs} electron density profile yields the residuals for determining the upper range of the M1 parameters by the methods used for the original M1 parameter determination.

B.2 Comparing the derived model M1 parameter ranges with the direkt M1 model results

A comparison between the derived model M1 parameter ranges with the "real" parameters of the model M1 layers is conducted to test the validity of the method for the M1 parameter derivation. While the model M1 parameter ranges have been determined with the described method, the direct model M1 parameters are derived by subtracting the IonA-1 electron density for the reduced solar flux from the full solar flux model results. Panels (a) to (d) of Figure B.2 contain the comparison of the determined ranges with the "real" parameters for the M1 altitude, electron density, vertical TEC and width of the modeled M1 region.
The agreement between the derived center M1 and the "real" M1 altitudes is quite good, while the difference between the derived and "real" M1 electron densities increases for increasing M1 electron density. The "real" vertical TEC is always underestimated, but still found within the provided M1 ranges. This is not the case for the M1 width. The

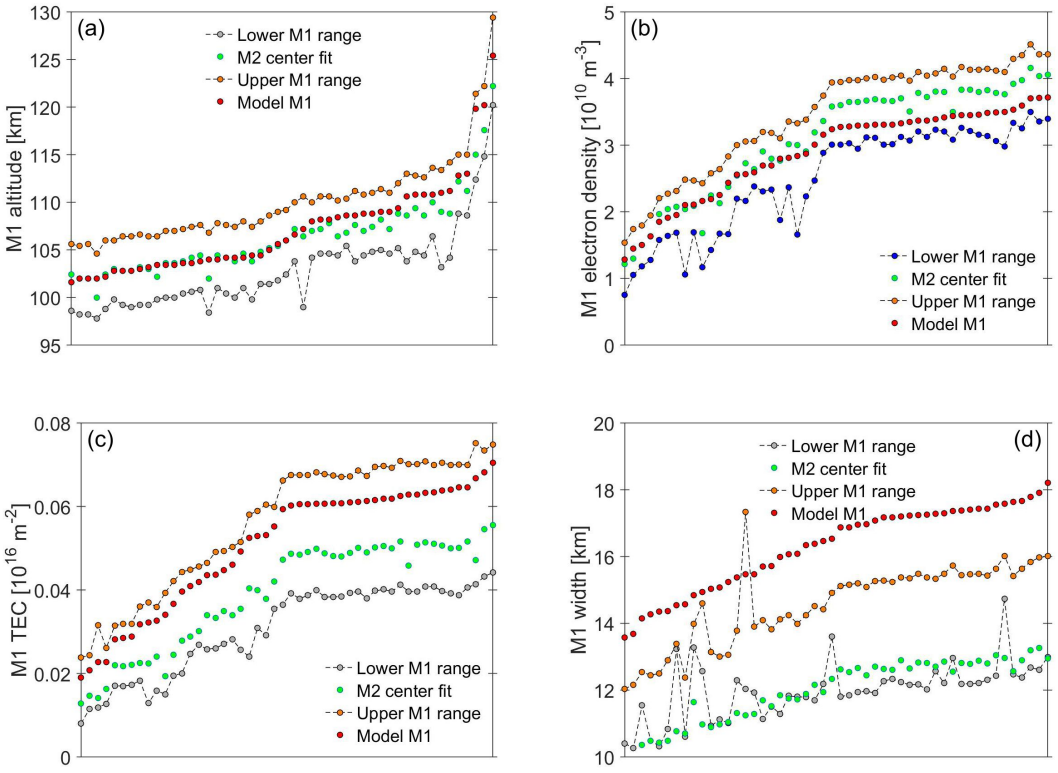

Figure B.2: Comparison between the derived model M1 parameter ranges with the "real" M1 parameters directly derived from the model results. No X-axis labels are provided, because the data sets are individually sorted for a clear view.

M1 width is the altitude difference of those points, where the M1 profile reaches 50% of $n_{e,max}^{obs}(M1)$. The derivation of the M1 parameters and their ranges with the straight line fitting method causes the detected M1 layer always to be too small compared to the "real" M1 width. In addition, the computed lower and upper width ranges do not always include the center M1 parameters. While the determined M1 ranges cover the "real' model M1 parameters for the M1 altitude, electron density and vertical TEC, determining $h_{width}^{obs}(M1)$ with the line fit method does not yield a realistic M1 width. This parameter cannot be used as absolute width, but only as a relative value for the comparison with other parameters.

Appendix C

Supporting information Chapter 6

C.1 Reaction scheme 1

Number	Reaction	Reaction coefficient $[m^3/s]$ bimolecular, $[m^6/s]$ termolecular	Source
GP001	$CO_2 + h\nu \rightarrow CO + O$		
GP002	$CO_2 + h\nu \rightarrow CO + O(^1D)$		
GP003	$H_2 + h\nu \rightarrow H + H$		
GP004	$H_2O + h\nu \rightarrow H + OH$		
GP005	$H_2O_2 + h\nu \rightarrow OH + OH$		
GP006	$N_2 + h\nu \rightarrow N + N$		
GP007	$NO + h\nu \rightarrow N + O$		
GP008	$NO_2 + h\nu \rightarrow NO + O$		
GP009	$O_2 + h\nu \rightarrow O + O$		
GP010	$O_2 + h\nu \rightarrow O + O(^1D)$		
GP011	$O_3 + h\nu \rightarrow O + O_2$		
GP012	$O_3 + h\nu \rightarrow O(^1D) + O_2$		
GP013	$CO + h\nu \rightarrow CO^+ + e^-$		
GP014	$CO + h\nu \rightarrow C^+ + O + e^-$		
GP015	$CO + h\nu \rightarrow O^+ + C + e^-$		
GP016	$CO_2 + h\nu \rightarrow CO_2^+ + e^-$		
GP017	$CO_2 + h\nu \rightarrow O^+ + CO + e^-$		
GP018	$CO_2 + h\nu \rightarrow CO^+ + O + e^-$		
GP019	$CO_2 + h\nu \rightarrow C^+ + O_2 + e^-$		
GP020	$H + h\nu \rightarrow H^+ + e^-$		

Table C.1: Reaction scheme 1 for IonA-2

Number	Reaction	Reaction coefficient $[m^3/s]$ bimolecular, $[m^6/s]$ termolecular	Source
GP021	$N + h\nu \rightarrow N_p + e^-$		
GP022	$NO + h\nu \rightarrow NO^+ + e^-$		
GP023	$N_2 + h\nu \rightarrow N_2^+ + e^-$		
GP024	$N_2 + h\nu \rightarrow N_p + N + e^-$		
GP025	$O + h\nu \rightarrow O^+ + e^-$		
GP026	$O_2 + h\nu \rightarrow O_2^+ + e^-$		
GR001	$CO + OH \rightarrow CO_2 + H$	$1.5 \cdot 10^{-19} \left(\frac{T_n}{300}\right)^{0.6}$	*Sander et al.* (2011)
GR002	$H + O_2 + M \rightarrow HO_2 + M$	$1.1 \cdot 10^{-43} \left(\frac{T_N}{300}\right)^{-1.3}$	*Sander et al.* (2011)
GR003	$H + HO_2 \rightarrow H_2 + O_2$	$6.9 \cdot 10^{-18}$	*Sander et al.* (2011)
GR004	$H + NO_2 \rightarrow NO + OH$	$4.0 \cdot 10^{-16} \exp\left(\frac{-340}{T_N}\right)$	*Sander et al.* (2011)
GR005	$HO_2 + HO_2 \rightarrow H_2O_2 + O_2$	$3.0 \cdot 10^{-19} \exp\left(\frac{460}{T_N}\right)$	*Sander et al.* (2011)
GR006	$N + NO \rightarrow N_2 + O$	$2.1 \cdot 10^{-17} \exp\left(\frac{100}{T_N}\right)$	*Sander et al.* (2011)
GR007	$N + O_2 \rightarrow NO + O$	$1.5 \cdot 10^{-17} \exp\left(\frac{-3600}{T_N}\right)$	*Sander et al.* (2011)
GR008	$N + OH \rightarrow NO + H$	$3.8 \cdot 10^{-17} \exp\left(\frac{85}{T_N}\right)$	*Atkinson et al.* (1989)
GR009	$N + O_3 \rightarrow NO + O_2$	$1.0 \cdot 10^{-22}$	*Sander et al.* (2011)
GR010	$N + HO_2 \rightarrow NO + OH$	$2.2 \cdot 10^{-17}$	*Brune et al.* (1983)
GR011	$N + O \rightarrow NO$	$2.8 \cdot 10^{-23} \left(\frac{T_N}{300}\right)^{-0.5}$	*Du and Dalgarno* (1990)
GR012	$N(^2D) + O \rightarrow N + O$	$3.3 \cdot 10^{-18} \exp\left(\frac{-260}{T_N}\right)$	*Herron* (1999)
GR013	$N(^2D) + N_2 \rightarrow N + N_2$	$1.7 \cdot 10^{-20}$	*Herron* (1999)
GR014	$N(^2D) + CO_2 \rightarrow NO + CO$	$3.6 \cdot 10^{-19}$	*Herron* (1999)
GR015	$N_2 + O(^1D) \rightarrow N_2 + O$	$2.15 \cdot 10^{-17} \exp\left(\frac{110}{T_N}\right)$	*Sander et al.* (2011)
GR016	$NO + HO_2 \rightarrow NO_2 + OH$	$3.3 \cdot 10^{-18} \exp\left(\frac{270}{T_N}\right)$	*Sander et al.* (2011)
GR017	$NO + O_3 \rightarrow NO_2 + O_2$	$3.0 \cdot 10^{-18} \exp\left(\frac{-1500}{T_N}\right)$	*Sander et al.* (2011)
GR018	$O + HO_2 \rightarrow OH + O_2$	$3.0 \cdot 10^{-17} \exp\left(\frac{200}{T_N}\right)$	*Sander et al.* (2011)
GR019	$O + OH \rightarrow O_2 + H$	$1.8 \cdot 10^{-17} \exp\left(\frac{180}{T_N}\right)$	*Sander et al.* (2011)
GR020	$O + O + M \rightarrow O_2 + M$	$1.3 \cdot 10^{-46} \exp\left(\frac{900}{T_N}\right)$	*Tsang and Hampson* (1986)
GR021	$O + O_2 + M \rightarrow O_3 + M$	$1.5 \cdot 10^{-45} \left(\frac{T_N}{300}\right)^{-2.4}$	*Sander et al.* (2011)

Table C.2: Reaction scheme 1 for IonA-2

Number	Reaction	Reaction coefficient $[m^3/s]$ bimolecular, $[m^6/s]$ termolecular	Source
GR022	$O + NO + M \rightarrow NO_2 + M$	$2.25 \cdot 10^{-43} \left(\frac{T_N}{300}\right)^{-1.5}$	*Sander et al.* (2011)
GR023	$O + NO_2 \rightarrow NO + O_2$	$5.1 \cdot 10^{-18} \exp\left(\frac{210}{T_N}\right)$	*Sander et al.* (2011)
GR024	$O(^1D) + H_2O \rightarrow OH + OH$	$1.63 \cdot 10^{-16} \exp\left(\frac{60}{T_N}\right)$	*Sander et al.* (2011)
GR025	$O(^1D) + H_2 \rightarrow H + OH$	$1.2 \cdot 10^{-16}$	*Sander et al.* (2011)
GR026	$O(^1D) + CO_2 \rightarrow O + CO_2$	$7.5 \cdot 10^{-17} \exp\left(\frac{115}{T_N}\right)$	*Sander et al.* (2011)
GR027	$O(^1D) + O_2 \rightarrow O + O_2$	$3.3 \cdot 10^{-17} \exp\left(\frac{55}{T_N}\right)$	*Sander et al.* (2011)
GR028	$O_3 + H \rightarrow OH + O_2$	$1.4 \cdot 10^{-16} \exp\left(\frac{-470}{T_N}\right)$	*Sander et al.* (2011)
GR029	$O_3 + OH \rightarrow HO_2 + O_2$	$1.7 \cdot 10^{-18} \exp\left(\frac{-940}{T_N}\right)$	*Sander et al.* (2011)
GR030	$O_3 + HO_2 \rightarrow OH + O_2 + O_2$	$1.0 \cdot 10^{-20} \exp\left(\frac{-490}{T_N}\right)$	*Sander et al.* (2011)
GR031	$OH + HO_2 \rightarrow O_2 + H_2O$	$4.8 \cdot 10^{-17} \exp\left(\frac{250}{T_N}\right)$	*Sander et al.* (2011)
GR032	$OH + H_2 \rightarrow H + H_2O$	$2.8 \cdot 10^{-18} \exp\left(\frac{-1800}{T_N}\right)$	*Sander et al.* (2011)
GR033	$OH + H_2O_2 \rightarrow H_2O + HO_2$	$1.8 \cdot 10^{-18}$	*Sander et al.* (2011)
GR034	$C^+ + CO_2 \rightarrow CO^+ + CO$	$1.10 \cdot 10^{-15}$	*McElroy et al.* (2013)
GR035	$CO^+ + CO_2 \rightarrow CO_2^+ + CO$	$1.00 \cdot 10^{-15}$	*McElroy et al.* (2013)
GR036	$CO^+ + O \rightarrow O^+ + CO$	$1.40 \cdot 10^{-16}$	*McElroy et al.* (2013)
GR037	$CO^+ + H \rightarrow H^+ + CO$	$4.00 \cdot 10^{-16}$	*Fox and Sung* (2001)
GR038	$CO_2^+ + O_2 \rightarrow O_2^+ + CO_2$	$5.50 \cdot 10^{-17} \left(\frac{T_i}{300}\right)^{-0.82}$	*Anicich* (1993)
GR039	$CO_2^+ + O \rightarrow O^+ + CO_2$	$9.6 \cdot 10^{-17}$	*McElroy et al.* (2013)
GR040	$CO_2^+ + O \rightarrow O_2^+ + CO$	$1.64 \cdot 10^{-16}$	*McElroy et al.* (2013)
GR041	$CO_2^+ + e^- \rightarrow CO + O$	$3.80 \cdot 10^{-13} \left(\frac{T_e}{300}\right)^{-0.5}$	*McElroy et al.* (2013)
GR042	$CO_2^+ + NO \rightarrow NO^+ + CO_2$	$1.2 \cdot 10^{-16}$	*McElroy et al.* (2013)
GR043	$CO_2^+ + N \rightarrow CO^+ + NO$	$3.40 \cdot 10^{-16}$	*Fox and Sung* (2001)
GR044	$CO_2^+ + H_2 \rightarrow HCO_2^+ + H$	$9.5 \cdot 10^{-16}$	*McElroy et al.* (2013)
GR045	$H^+ + O \rightarrow O^+ + H$	$6.86 \cdot 10^{-16} \left(\frac{T_i}{300}\right)^{0.26} \exp\left(\frac{-224.3}{T_i}\right)$	*McElroy et al.* (2013)
GR046	$N_p + CO_2 \rightarrow CO_2^+ + N$	$7.50 \cdot 10^{-16}$	*McElroy et al.* (2013)
GR047	$N_2^+ + CO_2 \rightarrow CO_2^+ + N_2$	$9.0 \cdot 10^{-16} \left(\frac{T_i}{300}\right)^{-0.23}$	*Fox and Sung* (2001)
GR048	$N_2^+ + O \rightarrow NO^+ + N$	$1.33 \cdot 10^{-16} \left(\frac{T_i}{300}\right)^{-0.44}$	*Fox and Sung* (2001)
GR049	$N_2^+ + CO \rightarrow N_2 + CO^+$	$7.4 \cdot 10^{-17}$	*McElroy et al.* (2013)
GR050	$N_2^+ + e^- \rightarrow N + N$	$1.70 \cdot 10^{-13} \left(\frac{T_e}{300}\right)^{-0.30}$	*McElroy et al.* (2013)

Table C.3: Reaction scheme 1 for IonA-2

Number	Reaction	Reaction coefficient $[m^3/s]$ bimolecular, $[m^6/s]$ termolecular	Source
GR051	$N_2^+ + O \rightarrow O^+ + N_2$	$7.00 \cdot 10^{-18} \left(\frac{T_i}{300}\right)^{-0.23}$	*Fox and Sung* (2001)
GR052	$NO^+ + e^- \rightarrow N + O$	$4.30 \cdot 10^{-13} \left(\frac{T_e}{300}\right)^{-0.37}$	*McElroy et al.* (2013)
GR053	$O^+ + CO_2 \rightarrow O_2^+ + CO$	$9.4 \cdot 10^{-16}$	*McElroy et al.* (2013)
GR054	$O^+ + N_2 \rightarrow NO^+ + N$	$1.2 \cdot 10^{-18} \left(\frac{T_i}{300}\right)^{-0.45}$	*Fox and Sung* (2001)
GR055	$O^+ + H \rightarrow H^+ + O$	$5.66 \cdot 10^{-16} \left(\frac{T_i}{300}\right)^{0.36} \exp\left(\frac{8.6}{T_i}\right)$	*McElroy et al.* (2013)
GR056	$O_2^+ + e^- \rightarrow O + O$	$2.0 \cdot 10^{-13} \left(\frac{T_e}{300}\right)^{-0.7}$	*McElroy et al.* (2013)
GR057	$O_2^+ + NO \rightarrow NO^+ + O_2$	$4.5 \cdot 10^{-16}$	*Midey and Viggiano* (1999)
GR058	$O_2^+ + N_2 \rightarrow NO^+ + NO$	$1.0 \cdot 10^{-21}$	*Fox and Sung* (2001)
GR059	$O_2^+ + N \rightarrow NO^+ + O$	$1.0 \cdot 10^{-16}$	*Fox and Sung* (2001)
GR060	$HCO_2^+ + e^- \rightarrow H + CO_2$	$3.4 \cdot 10^{-13} \left(\frac{T_e}{300}\right)^{-0.5}$	*Krasnopolsky* (2002)
GS001	$CO_2 + e^- \rightarrow CO_2^+ + e^- + e^-$		
GS002	$CO + e^- \rightarrow CO^+ + e^- + e^-$		
GS003	$N_2 + e^- \rightarrow N_2^+ + e^- + e^-$		
GS004	$N + e^- \rightarrow N^+ + e^- + e^-$		
GS005	$O_2 + e^- \rightarrow O_2^+ + e^- + e^-$		
GS006	$O + e^- \rightarrow O^+ + e^- + e^-$		

Table C.4: Reaction scheme 1 for IonA-2

C.2 Reaction scheme 2

Number	Reaction	Reaction coefficient $[m^3/s]$ bimolecular, $[m^6/s]$ termolecular	Source
IP001	$CO_2 + h\nu \rightarrow CO + O$		
IP002	$CO_2 + h\nu \rightarrow CO + O(^1D)$		
IP003	$H_2 + h\nu \rightarrow H + H$		
IP004	$H_2O + h\nu \rightarrow H + OH$		
IP005	$H_2O_2 + h\nu \rightarrow OH + OH$		
IP006	$N_2 + h\nu \rightarrow N + N(^2D)$		
IP007	$NO + h\nu \rightarrow N + O$		
IP008	$NO_2 + h\nu \rightarrow NO + O$		
IP009	$O_2 + h\nu \rightarrow O + O$		
IP010	$O_2 + h\nu \rightarrow O + O(^1D)$		
IP011	$O_3 + h\nu \rightarrow O + O_2$		
IP012	$O_3 + h\nu \rightarrow O(^1D) + O_2$		
IP013	$CO + h\nu \rightarrow CO^+ + e^-$		
IP014	$CO + h\nu \rightarrow C^+ + O + e^-$		
IP015	$CO + h\nu \rightarrow O^+ + C + e^-$		
IP016	$CO_2 + h\nu \rightarrow CO_2^+ + e^-$		
IP017	$CO_2 + h\nu \rightarrow O^+ + CO + e^-$		
IP018	$CO_2 + h\nu \rightarrow CO^+ + O + e^-$		
IP019	$CO_2 + h\nu \rightarrow C^+ + O_2 + e^-$		
IP020	$H + h\nu \rightarrow H^+ + e^-$		
IP021	$N + h\nu \rightarrow N^+ + e^-$		
IP022	$NO + h\nu \rightarrow NO^+ + e^-$		
IP023	$N_2 + h\nu \rightarrow N_2^+ + e^-$		
IP024	$N_2 + h\nu \rightarrow N^+ + N + e^-$		
IP025	$O + h\nu \rightarrow O^+ + e^-$		
IP026	$O_2 + h\nu \rightarrow O_2^+ + e^-$		
IP027	$Ar + h\nu \rightarrow Ar^+ + e^-$		
IR001	$C + CO_2 \rightarrow CO + CO$	$7.62 \cdot 10^{-20} \left(\frac{T_N}{300}\right)^{0.5} \exp\left(\frac{-3480.0}{T_N}\right)$	estimate; *Fox and Sung* (2001); *McElroy and McConnell* (1971)

Table C.5: Reaction scheme 2 for IonA-2

Number	Reaction	Reaction coefficient $[m^3/s]$ bimolecular, $[m^6/s]$ termolecular	Source
IR002	$C + NO \rightarrow CO + N$	$7.50 \cdot 10^{-17} \left(\frac{T_N}{298}\right)^{-0.16}$	branching estimated, *Chastaing et al.* (2000); *Fox and Sung* (2001)
IR003	$C + O_2 \rightarrow CO + O$	$4.90 \cdot 10^{-17} \left(\frac{T_N}{298}\right)^{-0.32}$	*Chastaing et al.* (2000)
IR004	$CO + OH \rightarrow CO_2 + H$	$1.5 \cdot 10^{-19} \left(\frac{T_N}{300}\right)^{0.6}$	*Sander et al.* (2011)
IR005	$H + H + M \rightarrow H_2 + M$	$1.20 \cdot 10^{-44} \left(\frac{T_N}{300}\right)^{-1.3}$	large uncertainty; *Fox and Sung* (2001); *Tsang and Hampson* (1986)
IR006	$H + HO_2 \rightarrow H_2 + O_2$	$6.9 \cdot 10^{-18}$	*Burkholder et al.* (2015)
IR007	$H + HO_2 \rightarrow OH + OH$	$7.2 \cdot 10^{-17}$	*Burkholder et al.* (2015)
IR008	$H + HO_2 \rightarrow O + H_2O$	$1.6 \cdot 10^{-18}$	*Burkholder et al.* (2015)
IR009	$H + NO_2 \rightarrow NO + OH$	$4.0 \cdot 10^{-16} \exp\left(\frac{-340}{T_N}\right)$	*Burkholder et al.* (2015)
IR010	$H + O_2 \rightarrow HO_2$	2.5· Eq. 6.15, $k_0^{300} = 4.44 \cdot 10^{-44}$, $n = 1.3$, $k_\infty^{300} = 7.5 \cdot 10^{-17}$, $m = 0.2$	*Burkholder et al.* (2015)
IR011	$HO_2 + HO_2 \rightarrow H_2O_2 + O_2$	$3.0 \cdot 10^{-19} \exp\left(\frac{460}{T_N}\right)$	*Burkholder et al.* (2015)
IR012	$N + CO_2 \rightarrow NO + CO$	$1.7 \cdot 10^{-22}$	estimate; *Fox and Sung* (2001); *Fernandez et al.* (1998)
IR013	$N + HO_2 \rightarrow NO + OH$	$2.2 \cdot 10^{-17}$	*Brune et al.* (1983)
IR014	$N + NO \rightarrow N_2 + O$	$2.1 \cdot 10^{-17} \exp\left(\frac{100}{T_N}\right)$	*Burkholder et al.* (2015)
IR015	$N + OH \rightarrow NO + H$	$3.8 \cdot 10^{-17} \exp\left(\frac{85}{T_N}\right)$	*Atkinson et al.* (1989)
IR016	$N + O \rightarrow NO$	$2.8 \cdot 10^{-23} \left(\frac{T_N}{300}\right)^{-0.5}$	*Du and Dalgarno* (1990)

Table C.6: Reaction scheme 2 for IonA-2

Number	Reaction	Reaction coefficient $[m^3/s]$ bimolecular, $[m^6/s]$ termolecular	Source
IR017	$N + O_2 \rightarrow NO + O$	$1.5 \cdot 10^{-17} \exp\left(\frac{-3600}{T_N}\right)$	*Burkholder et al.* (2015)
IR018	$N + O_3 \rightarrow NO + O_2$	$1.0 \cdot 10^{-22}$	upper limit; *Burkholder et al.* (2015)
IR019	$N(^2D) + CO_2 \rightarrow NO + CO$	$3.6 \cdot 10^{-19}$	*Herron* (1999)
IR020	$N(^2D) + O \rightarrow N + O$	$6.9 \cdot 10^{-19}$	*Fell et al.* (1990)
IR021	$N(^2D) + N_2 \rightarrow N + N_2$	$1.7 \cdot 10^{-20}$	*Herron* (1999)
IR022	$N_2 + O(^1D) \rightarrow N_2 + O$	$2.15 \cdot 10^{-17} \exp\left(\frac{110}{T_N}\right)$	*Burkholder et al.* (2015)
IR023	$NO + HO_2 \rightarrow NO_2 + OH$	$3.3 \cdot 10^{-18} \exp\left(\frac{270}{T_N}\right)$	*Burkholder et al.* (2015)
IR024	$NO + O_3 \rightarrow NO_2 + O_2$	$3.0 \cdot 10^{-18} \exp\left(\frac{-1500}{T_N}\right)$	*Burkholder et al.* (2015)
IR025	$O + HO_2 \rightarrow OH + O_2$	$3.0 \cdot 10^{-17} \exp\left(\frac{200}{T_N}\right)$	*Burkholder et al.* (2015)
IR026	$O + O + M \rightarrow O_2 + M$	$1.3 \cdot 10^{-46} \exp\left(\frac{900}{T_N}\right)$	upper limit; *Tsang and Hampson* (1986)
IR027	$O + OH \rightarrow O_2 + H$	$1.8 \cdot 10^{-17} \exp\left(\frac{180}{T_N}\right)$	*Burkholder et al.* (2015)
IR028	$O + O_2 + M \rightarrow O_3 + M$	$2.5 \cdot 6.0 \cdot 10^{-46} \left(\frac{T_N}{300}\right)^{-2.4}$	*Burkholder et al.* (2015)
IR029	$O + NO \rightarrow NO_2$	2.5· Eq. 6.15, $k_0^{300} = 9.0 \cdot 10^{-44}$, $n = 1.5$, $k_\infty^{300} = 3.0 \cdot 10^{-17}$, $m = 0$	*Burkholder et al.* (2015)
IR030	$O + NO_2 \rightarrow NO + O_2$	$5.1 \cdot 10^{-18} \exp\left(\frac{210}{T_N}\right)$	*Burkholder et al.* (2015)
IR031	$O(^1D) + CO_2 \rightarrow O + CO_2$	$7.5 \cdot 10^{-17} \exp\left(\frac{115}{T_N}\right)$	*Burkholder et al.* (2015)
IR032	$O(^1D) + H_2 \rightarrow H + OH$	$1.2 \cdot 10^{-16}$	*Burkholder et al.* (2015)
IR033	$O(^1D) + H_2O \rightarrow OH + OH$	$1.63 \cdot 10^{-16} \exp\left(\frac{60}{T_N}\right)$	*Burkholder et al.* (2015)

Table C.7: Reaction scheme 2 for IonA-2

Number	Reaction	Reaction coefficient $[m^3/s]$ bimolecular, $[m^6/s]$ termolecular	Source
IR034	$O(^1D) + O_2 \rightarrow O + O_2$	$3.3 \cdot 10^{-17} \exp\left(\frac{55}{T_N}\right)$	*Burkholder et al.* (2015)
IR035	$O_3 + H \rightarrow OH + O_2$	$1.4 \cdot 10^{-16} \exp\left(\frac{-470}{T_N}\right)$	*Burkholder et al.* (2015)
IR036	$O_3 + HO_2 \rightarrow OH + O_2 + O_2$	$1.0 \cdot 10^{-20} \exp\left(\frac{-490}{T_N}\right)$	*Burkholder et al.* (2015)
IR037	$O_3 + OH \rightarrow HO_2 + O_2$	$1.7 \cdot 10^{-18} \exp\left(\frac{-940}{T_N}\right)$	*Burkholder et al.* (2015)
IR038	$OH + H_2 \rightarrow H + H_2O$	$2.8 \cdot 10^{-18} \exp\left(\frac{-1800}{T_N}\right)$	*Burkholder et al.* (2015)
IR039	$OH + H_2O_2 \rightarrow H_2O + HO_2$	$1.8 \cdot 10^{-18}$	*Burkholder et al.* (2015)
IR040	$OH + HO_2 \rightarrow O_2 + H_2O$	$4.8 \cdot 10^{-17} \exp\left(\frac{250.0}{T_N}\right)$	*Burkholder et al.* (2015)
IR041	$Ar^+ + CO \rightarrow CO^+ + Ar$	$T_i \leq 900\,K$ $3.70 \cdot 10^{-17} \left(\frac{300}{T_i}\right)^{0.43} +$ $1.6 \cdot 10^{-15} \exp\left(\frac{-57.4}{k_B T_i}\right)$ $T_i > 900\,K$ $2.3 \cdot 10^{-17} \left(\frac{T_i}{900}\right)$	*Anicich* (2003); *Fox and Sung* (2001); *Midey and Viggiano* (1998)
IR042	$Ar^+ + CO_2 \rightarrow CO_2^+ + Ar$	$T_i \leq 700\,K : 5.0 \cdot 10^{-16}$ $T_i > 700\,K$ $5.0 \cdot 10^{-16} \left(\frac{700}{T_i}\right)$	*Anicich* (2003); *Dotan et al.* (1999)
IR043	$Ar^+ + N_2 \rightarrow N_2^+ + Ar$	$1.1 \cdot 10^{-17} \left(\frac{300}{T_i}\right)^{-1.13}$	*Anicich* (2003); *Dotan and Lindinger* (1982); *Fox and Sung* (2001)
IR044	$Ar^+ + NO \rightarrow Ar + NO^+$	$3.1 \cdot 10^{-16}$	*Anicich* (2003, 1993)
IR045	$Ar^+ + O_2 \rightarrow Ar + O_2^+$	$T_i \leq 900\,K$ $4.9 \cdot 10^{-17} \left(\frac{300}{T_i}\right)^{0.78} +$ $9.2 \cdot 10^{-16} \exp\left(\frac{-41.8}{k_B T_i}\right)$ $T_i > 900\,K$ $2.08 \cdot 10^{-17} \left(\frac{T_i}{900.0}\right)^{1.65}$	*Anicich* (2003); *Fox and Sung* (2001); *Midey and Viggiano* (1998)

Table C.8: Reaction scheme 2 for IonA-2

Number	Reaction	Reaction coefficient $[m^3/s]$ bimolecular, $[m^6/s]$ termolecular	Source
IR046	$C^+ + CO_2 \rightarrow CO^+ + CO$	$1.10 \cdot 10^{-15}$	*Anicich* (2003, 1993); *Fahey et al.* (1981b)
IR047	$C^+ + NO \rightarrow NO^+ + C$	$7.50 \cdot 10^{-16} \left(\frac{300}{T_i}\right)^{0.2}$	*Anicich* (2003); *Fox and Sung* (2001); *Miller et al.* (1984)
IR048	$C^+ + O_2 \rightarrow O^+ + CO$	$5.22 \cdot 10^{-16}$	*Anicich* (2003, 1993)
IR049	$C^+ + O_2 \rightarrow CO^+ + O$	$3.48 \cdot 10^{-16}$	*Anicich* (2003, 1993)
IR050	$CO^+ + CO_2 \rightarrow CO_2^+ + CO$	$1.10 \cdot 10^{-15}$	*Anicich* (2003, 1993)
IR051	$CO^+ + e^- \rightarrow C + O$	$1.80 \cdot 10^{-13} \left(\frac{300}{T_e}\right)^{0.55}$	*Rosén et al.* (1998); *Fox and Sung* (2001)
IR052	$CO^+ + e^- \rightarrow C + O(^1D)$	$0.25 \cdot 10^{-13} \left(\frac{300}{T_e}\right)^{0.55}$	*Rosén et al.* (1998); *Fox and Sung* (2001)
IR053	$CO^+ + H \rightarrow H^+ + CO$	$4.00 \cdot 10^{-16}$	*Scott et al.* (1997)
IR054	$CO^+ + H_2 \rightarrow HCO^+ + H$	$7.50 \cdot 10^{-16}$	*Scott et al.* (1997)
IR055	$CO^+ + N \rightarrow NO^+ + C$	$8.20 \cdot 10^{-17}$	*Scott et al.* (1997)
IR056	$CO^+ + NO \rightarrow CO + NO^+$	$4.20 \cdot 10^{-16}$	*Anicich* (2003, 1993)
IR057	$CO^+ + O \rightarrow O^+ + CO$	$1.40 \cdot 10^{-16}$	ass. error of 50 %, *Anicich* (2003); *Fehsenfeld and Ferguson* (1972)
IR058	$CO^+ + O_2 \rightarrow O_2^+ + CO$	$1.5 \cdot 10^{-16} \left(\frac{300}{T_i}\right)^{1.1}$	*Anicich* (2003, 1993); *Miller et al.* (1984)
IR059	$CO_2^+ + e^- \rightarrow CO + O$	$4.20 \cdot 10^{-13} \left(\frac{T_e}{300}\right)^{-0.75}$	*Viggiano et al.* (2005)
IR060	$CO_2^+ + H \rightarrow HCO^+ + O$	$4.5 \cdot 10^{-16}$	*Borodi et al.* (2009)
IR061	$CO_2^+ + H \rightarrow H^+ + CO_2$	$2.0 \cdot 10^{-17}$	*Fox* (2015); *Scott et al.* (1997)
IR062	$CO_2^+ + H_2 \rightarrow HCO_2^+ + H$	$9.5 \cdot 10^{-16} \left(\frac{T_i}{300}\right)^{-0.15}$	*Borodi et al.* (2009)
IR063	$CO_2^+ + N \rightarrow CO^+ + NO$	$3.40 \cdot 10^{-16}$	*Scott et al.* (1998)
IR064	$CO_2^+ + N(^2D) \rightarrow N^+ + CO_2$	$2.00 \cdot 10^{-16}$	estimate, *Fox and Sung* (2001); *Fox* (1982)
IR065	$CO_2^+ + NO \rightarrow NO^+ + CO_2$	$1.23 \cdot 10^{-16}$	*Anicich* (2003, 1993)
IR066	$CO_2^+ + O \rightarrow O_2^+ + CO$	$1.638 \cdot 10^{-16}$	*Fehsenfeld et al.* (1970); *Fehsenfeld and Ferguson* (1972)

Table C.9: Reaction scheme 2 for IonA-2

Number	Reaction	Reaction coefficient $[m^3/s]$ bimolecular, $[m^6/s]$ termolecular	Source
IR067	$CO_2^+ + O \rightarrow O^+ + CO_2$	$9.62 \cdot 10^{-17}$	*Fehsenfeld et al.* (1970); *Fehsenfeld and Ferguson* (1972)
IR068	$CO_2^+ + O_2 \rightarrow O_2^+ + CO_2$	$T_i \leq 1500\,K$ $5.5 \cdot 10^{-17} \left(\frac{T_i}{300}\right)^{-0.82}$ $T_i > 1500\,K$ $1.50 \cdot 10^{-17} \left(\frac{T_i}{1500.0}\right)^{-0.82}$	*Anicich* (2003, 1993); *Fox and Sung* (2001); *Miller et al.* (1984)
IR069	$H^+ + CO_2 \rightarrow HCO^+ + O$	$3.80 \cdot 10^{-15}$	*Anicich* (2003); *Smith et al.* (1992)
IR070	$H^+ + O \rightarrow O^+ + H$	$6.86 \cdot 10^{-16} \left(\frac{T_i}{300}\right)^{0.26} \exp\left(\frac{-224.30}{T_i}\right)$	*Stancil et al.* (1999)
IR071	$H^+ + O_2 \rightarrow O_2^+ + H$	$2.00 \cdot 10^{-15}$	*Anicich* (2003); *Smith et al.* (1992)
IR072	$H^+ + NO \rightarrow H + NO^+$	$2.90 \cdot 10^{-15}$	*Anicich* (2003); *Smith et al.* (1992)
IR073	$HCO^+ + e^- \rightarrow CO + H$	$T_i \leq 300\,K$ $2.0 \cdot 10^{-13} \left(\frac{T_e}{300}\right)^{-1.25}$ $T_i > 300\,K$ $2.00 \cdot 10^{-13} \left(\frac{T_e}{300}\right)^{-1.0}$	*Fox* (2015)
IR074	$HCO_2^+ + CO \rightarrow HCO^+ + CO_2$	$7.8 \cdot 10^{-16}$	estimate; *Prasad and Huntress* (1980)
IR075	$HCO_2^+ + e^- \rightarrow H + O + CO$	$3.128 \cdot 10^{-13} \left(\frac{T_e}{300}\right)^{-0.5}$	*Geppert et al.* (2004); *Gougousi et al.* (1997)
IR076	$HCO_2^+ + e^- \rightarrow H + CO_2$	$2.30 \cdot 10^{-14} \left(\frac{T_e}{300}\right)^{-0.5}$	*Geppert et al.* (2004); *Gougousi et al.* (1997)
IR077	$HCO_2^+ + e^- \rightarrow OH + CO$	$1.242 \cdot 10^{-13} \left(\frac{T_e}{300}\right)^{-0.5}$	*Geppert et al.* (2004); *Gougousi et al.* (1997)
IR078	$HCO_2^+ + O \rightarrow HCO^+ + O_2$	$5.8 \cdot 10^{-15}$	Langevin estimate *Fox* (2015)
IR079	$N^+ + CO \rightarrow NO^+ + C$	$6.16 \cdot 10^{-17} \left(\frac{300}{T_i}\right)^{0.5}$	*Anicich* (2003, 1993); *Fox and Sung* (2001); *Miller et al.* (1984)
IR080	$N^+ + CO \rightarrow CO^+ + N$	$4.93 \cdot 10^{-16} \left(\frac{300}{T_i}\right)^{0.5}$	*Anicich* (2003, 1993); *Fox and Sung* (2001); *Miller et al.* (1984)

Table C.10: Reaction scheme 2 for IonA-2

Number	Reaction	Reaction coefficient $[m^3/s]$ bimolecular, $[m^6/s]$ termolecular	Source
IR081	$N^+ + CO \rightarrow C^+ + NO$	$5.60 \cdot 10^{-18} \left(\frac{300}{T_i}\right)^{0.5}$	*Anicich* (2003, 1993); *Fox and Sung* (2001); *Miller et al.* (1984)
IR082	$N^+ + CO_2 \rightarrow CO^+ + NO$	$2.016 \cdot 10^{-16}$	*Anicich* (2003, 1993)
IR083	$N^+ + CO_2 \rightarrow CO_2^+ + N$	$9.184 \cdot 10^{-16}$	(*Anicich*, 2003, 1993)
IR084	$N^+ + NO \rightarrow N + NO^+$	$4.7175 \cdot 10^{-16} \left(\frac{300}{T_i}\right)^{0.24}$	*Anicich* (2003, 1993); *Fahey et al.* (1981a); *Fox and Sung* (2001)
IR085	$N^+ + NO \rightarrow N_2^+ + O$	$8.325 \cdot 10^{-17} \left(\frac{300}{T_i}\right)^{0.24}$	*Anicich* (2003, 1993); *Fahey et al.* (1981a); *Fox and Sung* (2001)
IR086	$N^+ + O \rightarrow N + O^+$	$2.20 \cdot 10^{-18}$	theoretical estimate; *Constantinides et al.* (1979); *Bates* (1989)
IR087	$N^+ + O_2 \rightarrow O_2^+ + N$	$T_i \leq 1000\,K$ $1.45 \cdot 10^{-16} \left(\frac{300}{T_i}\right)^{-0.3098}$ $T_i > 1000\,K$ $3.49 \cdot 10^{-16}$	*Viggiano et al.* (2003); *Anicich* (2003); *Fox and Sung* (2001); *Dotan et al.* (1997); *O'Keefe et al.* (1986)
IR088	$N^+ + O_2 \rightarrow O_2^+ + N(^2D)$	$T_i \leq 1000\,K$ $6.21 \cdot 10^{-17} \left(\frac{300}{T_i}\right)^{-0.3098}$ $T_i > 1000\,K$ $1.49 \cdot 10^{-16}$	*Viggiano et al.* (2003); *Anicich* (2003); *Fox and Sung* (2001); *Dotan et al.* (1997); *O'Keefe et al.* (1986)
IR089	$N^+ + O_2 \rightarrow NO^+ + O$	$T_i \leq 1000\,K$ $3.72 \cdot 10^{-17} \left(\frac{300}{T_i}\right)^{-0.3098}$ $T_i > 1000\,K$ $7.47 \cdot 10^{-17}$	*Viggiano et al.* (2003); *Anicich* (2003); *Fox and Sung* (2001); *Dotan et al.* (1997); *O'Keefe et al.* (1986)
IR090	$N^+ + O_2 \rightarrow NO^+ + O(^1D)$	$T_i \leq 1000\,K$ $1.49 \cdot 10^{-16} \left(\frac{300}{T_i}\right)^{-0.3098}$ $T_i > 1000\,K$ $3.02 \cdot 10^{-16}$	*Viggiano et al.* (2003); *Anicich* (2003); *Fox and Sung* (2001); *Dotan et al.* (1997); *O'Keefe et al.* (1986)

Table C.11: Reaction scheme 2 for IonA-2

Number	Reaction	Reaction coefficient $[m^3/s]$ bimolecular, $[m^6/s]$ termolecular	Source
IR091	$N^+ + O_2 \rightarrow O^+ + NO$	$T_i \leq 1000\,K$ $2.07{\cdot}10^{-17}\left(\frac{300}{T_i}\right)^{-0.3098}$ $T_i > 1000\,K$ $7.53 \cdot 10^{-17}$	*Viggiano et al.* (2003); *Anicich* (2003); *Fox and Sung* (2001); *Dotan et al.* (1997); *O'Keefe et al.* (1986)
IR092	$N_2^+ + Ar \rightarrow Ar^+ + N_2$	$1.1 \cdot 10^{-17} \exp\left(\frac{-2089}{T_i}\right)$	*Fox and Sung* (2001)
IR093	$N_2^+ + CO \rightarrow N_2 + CO^+$	$7.6 \cdot 10^{-17}$	*Anicich* (2003); *Frost et al.* (1998)
IR094	$N_2^+ + CO_2 \rightarrow CO_2^+ + N_2$	$9.0 \cdot 10^{-16}\left(\frac{T_i}{300}\right)^{-0.23}$	*Fox and Sung* (2001); *Dotan et al.* (2000)
IR095	$N_2^+ + e^- \rightarrow N + N(^2D)$	$1.012 \cdot 10^{-13}\left(\frac{T_e}{300}\right)^{-0.39}$	*Fox and Sung* (2001); *Zipf* (1980); *Kella et al.* (1996)
IR096	$N_2^+ + e^- \rightarrow N(^2D) + N(^2D)$	$1.012 \cdot 10^{-13}\left(\frac{T_e}{300}\right)^{-0.39}$	*Fox and Sung* (2001); *Zipf* (1980); *Kella et al.* (1996)
IR097	$NO^+ + e^- \rightarrow N(^2D) + O$	$3.895 \cdot 10^{-13}\left(\frac{T_e}{300}\right)^{-0.80}$	*Shuman et al.* (2015); *Hellberg et al.* (2003)
IR098	$NO^+ + e^- \rightarrow N + O$	$0.205 \cdot 10^{-13}\left(\frac{T_e}{300}\right)^{-0.80}$	*Shuman et al.* (2015); *Hellberg et al.* (2003)
IR099	$N_2^+ + N \rightarrow N^+ + N_2$	$1.0 \cdot 10^{-17}$	upper border; *Ferguson* (1973)
IR100	$N_2^+ + NO \rightarrow N_2 + NO^+$	$3.6 \cdot 10^{-16}$	*Scott et al.* (1999)
IR101	$N_2^+ + O \rightarrow NO^+ + N(^2D)$	$T_i \leq 1500\,K$ $1.33 \cdot 10^{-16}\left(\frac{T_i}{300}\right)^{-0.44}$ $T_i > 1500\,K$: $6.55 \cdot 10^{-17}\left(\frac{1500}{T_i}\right)^{-0.2}$	*Fox and Sung* (2001); *Scott et al.* (1999); *McFarland et al.* (1974)
IR102	$N_2^+ + O \rightarrow O^+ + N_2$	$T_i \leq 1500\,K$ $7.00 \cdot 10^{-18}\left(\frac{T_i}{300}\right)^{-0.23}$ $T_i > 1500\,K$: $4.83 \cdot 10^{-18}\left(\frac{1500}{T_i}\right)^{-0.41}$	*Fox and Sung* (2001); *Scott et al.* (1999); *McFarland et al.* (1974)

Table C.12: Reaction scheme 2 for IonA-2

Number	Reaction	Reaction coefficient $[m^3/s]$ bimolecular, $[m^6/s]$ termolecular	Source
IR103	$N_2^+ + O_2 \rightarrow N_2 + O_2^+$	$T_i \leq 1000\,K$ $5.10 \cdot 10^{-17} \left(\frac{300}{T_i}\right)^{1.16}$ $1000 > T_i \leq 2000\,K$ $1.26 \cdot 10^{-17} \left(\frac{T_i}{1000}\right)^{0.67}$ $T_i > 2000\,K$ $2.39 \cdot 10^{-17}$	(*Fox and Sung*, 2001; *Scott et al.*, 1999; *Dotan et al.*, 1997)
IR104	$O^+ + C \rightarrow C^+ + O$	$1.0 \cdot 10^{-16}$	estimate; *Fox and Sung* (2001)
IR105	$O^+ + CO_2 \rightarrow O_2^+ + CO$	$T_i \leq 800\,K$ $1.1 \cdot 10^{-15}$ $T_i > 800\,K$ $1.1 \cdot 10^{-15} \left(\frac{T_i}{800}\right)^{-0.39}$	(*Anicich*, 2003, 1993)
IR106	$O^+ + e^- \rightarrow O$	$3.24 \cdot 10^{-18} \left(\frac{T_e}{300}\right)^{-0.66}$	calculated; *McElroy et al.* (2013); *Nahar* (1999)
IR107	$O^+ + H \rightarrow H^+ + O$	$5.66 \cdot 10^{-16} \left(\frac{T_i}{300}\right)^{0.36}$ $\exp\left(\frac{8.6}{T_i}\right)$	*McElroy et al.* (2013); *Stancil et al.* (1999)
IR108	$O^+ + N(^2D) \rightarrow N^+ + O$	$1.30 \cdot 10^{-16}$	*Bates* (1989); *Constantinides et al.* (1979)
IR109	$O^+ + N_2 \rightarrow NO^+ + N$	$T_i \leq 1000\,K$ $1.2 \cdot 10^{-18} \left(\frac{T_i}{300}\right)^{-0.45}$ $T_i > 1000\,K$ $7.0 \cdot 10^{-19} \left(\frac{T_i}{1000}\right)^{2.12}$	(*Fox and Sung*, 2001; *Hierl et al.*, 1997)
IR110	$O^+ + NO \rightarrow NO^+ + O$	$T_i \leq 300\,K$ $7.0 \cdot 10^{-19} \left(\frac{300}{T_i}\right)^{0.66}$ $T_i > 300\,K$ $7.0 \cdot 10^{-19} \left(\frac{T_i}{300}\right)^{0.87}$	*Fox and Sung* (2001)
IR111	$O^+ + O_2 \rightarrow O + O_2^+$	$T_i \leq 900\,K$ $1.60 \cdot 10^{-17} \left(\frac{300}{T_i}\right)^{0.52}$ $T_i > 900\,K$ $9.0 \cdot 10^{-18} \left(\frac{T_i}{900}\right)^{0.92}$	(*Fox and Sung*, 2001; *Hierl et al.*, 1997)
IR112	$O_2^+ + C \rightarrow CO^+ + O$	$5.2 \cdot 10^{-17}$	estimate; *Prasad and Huntress* (1980)

Table C.13: Reaction scheme 2 for IonA-2

Number	Reaction	Reaction coefficient $[m^3/s]$ bimolecular, $[m^6/s]$ termolecular	Source
IR113	$O_2^+ + C \rightarrow C^+ + O_2$	$5.2 \cdot 10^{-17}$	estimate; *Prasad and Huntress* (1980)
IR114	$O_2^+ + e^- \rightarrow O + O$	$0.52 \cdot 10^{-13} \left(\frac{T_e}{300}\right)^{-0.7}$	*Fox* (2012); *Mehr and Biondi* (1969); *Petrignani et al.* (2005)
IR115	$O_2^+ + e^- \rightarrow O + O(^1D)$	$0.92 \cdot 10^{-13} \left(\frac{T_e}{300}\right)^{-0.7}$	*Fox* (2012); *Mehr and Biondi* (1969); *Petrignani et al.* (2005)
IR116	$O_2^+ + e^- \rightarrow O(^1D) + O(^1D)$	$0.3978 \cdot 10^{-13} \left(\frac{T_e}{300}\right)^{-0.7}$	*Fox* (2012); *Mehr and Biondi* (1969); *Petrignani et al.* (2005)
IR117	$O_2^+ + N \rightarrow NO^+ + O$	$1.0 \cdot 10^{-16}$	*Scott et al.* (1998)
IR118	$O_2^+ + N(^2D) \rightarrow NO^+ + O$	$1.80 \cdot 10^{-16}$	*Fox and Sung* (2001); *Goldan et al.* (1966)
IR119	$O_2^+ + N(^2D) \rightarrow N^+ + O_2$	$8.65 \cdot 10^{-17}$	estimate; *Fox and Sung* (2001)
IR120	$O_2^+ + NO \rightarrow NO^+ + O_2$	$4.5 \cdot 10^{-16}$	*Midey and Viggiano* (1999)
IR121	$O_2^+ + N_2 \rightarrow NO^+ + NO$	$1.0 \cdot 10^{-21}$	upper border; *Ferguson* (1973)
IR122	$N(^2D) + e^- \rightarrow N + e^-$	$3.8 \cdot 10^{-16} \left(\frac{T_e}{300}\right)^{0.81}$	*Berrington and Burke* (1981)
IR123	$N(^2D) + NO \rightarrow N_2 + O$	$6.7 \cdot 10^{-17}$	*Fell et al.* (1990)
IR124	$N(^2D) + O_2 \rightarrow NO + O(^1D)$	$9.70 \cdot 10^{-18} \exp\left(\frac{-185}{T_N}\right)$	*Herron* (1999)
IR125	$O(^1D) + Ar \rightarrow O + Ar$	$2.1 \cdot 10^{-18} \exp\left(\frac{-310}{T_N}\right)$	*Blitz et al.* (2004)
IR126	$O(^1D) + CO \rightarrow O + CO$	$3.60 \cdot 10^{-17}$	*Schofield* (1978)
IR127	$O(^1D) + CO_2 \rightarrow O + CO_2$	$7.5 \cdot 10^{-17} \exp\left(\frac{115}{T_N}\right)$	*Burkholder et al.* (2015)
IR128	$O(^1D) + e^- \rightarrow O + e^-$	$2.87 \cdot 10^{-16} \left(\frac{T_e}{300}\right)^{0.91}$	*Berrington and Burke* (1981)
IR129	$O(^1D) + H \rightarrow O + H$	$7.445 \cdot 10^{-19} \left(\frac{T_N}{300}\right)^{0.1484} \exp\left(\frac{-78.97}{T_N}\right)$	*Fox* (2012); *Krems et al.* (2006)

Table C.14: Reaction scheme 2 for IonA-2

Number	Reaction	Reaction coefficient $[m^3/s]$ bimolecular, $[m^6/s]$ termolecular	Source
IR130	$O(^1D) + H_2 \rightarrow OH + H$	$1.5 \cdot 10^{-16}$	*Fox* (2012); *Blitz et al.* (2004)
IR131	$O(^1D) + N_2 \rightarrow O + N_2$	$2.15 \cdot 10^{-17} \exp\left(\frac{110}{T_N}\right)$	*Burkholder et al.* (2015)
IR132	$O(^1D) + O \rightarrow O + O$	$2.2 \cdot 10^{-17} \left(\frac{T_N}{300}\right)^{0.14}$	*Fox* (2012); *Jamieson et al.* (1992); *Kalogerakis et al.* (2009)
IR133	$O(^1D) + O_2 \rightarrow O + O_2$	$3.12 \cdot 10^{-17} \exp\left(\frac{70}{T_N}\right)$	*Fox* (2012)
IR134	$O(^1D) \rightarrow O$	$8.604 \cdot 10^{-3}$	*Fox* (2012); *Froese Fischer and Tachiev* (2004)
IS001	$CO_2 + e^- \rightarrow CO_2^+ + e^- + e^-$		
IS002	$CO + e^- \rightarrow CO^+ + e^- + e^-$		
IS003	$N_2 + e^- \rightarrow N_2^+ + e^- + e^-$		
IS004	$N + e^- \rightarrow N^+ + e^- + e^-$		
IS005	$O_2 + e^- \rightarrow O_2^+ + e^- + e^-$		
IS006	$O + e^- \rightarrow O^+ + e^- + e^-$		

Table C.15: Reaction scheme 2 for IonA-2

Appendix D

Supporting information Chapter 7

D.1 Merged excess electron densities in correlation with observational and environmental parameters

	all [number]	$Mm_{a,5km}$ [number]	[%]	$Mm_{c,5km}$ [number]	[%]		all [number]	$Mm_{a,5km}$ [number]	[%]	$Mm_{c,5km}$ [number]	[%]
Φ_{SUM}						Φ_{EARTH}					
low	37	13	**35.1**	4	**10.8**	*low*	26	7	**26.9**	3	**11.5**
moderate	168	69	**41.1**	12	**7.1**	*moderate*	185	70	**37.8**	14	**7.6**
high	34	8	**23.5**	5	**14.7**	*high*	28	13	**46.4**	4	**14.3**
Φ_{Xray}											
low	27	7	**25.9**	2	**7.4**						
moderate	178	71	**39.9**	14	**7.9**						
high	34	12	**35.3**	5	**14.7**						
$\Phi_{0.45\text{-}3.0}$						$\Phi_{0.45\text{-}1.0}$					
low	93	34	**36.6**	9	**9.7**	*low*	90	33	**36.7**	8	**8.9**
moderate	110	42	**38.2**	8	**7.3**	*moderate*	115	44	**38.3**	9	**7.8**
high	36	14	**38.9**	4	**11.1**	*high*	36	14	**38.9**	4	**11.1**

Table D.1: Occurrence rates of $Mm_{a,5km}$ in the low, moderate and high Φ_{SUM}, Φ_{Xray}, $\Phi_{0.45-3nm}$, $\Phi_{0.45-1nm}$ and Φ_{EARTH} solar proxy intervals. For each parameter, the first column contains all observations in a given solar proxy interval, the second column contains the number of Mm occurrences, the third column the occurrence percentage, while the fourth and fifth columns contain the number and percentage of $Mm_{c,5km}$ observations in each solar proxy interval.

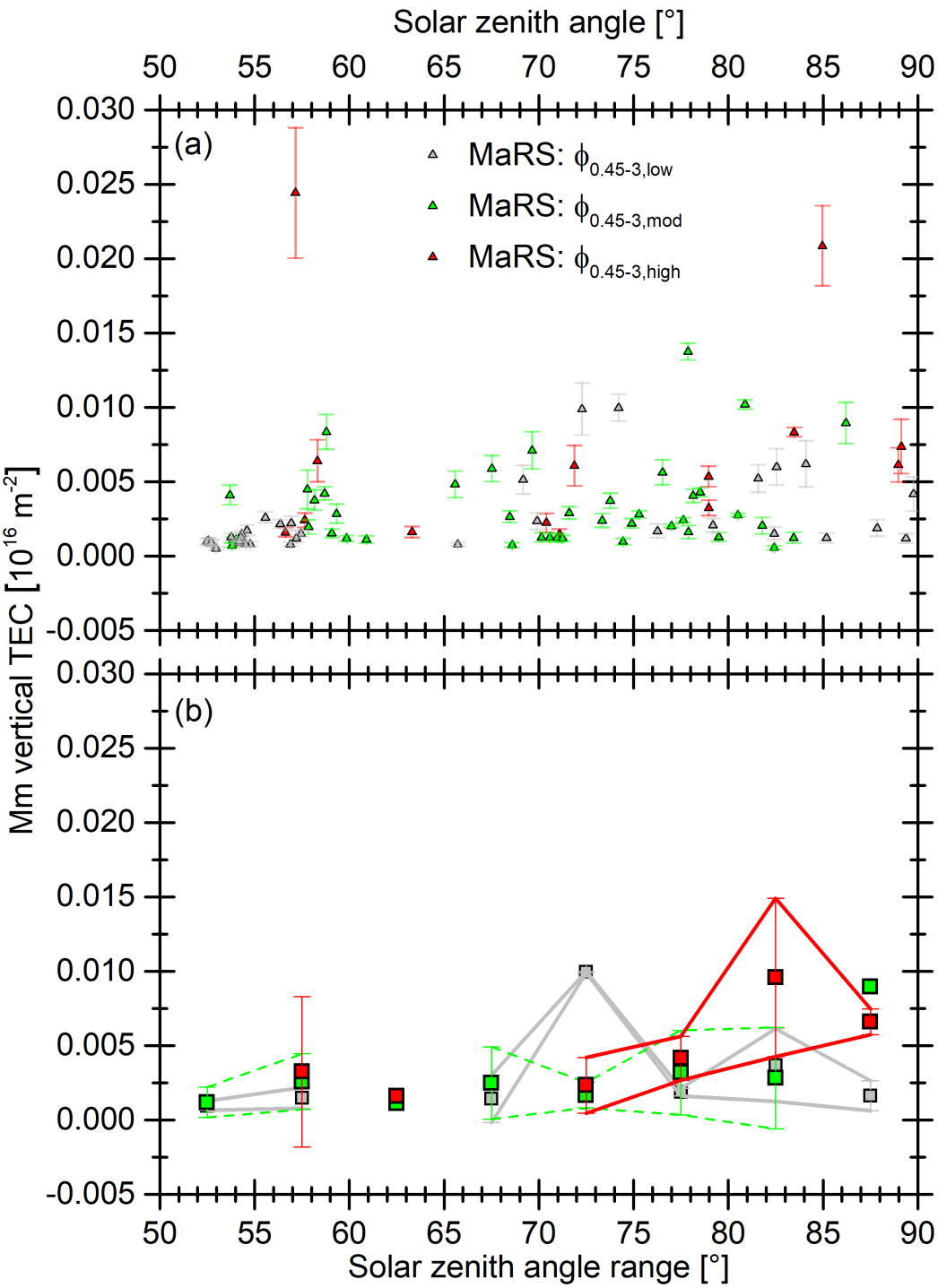

Figure D.1: (a) $Mm_{a,5km}$ vertical TEC in dependence of the solar zenith angle χ. (b) The weighted average Mm TEC $\overline{n}^{obs}_{TEC}(Mm)$ (squares) and weighted standard deviation (error bars) calculated for 5° solar zenith angle bins and the $\Phi_{0.45-3nm}$ proxy levels used in Panel (a).

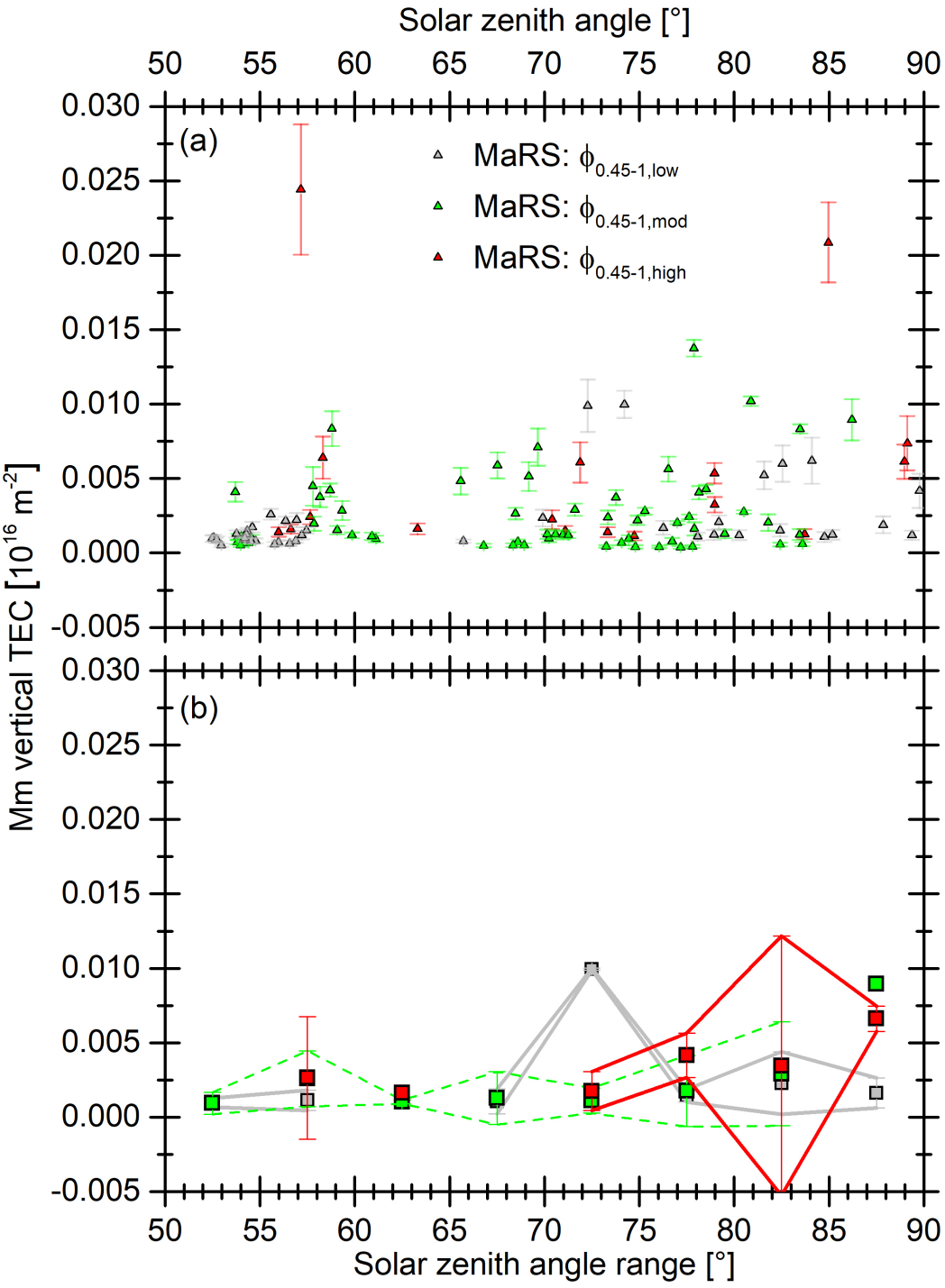

Figure D.2: (a) $Mm_{a,3km}$ vertical TEC in dependence of the solar zenith angle χ. (b) The weighted average Mm TEC $\overline{n}^{obs}_{TEC}(Mm)$ (squares) and weighted standard deviation (error bars) for 5° solar zenith angle bins and the $\Phi_{0.45-1nm}$ proxy levels illustrated in Panel (a).

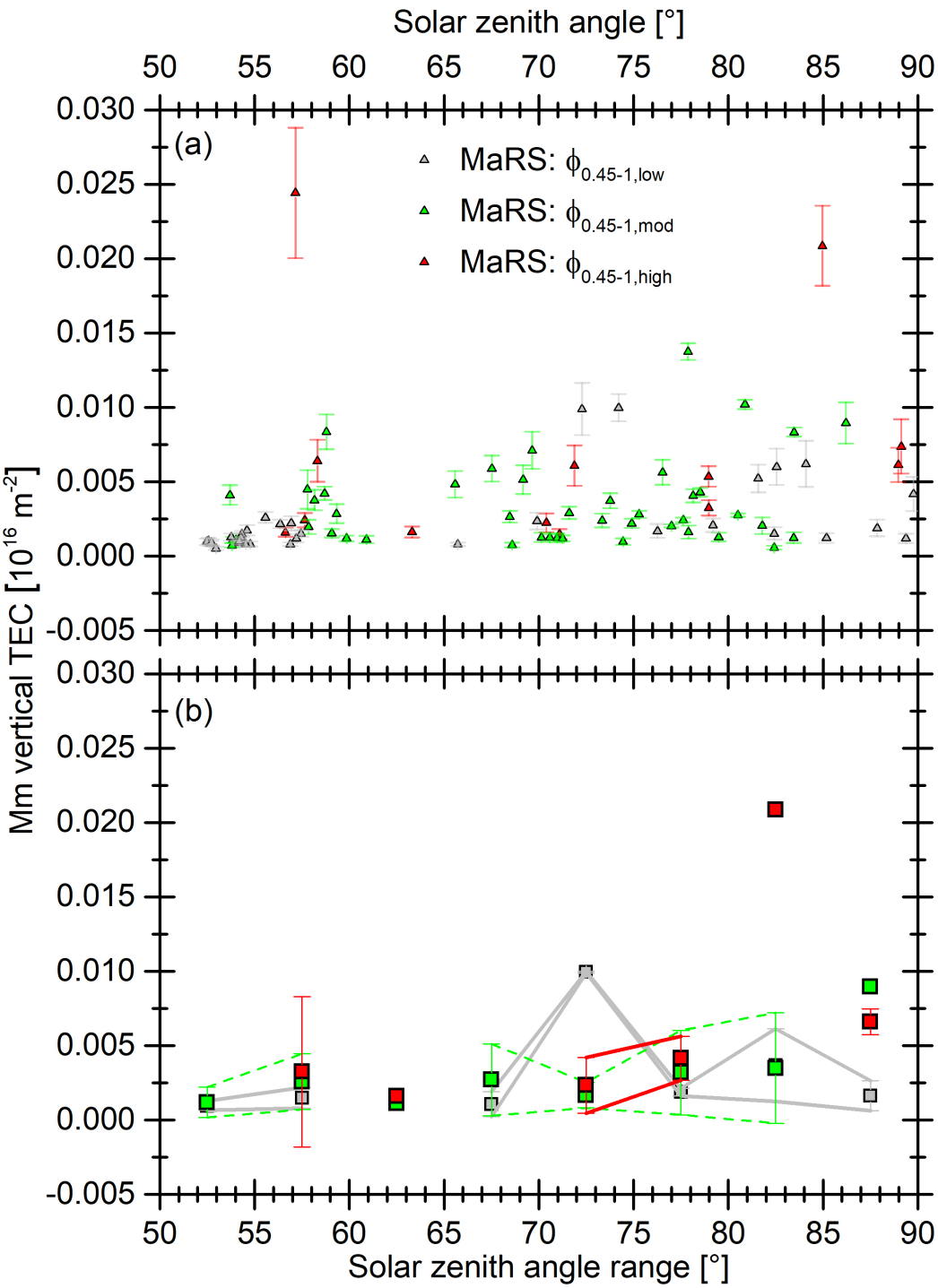

Figure D.3: (a) $Mm_{a,5km}$ vertical TEC in dependence of the solar zenith angle χ. (b) The weighted average Mm TEC $\overline{n}^{obs}_{TEC}(Mm)$ (squares) and weighted standard deviation (error bars) for 5° solar zenith angle bins and the $\Phi_{0.45-1nm}$ proxy levels illustrated in Panel (a).

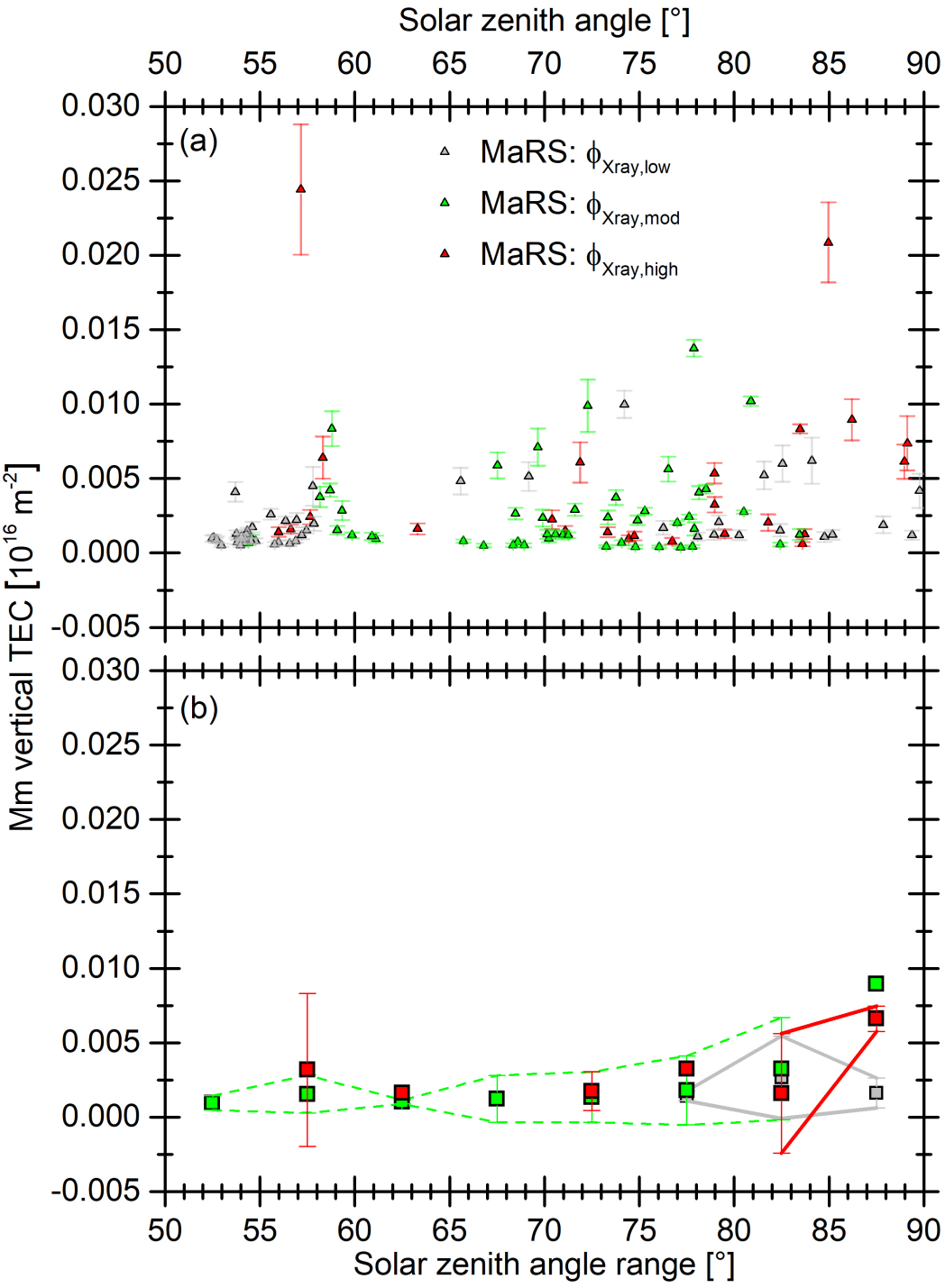

Figure D.4: (a) $Mm_{a,3km}$ vertical TEC in dependence of the solar zenith angle χ. (b) The weighted average Mm TEC $\overline{n}^{obs}_{TEC}(Mm)$ (squares) and weighted standard deviation (error bars) for 5° solar zenith angle bins and the Φ_{Xray} proxy levels illustrated in Panel (a).

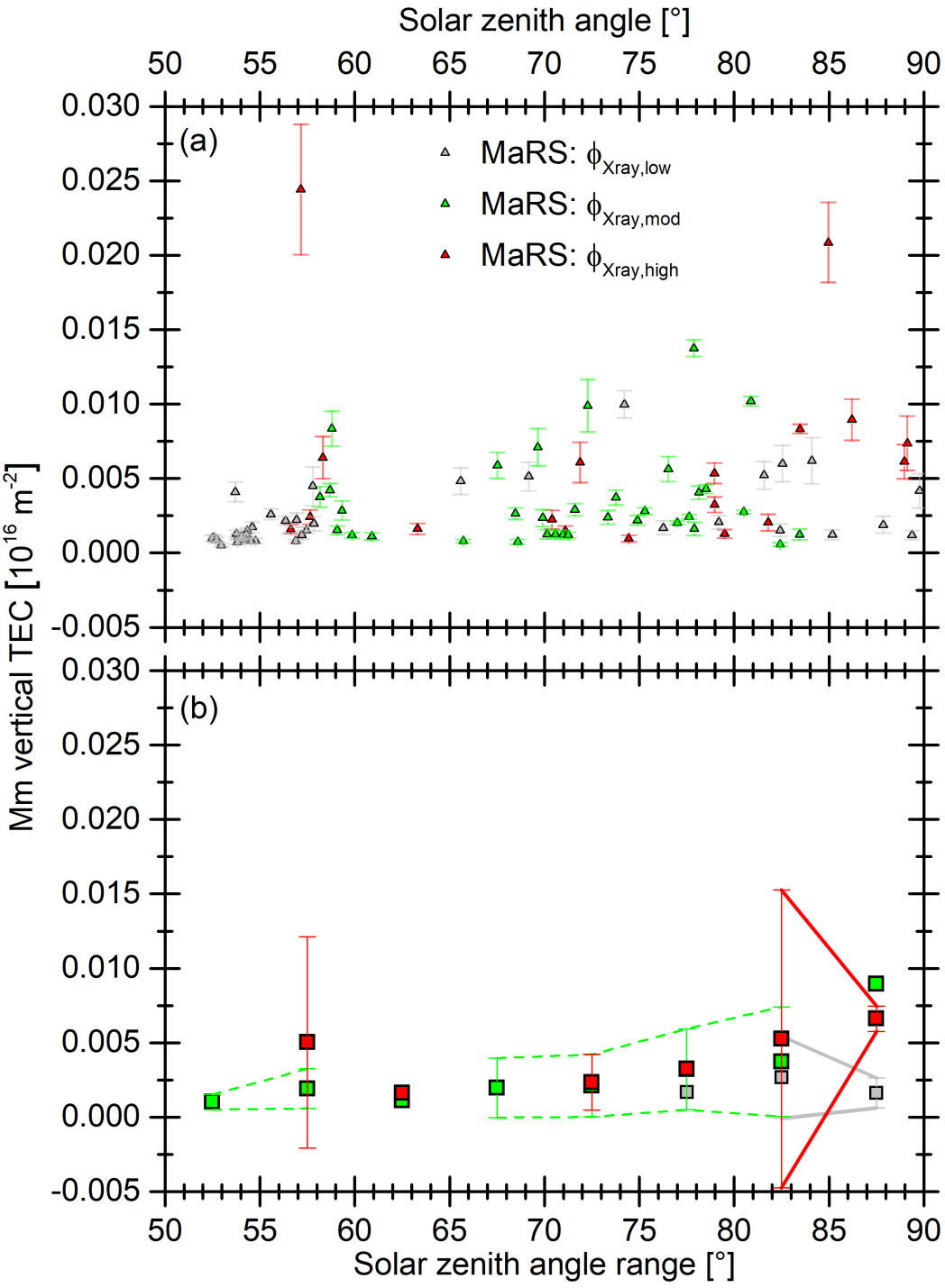

Figure D.5: (a) $Mm_{a,5km}$ vertical TEC in dependence of the solar zenith angle χ. (b) The weighted average Mm TEC $\overline{n}^{obs}_{TEC}(Mm)$ (squares) and weighted standard deviation (error bars) for 5° solar zenith angle bins and the Φ_{Xray} proxy levels illustrated in Panel (a).

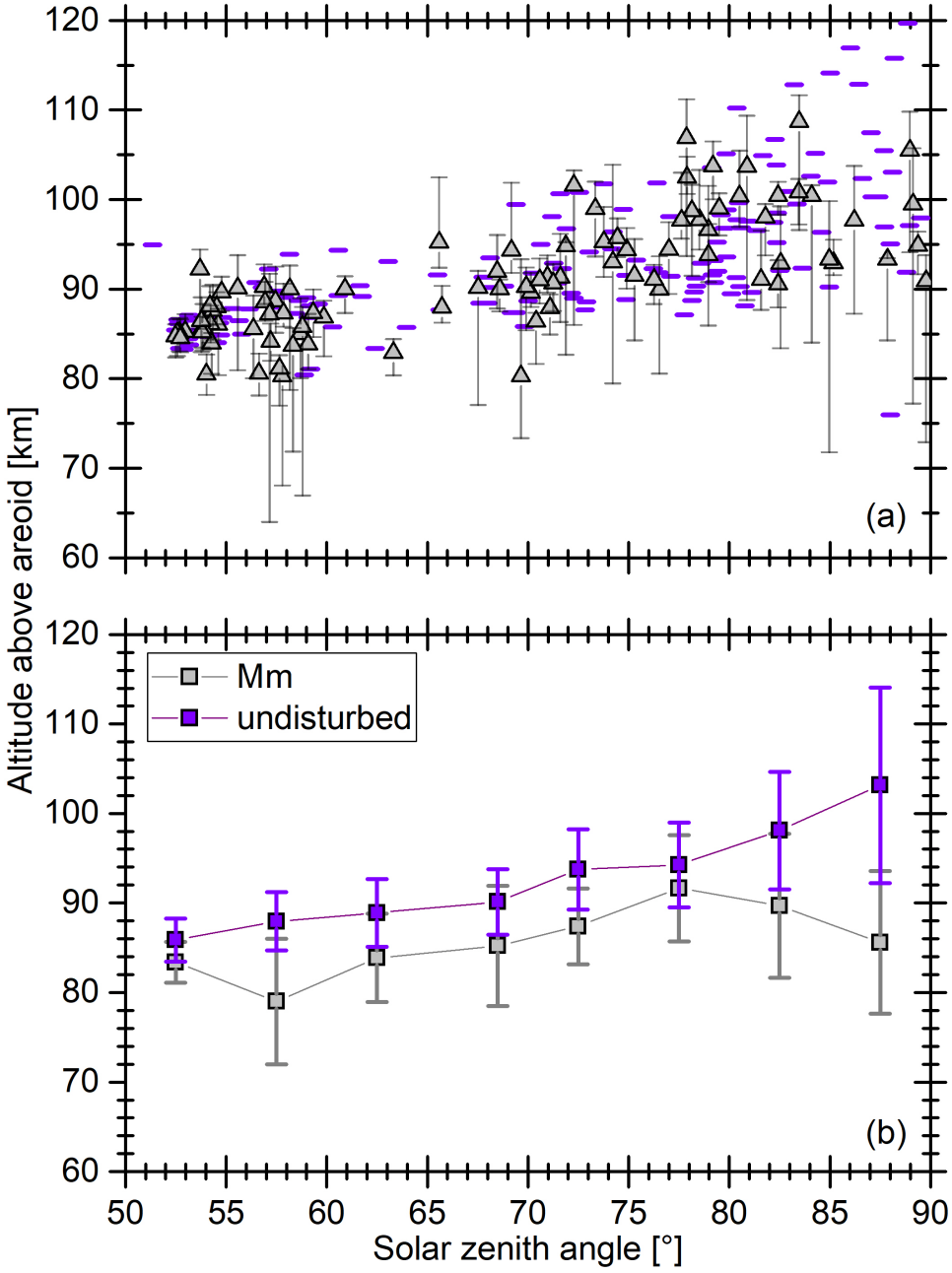

Figure D.6: Comparison between the $Mm_{a,5km}$ altitude ranges and the smoothed lower border of the undisturbed profiles of the associated $MaRS_{quiet,5km}$ data set. (a) Gray triangles indicate the Mm altitude $h^{obs}_{max}(Mm)$. The upper and lower error bars indicate the smoothed upper $h_{U,smooth}(Mm)$ and lower $h_{L,smooth}(Mm)$ borders of the Mm excess density. The violet minuses indicate the smoothed lower borders $h_{L,smooth}$ of the undisturbed profiles. (b) $h_{L,smooth}$ of the Mm and undisturbed profiles, separately averaged in 5° solar zenith angle bins. The given error bars indicate the calculated standard deviation of the data points.

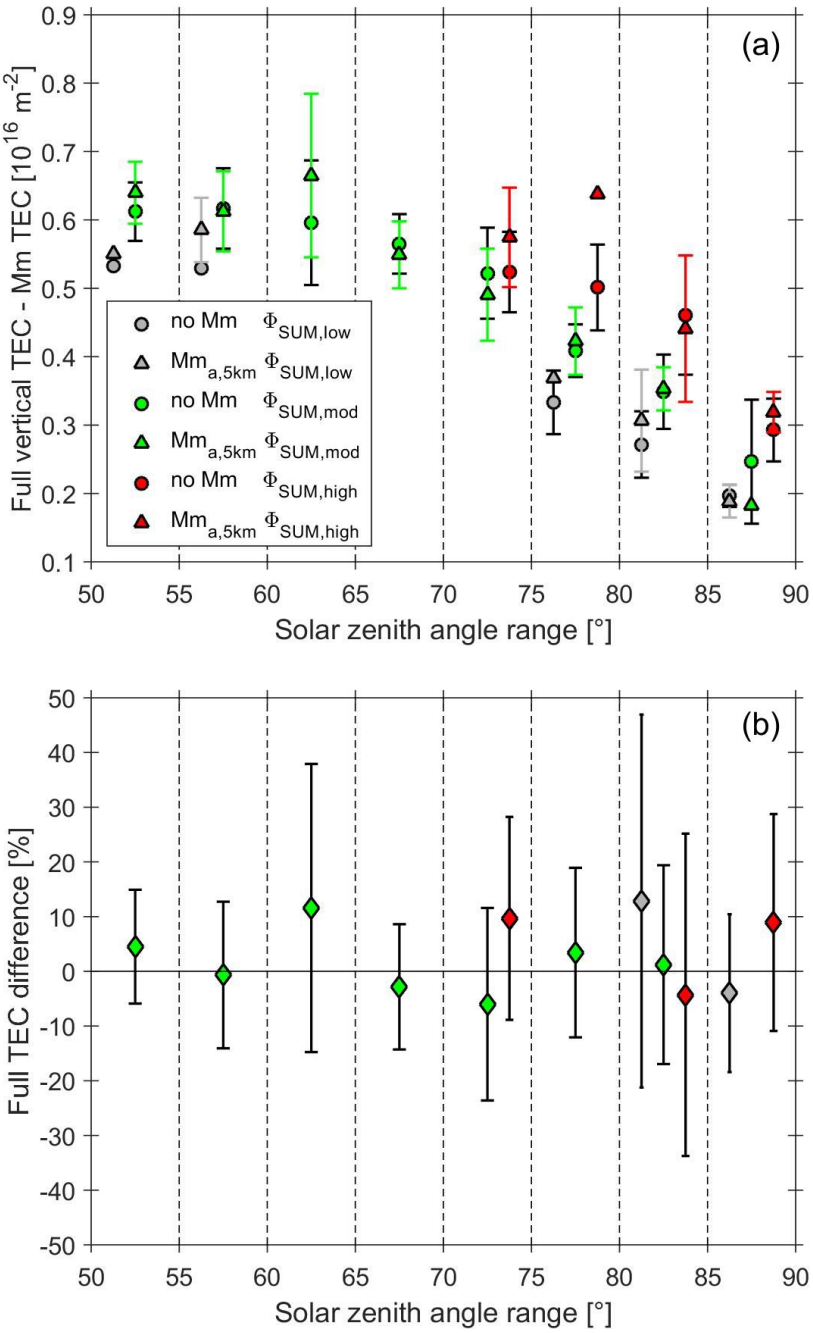

Figure D.7: (a) Weighted average (circles) and weighted standard deviation (error bars) of the $MaRS_{quiet,5km}$ TEC separately calculated for observations with (n^{obs}_{TEC}-$n^{obs}_{TEC}(Mm)$) and without Mm (n^{obs}_{TEC}) in the Φ_{SUM} proxy intervals. The colored error bars are associated with the triangles. (b) Differences between the averaged TEC values of Panel (a) in percent of the undisturbed TEC. The error bars are calculated with the classical error propagation.

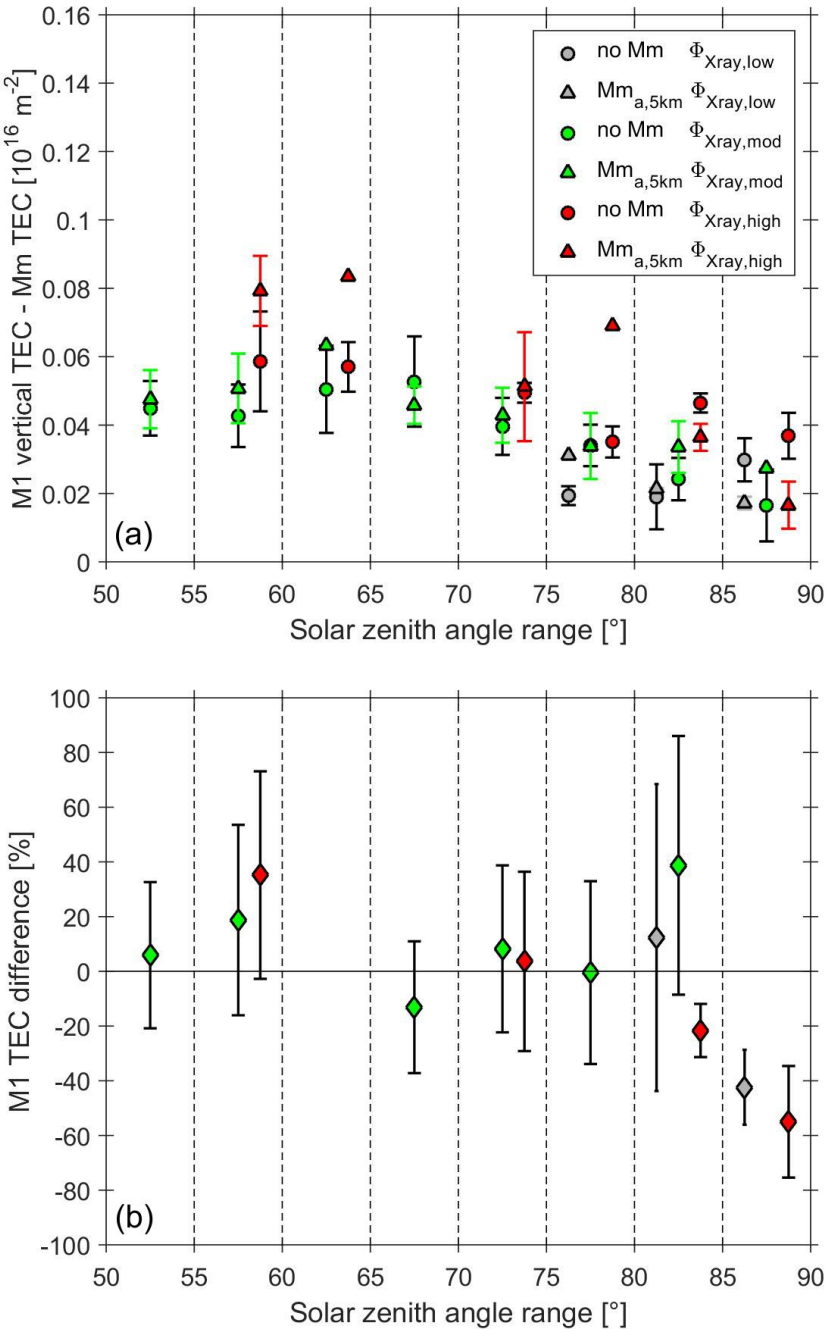

Figure D.8: (a) Weighted average (circles) and weighted standard deviation (error bars) of the $MaRS_{quiet,5km}$ M1 TEC separately calculated for observations with ($n_{TEC}^{obs}(M1)$-$n_{TEC}^{obs}(Mm)$) and without Mm ($n_{TEC}^{obs}(M1)$) in the Φ_{Xray} proxy intervals. The colored error bars are associated with the triangles. (b) Differences between the averaged TEC values of Panel (a) in percent of the undisturbed TEC. The error bars are calculated with the classical error propagation.

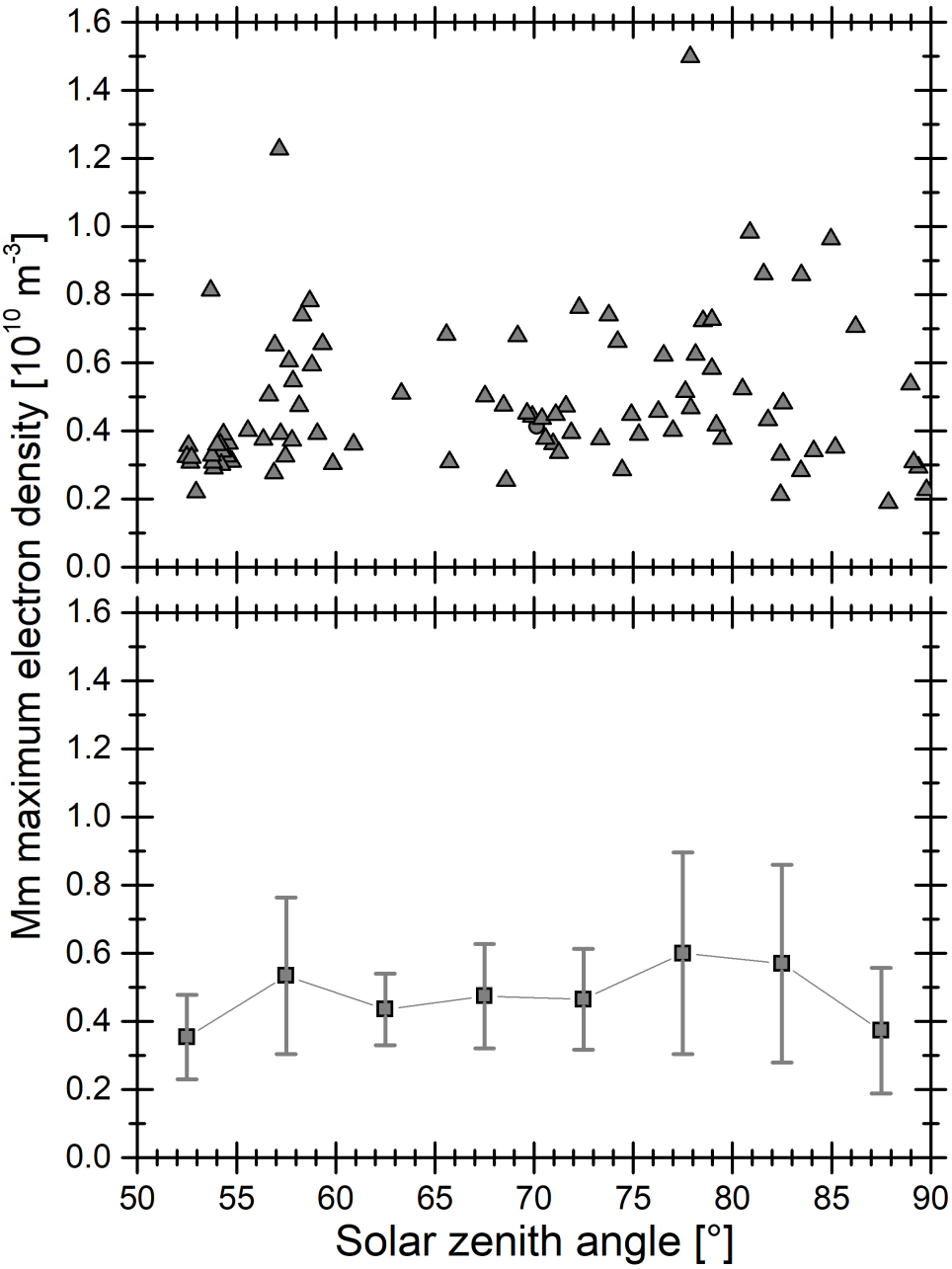

Figure D.9: Mm maximum electron density. (a) The gray triangles indicate the Mm maximum electron density $n_{e,max}^{obs}(Mm)$ of $MaRS_{quiet,5km}$. (b) $n_{e,max}^{obs}(Mm)$ averaged in 5° solar zenith angle bins. The given error bars indicate the calculated standard deviation of the data points.

Bibliography

Acuña, M. H., J. E. P. Connerney, N. F. Ness et al. Global Distribution of Crustal Magnetization Discovered by the Mars Global Surveyor MAG/ER Experiment. *Science*, vol. 284, 5415, pp. 790–793, 1999.

Acuña, M. H., J. E. P. Connerney, P. Wasilwski et al. Magnetic field of Mars: Summary of results from the aerobraking and mapping orbits. *Journal of Geophysical Research: Planets*, vol. 106, E10, pp. 23403–23417, 2001.

Albee, A. L., F. D. Palluconi and R. E. Arvidson. Mars Global Surveyor Mission: Overview and Status. *Science*, vol. 279, 5357, pp. 1671–1672, 1998.

Alge, E., N. G. Adams and D. Smith. Measurements of the dissociative recombination coefficients of O_2^+ , NO^+ and NH_4^+ in the temperature range 200-600K. *Journal of Physics B: Atomic and Molecular Physics*, vol. 16, 8, pp. 1433–1444, 1983.

Anbar, A. D., M. Allen and H. A. Nair. Photodissociation in the atmosphere of Mars: Impact of high resolution, temperature–dependent CO_2 cross–section measurements. *Journal of Geophysical Research: Planets*, vol. 98, E6, pp. 10925–10931, 1993.

Andersson, L., R. E. Ergun, G. T. Delory et al. The Langmuir Probe and Waves (LPW) Instrument for MAVEN. *Space Science Reviews*, vol. 195, 1, pp. 173–198, 2015.

Angelats i Coll, M., F. Forget, M. A. López-Valverde et al. The first Mars thermospheric general circulation model: The Martian atmosphere from the ground to 240 km. *Geophysical Research Letters*, vol. 32, 4, 2005.

Anicich, V. G. Evaluated Bimolecular Ion–Molecule Gas Phase Kinetics of Positive Ions for Use in Modeling Planetary Atmospheres, Cometary Comae, and Interstellar Clouds. *Journal of Physical and Chemical Reference Data*, vol. 22, 6, pp. 1469–1569, 1993.

Anicich, V. G. An index of the literature for bimolecular gas phase cation-molecule reaction kinetics. 2003.

Arras, C., J. Wickert, G. Beyerle et al. A global climatology of ionospheric irregularities derived from GPS radio occultation. *Geophysical Research Letters*, vol. 35, 14, 2008.

Aschwanden, M. J. Irradiance observations of the 1-8 A solar soft X-ray flux from GOES. *Solar Physics*, vol. 152, 1, pp. 53–59, 1994.

Atkinson, R., D. L. Baulch, R. A. Cox et al. Evaluated Kinetic and Photochemical Data for Atmospheric Chemistry: Supplement III. IUPAC Subcommittee on Gas Kinetic Data Evaluation for Atmospheric Chemistry. *Journal of Physical and Chemical Reference Data*, vol. 18, 2, pp. 881–1097, 1989.

Avakyan, S. V., R. N. Il'in, V. M. Lavrov et al. *Collision processes and excitation of UV emission from planetary atmospheric gases: A handbook of cross sections.* Gordon and Breach Science Publishers, Australia [etc.], 1998. ISBN 9789056991470.

Banks, P. M. and G. Kockarts. *Aeronomy - Part A.* Acad. Press, New York, NY, 1973. ISBN 0120778017.

Barabash, S., R. Lundin, H. Andersson et al. ASPERA-3: Analyser of Space Plasmas and Energetic Ions for Mars Express. In A. Wilson, ed., *Mars express*, pp. 121–139. ESA Publications Division, Noordwijk, 2004. ISBN 92-9092-556-6.

Barth, C. A., C. W. Hord, J. B. Pearce et al. Mariner 6 and 7 Ultraviolet Spectrometer Experiment: Upper atmosphere data. *Journal of Geophysical Research*, vol. 76, 10, pp. 2213–2227, 1971.

Bates, D. R. Theoretical considerations regarding some inelastic atomic collision processes of interest in aeronomy: Deactivation and charge transfer. *Planetary and Space Science*, vol. 37, 3, pp. 363–368, 1989.

Bauer, S. J. and M. H. Hantsch. Solar cycle variation of the upper atmosphere temperature of Mars. *Geophysical Research Letters*, vol. 16, 5, p. 373, 1989.

Bauer, S. J. and H. Lammer. *Planetary Aeronomy: Atmosphere Environments in Planetary Systems.* Springer, Berlin, Heidelberg, 2004. ISBN 3-540-21472-0.

Bellucci, G., F. Altieri, J. P. Bibring et al. The OMEGA Instrument on board Mars Express: First Results. *Memorie della Societa Astronomica Italiana Supplementi*, vol. 5, p. 27, 2004.

Benna, M., P. R. Mahaffy, J. M. Grebowsky et al. First measurements of composition and dynamics of the Martian ionosphere by MAVEN's Neutral Gas and Ion Mass Spectrometer. *Geophysical Research Letters*, vol. 42, 21, pp. 8958–8965, 2015a.

Benna, M., P. R. Mahaffy, J. M. Grebowsky et al. Metallic ions in the upper atmosphere of Mars from the passage of comet C/2013 A1 (Siding Spring). *Geophysical Research Letters*, vol. 42, 12, pp. 4670–4675, 2015b.

Berkowitz, J. *Atomic and molecular photoabsorption: Absolute total cross sections.* Academic Press, San Diego, CA, 2002. ISBN 9780120918416.

Berkowitz, J. *Atomic and molecular photoabsorption: Absolute partial cross sections.* Science Direct e-books. Academic Press, an imprint of Elsevier, London, 2015. ISBN 0128019433.

Berrington, K. A. and P. G. Burke. Effective collision strengths for forbidden transitions in e-N and e-o scattering. *Planetary and Space Science*, vol. 29, 3, pp. 377–381, 1981.

Bertaux, J.-L., D. Fonteyn, O. Korablev et al. SPICAM: Studying the Global Structure and Composition of the Martian Atmosphere. In A. Wilson, ed., *Mars express*, pp. 95–120. ESA Publications Division, Noordwijk, 2004. ISBN 92-9092-556-6.

Bertucci, C., C. Mazelle, J. A. Slavin et al. Magnetic field draping enhancement at Venus: Evidence for a magnetic pileup boundary. *Geophysical Research Letters*, vol. 30, 17, 2003.

Bhardwaj, A. and S. Raghuram. Model for Cameron-band emission in comets: A case for the EPOXI mission target comet 103P/Hartley 2. *Monthly Notices of the Royal Astronomical Society: Letters*, vol. 412, 1, pp. L25–L29, 2011.

Blitz, M. A., T. J. Dillon, D. E. Heard et al. Laser induced fluorescence studies of the reactions of $O(^1D_2)$ with N_2, O_2, N_2O, CH_4, H_2, CO_2, Ar, Kr and $n-C_4H_{10}$. *Physical Chemistry Chemical Physics*, vol. 6, 9, p. 2162, 2004.

Born, M. and E. Wolf. *Principles of optics: Electromagnetic theory of propagation, interference and diffraction of light.* Cambridge University Press, Cambridge and New York, 7th expanded edn., 1999. ISBN 9780521639217.

Borodi, G., A. Luca and D. Gerlich. Reactions of CO_2^+ with H, H_2 and deuterated analogues. *International Journal of Mass Spectrometry*, vol. 280, 1-3, pp. 218–225, 2009.

Bougher, S. W., D. A. Brain, J. L. Fox et al. Upper Neutral Atmosphere and Ionosphere. In R. M. Haberle, R. T. Clancy, F. Forget, M. D. Smith and R. W. Zurek, eds., *The Atmosphere and Climate of Mars*, pp. 433–463. Cambridge Univ. Pr, Cambridge, 2017. ISBN 978-1107016187.

Bougher, S. W., S. Engel, D. P. Hinson et al. Mars Global Surveyor radio science electron density profiles: Neutral atmosphere implications. *Geophysical Research Letters*, vol. 28, 16, pp. 3091–3094, 2001.

Bougher, S. W., S. Engel, D. P. Hinson et al. MGS Radio Science electron density profiles: Interannual variability and implications for the Martian neutral atmosphere. *Journal of Geophysical Research*, vol. 109, E3, 2004.

Bougher, S. W., B. M. Jakosky, J. S. Halekas et al. Early MAVEN Deep Dip campaign reveals thermosphere and ionosphere variability. *Science (New York, N.Y.)*, vol. 350, 6261, p. aad0459, 2015a.

Bougher, S. W., D. Pawlowski, J. M. Bell et al. Mars Global Ionosphere-Thermosphere Model: Solar cycle, seasonal, and diurnal variations of the Mars upper atmosphere. *Journal of Geophysical Research: Planets*, vol. 120, 2, pp. 311–342, 2015b.

Brace, L. and A. J. Kliore. The structure of the Venus ionosphere. *Space Science Reviews*, vol. 55, 1-4, pp. 81–163, 1991.

Bracewell, R. N. *The fourier transform and its applications*. McGraw-Hill, Boston, 3rd ed. edn., 2000. ISBN 9780073039381.

Brain, D. A., S. Barabash, S. W. Bougher et al. Solar Wind Interaction and Atmospheric Escape. In R. M. Haberle, R. T. Clancy, F. Forget, M. D. Smith and R. W. Zurek, eds., *The Atmosphere and Climate of Mars*, pp. 464–496. Cambridge Univ. Pr, Cambridge, 2017. ISBN 978-1107016187.

Brune, W. H., J. J. Schwab and J. G. Anderson. Laser magnetic resonance, resonance fluorescence, resonance absorption studies of the reaction kinetics of atomic oxygen + hydroxyl .fwdarw. atomic hydrogen + molecular oxygen, atomic oxygen + perhydroxyl .fwdarw. hydroxyl + molecular oxygen, atomic nitrogen + hydroxyl .fwdarw. atomic hydrogen + nitric oxide, atomic nitrogen + perhydroxyl .fwdarw. products at 300 K between 1 and 5 torr. *The Journal of Physical Chemistry*, vol. 87, 22, pp. 4503–4514, 1983.

Burkholder, J. B., S. P. Sander, J. Abbatt et al. Chemical Kinetics and Photochemical Data for Use in Atmospheric Studies, Evaluation Number 18. 2015.

Cain, J. C., B. B. Ferguson and D. Mozzoni. An n = 90 internal potential function of the Martian crustal magnetic field. *Journal of Geophysical Research: Planets*, vol. 108, E2, 2003.

Carr, M. H. *The Surface of Mars*. Cambridge University Press, New Yourk, 2006. ISBN 978-0-521-87201-0.

Chan, W. F., G. Cooper, R. Sodhi et al. Absolute optical oscillator strengths for discrete and continuum photoabsorption of molecular nitrogen (11–200 eV). *Chemical Physics*, vol. 170, 1, pp. 81–97, 1993.

Chapman, S. The absorption and dissociative or ionizing effect of monochromatic radiation in an atmosphere on a rotating earth. *Proceedings of the Physical Society*, vol. 43, 1, pp. 26–45, 1931a.

Chapman, S. The absorption and dissociative or ionizing effect of monochromatic radiation in an atmosphere on a rotating earth part II. Grazing incidence. *Proceedings of the Physical Society*, vol. 43, 5, pp. 483–501, 1931b.

Chapman, S. and T. G. Cowling. *The Mathematical Theory of Nonuniform Gases*. Cambridge Univ. Pr, New York, 1939.

Chastaing, D., S. D. Le Picard and I. R. Sims. Direct kinetic measurements on reactions of atomic carbon, $C(^3P)$, with O_2 and NO at temperatures down to 15 K. *The Journal of Chemical Physics*, vol. 112, 19, pp. 8466–8469, 2000.

Chaufray, J.-Y., F. González-Galindo, F. Forget et al. Variability of the hydrogen in the martian upper atmosphere as simulated by a 3D atmosphere–exosphere coupling. *Icarus*, vol. 245, pp. 282–294, 2015.

Chen, R. H., T. E. Cravens and A. F. Nagy. The Martian ionosphere in light of the Viking observations. *Journal of Geophysical Research*, vol. 83, A8, p. 3871, 1978.

Chicarro, A., P. Martin and R. Trautner. The Mars Express Mission: An Overview. In A. Wilson, ed., *Mars Express*, pp. 3–13. ESA Publications Division, Noordwijk, 2004. ISBN 92-9092-556-6.

Chu, Y. H., C. Y. Wang, K. H. Wu et al. Morphology of sporadic E layer retrieved from COSMIC GPS radio occultation measurements: Wind shear theory examination. *Journal of Geophysical Research: Space Physics*, vol. 119, 3, pp. 2117–2136, 2014.

Clancy, R. T., B. J. Sandor, M. J. Wolff et al. An intercomparison of ground-based millimeter, MGS TES, and Viking atmospheric temperature measurements: Seasonal and interannual variability of temperatures and dust loading in the global Mars atmosphere. *Journal of Geophysical Research: Planets*, vol. 105, E4, pp. 9553–9571, 2000.

Cole, B. E. and R. N. Dexter. Photoabsorption and photoionisation measurements on some atmospheric gases in the wavelength region 50-340 A. *Journal of Physics B: Atomic and Molecular Physics*, vol. 11, 6, pp. 1011–1023, 1978.

Colegrove, F. D., F. S. Johnson and W. B. Hanson. Atmospheric composition in the lower thermosphere. *Journal of Geophysical Research*, vol. 71, 9, pp. 2227–2236, 1966.

Connerney, J. E. P., M. H. Acuña, N. F. Ness et al. Tectonic implications of Mars crustal magnetism. *Proceedings of the National Academy of Sciences of the United States of America*, vol. 102, 42, pp. 14970–14975, 2005.

Connerney, J. E. P., M. H. Acuña, P. J. Wasilewski et al. The global magnetic field of Mars and implications for crustal evolution. *Geophysical Research Letters*, vol. 28, 21, pp. 4015–4018, 2001.

Connerney, J. E. P., J. R. Espley, P. Lawton et al. The MAVEN Magnetic Field Investigation. *Space Science Reviews*, vol. 195, 1, pp. 257–291, 2015.

Constantinides, E. R., J. H. Black, A. Dalgarno et al. The photochemistry of N^+ ions. *Geophysical Research Letters*, vol. 6, 7, pp. 569–572, 1979.

Creasey, J. E., J. M. Forbes and G. M. Keating. Density variability at scales typical of gravity waves observed in Mars' thermosphere by the MGS accelerometer. *Geophysical Research Letters*, vol. 33, 22, 2006.

Crismani, M. M. J., N. M. Schneider, J. M. C. Plane et al. Detection of a persistent meteoric metal layer in the Martian atmosphere. *Nature Geoscience*, vol. 10, pp. 401–404, 2017.

Demtröder, W. *Atoms, molecules and photons: An introduction to atomic-, molecular- and quantum-physics*. Graduate texts in physics. Springer, Heidelberg and London, 2. edn., 2010. ISBN 3642102972.

Domingo, V., B. Fleck and A. I. Poland. SOHO: The Solar and Heliospheric Observatory. *Space Science Reviews*, vol. 72, 1-2, pp. 81–84, 1995.

Dong, C., S. W. Bougher, Y. Ma et al. Solar wind interaction with Mars upper atmosphere: Results from the one-way coupling between the multifluid MHD model and the MTGCM model. *Geophysical Research Letters*, vol. 41, 8, pp. 2708–2715, 2014.

Dotan, I., P. M. Hierl, R. A. Morris et al. Rate constants for the reactions of N^+ and N_2^+ with O_2 as a function of temperature (300–1800 K). *International Journal of Mass Spectrometry and Ion Processes*, vol. 167-168, pp. 223–230, 1997.

Dotan, I. and W. Lindinger. Energy dependencies of the reactions of Ar^+ with H_2 , N_2 , CO, O_2 , CO_2 , N_2O, and COS. *The Journal of Chemical Physics*, vol. 76, 10, pp. 4972–4977, 1982.

Dotan, I., A. J. Midey and A. A. Viggiano. Rate constants for the reactions of Ar^+ with CO_2 and SO_2 as a function of temperature (300–1500 K). *Journal of the American Society for Mass Spectrometry*, vol. 10, 9, pp. 815–820, 1999.

Dotan, I., A. J. Midey and A. A. Viggiano. Kinetics of the reactions of N_2^+ with CO_2 and SO_2 from 300–1400 K. *The Journal of Chemical Physics*, vol. 113, 5, pp. 1732–1737, 2000.

Du, M. L. and A. Dalgarno. The radiative association of N and O atoms. *Journal of Geophysical Research*, vol. 95, A8, p. 12265, 1990.

Duru, F., D. A. Gurnett, T. F. Averkamp et al. Magnetically controlled structures in the ionosphere of Mars. *Journal of Geophysical Research*, vol. 111, A12, 2006.

Duru, F., D. A. Gurnett, R. A. Frahm et al. Steep, transient density gradients in the Martian ionosphere similar to the ionopause at Venus. *Journal of Geophysical Research*, vol. 114, A12, 2009.

England, S. L., G. Liu, E. Yiğit et al. MAVEN NGIMS observations of atmospheric gravity waves in the Martian thermosphere. *Journal of Geophysical Research: Space Physics*, vol. 122, 2, pp. 2310–2335, 2017.

Eparvier, F., P. C. Chamberlin, T. N. Woods et al. The Solar Extreme Ultraviolet Monitor for MAVEN. *Space Science Reviews*, vol. 195, 1, pp. 293–301, 2015.

Ergun, R. E., M. W. Morooka, L. A. Andersson et al. Dayside electron temperature and density profiles at Mars: First results from the MAVEN Langmuir probe and waves instrument. *Geophysical Research Letters*, vol. 42, 21, pp. 8846–8853, 2015.

Espley, J. R., G. A. DiBraccio, J. E. P. Connerney et al. A comet engulfs Mars: MAVEN observations of comet Siding Spring's influence on the Martian magnetosphere. *Geophysical Research Letters*, vol. 42, 21, pp. 8810–8818, 2015.

Essen, L. and K. D. Froome. The Refractive Indices and Dielectric Constants of Air and its Principal Constituents at 24,000 Mc/s. *Proceedings of the Physical Society. Section B*, vol. 64, 10, pp. 862–875, 1951.

Fahey, D. W., I. Dotan, F. C. Fehsenfeld et al. Energy dependence of the rate constant of the reaction N^++NO at collision energies 0.04 to 2.5 eV. *The Journal of Chemical Physics*, vol. 74, 6, pp. 3320–3323, 1981a.

Fahey, D. W., F. C. Fehsenfeld and E. E. Ferguson. Rate constant for the reaction $C^+ + CO_2$ at collision energies 0.04 to 2.5eV. *Geophysical Research Letters*, vol. 8, 10, pp. 1115–1117, 1981b.

Fallows, K., P. Withers and M. Matta. An observational study of the influence of solar zenith angle on properties of the M1 layer of the Mars ionosphere. *Journal of Geophysical Research: Space Physics*, vol. 120, 2, pp. 1299–1310, 2015.

Fehsenfeld, F. C., D. B. Dunkin and E. E. Ferguson. Rate constants for the reaction of CO_2^+ with O, O_2 and NO; N_2^+ with O and NO; and O_2^+ with NO. *Planetary and Space Science*, vol. 18, 8, pp. 1267–1269, 1970.

Fehsenfeld, F. C. and E. E. Ferguson. Recent Laboratory Measurements of D - and E -Region Ion-Neutral Reactions. *Radio Science*, vol. 7, 1, pp. 113–115, 1972.

Fell, C., J. I. Steinfeld and S. Miller. Quenching of $N(^2D)$ by $O(^3P)$. *The Journal of Chemical Physics*, vol. 92, 8, pp. 4768–4777, 1990.

Ferguson, E. E. Rate constants of thermal energy binary ion-molecule reactions of aeronomic interest. *Atomic Data and Nuclear Data Tables*, vol. 12, 2, pp. 159–178, 1973.

Fernandez, A., A. Goumri and A. Fontijn. Kinetics of the Reactions of $N(^4S)$ Atoms with O_2 and CO_2 over Wide Temperatures Ranges. *The Journal of Physical Chemistry A*, vol. 102, 1, pp. 168–172, 1998.

Feynman, R. P., R. B. Leighton and M. L. Sands. *The Feynman lectures on physics*, vol. 2 of *The Feynman lectures on physics*. Basic Books, New York, new millennium edition edn., 2010. ISBN 0465073999.

Fjeldbo, G. and V. R. Eshleman. The bistatic radar-occultation method for the study of planetary atmospheres. *Journal of Geophysical Research*, vol. 70, 13, pp. 3217–3225, 1965.

Fjeldbo, G., A. J. Kliore and R. von Eshleman. The Neutral Atmosphere of Venus as Studied with the Mariner V Radio Occultation Experiments. *The Astronomical Journal*, vol. 76, pp. 123–140, 1971.

Fletcher, K., ed. *Mars Express: The scientific investigations*. ESA Communication Production Office, Noordwijk and the Netherlands, 2009. ISBN 92-9221-975-8.

Forget, F., F. Hourdin, R. Fournier et al. Improved general circulation models of the Martian atmosphere from the surface to above 80 km. *Journal of Geophysical Research: Planets*, vol. 104, E10, pp. 24155–24175, 1999.

Forget, F., E. Millour and S. R. Lewis. Mars Climate database v5.1 Detailed Design Document. 2015.

Formisano, V., D. Grassi, R. Orfei et al. PFS: the Planetary Fourier Spectrometer for Mars Express. In A. Wilson, ed., *Mars Express*, pp. 71–94. ESA Publications Division, Noordwijk, 2004. ISBN 92-9092-556-6.

Fowler, C. M. R. *The solid earth: An introduction to global geophysics*. Cambridge Univ. Press, Cambridge [u.a.], 2. ed., 8. print edn., 2011. ISBN 0521584094.

Fox, J. L. The chemistry of metastable species in the Venusian ionosphere. *Icarus*, vol. 51, 2, pp. 248–260, 1982.

Fox, J. L. Response of the Martian thermosphere/ionosphere to enhanced fluxes of solar soft X rays. *Journal of Geophysical Research*, vol. 109, A11310, 2004.

Fox, J. L. The ionospheric source of the red and green lines of atomic oxygen in the Venus nightglow. *Icarus*, vol. 221, 2, pp. 787–799, 2012.

Fox, J. L. The chemistry of protonated species in the martian ionosphere. *Icarus*, vol. 252, pp. 366–392, 2015.

Fox, J. L. and A. Dalgarno. Ionization, luminosity, and heating of the upper atmosphere of Mars. *Journal of Geophysical Research*, vol. 84, A12, p. 7315, 1979.

Fox, J. L., M. I. Galand and R. E. Johnson. Energy Deposition in Planetary Atmospheres by Charged Particles and Solar Photons. In A. F. Nagy, A. Balogh, T. E. Cravens, M. Mendillo and I. Mueller-Wodarg, eds., *Comparative Aeronomy*, vol. 29 of *Space Sciences Series of ISSI*, pp. 3–62. Springer New York, New York, NY, 2009. ISBN 978-0-387-87824-9.

Fox, J. L. and K. Y. Sung. Solar activity variations of the Venus thermosphere/ionosphere. *Journal of Geophysical Research: Space Physics*, vol. 106, A10, pp. 21305–21335, 2001.

Fox, J. L. and K. E. Yeager. Morphology of the near-terminator Martian ionosphere: A comparison of models and data. *Journal of Geophysical Research*, vol. 111, A10309, 2006.

Fox, J. L., P. Zhou and S. W. Bougher. The Martian thermosphere/ionosphere at high and low solar activities. *Advances in Space Research*, vol. 17, 11, p. (11)203, 1996.

Freeman, R. L. *Radio system design for telecommunications*. Wiley series in telecommunications and signal processing. IEEE and Wiley-Interscience, New York and Hoboken, N.J., 3rd edn., 2007. ISBN 0470050438.

Fritts, D. C., L. Wang and R. H. Tolson. Mean and gravity wave structures and variability in the Mars upper atmosphere inferred from Mars Global Surveyor and Mars Odyssey aerobraking densities. *Journal of Geophysical Research*, vol. 111, 2006.

Froese Fischer, C. and G. Tachiev. Breit–Pauli energy levels, lifetimes, and transition probabilities for the beryllium-like to neon-like sequences. *Atomic Data and Nuclear Data Tables*, vol. 87, 1, pp. 1–184, 2004.

Frost, M. J., S. Kato, V. M. Bierbaum et al. Reactions of $N_2^+(v)$ with CO and NO at thermal energy. *Chemical Physics*, vol. 231, 2-3, pp. 145–153, 1998.

Gagné, M.-È., J.-L. Bertaux, F. González-Galindo et al. New nitric oxide (NO) nightglow measurements with SPICAM/MEx as a tracer of Mars upper atmosphere circulation and comparison with LMD-MGCM model prediction: Evidence for asymmetric hemispheres. *Journal of Geophysical Research: Planets*, vol. 118, 10, pp. 2172–2179, 2013.

Gear, C. W. *Numerical initial value problems in ordinary differential equations*. Prentice-Hall series in automatic computation. Prentice-Hall, Englewood Cliffs N.J, 1971. ISBN 9780136266068.

Geppert, W. D., R. Thomas, A. Ehlerding et al. Extraordinary branching ratios in astrophysically important dissociative recombination reactions. *Faraday Discussions*, vol. 127, E12, pp. 425–437, 2004.

Girazian, Z., P. R. Mahaffy, R. J. Lillis et al. Nightside ionosphere of Mars: Composition, vertical structure, and variability. *Journal of Geophysical Research: Space Physics*, vol. 122, 4, pp. 4712–4725, 2017.

Girazian, Z., P. Withers, B. Häusler et al. Characterization of the lower layer in the dayside Venus ionosphere and comparison with Mars. *Planetary and Space Science*, vol. 117, pp. 146–158, 2015.

Goldan, P. D., A. L. Schmeltekopf, F. C. Fehsenfeld et al. Thermal Energy Ion—Neutral Reaction Rates. II. Some Reactions of Ionospheric Interest. *The Journal of Chemical Physics*, vol. 44, 11, pp. 4095–4103, 1966.

González-Galindo, F. *Modelos energéticos, químicos y dinámicos de la alta atmósfera de Marte*. Phd thesis, Universidad de Granada, Granada, 2006.

González-Galindo, F., J.-Y. Chaufray, M. A. López-Valverde et al. 3D Martian Ionosphere model: I. The photochemical ionosphere below 180 km. *Journal of Geophysical Research*, vol. submitted, 2013.

González-Galindo, F., F. Forget, M. Angelats i Coll et al. The Martian upper atmosphere. *Lecture Notes and Essays in Astrophysics*, vol. 3, pp. 151–162, 2008.

González-Galindo, F., F. Forget, M. A. López-Valverde et al. A ground-to-exosphere Martian general circulation model: 1. Seasonal, diurnal, and solar cycle variation of thermospheric temperatures. *Journal of Geophysical Research: Planets*, vol. 114, E4, 2009.

González-Galindo, F., M. A. López-Valverde, M. Angelats i Coll et al. Extension of a Martian general circulation model to thermospheric altitudes: UV heating and photochemical models. *Journal of Geophysical Research*, vol. 110, E9, 2005.

González-Galindo, F., M. A. López-Valverde, F. Forget et al. Variability of the Martian thermosphere during eight Martian years as simulated by a ground-to-exosphere global circulation model. *Journal of Geophysical Research: Planets*, vol. 120, 11, pp. 2020–2035, 2015.

González-Galindo, F., M. A. López-Valverde, G. Gilli et al. 3D Simulations of the Ionosphere: SZA Variability and the Post-Terminator Ionosphere. 2014.

Gopalswamy, N. History and development of coronal mass ejections as a key player in solar terrestrial relationship. *Geoscience Letters*, vol. 3, 1, p. 195, 2016.

Gougousi, T., M. F. Golde and R. Johnsen. Electron-ion recombination rate coefficient measurements in a flowing afterglow plasma. *Chemical Physics Letters*, vol. 265, 3-5, pp. 399–403, 1997.

Gubenko, V. N., A. G. Pavelyev, I. A. Kirillovich et al. Case study of inclined sporadic E layers in the Earth's ionosphere observed by CHAMPS/GPS radio occultations: Coupling between the tilted plasma layers and internal waves. *Advances in Space Research*, vol. in Press, 2017.

Gurnett, D. A., R. L. Huff, D. D. Morgan et al. An overview of radar soundings of the martian ionosphere from the Mars Express spacecraft. *Advances in Space Research*, vol. 41, 9, pp. 1335–1346, 2008.

Gurnett, D. A., D. L. Kirchner, R. L. Huff et al. Radar soundings of the ionosphere of Mars. *Science (New York, N.Y.)*, vol. 310, 5756, pp. 1929–1933, 2005.

Gurnett, D. A., D. D. Morgan, A. M. Persoon et al. An ionized layer in the upper atmosphere of Mars caused by dust impacts from comet Siding Spring. *Geophysical Research Letters*, vol. 42, 12, pp. 4745–4751, 2015.

Haider, S. A., M. A. Abdu, I. S. Batista et al. D, E, and F layers in the daytime at high-latitude terminator ionosphere of Mars: Comparison with Earth's ionosphere using COSMIC data. *Journal of Geophysical Research*, vol. 114, A3, 2009.

Haldoupis, C. Midlatitude Sporadic E. A Typical Paradigm of Atmosphere-Ionosphere Coupling. *Space Science Reviews*, vol. 168, 1-4, pp. 441–461, 2012.

Haldoupis, C., D. Pancheva, W. Singer et al. An explanation for the seasonal dependence of midlatitude sporadic E layers. *Journal of Geophysical Research: Space Physics*, vol. 112, A6, 2007.

Halekas, J. S., E. R. Taylor, G. Dalton et al. The Solar Wind Ion Analyzer for MAVEN. *Space Science Reviews*, vol. 195, 1, pp. 125–151, 2015.

Hanson, W. B. and G. P. Mantas. Viking electron temperature Measurements: evidence for a magnetic field in the Martian ionosphere. *Journal of Geophysical Research*, vol. 93, A7, pp. 7538–7544, 1988.

Hanson, W. B., S. Sanatani and D. R. Zuccaro. The Martian Ionosphere as Observed by the Viking Retarding Potential Analyzers. *Journal of Geophysical Research*, vol. 82, 28, pp. 4351–4363, 1977.

Hathaway, D. H. The Solar Cycle. *Living reviews in solar physics*, vol. 12, p. 4, 2015.

Hellberg, F., S. Rosén, R. Thomas et al. Dissociative recombination of NO^+: Dynamics of the $X^1\Sigma^+$ and $a^3\Sigma^+$ electronic states. *The Journal of Chemical Physics*, vol. 118, 14, pp. 6250–6259, 2003.

Henke, B. L., E. M. Gullikson and J. C. Davis. X-Ray Interactions: Photoabsorption, Scattering, Transmission, and Reflection at E = 50-30,000 eV, Z = 1-92. *Atomic Data and Nuclear Data Tables*, vol. 54, 2, pp. 181–342, 1993.

Herron, J. T. Evaluated Chemical Kinetics Data for Reactions of $N(^2D)$, $N(^2P)$, and $N_2(A_3\Sigma_u^+)$ in the Gas Phase. *Journal of Physical and Chemical Reference Data*, vol. 28, 5, pp. 1453–1483, 1999.

Hierl, P. M., I. Dotan, J. V. Seeley et al. Rate constants for the reactions of O^+ with N_2 and O_2 as a function of temperature (300–1800 K). *The Journal of Chemical Physics*, vol. 106, 9, pp. 3540–3544, 1997.

Hinson, D. P., M. Pätzold, S. Tellmann et al. The depth of the convective boundary layer on Mars. *Icarus*, vol. 198, 1, pp. 57–66, 2008a.

Hinson, D. P., M. Pätzold, B. L. Wilkerson et al. Radio occultation measurements and MGCM simulations of Kelvin waves on Mars. *Icarus*, vol. 193, 1, pp. 125–138, 2008b.

Hinson, D. P., R. A. Simpson, J. D. Twicken et al. Initial results from radio occultation measurements with Mars Global Surveyor. *Journal of Geophysical Research*, vol. 104, E11, pp. 26997–27012, 1999.

Huebner, W. F. and J. Mukherjee. Photoionization and photodissociation rates in solar and blackbody radiation fields. *Planetary and Space Science*, vol. 106, pp. 11–45, 2015.

Huestis, D. and J. Berkowitz. Critical evaluation of the photoabsorption cross section of CO_2 from 0.125 to 201.6 nm at room temperature. *Advances in Geosciences*, pp. 229–242, 2011.

Hunten, D. M. The Escape of Light Gases from Planetary Atmospheres. *Journal of the Atmospheric Sciences*, vol. 30, 8, pp. 1481–1494, 1973.

Istomin, V. G. Absolute concentrations of ion components of the earth's atmosphere at altitudes between 100 and 200 km. *Planetary and Space Science*, vol. 11, 2, pp. 169–172, 1963.

Jacobson, M. Z. *Fundamentals of atmospheric modeling*. Cambridge University Press, Cambridge, 2nd ed., transferred to digital print edn., 2007. ISBN 9780521548656.

Jain, S. K. and A. Bhardwaj. Impact of solar EUV flux on CO Cameron band and CO2+ UV doublet emissions in the dayglow of Mars. *Planetary and Space Science*, vol. 63-64, pp. 110–122, 2012.

Jakosky, B. M., J. M. Grebowsky, J. G. Luhmann et al. Initial results from the MAVEN mission to Mars. *Geophysical Research Letters*, vol. 42, 21, pp. 8791–8802, 2015a.

Jakosky, B. M., R. P. Lin, J. M. Grebowsky et al. The Mars Atmosphere and Volatile Evolution (MAVEN) Mission. *Space Science Reviews*, vol. 195, 1, pp. 3–48, 2015b.

Jamieson, M. J., M. Finch, R. S. Friedman et al. Collisional excitation of metastable oxygen $O(^1D)$ atoms through the $B^3\sum_u^-$ channel of O_2. *Planetary and Space Science*, vol. 40, 12, pp. 1719–1721, 1992.

Kalogerakis, K. S., T. G. Slanger, E. A. Kendall et al. Remote Oxygen Sensing by Ionospheric Excitation (ROSIE). *Annales Geophysicae*, vol. 27, 5, pp. 2183–2189, 2009.

Keating, G. M., S. W. Bougher, J. M. Forbes et al. The Mars Thermosphere and Exosphere Climatology from Accelerometer Experiment Measurements. *European Planetary Science Congress*, vol. 4, EPSC2009-664, 2009.

Keating, G. M., S. W. Bougher, R. W. Zurek et al. The Structure of the Upper Atmosphere of Mars: In Situ Accelerometer Measurements from Mars Global Surveyor. *Science*, vol. 279, 5357, pp. 1672–1676, 1998.

Kella, D., Johnson, Pedersen et al. Branching Ratios for Dissociative Recombination of $^{15}N^{14}N^{+}$. *Physical review letters*, vol. 77, 12, pp. 2432–2435, 1996.

Keller-Rudek, H., G. K. Moortgat, R. Sander et al. The MPI-Mainz UV/VIS Spectral Atlas of Gaseous Molecules of Atmospheric Interest. *Earth System Science Data*, vol. 5, 2, pp. 365–373, 2013.

Kerzhanovich, V. V. Mars 6: Improved Analysis of the Descent Module Measurements. *Icarus*, vol. 30, 1, pp. 1–25, 1977.

Kieffer, H. H., B. M. Jakosky, C. W. Snyder et al., eds. *Mars*. Space science series. Univ. of Arizona Press, Tucson, Ariz., 3. edn., 1992. ISBN 9780816512577.

Kliore, A. J., D. L. Cain, G. Fjeldbo et al. The Atmosphere of Mars from Mariner 9 Radio Occultation Measurements. *Icarus*, vol. 17, 2, pp. 484–516, 1972.

Kliore, A. J., D. L. Cain, G. S. Levy et al. Occultation Experiment: Results of the First Direct Measurement of Mars's Atmosphere and Ionosphere. *Science (New York, N.Y.)*, vol. 149, 3689, pp. 1243–1248, 1965.

Kopp, E. On the abundance of metal ions in the lower ionosphere. *Journal of Geophysical Research: Space Physics*, vol. 102, A5, pp. 9667–9674, 1997.

Krasnopolsky, V. A. *Photochemistry of the Atmospheres of Mars and Venus*, vol. 13 of *Physics and Chemistry in Space*. Springer, Berlin and Heidelberg, 1986. ISBN 9783642704031.

Krasnopolsky, V. A. Photochemistry of the Martian Atmosphere (Mean Conditions). *Icarus*, vol. 101, pp. 313–332, 1993.

Krasnopolsky, V. A. Mars' upper atmosphere and ionosphere at low, medium, and high solar activities: Implications for evolution of water. *Journal of Geophysical Research: Planets*, vol. 107, E12, pp. 11–1–11–11, 2002.

Krems, R. V., M. J. Jamieson and A. Dalgarno. The $^{1}D - ^{3}P$ Transitions in Atomic Oxygen Induced by Impact with Atomic Hydrogen. *The Astrophysical Journal*, vol. 647, 2, pp. 1531–1534, 2006.

Larson, D. E., R. J. Lillis, C. O. Lee et al. The MAVEN Solar Energetic Particle Investigation. *Space Science Reviews*, vol. 195, 1, pp. 153–172, 2015.

Lawrence, G. M. Quenching and radiation rates of $CO(a^3\Pi)$. *Chemical Physics Letters*, vol. 9, 6, pp. 575–577, 1971.

Lefèvre, F. and V. A. Krasnopolsky. Atmospheric Photochemistry. In R. M. Haberle, R. T. Clancy, F. Forget, M. D. Smith and R. W. Zurek, eds., *The Atmosphere and Climate of Mars*, pp. 405–432. Cambridge Univ. Pr, Cambridge, 2017. ISBN 978-1107016187.

Lemoine, F. G., D. E. Smith, D. D. Rowlands et al. An improved solution of the gravity field of Mars (GMM-2B) from Mars Global Surveyor. *Journal of Geophysical Research: Planets*, vol. 106, E10, pp. 23359–23376, 2001.

Lewis, S. R., M. Collins, P. L. Read et al. A climate database for Mars. *Journal of Geophysical Research*, vol. 104, E10, pp. 24177–24194, 1999.

Liemohn, M. W., A. Dupre, S. W. Bougher et al. Time-history influence of global dust storms on the upper atmosphere at Mars. *Geophysical Research Letters*, vol. 39, 11, 2012.

Lillis, R. J., D. A. Brain, G. T. Delory et al. Evidence for superthermal secondary electrons produced by SEP ionization in the Martian atmosphere. *Journal of Geophysical Research*, vol. 117, E3, 2012.

Lindal, G. F., H. B. Hotz, D. N. Sweetnam et al. Radio Occultation Measurements of the Atmosphere and Topography of Mars: Data Acquired During 1 Martian Year of Tracking. *Journal of Geophysical Research: Solid Earth*, vol. 84, B14, pp. 8443–, 1979.

Maeda, J. and K. Heki. Morphology and dynamics of daytime mid-latitude sporadic-E patches revealed by GPS total electron content observations in Japan. *Earth, Planets and Space*, vol. 67, 1, 2015.

Mahaffy, P. R., M. Benna, M. Elrod et al. Structure and composition of the neutral upper atmosphere of Mars from the MAVEN NGIMS investigation. *Geophysical Research Letters*, vol. 42, 21, pp. 8951–8957, 2015a.

Mahaffy, P. R., M. Benna, T. King et al. The Neutral Gas and Ion Mass Spectrometer on the Mars Atmosphere and Volatile Evolution Mission. *Space Science Reviews*, vol. 195, 1, pp. 49–73, 2015b.

Mahajan, K. K., N. K. Lodhi and S. Singh. Ionospheric effects of solar flares at Mars. *Geophysical Research Letters*, vol. 36, 15, 2009.

Marrero, T. R. and E. A. Mason. Gaseous Diffusion Coefficients. *Journal of Physical and Chemical Reference Data*, vol. 1, 1, pp. 3–118, 1972.

Martinis, C. R., J. K. Wilson and M. Mendillo. Modeling day-to-day ionospheric variability on Mars. *Journal of Geophysical Research*, vol. 108, A10, 2003.

Mason, E. A. and E. W. McDaniel. *Transport properties of ions in gases*. Wiley, New York, 1988. ISBN 9780471883852.

Masuoka, T. Single- and double-photoionization cross sections of carbon dioxide (CO2) and ionic fragmentation of CO2+ and CO22+. *Physical Review A*, vol. 50, 5, pp. 3886–3894, 1994.

Masuoka, T. and J. A. R. Samson. Dissociative and double photoionization of CO2 from threshold to 90 A. *Journal de Chimie Physique*, vol. 77, pp. 623–630, 1980.

Mathews, J. D. Sporadic E: current views and recent progress. *Journal of Atmospheric and Solar-Terrestrial Physics*, vol. 60, 4, pp. 413–435, 1998.

Matta, M., M. I. Galand, L. Moore et al. Numerical simulations of ion and electron temperatures in the ionosphere of Mars: Multiple ions and diurnal variations. *Icarus*, vol. 227, pp. 78–88, 2014.

Matta, M., P. Withers and M. Mendillo. The composition of Mars' topside ionosphere: Effects of hydrogen. *Journal of Geophysical Research: Space Physics*, vol. 118, 5, pp. 2681–2693, 2013.

McClintock, W. E., N. M. Schneider, G. M. Holsclaw et al. The Imaging Ultraviolet Spectrograph (IUVS) for the MAVEN Mission. *Space Science Reviews*, vol. 195, 1, pp. 75–124, 2015.

McCord, T. B., J. B. Adams, G. Bellucci et al. Mars Express High Resolution Stereo Camera spectrophotometric data: Characteristics and science analysis. *Journal of Geophysical Research: Planets*, vol. 112, E6, 2007.

McElroy, D., C. Walsh, A. J. Markwick et al. The UMIST database for astrochemistry 2012. *Astronomy & Astrophysics*, vol. 550, p. A36, 2013.

McElroy, M. B. and J. C. McConnell. Atomic carbon in the atmospheres of Mars and Venus. *Journal of Geophysical Research*, vol. 76, 28, pp. 6674–6690, 1971.

McFadden, J. P., O. Kortmann, D. Curtis et al. MAVEN SupraThermal and Thermal Ion Compostion (STATIC) Instrument. *Space Science Reviews*, vol. 195, 1, pp. 199–256, 2015.

McFarland, M., D. L. Albritton, F. C. Fehsenfeld et al. Energy dependence and branching ratio of the N_2^+ + O reaction. *Journal of Geophysical Research*, vol. 79, 19, pp. 2925–2926, 1974.

McNaught, R. H., H. Sato and G. V. Williams. Comet C/2013 A1 (Siding Spring). *Central Bureau Electronic Telegrams*, vol. 3368, 2013.

Mehr, F. J. and M. A. Biondi. Electron Temperature Dependence of Recombination of O_2^+ and N_2^+ Ions with Electrons. *Physical Review*, vol. 181, 1, pp. 264–271, 1969.

Mendillo, M., A. Lollo, P. Withers et al. Modeling Mars' ionosphere with constraints from same-day observations by Mars Global Surveyor and Mars Express. *Journal of Geophysical Research*, vol. 116, 2011.

Mendillo, M., C. Narvaez and B. A. Campbell. The total electron content of the Martian ionosphere from MRO/SHARAD observations. *Journal of Geophysical Research: Planets*, vol. accepted, 2017.

Mendillo, M., P. Withers, D. P. Hinson et al. Effects of Solar Flares on the Ionosphere of Mars. *Science*, vol. 311, 5764, pp. 1135–1138, 2006.

Midey, A. J. and A. A. Viggiano. Rate constants for the reaction of Ar^+ with O_2 and CO as a function of temperature from 300 to 1400 K: Derivation of rotational and vibrational energy effects. *The Journal of Chemical Physics*, vol. 109, 13, pp. 5257–5263, 1998.

Midey, A. J. and A. A. Viggiano. Rate constants for the reaction of O_2^+ with NO from 300 to 1400 K. *The Journal of Chemical Physics*, vol. 110, 22, pp. 10746–10748, 1999.

Miller, T. M., R. E. Wetterskog and J. F. Paulson. Temperature dependence of the ion–molecule reactions $N^+ + CO$, $C^+ + NO$, and C^+ , CO^+ , $CO_2^+ + O_2$ from 90–450 K. *The Journal of Chemical Physics*, vol. 80, 10, pp. 4922–4925, 1984.

Millour, E., F. Forget, A. Spiga et al. The Mars Climate Database (MCD version 5.2): Paper presented at the EPSC 2015 in Nantes. 2015.

Mitchell, D. L., C. Mazelle, J.-A. Sauvaud et al. The MAVEN Solar Wind Electron Analyzer. *Space Science Reviews*, vol. 200, 1-4, pp. 495–528, 2016.

Molina-Cuberos, G. J., J. J. López-Moreno and F. Arnold. Meteoric Layers in Planetary Atmospheres. *Space Science Reviews*, vol. 137, 1-4, pp. 175–191, 2008.

Molina-Cuberos, G. J., O. Witasse, J.-P. Lebreton et al. Meteoric ions in the atmosphere of Mars. *Planetary and Space Science*, vol. 51, 3, pp. 239–249, 2003.

Montabone, L., F. Forget, E. Millour et al. Eight-year climatology of dust optical depth on Mars. *Icarus*, vol. 251, pp. 65–95, 2015.

Montmessin, F., O. Korablev, F. Lefèvre et al. SPICAM on Mars Express: A 10 year in-depth survey of the Martian atmosphere. *Icarus*, vol. 297, pp. 195–216, 2017.

Nahar, S. N. Electron–Ion Recombination Rate Coefficients, Photoionization Cross Sections, and Ionization Fractions for Astrophysically Abundant Elements. II. Oxygen Ions. *The Astrophysical Journal Supplement Series*, vol. 120, 1, pp. 131–145, 1999.

Nair, H. A., M. Allen, A. D. Anbar et al. A Photochemical Model of the Martian Atmosphere. *Icarus*, vol. 111, 1, pp. 124–150, 1994.

Neufeld, P. D., A. R. Janzen and R. A. Aziz. Empirical Equations to Calculate 16 of the Transport Collision Integrals $\Omega^{(l,s)^*}$ for the Lennard–Jones (12–6) Potential. *The Journal of Chemical Physics*, vol. 57, 3, pp. 1100–1102, 1972.

Nicholson, W. P., G. Gronoff, J. Lilensten et al. A fast computation of the secondary ion production in the ionosphere of Mars. *Monthly Notices of the Royal Astronomical Society*, vol. 400, 1, pp. 369–382, 2009.

Nier, A. O. and M. B. McElroy. Structure of the Neutral Upper Atmosphere of Mars: Results from Viking 1 and Viking 2. *Science (New York, N.Y.)*, vol. 194, 4271, pp. 1298–1300, 1976.

Nier, A. O. and M. B. McElroy. Composition and structure of Mars' Upper atmosphere - Results from the neutral mass spectrometers on Viking 1 and 2. *Journal of Geophysical Research*, vol. 82, 28, pp. 4341–4349, 1977.

O'Keefe, A., G. Mauclaire, D. Parent et al. Product energy disposal in the reaction of $N^+(^3P)$ with $O_2(X^3\Sigma)$. *The Journal of Chemical Physics*, vol. 84, 1, pp. 215–219, 1986.

Pandya, B. M. and S. A. Haider. Numerical simulation of the effects of meteoroid ablation and solar EUV/X-ray radiation in the dayside ionosphere of Mars: MGS/MEX observations. *Journal of Geophysical Research: Space Physics*, vol. 119, 11, pp. 9228–9245, 2014.

Pannekoek, A. Über die Erscheinungen, welche bei einer Sternbedeckung durch einen Planeten auftreten. *Astronomische Nachrichten*, vol. 164, 1, pp. 5–10, 1903.

Parkinson, W. H., J. Rufus and K. Yoshino. Absolute absorption cross section measurements of in the wavelength region 163 - 200 nm and the temperature dependence. *Chemical Physics*, vol. 290, 2-3, pp. 251–256, 2003.

Pätzold, M., M. K. Bird, B. Häusler et al. Comment on the paper "Mars Express radio occultation data: A novel analysis approach" by Grandin et al. (2014). *Journal of Geophysical Research: Space Physics*, 2016a.

Pätzold, M., B. Häusler, G. L. Tyler et al. Mars Express 10 years at Mars: Observations by the Mars Express Radio Science Experiment (MaRS). *Planetary and Space Science*, vol. 127, pp. 44–90, 2016b.

Pätzold, M., F. M. Neubauer, L. Carone et al. MaRS: Mars Express Orbiter Radio Science. In A. Wilson, ed., *Mars Express*, pp. 140–163. ESA Publications Division, Noordwijk, 2004. ISBN 92-9092-556-6.

Pätzold, M., S. Tellmann, T. Andert et al. MaRS: Mars Express Radio Science Experiment. In K. Fletcher, ed., *Mars Express*, pp. 217–245. ESA Communication Production Office, Noordwijk and the Netherlands, 2009. ISBN 92-9221-975-8.

Pätzold, M., S. Tellmann, B. Häusler et al. A Sporadic Third Layer in the Ionosphere of Mars. *Science*, vol. 310, pp. 837–839, 2005.

Pesnell, W. D. and J. M. Grebowsky. Meteoric magnesium ions in the Martian atmosphere. *Journal of Geophysical Research*, vol. 105, E1, pp. 1695–1707, 2000.

Peter, K. *Beobachtungen der Ionosphären- und Ionopausenstrukturen des Mars mit dem Radio Science Experiment MaRS auf Mars Express*. Diplomarbeit, Universität zu Köln, Köln, 2008.

Peter, K., M. Pätzold, B. Häusler et al. Ionopause Features of Mars as Observed by the Radio Science Experiment MaRS on Mars Express. *American Geophysical Union, Fall Meeting 2008 abstract #P13B-1319*, 2008.

Peter, K., M. Pätzold, G. J. Molina-Cuberos et al. The dayside ionospheres of Mars and Venus: Comparing a one-dimensional photochemical model with MaRS (Mars Express) and VeRa (Venus Express) observations. *Icarus*, vol. 233, pp. 66–82, 2014.

Petrignani, A., W. J. van der Zande, P. C. Cosby et al. Vibrationally resolved rate coefficients and branching fractions in the dissociative recombination of O_2^+. *The Journal of Chemical Physics*, vol. 122, 1, p. 14302, 2005.

Picardi, G., D. Biccari, R. Seu et al. MARSIS: Mars Advanced Radar for Subsurface and Ionosphere Sounding. In A. Wilson, ed., *Mars Express*, pp. 51–69. ESA Publications Division, Noordwijk, 2004. ISBN 92-9092-556-6.

Poling, B. E., J. M. Prausnitz and J. O'Connell. *The properties of gases and liquids*. McGraw-Hill, New York NY u.a., 5. edn., 2001. ISBN 0-07-011682-2.

Prasad, S. S. and W. T. Huntress, JR. A model for gas phase chemistry in interstellar clouds. I - The basic model, library of chemical reactions, and chemistry among C, N, and O compounds. *The Astrophysical Journal Supplement Series*, vol. 43, p. 1, 1980.

Priest, E. R. *Magnetohydrodynamics of the Sun.* Cambridge University Press, New York, NY, 2014. ISBN 0521854717.

Prölss. *Physics of the Earth's Space Environment.* Springer, Berlin, Heidelberg, 2004. ISBN 978-3642059797.

Restano, M., J. J. Plaut, B. A. Campbell et al. Effects of the passage of Comet C/2013 A1 (Siding Spring) observed by the Shallow Radar (SHARAD) on Mars Reconnaissance Orbiter. *Geophysical Research Letters*, vol. 42, 12, pp. 4663–4669, 2015.

Richards, P. G., D. G. Torr and M. R. Torr. Photodissociation of N_2: A significant source of thermospheric atomic nitrogen. *Journal of Geophysical Research*, vol. 86, A3, p. 1495, 1981.

Rishbeth, H. and M. Mendillo. Ionospheric layers of Mars and Earth. *Planetary and Space Science*, vol. 52, 9, pp. 849–852, 2004.

Rohrbaugh, R. P., J. S. Nisbet, E. Bleuler et al. The effect of energetically produced O_2^+ on the ion temperatures of the Martian thermosphere. *Journal of Geophysical Research: Space Physics*, vol. 84, A7, pp. 3327–3338, 1979.

Rosén, S., R. Peverall, M. Larsson et al. Absolute cross sections and final-state distributions for dissociative recombination and excitation of CO^+(v=0) using an ion storage ring. *Physical Review A*, vol. 57, 6, pp. 4462–4471, 1998.

Samson, J. A. R., T. Masuoka, P. N. Pareek et al. Total and dissociative photoionization cross sections of N_2 from threshold to 107 eV. *The Journal of Chemical Physics*, vol. 86, 11, pp. 6128–6132, 1987.

Sander, S. P., J. R. Abbatt, J. B. Burkholder et al. Chemical Kinetics and Photochemical Data for Use in Atmospheric Studies, Evaluation Number 17. 2011.

Saunders, R. S., R. E. Ervidson, G. D. Badhwar et al. 2001 Mars Odyssey Mission Summary. In C. T. Russell, ed., *2001 Mars Odyssey*, pp. 1–36. Springer, Dordrecht, 2004. ISBN 978-94-015-6958-3.

Schaa, R. *Abel-Inversion von Radio-Okkultationsdaten.* Diplomarbeit, Universität zu Köln, Köln, 2005.

Schaer, S. *Mapping and Predicting the Earth's Ionosphere Using the Global Positioning System.* Ph.d. dissertation, Universität Bern, Bern, Switzerland, 1999.

Schneider, N. M., J. Deighan, A. I. F. Stewart et al. MAVEN IUVS observations of the aftermath of the Comet Siding Spring meteor shower on Mars. *Geophysical Research Letters*, vol. 42, 12, pp. 4755–4761, 2015.

Schofield, K. Rate constants for the gaseous interaction of $O(2^1D_2)$ and $O(2^1S_0)$ - a critical evaluation. *Journal of Photochemistry*, vol. 9, 1, pp. 55–68, 1978.

Schunk, R. W. and A. F. Nagy. *Ionospheres: Physics, plasma physics, and chemistry.* Cambridge Univ. Press, Cambridge and others, 2. edn., 2009. ISBN 0521877067.

Scott, G. B., D. A. Fairley, C. G. Freeman et al. Gas phase reactions of some positive ions with atomic and molecular hydrogen at 300 K. *The Journal of Chemical Physics*, vol. 106, 10, pp. 3982–3987, 1997.

Scott, G. B. I., D. A. Fairley, C. G. Freeman et al. Gas-phase reactions of some positive ions with atomic and molecular nitrogen. *The Journal of Chemical Physics*, vol. 109, 20, pp. 9010–9014, 1998.

Scott, G. B. I., D. A. Fairley, D. B. Milligan et al. Gas Phase Reactions of Some Positive Ions with Atomic and Molecular Oxygen and Nitric Oxide at 300 K. *The Journal of Physical Chemistry A*, vol. 103, 37, pp. 7470–7473, 1999.

Seiff, A. and D. B. Kirk. Structure of the Atmosphere of Mars in Summer at Mid-Latitudes. *Journal of Geophysical Research*, vol. 82, 28, pp. 4364–4378, 1977.

Seu, R., R. J. Phillips, D. Biccari et al. SHARAD sounding radar on the Mars Reconnaissance Orbiter. *Journal of Geophysical Research: Planets*, vol. 112, E5, 2007.

Shaw, D. A., D. Holland, M. A. Hayes et al. A study of the absolute photoabsorption, photoionisation and photodissociation cross sections and the photoionisation quantum efficiency of carbon dioxide from the ionisation threshold to 345 A. *Chemical Physics*, vol. 198, 3, pp. 381–396, 1995.

Shaw, D. A., D. Holland, M. A. MacDonald et al. A study of the absolute photoabsorption cross section and the photoionization quantum efficiency of nitrous oxide from the ionization threshold to 480 A. *Chemical Physics*, vol. 163, 3, pp. 387–404, 1992.

Shi, X., Q.-Z. Yin, H. Gao et al. Branching Ratios in Vacuum Ultraviolet Photodissociation of CO and N_2: Implications for Oxygen and Nitrogen Isotopic Compositions of the Solar Nebula. *The Astrophysical Journal*, vol. 850, 1, p. 48, 2017.

Shinagawa, H., Y. Miyoshi, H. Jin et al. Global distribution of neutral wind shear associated with sporadic E layers derived from GAIA. *Journal of Geophysical Research: Space Physics*, vol. 122, 4, pp. 4450–4465, 2017.

Shuman, N. S., D. E. Hunton and A. A. Viggiano. Ambient and modified atmospheric ion chemistry: from top to bottom. *Chemical reviews*, vol. 115, 10, pp. 4542–4570, 2015.

Simmons, G. F. *Calculus gems: Brief lives and memorable mathematics*. Spectrum series. Mathematical Association of America, Washington, DC, 2007. ISBN 0883855615.

Smith, D., P. Spanel and C. A. Mayhew. A selected ion-flow tube study of the reactions of O^+, H^+ and $HeH]^+$ with several molecular gases at 300 K. *International Journal of Mass Spectrometry and Ion Processes*, vol. 117, pp. 457–473, 1992.

Smith, D. E., Sjogren, William, L., G. L. Tyler et al. The Gravity Field of Mars: Results from Mars Global Surveyor. *Science*, vol. 286, 5437, pp. 94–97, 1999a.

Smith, D. E., M. T. Zuber, H. V. Frey et al. Mars Orbiter Laser Altimeter: Experiment summary after the first year of global mapping of Mars. *Journal of Geophysical Research: Planets*, vol. 106, E10, pp. 23689–23722, 2001.

Smith, D. E., M. T. Zuber, S. C. Solomon et al. The Global Topography of Mars and Implications for Surface Evolution. *Science*, vol. 284, 5419, pp. 1495–1503, 1999b.

Smith, F. L., III and C. Smith. : Numerical evaluation of Chapman's grazing incidence integral ch(X,x). *Journal of Geophysical Research*, vol. 77, 19, pp. 3592–3597, 1972.

Smith, M. D., S. W. Bougher, T. Encrenaz et al. Thermal Structure and Composition. In R. M. Haberle, R. T. Clancy, F. Forget, M. D. Smith and R. W. Zurek, eds., *The Atmosphere and Climate of Mars*, pp. 42–75. Cambridge Univ. Pr, Cambridge, 2017. ISBN 978-1107016187.

Soffen, G. A. The Viking Project. *Journal of Geophysical Research*, vol. 82, 28, pp. 3959–3970, 1977.

Stancil, P. C., D. R. Schultz, M. Kimura et al. Charge transfer in collisions of O^+ with H and H^+ with O. *Astronomy and Astrophysics Supplement Series*, vol. 140, 2, pp. 225–234, 1999.

Stark, G., K. Yoshino, P. L. Smith et al. Photoabsorption cross section measurements of CO_2 between 106.1 and 118.7nm at 295 and 195K. *Journal of Quantitative Spectroscopy and Radiative Transfer*, vol. 103, 1, pp. 67–73, 2007.

Stewart, A. I. Mariner 6 and 7 Ultraviolet Spectrometer Experiment: Implications of CO_2^+ , CO and O Airglow. *Journal of Geophysical Research*, vol. 77, 1, pp. 54–68, 1972.

Stiepen, A., J.-C. Gérard, M.-È. Gagné et al. Ten years of Martian nitric oxide nightglow observations. *Geophysical Research Letters*, vol. 42, 3, pp. 720–725, 2015.

Stiepen, A., S. K. Jain, N. M. Schneider et al. Nitric oxide nightglow and Martian mesospheric circulation from MAVEN/IUVS observations and LMD-MGCM predictions. *Journal of Geophysical Research: Space Physics*, vol. 122, 5, pp. 5782–5797, 2017.

Stolte, W. C., Z. X. He, J. N. Cutler et al. Dissociative photoionization cross sections of N_2 and O_2 from 100 to 800 eV. *Atomic Data and Nuclear Data Tables*, vol. 69, 1, pp. 171–179, 1998.

Tellmann, S., M. Pätzold, B. Häusler et al. The structure of Mars lower atmosphere from Mars Express Radio Science (MaRS) occultation measurements. *Journal of Geophysical Research: Planets*, vol. 118, 2, pp. 306–320, 2013.

Terada, N., F. Leblanc, H. Nakagawa et al. Global distribution and parameter dependences of gravity wave activity in the Martian upper thermosphere derived from MAVEN/NGIMS observations. *Journal of Geophysical Research: Space Physics*, vol. 122, 2, pp. 2374–2397, 2017.

Tian, H., E. Marsch, C.-Y. Tu et al. Sizes of transition-region structures in coronal holes and in the quiet Sun. *Astronomy & Astrophysics*, vol. 482, 1, pp. 267–272, 2008.

Tobiska, W. K., T. Woods, F. Eparvier et al. The SOLAR2000 empirical solar irradiance model and forecast tool. *Journal of Atmospheric and Solar-Terrestrial Physics*, vol. 62, 14, pp. 1233–1250, 2000.

Tsang, W. and R. F. Hampson. Chemical Kinetic Data Base for Combustion Chemistry. Part I. Methane and Related Compounds. *Journal of Physical and Chemical Reference Data*, vol. 15, 3, pp. 1087–1279, 1986.

Ulusen, D., D. A. Brain, J. G. Luhmann et al. Investigation of Mars' ionospheric response to solar energetic particle events. *Journal of Geophysical Research*, vol. 117, A12, 2012.

Unsöld, A. and B. Baschek. *The new cosmos: An introduction to astronomy and astrophysics*. Springer, Berlin and New York, 5th ed. corr. 2nd printing edn., 2005. ISBN 3540678778.

Viggiano, A. A., A. Ehlerding, F. Hellberg et al. Rate constants and branching ratios for the dissociative recombination of CO_2^+. *The Journal of Chemical Physics*, vol. 122, 22, p. 226101, 2005.

Viggiano, A. A., W. Knighton, S. Williams et al. A reexamination of the temperature dependence of the reaction of N^+ with O_2. *International Journal of Mass Spectrometry*, vol. 223-224, pp. 397–402, 2003.

Vlasov, M. and V. Davydov. Theoretical description of the main neutral constituents in the earth's upper atmosphere. *Journal of Atmospheric and Terrestrial Physics*, vol. 44, 8, pp. 641–647, 1982.

von Zahn, U., K. H. Fricke, D. E. Hunton et al. The upper atmosphere of Venus during morning conditions. *Journal of Geophysical Research*, vol. 85, A13, p. 7829, 1980.

Wang, J.-S. and E. Nielsen. Wavelike structures in the Martian topside ionosphere observed by Mars Global Surveyor. *Journal of Geophysical Research*, vol. 108, E7, 2003.

Warren, H. P., J. T. Mariska and J. Lean. A new reference spectrum for the EUV irradiance of the quiet Sun: 1. Emission measure formulation. *Journal of Geophysical Research: Space Physics*, vol. 103, A6, pp. 12077–12089, 1998.

Watters, T. R., P. J. McGovern and R. P. Irwin III. Hemispheres Apart: The Crustal Dichotomy on Mars. *Annual Review of Earth and Planetary Sciences*, vol. 35, 1, pp. 621–652, 2007.

Wedlund, C. S., G. Gronoff, J. Lilensten et al. Comprehensive calculation of the energy per ion pair or W values for five major planetary upper atmospheres. *Annales Geophysicae*, vol. 29, 1, pp. 187–195, 2011.

Whalley, C. L. and J. M. C. Plane. Meteoric ion layers in the Martian atmosphere. *Faraday Discussions*, vol. 147, pp. 349–368, 2010.

Whitehead, J. D. Formation of the Sporadic E Layer in the Temperate Zones. *Nature*, vol. 188, p. 567, 1960.

Wilson, A., ed. *Mars Express: The scientific payload*, vol. 1240. ESA Publications Division, Noordwijk, 2004. ISBN 92-9092-556-6.

Witasse, O., S. W. Bougher, J.-C. Cerisier et al. Effects of a dust storm on the coupled Mars thermosphere-ionosphere. *EGS - AGU - EUG Joint Assembly, Abstracts Nice, France, 6 - 11 April 2003, abstract #2192*, 2003.

Withers, P. A review of observed variability in the dayside ionosphere of Mars. *Advances in Space Research*, vol. 44, 3, pp. 277–307, 2009.

Withers, P., S. W. Bougher and G. M. Keating. The effects of topographically-controlled thermal tides in the martian upper atmosphere as seen by the MGS accelerometer. *Icarus*, vol. 164, 1, pp. 14–32, 2003.

Withers, P., K. Fallows, Z. Girazian et al. A clear view of the multifaceted dayside ionosphere of Mars. *Geophysical Research Letters*, vol. 39, 18, 2012a.

Withers, P., M. O. Fillingim, R. J. Lillis et al. Observations of the nightside ionosphere of Mars by the Mars Express Radio Science Experiment (MaRS). *Journal of Geophysical Research*, vol. 117, A12, 2012b.

Withers, P. and M. Mendillo. Response of peak electron densities in the martian ionosphere to day-to-day changes in solar flux due to solar rotation. *Planetary and Space Science*, vol. 53, 14-15, pp. 1401–1418, 2005.

Withers, P., M. Mendillo, D. P. Hinson et al. Physical characteristics and occurrence rates of meteoric plasma layers detected in the Martian ionosphere by the Mars Global Surveyor Radio Science Experiment. *Journal of Geophysical Research*, vol. 113, A12, 2008.

Woods, T. N., F. G. Eparvier, S. M. Bailey et al. Solar EUV Experiment (SEE): Mission overview and first results. *Journal of Geophysical Research*, vol. 110, A1, p. 441, 2005.

Woods, T. N. and G. J. Rottman. Solar ultraviolet variability over time periods of aeronomic interest. In A. F. Nagy, J. H. Waite and M. Mendillo, eds., *Atmospheres in the solar system*, vol. 130 of *Geophysical monograph*, pp. 221–233. American Geophysical Union, Washington, D.C, 2002. ISBN 0-87590-989-2.

Yiğit, E., S. L. England, G. Liu et al. High-altitude gravity waves in the Martian thermosphere observed by MAVEN/NGIMS and modeled by a gravity wave scheme. *Geophysical Research Letters*, vol. 42, 21, pp. 8993–9000, 2015.

Yiğit, E., P. Koucká Knížová and Georgieva, Katya, Ward, William. A review of vertical coupling in the Atmosphere–Ionosphere system: Effects of waves, sudden stratospheric warmings, space weather, and of solar activity. *Journal of Atmospheric and Solar-Terrestrial Physics*, vol. 141, pp. 1–12, 2016.

Yiğit, E. and A. S. Medvedev. Internal wave coupling processes in Earth's atmosphere. *Advances in Space Research*, vol. 55, 4, pp. 983–1003, 2015.

Yoshino, K., J. R. Esmond, Y. Sun et al. Absorption cross section measurements of carbon dioxide in the wavelength region 118.7–175.5 nm and the temperature dependence. *Journal of Quantitative Spectroscopy and Radiative Transfer*, vol. 55, 1, pp. 53–60, 1996.

Zipf, E. C. The dissociative recombination of vibrationally excited N_2^+ ions. *Geophysical Research Letters*, vol. 7, 9, pp. 645–648, 1980.

Zolesi, B. and L. R. Cander. *Ionospheric Prediction and Forecasting*. Springer, Berlin, Heidelberg, 2013. ISBN 9Â´78-3-642-38429-5.

Zurek, R. W. Comparative aspects of the climate of Mars: an Comparative aspects of the climate of Mars: an introduction to the current atmosphere. In H. H. Kieffer, B. M. Jakosky, C. W. Snyder and M. S. Matthews, eds., *Mars*, Space science series, pp. 799–817. Univ. of Arizona Press, Tucson, Ariz., 1992. ISBN 9780816512577.

Zurek, R. W. Understanding Mars and Its Atmosphere. In R. M. Haberle, R. T. Clancy, F. Forget, M. D. Smith and R. W. Zurek, eds., *The Atmosphere and Climate of Mars*, pp. 3–19. Cambridge Univ. Pr, Cambridge, 2017. ISBN 978-1107016187.

Zurek, R. W. and S. E. Smrekar. An overview of the Mars Reconnaissance Orbiter (MRO) science mission. *Journal of Geophysical Research: Planets*, vol. 112, E5, 2007.

Danksagung

Diese Doktorarbeit wäre ohne die vielen Menschen nicht möglich gewesen, welche mir in dieser Zeit zur Seite gestanden haben. Als erstes möchte ich meinem Doktorvater Priv. Doz. Dr. Martin Pätzold für die Möglichkeiten danken, die er mir mit der Arbeit in seinem Team eröffnet hat. Meinen Kollegen möchte ich für die vielen fruchtbaren Diskussionen danken, dabei besonders Dr. Silvia Tellmann und Janusz Oschlisniok, die immer ein offenes Ohr für meine wissenschaftlichen Fragen hatten und haben. Meinen internationalen Kollegen möchte ich meinen besonderen Dank aussprechen: Dr. Olivier Witasse und Dr. Gregorio Molina-Cuberos, die mir den Einstieg in die Ionosphären-Modellierung erleichtert haben und Dr. Franscisco González-Galindo, der mich in der weiterführenden Modellierung unterstützt hat. Ich möchte auch den internationalen MaRS, VeRa und RSI teams für die guten Gespräche danken, die ich auf den team meetings führen durfte.
Ich danke meinen Eltern für ihre emotionale Unterstützung und ganz besonders meinem Mann Oliver, der auch in schwierigen Situationen immer für mich da war. Auch meinen Freunden möchte ich Danke sagen für den schönen Ausgleich zu den langen Arbeitstagen, hier besonders Christine Medebach, die für meine Hochzeit ihre Doktorarbeit unterbrochen hat. Vielen Dank, ohne Euch alle hätte ich diese Arbeit nicht zu einem guten Ende bringen können!

Ich versichere, dass ich die von mir vorgelegte Dissertation selbständig angefertigt, die benutzten Quellen und Hilfsmittel vollständig angegeben und die Stellen der Arbeit - einschließlich Tabellen, Karten und Abbildungen -, die anderen Werken im Wortlaut oder dem Sinn nach entnommen sind, in jedem Einzelfall als Entlehnung kenntlich gemacht habe; dass diese Dissertation noch keiner anderen Fakultät oder Universität zur Prüfung vorgelegen hat; dass sie - abgesehen von unten angegebenen Teilpublikationen - noch nicht veröffentlicht worden ist sowie, dass ich eine solche Veröffentlichung vor Abschluss des Promotionsverfahrens nicht vornehmen werde.
Die Bestimmungen der Promotionsordnung sind mir bekannt. Die von mir vorgelegte Dissertation ist von Priv. Doz. Dr. Martin Pätzold betreut worden.

Nachfolgende Teilpublikationen liegen vor:
The dayside ionospheres of Mars and Venus: Comparing a one-dimensional photochemical model with MaRS (Mars Express) and VeRa (Venus Express) observations
Kerstin Peter, M. Pätzold, G. Molina-Cuberos, O. Witasse, F. González-Galindo, P. Withers, M. K. Bird, B. Häusler, D. P.Hinson, S. Tellmanna, G. L. Tyler
Icarus, Volume 233, Pages 66-82, 2014

Köln, den 10.03.2018